TECHNISCHE UNIVERSITÄT
KAISERSLAUTERN

OPTIMAS

AG Magnetismus

Annual Report 2010

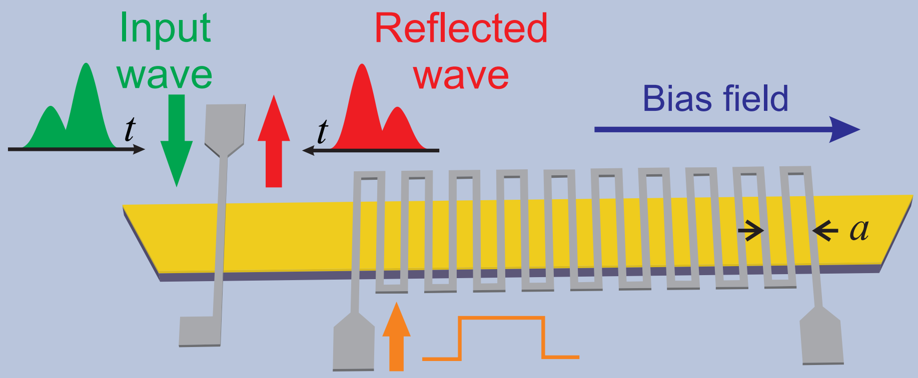

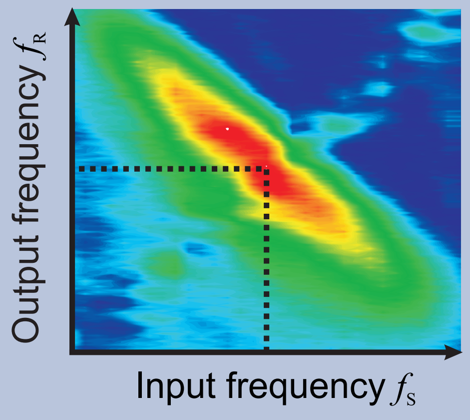

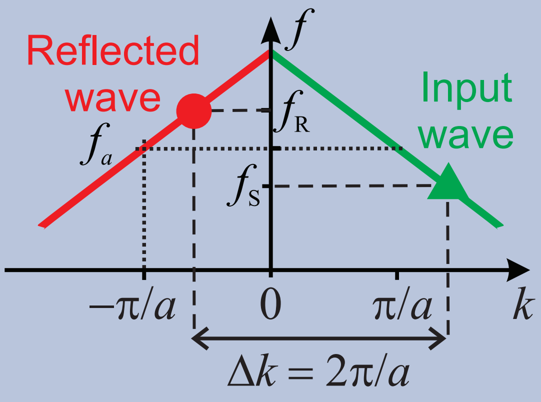

AG MAGNETISMUS
TU KAISERSLAUTERN

Front page: All-linear time reversal by a dynamic magnonic crystal (DMC). The top image shows the experimental DMC system which comprises a planar current-carrying meander structure of period a positioned close to the surface of an Yttrium Iron Garnet thin-film spin-wave waveguide. With the application of a current pulse to the meander structure, the crystal is switched from an homogeneous state to one in which its bias magnetic field is periodically modulated, while a propagating input spin-wave packet is inside. As a result, a linear coupling between spectral components of the input packet (green) with wave vectors $k \approx \pi/a$ and $k' = k - 2\pi/a \approx -\pi/a$ is produced, which leads to an inversion of its spectrum around the DMC band-gap center frequency f_a, and thus to the formation of a time-reversed, reflected wave packet (red). The frequency inversion process is illustrated schematically in the bottom right-hand panel and experimental data confirming the effect, is shown on the bottom left. For more details about this effect see Section 4.11 of this Report and A.V. Chumak et al. (Nature Communications, 2010, in press).

Annual Report 2010

AG MAGNETISMUS
TU KAISERSLAUTERN

Address: Prof. Dr. Burkard Hillebrands
Fachbereich Physik
Landesforschungszentrum OPTIMAS
Technische Universität Kaiserslautern
Erwin-Schrödinger-Straße 56
67663 Kaiserslautern, Germany
Tel.: +49-(0)631-205-4228
Fax.: +49-(0)631-205-4095

Postal address: Postfach 3049
67653 Kaiserslautern, Germany

Internet: http://www.physik.uni-kl.de/hillebrands/
E-Mail: hilleb@physik.uni-kl.de

Our Group

From left to right:

Florin Ciubotaru, Dr. Britta Leven, Dr. Isabel Sattler, Dr. Alexander Serga, Tomohiro Koyama (guest), Yosuke Kajiwara (guest), Philipp Pirro, Roland Neb, Thomas Brächer, Thomas Meyer, Björn Obry, Thomas Sebastian, Dr. Sebastian Schäfer, Christian Sandweg, Dr. Thomas Schneider, Frederik Fohr, Sibylle Müller, Dr. Andreas Beck, Ana Ruiz Calaforra, Dieter Weller, Benjamin Jungfleisch, Dr. Andrés Conca Parra, Dr. Vitaliy Vasyuchka, Thomas Langner, Georg Wolf, Katrin Vogt, Dr. Andrii Chumak, Prof. Dr. Burkard Hillebrands

Contents

Chapter 1: Preface

Dear Colleagues and Friends,

keeping with our tradition, we have prepared our Annual Report covering the period November 2009 to October 2010. A few highlights of our research in 2010: in the field of magnon gases we progressed in investigating the interplay between various magnon groups, in particular with the Bose Einstein condensate. A particular highlight was the radiation of caustic beams from a collapsing bullet as well as the parametrical recovery of a spin-wave signal stored in a magnonic crystal. We continued to move into the field of information processing using magnons, the quanta of spin waves. We decided to name this field "magnon spintronics" indicating that the magnon is serving as the carrier of spin information and also referring to the widely known field of spintronics. Highlights were the investigation of the inverse spin-Hall effect in magnetic insulator/nonmagnetic metal hetero-structures including a study of time dependent phenomena and the enhancement of the spin pumping efficiency by spin-wave mode selection. The field of magnonic crystals is flourishing very well. We were able to demonstrate experimentally the effect of all-linear time reversal and frequency inversion using a dynamic magnonic crystal. In the field of spin-wave phenomena in nanostructures we addressed the issue of near and far field excitation of spin waves in spin-wave waveguides. And we continued our work on Heusler materials.

A big issue for us in 2010 was the start of new research initiatives as well as the ending of existing ones. The new Japanese-German Research Unit "Advanced Spintronic Materials and Transport Phenomena (ASPIMATT)", funded jointly by the Japanese Science and Technology Agency (JST) and the Deutsche Forschungsgemeinschaft (DFG), comprises groups from Tohoku University in Sendai, Johannes Gutenberg University in Mainz and the University of Kaiserslautern. We held our inaugural workshop in October, after we had to cancel the initial workshop planned for end of April due to the volcano ash cloud, which prevented us from travelling to Japan. We started new collaborations with Prof. Eiji Saitoh/Sendai and with Prof. Yoshishige Suzuki/Osaka including short-term exchanges of Ph.D. students. A particular highlight was the Japanese-German workshop on "Spin-wave aspects in spintronics" in October in Villa Denis near Kaiserslautern organized jointly between Prof. YoshiChika Otani/RIKEN and University of Tokyo, and myself, putting particular emphasis on student training and presentations. Feedback indicates that this workshop was well received, in particular the evening lecture on the art of making wine in Rhineland Palatinate. We finished our Marie Curie Research Training Network "Spin current induced ultrafast switching (SPINSWITCH)" after four successful years of work. The work with our Ph.D. students and postdocs as well as the interaction with our colleagues in the network has been mostly enjoyable. Also our DFG funded Research Unit "New materials with high spin polarization", Mainz/Kaiserslautern and Prof. Yasuo Ando/Sendai as external partner came to its end - it is succeeded now by the ASPIMATT initiative.

Furthermore, we finished two very successful BMBF research initiatives, the HEUSPIN project - Innovative Spintronik - Bauelemente für Sensorik und Logik (innovative spintronics - devices for sensors and logic) - coordinated by PREMA Semiconductor GmbH, Mainz, and the MULTIMAG project - Entwicklung von elementaren, industriell nutzbaren magnetoelektrischen Funktionseinheiten durch Weiterentwicklung der XMR-Technologien (development of elementary, industrially feasible magneto-electric devices via advancing XMR technologies) - conducted jointly with the Universities of Mainz and Bielefeld as well as with SENSITEC GmbH, Mainz. To realize the MULTIMAG project the State of Rhineland Palatinate funded a SPINTRONICS platform in industrial environment located at SENSITEC GmbH.

Again, there have been several changes in our group. We are happy to welcome (in alphabetical order) Gerd Baldsiefen, Thomas Brächer, Thomas Langner, and Jürgen Momper as new members of our team. Jarsolav Hamrle has left our group, he now continues his career at University of Ostrava (Czech Republic) as an assistant professor. Benjamin Jungfleisch, Peter Clausen, Philipp Pirro, Thomas Sebastian and Katrin Vogt started their Ph.D. research work, whereas Sebastian Hermsdörfer, Timo Neumann, Helmut Schultheiss and Sebastian Schäfer finished their Ph.D. successfully. Timo Neumann and Sebastian Hermsdörfer left our group for jobs in the private sector, Helmut Schultheiss started a postdoc with Axel Hoffmann at Argonne Research Lab, and Sebastian Schäfer with Tim Mewes at the MINT Center of University of Alabama, Tuscaloosa.

In 2010, two of our young researchers obtained honorable awards: Timo Neumann was awarded “Promotionspreis 2009 der Alumni-Vereinigung Physik” for his Ph.D. thesis “Dynamische Kontrolle von Spinwellen durch lokalisierte, magnetische Inhomogenitäten” (dynamic control of spin waves by localized magnetic inhomogeneities) and Katrin Vogt obtained a personal scholarship by the Carl Zeiss Foundation for supporting her Ph.D. work on “Zeit- und phasenaufgelöste Brillouin-Lichtstreumikroskopie an propagierenden Spinwellen” (time and phase resolved Brillouin light scattering microscopy from propagating spin waves). Personally, I felt very honored about my recognition as IEEE Fellow and for being elected as member by to the Academy of Sciences and Literature in Mainz. I am also very grateful for the confidence of my colleagues at TU Kaiserslautern for being re-elected Vice President for Technology and Research of our university.

Our work would not have been possible without valuable collaborations with people all over the world. They are too many to list them here all. In particular we would like to thank, in alphabetical order, Yasuo Ando, Christian Back, Jozef Barnas, Gerrit Bauer, Hartmut Benner, John Chapman, Claude Chappert, Horia Chiriac, Oksana Chubykalo-Fesenko, Russell Cowburn, Vincent Cros, Sergei Demokritov, Thibaut Devolder, Pallavi Dhagat, Bernard Dieny, Hajo Elmers, Jürgen Fassbender, Gerhard Fecher, Claudia Felser, Jacques Ferré, Albert Fert, Suzanna and Paulo Freitas, Yasuhiro Fukuma, John Gregg, Natalia Grigoryeva, Hartmut Grützediek, Dirk Grundler, Konstantin Gusliyenko, Jarsolav Hamrle, Kouichiro Inomata, Gerhard Jakob, Albrecht Jander, Xiaofeng Jin, Martin Jourdan, Gleb Kakazei, Boris Kalinikos, Alexy Karenowska, Sang-Koog Kim, Mathias Kläui, Peter Kopietz, Mikhail Kostylev, Jürgen Kübler, Liesbet Lagae, Luis Lopez Diaz, Wolfram Maaß, Jean-Claude Mage, Jan Marien, Roland Mattheis, Stephen McVitie, Gennadiy Melkov, Claudia and Tim Mewes, Jacques Miltat, Alexandra Mougin, Markus Münzenberg, Hans Nembach, Takyuki Nozaki, Yoshichika Otani, Carl Patton, Johannes Paul, Dorothée Petit, Kamil Postava, Günter Reiss, Bernhard Reuscher, Karsten Rott, Jürgen Rühl, Manfred Rührig, Eiji Saitoh, John R. Sandercock, Rudi Schäfer, Gerd Schönhense, Justin Shaw, Andrei Slavin, Bob Stamps, Thomasz Stobiecki, Yoshishige Suzuki, Koki Takanashi, André Thiaville, Vasyl Tiberkevich, Simon Trudel, Stefan Visnovsky, Joachim Wecker and Matsufumi Yamamoto for their interactions with us and their strong input to our work.

Collaborations within the Fachbereich Physik at the University of Kaiserslautern (in particular Martin Aeschlimann, James Anglin, Sebastian Eggert, Michael Fleischhauer, Herwig Ott, Hans-Christian Schneider, and Volker Schünemann and their groups), the Institut für Oberflächen- und Schichtanalytik, as well as the Nano+Bio Center have been very stimulating. We are very grateful to be a member of the State Research Center for Optics and Material Sciences OPTIMAS.

I would also like to thank all our sponsors, which are the Deutsche Forschungsgemeinschaft (DFG), the Bundesministerium für Bildung und Forschung (BMBF), the Deutscher Akademischer Austauschdienst (DAAD), the European Community, INTAS, the Carl Zeiss Foundation, the State of Rhineland Palatinate and the University of Kaiserslautern. Concerning our projects in applied research, I would like to express my gratitude to Prema GmbH and Sensitec GmbH, our strong partners in R&D on spintronic sensors. Finally, I am much obliged to Peter Pesch and his team from the TZO GmbH for providing convenient general conditions for our work in Rheinbreitbach.

My special thanks go to Andreas Beck, Isabel Sattler, and Sibylle Müller for their help in preparing this report and to Hubert Gerber from Photo-Repro-Druck, TU Kaiserslautern.

It is my special pleasure to greet all former group members. May this report help to stay in touch. If you are interested in our work I would be happy to hear from you. If you have any questions, comments or suggestions please contact us.

With all my best wishes for Christmas, and a Happy New Year,

Burkard Hillebrands

Kaiserslautern, November 2010

Vorwort

Liebe Kolleginnen und Kollegen und Freunde unserer Arbeitsgruppe,

guter Tradition folgend legen wir hiermit unseren Jahresbericht 2010 vor, der den Zeitraum November 2009 bis Oktober 2010 umfasst. Einige "Highlights" aus unserer Forschung im vergangenen Jahr: auf dem Gebiet der Magnonengase konnten wir gute Fortschritte bei der Wechselwirkung verschiedener Magnonengruppen, speziell mit Bose-Einstein Kondensaten erzielen. Ein besonderes Highlight war die Beobachtung von kaustischer Abstrahlung von Spinwellen eines kollabierenden Spinwellen-Bullets, sowie die parametrische Wiederherstellung eines Spinwellensignals, welches in einem magnonischen Kristall gespeichert war. Weiter vorgearbeitet haben wir uns auf das Gebiet der Informationsverarbeitung mittels Magnonen, den Quanten der Spinwellen. Um aufzuzeigen, dass Magnonen Spininformationen transportieren können, und um einen Bezug zu dem bekannten Gebiet der Spintronik herzustellen, nennen wir dieses Forschungsgebiet "Magnon-Spintronik". Weitere Highlights waren Ergebnisse zum inversen Spin-Halleffekt in magnetischen Isolator/nichtmagnetischen Metall-Heterostrukturen, die Untersuchungen zur Zeitabhängigkeit und die Verstärkung der Spinpumpeffizienz durch Spinwellen-Modenselektion einschlossen. Das Forschungsgebiet der magnonischen Kristalle entwickelt sich sehr erfreulich. So konnten wir experimentell den Effekt einer rein linearen Zeitumkehr und Frequenzinversion in einem dynamischen magnonischen Kristall zeigen. Auf dem Gebiet der Spinwellen in Nanostrukturen haben wir uns mit Nah- und Fernfeldanregungen von Spinwellen in Spinwellen-Wellenleiterstrukturen beschäftigt. Außerdem haben wir unsere Arbeiten an Heusler-Materialien fortgesetzt.

Ein wichtiges Anliegen war uns in 2010 der Start neuer Forschungsinitiativen und der Abschluss bestehender Initiativen. Die deutsch-japanische Forschergruppe "Advanced Spintronic Materials and Transport Phenomena (ASPIMATT)" die gemeinsam von der Japanese Science and Technology Agency (JST) und der Deutschen Forschungsgemeinschaft (DFG) gefördert wird, umfasst Arbeitsgruppen der Tohoku University in Sendai, der Johannes Gutenberg Universität Mainz und der TU Kaiserslautern. Nachdem wir wegen der Vulkanaschewolke im April nicht zu dem eigentlichen Auftaktworkshop nach Japan reisen konnten, hielten wir unseren ersten gemeinsamen Workshop im Oktober ab. Mit kurzen Doktorandenaustauschen haben wir haben neue Kooperationen mit Prof. Eiji Saitoh/Sendai sowie mit Prof. Yoshishige Suzuki/Osaka gestartet. Ein besonderer Höhepunkt war der deutsch-japanische Workshop "Spin-wave aspects in spintronics" den wir im Oktober mit Prof. YoshiChika Otani/RIKEN and University of Tokyo in der Villa Denis bei Kaiserslautern durchgeführt haben, wobei wir ein besonderes Augenmerk auf Vorträge von Doktoranden legten. Rückmeldungen haben uns gezeigt, dass der Workshop gut angenommen wurde, insbesondere der Abendvortrag über die Kunst des Weinbaus in Rheinland-Pfalz. Nach vier Jahren der erfolgreichen Zusammenarbeit haben wir unser Marie Curie Research Training Network "Spin current induced ultrafast switching (SPINSWITCH)" abgeschlossen. Die Zusammenarbeit mit den DoktorandInnen und Postdocs, sowie das Miteinander mit unseren Kolleginnen und Kollegen aus dem Netzwerk hat uns viel Freude gemacht. Auch die DFG Forschergruppe "New materials with high spin polarization", Mainz/Kaiserslautern mit Prof. Yasuo Ando/Sendai haben wir zum Abschluss gebracht - sie wird durch die ASPIMATT Initiative abgelöst.

Außerdem haben wir zwei sehr erfolgreiche BMBF-Verbundprojekte abgeschlossen. Zum einen war dies "Innovative Spintronik - Bauelemente für Sensorik und Logik (HEUSPIN)" koordiniert von der PREMA Semiconductor GmbH, Mainz, und zum anderen war es das mit den Universitäten Mainz und Bielefeld, sowie der SENSITEC GmbH, Mainz gemeinsam durchgeführte Projekt "Entwicklung von elementaren, industriell nutzbaren magnetoelektrischen Funktionseinheiten durch Weiterentwicklung der XMR-Technologien (MULTIMAG)”. Um das MULTIMAG Projekt zu ermöglichen, hatte das Land Rheinland-Pfalz die SPINTRONICS Plattform im industriellen Umfeld der SENSITEC GmbH gefördert.

Die Gruppe hat sich auch dieses Jahr wieder in ihrer Zusammensetzung verändert. Wir freuen uns, als neue Gruppenmitglieder Gerd Baldsiefen, Thomas Brächer, Thomas Langner, und Jürgen Momper bei uns zu haben. Jarsolav Hamrle hat unsere Gruppe für einen Assistenzprofessur an der Universität Ostrava (Tschechien) verlassen. Benjamin Jungfleisch, Peter Clausen, Philipp Pirro, Thomas Sebastian und Katrin Vogt haben ihre Promotionen gestartet, und Sebastian Hermsdörfer, Timo Neumann, Helmut Schultheiss und Sebastian Schäfer haben ihre Promotionen abgeschlossen. Timo Neumann und Sebastian Hermsdörfer haben Stellen in der Privatwirtschaft angetreten, Helmut Schultheiss einen Postdoc-Aufenthalt bei Axel Hoffmann am Argonne Research Lab, und Sebastian Schäfer bei Tim Mewes am MINT Center der University of Alabama, Tuscaloosa.

In 2010 haben zwei unserer jungen Nachwuchswissenschaftler ehrenhafte Auszeichnungen bekommen: Timo Neumann wurde für seine Doktorarbeit “Dynamische Kontrolle von Spinwellen durch lokalisierte, magnetische Inhomogenitäten” den Promotionspreis 2009 der Alumni-Vereinigung des Fachbereichs Physik der TU Kaiserslautern verliehen. Katrin Vogt hat für die Anfertigung Ihrer Doktorarbeit über “Zeit- und phasenaufgelöste Brillouin-Lichtstreumikroskopie an propagierenden Spinwellen” ein Stipendium der Carl Zeiss Stiftung erhalten. Ich selbst wurde zum “IEEE Fellow” ernannt und in die Akademie der Wissenschaften und der Literatur Mainz als ordentliches Mitglied aufgenommen. Ich bin außerdem sehr dankbar für das entgegengebrachte Vertrauen meiner Kolleginnen und Kollegen bei der Wiederwahl zum Vizepräsidenten für Forschung und Technologie unserer Universität.

Unsere Arbeit wäre nicht möglich gewesen ohne die vielen wertvollen Zusammenarbeiten mit Forscherkollegen rund um die Welt. Beispielhaft möchten wir uns bedanken bei (in alphabetischer Reihenfolge) Yasuo Ando, Christian Back, Jozef Barnas, Gerrit Bauer, Hartmut Benner, John Chapman, Claude Chappert, Horia Chiriac, Oksana Chubykalo-Fesenko, Russell Cowburn, Vincent Cros, Sergei Demokritov, Thibaut Devolder, Pallavi Dhagat, Bernard Dieny, Hajo Elmers, Jürgen Fassbender, Gerhard Fecher, Claudia Felser, Jacques Ferré, Albert Fert, Suzanna and Paulo Freitas, Yasuhiro Fukuma, John Gregg, Natalia Grigoryeva, Hartmut Grützediek, Dirk Grundler, Konstantin Gusliyenko, Jaroslav Hamrle, Kouichiro Inomata, Gerhard Jakob, Albrecht Jander, Xiaofeng Jin, Martin Jourdan, Gleb Kakazei, Boris Kalinikos, Alexy Karenowska, Sang-Koog Kim, Mathias Kläui, Peter Kopietz, Mikhail Kostylev, Jürgen Kübler, Liesbet Lagae, Luis Lopez Diaz, Wolfram Maaß, Jean-Claude Mage, Jan Marien, Roland Mattheis, Stephen McVitie, Gennadiy Melkov, Claudia and Tim Mewes, Jacques Miltat, Alexandra Mougin, Markus Münzenberg, Hans Nembach, Takyuki Nozaki, Yoshichika Otani, Carl Patton, Johannes Paul, Dorothée Petit, Kamil Postava, Günter Reiss, Bernhard Reuscher, Karsten Rott, Jürgen Rühl, Manfred Rührig, Eiji Saitoh, John R. Sandercock, Rudi Schäfer, Gerd Schönhense, Justin Shaw, Andrei Slavin, Bob Stamps, Thomasz Stobiecki, Yoshishige Suzuki, Koki Takanashi, André Thiaville, Vasyl Tiberkevich, Simon Trudel, Stefan Visnovsky, Joachim Wecker und Matsufumi Yamamoto.

Für finanzielle Unterstützungen danken wir der Deutschen Forschungsgemeinschaft (DFG), dem Bundesministerium für Bildung und Forschung (BMBF), dem Deutschen Akademischen Austauschdienst (DAAD), der Europäischen Gemeinschaft, INTAS, der Carl Zeiss-Stiftung, dem Land Rheinland-Pfalz und der TU Kaiserslautern. Ich möchte außerdem unseren Partnern in der angewandten Forschung an Spintronik-Sensoren, der Prema GmbH und der Sensitec GmbH, danken.

Schließlich möchte ich mich bei Peter Pesch und seinem Team des Technologiezentrums Oberflächen (TZO GmbH) in Rheinbreitbach für die dortigen guten Arbeitsmöglichkeiten bedanken.

Zusammenarbeiten im Fachbereich Physik an der TU Kaiserslautern waren ebenfalls sehr wertvoll. Besonders bedanken möchten wir uns bei Martin Aeschlimann, James Anglin, Sebastian Eggert, Michael Fleischhauer, Herwig Ott, Hans-Christian Schneider, und Volker Schünemann und ihren Gruppen, wie auch beim Institut für Oberflächen- und Schichtanalytik und dem Nano+Bio Center. Wir sind außerdem dankbar Mitglied im Landesforschungszentrum für Optik und Materialwissenschaften (OPTIMAS) zu sein.

Mein spezieller Dank geht an Andreas Beck, Isabel Sattler und Sibylle Müller für ihre Hilfe in der Erstellung dieses Berichts, sowie an Hubert Gerber von Photo-Repro-Druck, TU Kaiserslautern.

Es ist meine besondere Freude, an dieser Stelle alle früheren Gruppenmitglieder zu grüßen. Vielleicht hilft dieser Bericht ein wenig, Kontakt zu halten. Wenn Sie/Ihr an unserer Arbeit interessiert sind, würden wir uns freuen von Ihnen/Euch zu hören. Das Gleiche gilt bei Fragen, Kommentare oder Anregungen.

Mit den besten Wünschen für ein frohes Weihnachtsfest und ein gutes Neues Jahr

Burkard Hillebrands

Kaiserslautern, im November 2010

Chapter 2: Personnel

2.1 Members of the group

Group leader:

Prof. Dr. Burkard Hillebrands

Senior scientists:

Dr. Britta Leven, Akad. Oberrätin	
Dr. Andrii Chumak	
Dr. Jaroslav Hamrle	until 01/10
Dr. Alexander Serga	

Postdocs and long-term guest scientists:

Dr. Gerhard Baldsiefen (Rheinbreitbach)	since 11/09
Dr. Andreas Beck	
Dr. Andrés Conca Parra	
Dr. Thomas Schneider	
Dr. Helmut Schultheiss	until 09/10
Dr. Vitaliy Vasyuchka	

Ph.D. students:

Dipl.-Phys.	Florin Ciubotaru	
Dipl.-Phys.	Peter Clausen	since 10/10
Dipl.-Phys.	Frederik Fohr	
Dipl.-Phys.	Sebastian Hermsdörfer	until 12/09
Dipl.-Phys.	Benjamin Jungfleisch	since 04/10
Dipl.-Phys.	Lisa Kleinen (Rheinbreitbach)	
Dipl.-Phys.	Roland Neb	
Dipl.-Math.	Timo Neumann	until 12/09
Dipl.-Phys.	Björn Obry	
Dipl.-Phys.	Philipp Pirro	since 01/10
Dipl.-Phys.	Ana Ruiz Calaforra	
Dipl.-Phys.	Christian Sandweg	
Dipl.-Phys.	Sebastian Schäfer	until 10/10
Dipl.-Phys.	Helmut Schultheiss	until 06/10
Dipl.-Phys.	Thomas Sebastian	since 01/10
Dipl.-Phys.	Georg Wolf	
Dipl.-Phys.	Katrin Vogt	since 03/10

Diploma Students:

Thomas Brächer	since 12/09
Peter Clausen	until 06/10
Benjamin Jungfleisch	until 12/09
Volker Kegel	until 12/09
Thomas Langner	since 05/10

Diploma Students:

Philipp Pirro	until 12/09
Thomas Sebastian	until 12/09
Katrin Vogt	until 02/10

Engineers and Technicians

Jörg Elmer (Rheinbreitbach)	until 12/09
Klaus-Peter Frohnhöfer	until 10/10
Eugen Momper (Rheinbreitbach)	since 03/10
Dipl.-Ing. (FH) Dieter Weller	

Adminstration:

Sibylle Müller
Dr. Isabel Sattler

2.2 Visiting scientists, postdoctoral fellows and exchange students

(sorted by date of first arrival in our group)

Prof. Eiji Saitoh, Institute for Materials Research, Tohoku University, Sendai, Japan

13.12.09 - 20.12.09
26.10.10 - 31.10.10

Professor Saitoh is an important collaboration partner in the field of spintronics and we are collaborating on “Magnon Spintronics”. During his visit he gave a lecture on “Spin pumping and spin Seebeck effects in magnetic films”. His visit was devoted to discussions of current results of our joint research and to the development plans for future studies.

Prof. John F. Gregg, Department of Condensed Matter Physics, University of Oxford, United Kingdom

08.01.10 - 11.01.10

Professor Gregg heads the spintronics group based in the Clarendon Laboratory at the University of Oxford. He visited us in January to discuss and plan collaborative work in the areas of magnonics and spin-wave spin mechatronics.

Alexy Karenowska, Department of Condensed Matter Physics, University of Oxford, United Kingdom

08.01.10 - 14.01.10
01.02.10 - 20.03.10
15.05.10 - 26.05.10
15.08.10 - 22.08.10

Alexy Karenowska is a graduate student working in the spintronics group of Prof. John Gregg at the University of Oxford. Her visits to Kaiserslautern have been supported by the State Research Center OPTIMAS of TU Kaiserslautern and Magdalen College, Oxford. During her time with us, Alexy undertook experimental work on novel wave phenomena in magnonic crystal systems. We developed a programme of joint research and prepared joint publications. Our joint research also includes theoretical studies by Profs. Andrei Slavin and Vasyl Tiberkevich (both Oakland University, U.S.A.).

Eleonora Bellini, University of Glasgow, United Kingdom

18.01.10 - 18.02.10

Eleonora Bellini stayed with us in the framework of her secondment within the MRTN project “Spin Current Induced Ultrafast Switching (SPINSWITCH)”. She is a Ph.D. student in the Solid State Physics Group of Prof. Chapman. During her research stay in our group she participated in Brillouin light scattering microscopy measurements of various magnetic micro structures.

Dr. Yasuhiro Fukuma, Quantum Nano-Scale Magnetics Laboratory, Advanced Research Institute, RIKEN, Japan
21.01.10 - 27.01.10
11.08.10 - 18.08.10

Dr. Fukuma visited our group in the framework of our JST/DFG collaboration project "Mapping of spin accumulation using Brillouin light scattering spectroscopy". Jointly we performed BLS investigations on devices that he and his coworkers build in the RIKEN laboratories and in the university research group of Prof. Y. Otani.

Yoichi Shiota, Graduate School of Engineering Science, Osaka University
23.01.10 - 07.03.10

Yoichi Shiota is a student in the group of Prof. Suzuki. He came for a research stay to our group for studying spin wave propagation in strongly anisotropic iron monocrystalline waveguides. He used our BLS techniques for investigations of the iron waveguides that were build in his home laboratory.

Dr. Natalia Grigoryeva, St. Petersburg Electrotechnical University, Russia
28.01.10 - 11.03.10
19.08.10 - 30.09.10

Dr. Grigoryeva's stay was supported in the framework of our long term project "Coherent nonlinear spin-wave states in ferromagnetic films and ferromagnetic/ferroelectric layered structures" (DFG RUS 113/644/0). During her visit she was working on the development of the general analytical theory for the spin-wave dynamics in magnonic crystals. Developed model has been used for the interpretation of the experimental results on the spin-wave scattering in the microstructured magnonic crystals.

Prof. Xiaofeng Jin, Fudan University, Shanghai, China
06.05.10 - 09.05.10

Professor Jin is an expert in the magnetism of MBE grown magnetic epitaxial films. We discussed with him novel experiments using these films.

Dr. Konstantin Gusliyenko, Universidad del Pais Vasco, Bilbao, Spain
08.05.10 - 12.05.10

Dr. Guslienko gave a lecture on the vortex and spin-wave dynamics in microstructures. We also discussed our experimental results on spin waves in magnetic dishes in comparison tothe theoretical models developed by him.

Prof. Andrei Slavin, Oakland University, U.S.A.
10.05.10 - 12.06.10

Professor Slavin's stay was supported by our DFG Graduate School (GRK 792 "Non-linear Optics and Ultrafast Physics"). He delivered lectures on correlated states of an array of coupled nonlinear spin-torque nano-oscillators and nanomagnetism. During his visit he also was working on theoretical studies of nonlinear transition processes in magnon gases and condensates.

Prof. Vasyl Tiberkevich, Oakland University , U.S.A. 10.05.10 - 12.06.10

Prof. Tiberkevich's visit was supported by the Deutsche Forschungsgemeinschaft in the frame of the SFB/Transregio 49 "Condensed Matter Systems with Variable Many-Body Interactions". During his visit he was working on theoretical description of transitional dynamics, of both, parametrically driven magnon gases and fast switchable linear magnonic crystals.

Asst. Prof. Kristen Buchanan, Colorado State University, U.S.A. 07.07.10 - 17.07.10

Asst. Prof. Buchanan stayed with us for an exchange of knowhow on Brillouin light scattering spectroscopy. In particular, she was interested in our methods for aligning the Brillouin light scattering spectrometer as well as in our Brillouin light scattering microscope. In addition, we discussed our software tool "TFPDAS4".

Dr. Mikhail Kostylev, University of Western Australia, Perth, Australia 15.08.10 - 19.10.10

Dr. Kostylev's stay was supported by our DFG Graduate School (GRK 792 "Non-linear Optics and Ultrafast Physics"). During his visit he was working on theoretical studies on anisotropic spin-wave emission during spin-wave bullet collapses and on the storage-recovery phenomenon in ferrite films. A lot of his time and efforts have been devoted to our projects on magnonic crystals where we have a long collaboration. Mikhail delivered several lectures on linear and nonlinear spin wave dynamics and several manuscripts have been prepared during his stay.

Prof. Takyuki Nozaki, Osaka University, Japan 18.08.10 - 17.09.10

Professor Nozaki's visit has been realized in the frame of our joint research interests on spin-wave dynamics in samples with strong magnetic anisotropies. Such samples are fabricated in Osaka University and we studied them together in Kaiserslautern by means of BLS microscopy. Prof. Nozaki's attention has been concentrated on the features of the space and time resolved BLS technique. In very fruitful discussions we established the directions our future research.

Yosuke Kajiwara, Tohoku University, Japan 30.09.10 - 07.11.10

Yosuke Kajiwara is a Ph.D. student in the group of Prof. E. Saitoh. His particular interest is the investigation of the spin-Hall effect and the inverse spin-Hall effect in magnetic insulators. He visited our lab to combine both groups' expertises in a joint measurement of the dectection of parametrically injected magnons by means of the inverse spin-Hall effect.

Tomohiro Koyama, Kyoto University, Japan 01.10.10 - 31.10.10

Tomohiro is a Ph.D. student in the group of Prof. Ono, working on magnetic domain walls in materials with strong out-of plane anisotropy. During his stay in our group he dedicated himself to the investigation of spin waves in Co-Ni layers with an out-of-plane anisotropy by means of Brillouin light scattering microscopy. The samples were fabricated in his home laboratory and covered with an additional Py layer in the MBE chamber of the AG Magnetismus to study the influence of the Co-Ni layer on the excitation spectrum of Py.

Dr. Gleb Kakazei, Universidade do Porto, Portugal 09.10.10 - 15.10.10

Dr. Kakazei's stay was supported in the framework of our joint DAAD project "Full metallic, nanoscale magnonic crystals". The visit was devoted to discuss the progress of the joint research on metallic magnonic crystals by means of BLS and FMR-oriented microwave techniques. We developed a design of new structures and made plans for future research.

2.3 Guest seminars

Prof. Kornelius Nielsch 23.11.2009	Universität Hamburg, Germany *Cylindrical Magnetic Nanoobjects based on Atomic Layer Deposition* Physics colloquium
Prof. Xiaofeng Jin 05.05.2010	Fudan University, Shanghai, China *Nano-magnetism by surface manipulation* Special seminar
Dr. Konstantin Gusliyenko 10.05.2010	Universidad del Pais Vasco, Bilbao, Spain *New aspects of vortex dynamics* Special group seminar
Prof. Andrei Slavin 17.05.2010	Oakland University, Rochester, U.S.A. *"Devil's staircase" in nanomagnetism: Fractional synchronization of a nonlinear spin-torque nano-oscillator* Special group seminar
Prof. Vasyl Tiberkevich 31.05.2010	Oakland University, U.S.A. *Parametric excitation of a spin-torque nano-oscillator* Special group seminar
Prof. Andrei Slavin 04.06.2010	Oakland University, U.S.A. *Correlated states of an array of coupled nonlinear spin-torque nano-oscillators: quasi-chaos, global synchronization, frustration* Seminar of DFG Graduate School GRK 792
Matthias Gottwald 07.07.2010	Nancy-Université, France *New materials for spin-torque experiments* Seminar Graduiertenkolleg 792
Prof. Kevin O'Grady 13.08.2010	Distinguished Lecturer of IEEE Magnetics Society University of York, U.K. *A New Paradigm for Exchange Bias in Polycrystalline Films* Special seminar
Prof. Koji Sekiguchi 31.08.2010	Kyoto University, Japan *Time domain detection of spin wave Doppler shift* Special group seminar
Prof. Eiji Saitoh 29.10.2010	Tohoku University, Sendai, Japan *Spin pumping and spin Seebeck effects in magnetic films* Seminar Graduiertenkolleg 792

2.4 Visits of group members at other laboratories

Frederik Fohr	Institute of Physical and Chemical Research (RIKEN), Tokyo, Japan 29.09. - 12.10.2009 Host: Prof. Y. Otani
Andrii Chumak	Oregon State University, Corvallis, U.S.A. 22.01. - 29.01.2010 Host: Prof. P. Dhagat
Florin Ciubotaru	Commissariat a l'Energie Atomique (CEA), France 12.04. - 16.04.2010 Host: Dr. B. Dieny
Helmut Schultheiss	Université Paris Nord, France 03.05. - 07.05.2010 Host: Prof. M. Cherif
Katrin Vogt	Université Paris Nord, France 03.05. - 07.05.2010 Host: Prof. M. Cherif
Christian Sandweg	Institute for Materials Research, Tohoku University, Sendai, Japan 01.06. - 01.09.2010 Host: Prof. E. Saitoh
Roland Neb	University of York, Great Britain 04.10. - 08.10.2010 Host: Prof. K. O'Grady

2.5 Group member photo gallery


Dr. Gerhard Baldsiefen
Postdoc


Dr. Andreas Beck
Postdoc

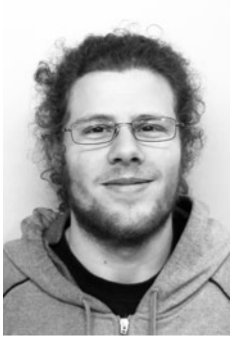
Thomas Brächer
Diploma student


Dr. Andrii Chumak
Senior scientist


Florin Ciubotaru
Ph.D. student


Peter Clausen
Ph.D. student


Dr. Andrés Conca Parra
Postdoc


Jörg Elmer
Technician


Frederik Fohr
Ph.D. student


Klaus-Peter Frohnhöfer
Technician


Dr. Jaroslav Hamrle
Senior scientist


Dr. Sebastian Hermsdörfer
Ph.D. student

Prof. Dr. Burkard Hillebrands
Group leader

Benjamin Jungfleisch
Diploma student

Volker Kegel
Diploma student

Lisa Kleinen
Ph.D. student

Thomas Langner
Diploma student

Dr. Britta Leven
Senior scientist

Eugen Momper
Technician

Sibylle Müller
Secretary

Roland Neb
Ph.D. student

Dr. Timo Neumann
Ph.D. student

Björn Obry
Ph.D. student

Philipp Pirro
Ph.D. student

Ana Ruiz Calaforra
Ph.D. student

Christian Sandweg
Ph.D. student

Dr. Isabel Sattler
Administration

Dr. Sebastian Schäfer
Ph.D. student

Dr. Thomas Schneider
Postdoc

Dr. Helmut Schultheiss
Postdoc

Thomas Sebastian
Ph.D. student

Dr. Alexander Serga
Senior scientist

Dr. Vitaliy Vasyuchka
Postdoc

Katrin Vogt
Ph.D. student

Dieter Weller
Mechanical engineer

Georg Wolf
Ph.D. student

Chapter 3: Methods

3.1 Brillouin light scattering spectroscopy (BLS)

Brillouin light scattering (BLS) spectroscopy is the key technique in our laboratory to investigate the dynamic properties of magnetic materials and devices. It is based on the interaction of photons with quanta of the fundamental excitations of a solid state body, such as phonons and magnons as the quanta of lattice vibrations and spin waves. The interaction can be understood as inelastic scattering of an incident photon by a phonon or magnon, as indicated in Fig. 1, taking into account energy and momentum conservation. Thus the inelastically scattered light carries information of the frequency and the wavevector of the lattice vibrations and spin waves. While the shift in frequency between the incident and the scattered light directly relates to the frequency of the investigated dynamic excitation in the solid, the change in direction of the scattered photons with respect to the incoming light relates to the wavevector.

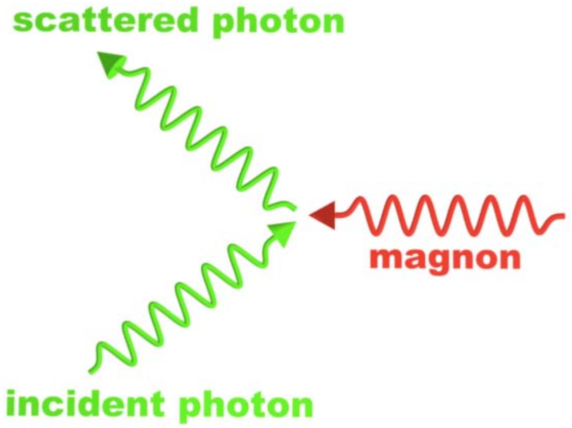

Fig. 1: Scheme of inelastic scattering of an incident photon by a phonon or magnon

Thermal phonons and magnons can be detected with a detection limit down to the monolayer range. This is possible due to the development of interferometry with extremely high contrast and sensitivity. In our laboratory we implemented the (3+3) tandem Fabry-Perot interferometer, designed and build by John R. Sandercock and schematically shown in Fig. 2. It consists of two Fabry-Pérot interferometers (FPI), each one passed three times by the inelastically scattered light. This approach results in a contrast better than 10^{10} for the separation of the elastically and inelastically scattered photons in a frequency range from 500 MHz up two 1 THz.

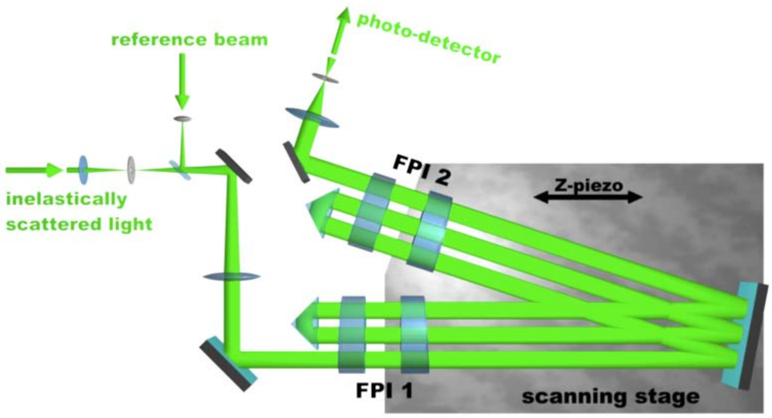

Fig. 2: Scheme of a (3+3) tandem Fabry-Perot interferometer, designed and build by John R. Sandercock (JRS Scientific Instruments, Zürich)

Often, also microwave-excited spin waves are investigated. Among many other applications, the use of pulsed microwave excitation allows for time resolution by using a time-of-flight measurement technique. Here the time difference between the launch of a spin-wave pulse and the detection of according inelastically scattered photons is measured.

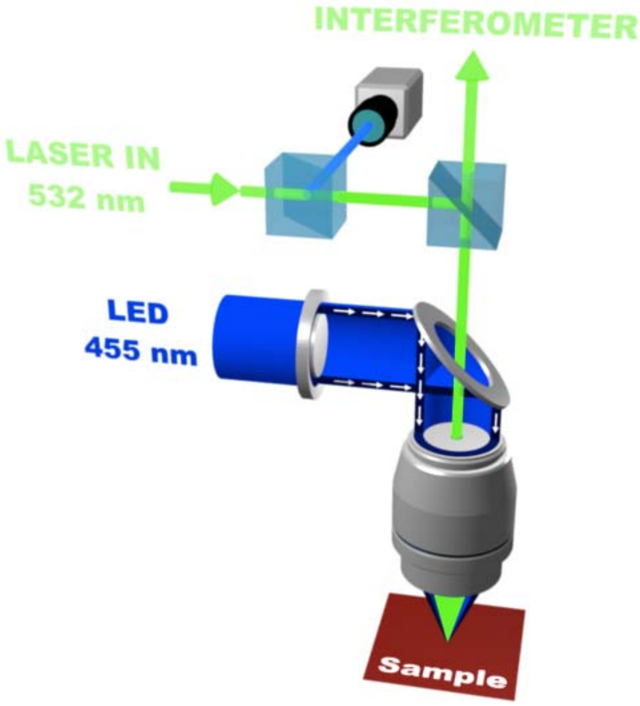

Fig. 3: Schematic setup of a BLS microscope

In the last decade we made significant progress in the further enhancement of BLS spectroscopy. Spatial resolution was pushed to the fundamental limit of classical optics by constructing a BLS microscope (Fig. 3) employing active stabilisation for the sample stage. Spin-wave transport phenomena can be investigated by time, phase- and wavevector resolution. The following list gives an overview of the different BLS setups used in our group:

- BLS1: (3+3) pass Brillouin light scattering spectrometer equipped with high-field electromagnet (1.2 T), time resolution, phase resolution, space resolution (50 µm), wave-vector resolution
- BLS2: (3+3) pass Brillouin light scattering spectrometer equipped with high-field electromagnet (1.2 T), microscope stage with 200 nm spatial resolution and build-in time and phase resolution
- BLS3: (3+3) pass Brillouin light scattering spectrometer equipped with high-field electromagnet (1.2 T), microscope stage with 200 nm spatial resolution and build-in time and phase resolution, *in-situ* MOKE-microscope for domain-pattern characterisation
- BLS4: (3+3) pass Brillouin light scattering spectrometer equipped with sample stage for nano-optic Brillouin light scattering experiments

3.2 Microwave setups

In our laboratory various microwave techniques are used to study both linear and nonlinear dynamics of magnetization in nano-structured and in macroscopic samples.

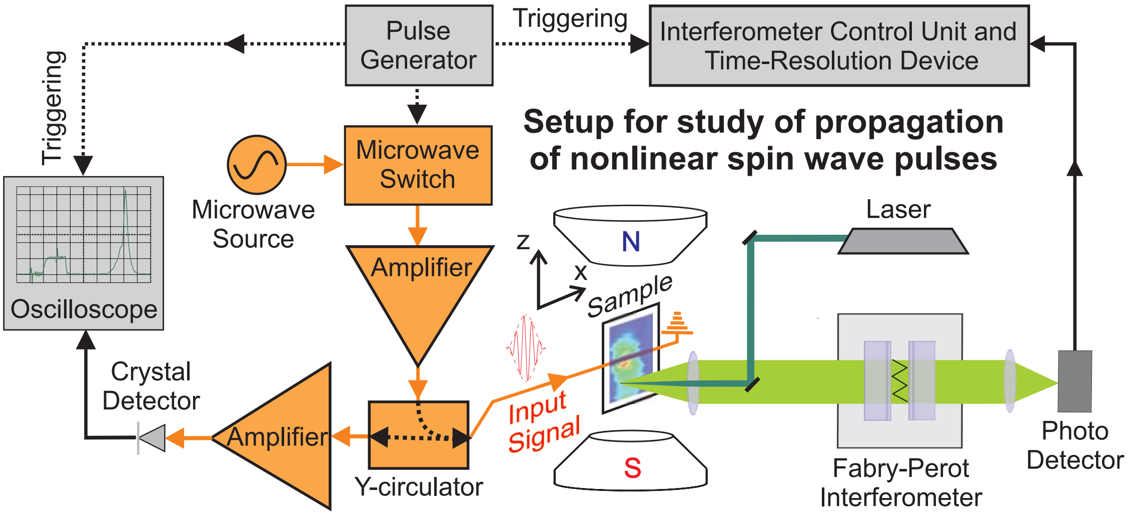

Fig. 1: Scheme of time and space resolved BLS setup

We use continuous and pulsed microwave signals having powers up to 100 W in a frequency range from 1 to 20 GHz. They are used for coherent excitation of eigen excitations and spin waves in magnetic structures. We are able both to perform continuous wave measurements and to characterize travelling spin-wave packets. The spin-wave subsystem of the magnetic material is coupled to electromagnetic sources using various types of microstrip and coplanar antennas, wire loops and cavities. These devices generate microwave Oersted fields which force the precession of magnetic moments in a sample. Vice versa, the precessional motion of magnetic moments is converted by the same devices into microwave currents, which are then electrically detected. The small microwave signals emitted by a magnetic sample are amplified by high-sensitive low-noise amplifiers and rectified by crystal detectors. These signals are observed and analyzed with an oscilloscope, e.g., to reveal their temporal structure. Precise spin-wave amplitude and phase measurements in a wide frequency range are performed using spectrum and network analysers (the latter devices are functionally identical to a spectrum analyzer in combination with a frequency sweep generator).

The parametric pumping process provides a second powerful microwave technique used in our laboratory. This technique plays an important role in experiments on fundamental properties of magnetic excitations as well as in applications since it allows the amplification, generation, and processing of microwave signals. Moreover, this technique allows one to generate exchange-dominant spin waves with very short wavelength. In the case of spatially uniform parallel pumping (microwave magnetic field is parallel to the magnetization) each microwave photon of the pump field splits in two spin-wave quanta (i.e. magnons) having half the energy and propagating in opposite directions. As soon as the quantity of parametrically created magnons exceeds the quantity of magnons which disappear due to magnetic decay the intensity of the corresponding spin-wave mode starts to exponentially increase up to the level of nonlinear saturation. In this process a pumped magnon density of 10^{18}-$10^{19}\,\mathrm{cm}^{-3}$ can be reached, which is enough, for example, to cause the transition of the spin-wave system to a Bose-Einstein condensate state.

The combination of microwave methods with space-, time-, and phase-resolved Brillouin light scattering spectroscopy gives us a unique capability to visualise the evolution of two-dimensional distributions of intensity and phase of artificially excited spin waves. Moreover, with this technique we can detect short-wavelength spin-waves which are inaccessible by conventional microwave antennas.

3.3 Magneto-optic Kerr effect magnetometry and microscopy (MOKE)

The magneto-optical Kerr effect (MOKE) is a well established technique to study the magnetization properties. The effect is based on the fact, that the plane of the polarization of light is rotated when the light is reflected on a magnetic material [1]. The physical origin of the MOKE is the magnetic circular dichroism. The exchange and spin-orbit coupling in a magnetic material lead to different absorption spectra for left- and right circular polarized light. Measuring change of the the polarization of the reflected beam (often refered as Kerr angle Θ_{Kerr}) gives direct access to the magnetiazion state of the sample.

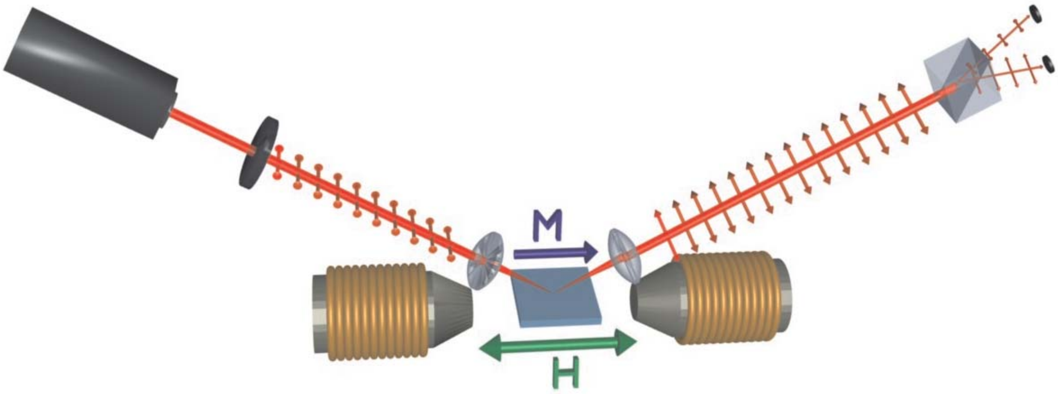

Fig. 1: Schematic setup of a longitudinal vector Kerr magnetometer

Using the magneto-optic Kerr effect(MOKE) it is possible to study the quasi-static magnetization reversal properties and magnetic anisotropies. When using a pulsed laser system it is also possible to study the time dependency of the magnetization under the influence of pulsed magnetic fields or microwave fields. Since it is an optical technique it is non invasive and the spacial resolution is only limited by the optical resolution. Thus we are able to study the static and dynamic properties of magnetic thin films and magnetic structures with lateral dimension down to 1 µm.

We operate four different MOKE setups. All of them work by the same principle. The light of a laser source is s-polarized through a thin film polarizer. The beam is focused on the sample. The polarization of the reflected light is analyzed by a detector unit, developed and produced in our group since many years. A Wollaston prism divides the beam into two orthogonally polarized beams, which are monitored by a pair of photodiodes. The detector works as an opto-electrical bridge circuit to enhance the signal-to-noise ratio. The normalized differential signal $(I_1 - I_2)/(I_1 + I_2)$ is directly proportional to the Kerr angle Θ_{Kerr}.

Longitudinal vector Kerr magnetometer: Longitudinal MOKE geometry to probe quasi-static properties of magnetic thin films. Optical resolution $\gtrsim 100\,\mu\text{m}$, magnetic field up to 1.2 T, automated sample positioning and rotation.

Scanning Kerr microscope with rotation unit: Longitudinal MOKE geometry to probe quasi-static properties of micro-structured magnetic elements. Optical resolution $\gtrsim 1\,\mu\text{m}$, magnetic field up to 0.3 T, automated sample positioning, rotation and stabilization.

Tandem MOKE magnetometer: Two combined MOKE magnetometers working in parallel. One in longitudinal and one in polar geometry to study quadratic MOKE effects on magnetic thin films. Optical resolution $\gtrsim 100\,\mu\text{m}$, two orthogonal pairs of magnet coils to provide any in-plane field direction up to 0.25 T, automated sample positioning and rotation.

Time resolved scanning Kerr microscope: Longitudinal or polar MOKE geometry to study dynamic magnetization reversal properties of micro structured elements. Optical resolution $\gtrsim$ 500 nm, time resolution $\gtrsim$ 60 ps, magnetic field up to 15 mT, automated sample positioning and stabilization.

References

[1] J. Kerr, *On rotation of the plane of polarization by reflection from the pole of a magnet*, Phil. Mag. **4(5), 321 (1877).**

3.4 Molecular beam epitaxy (MBE)

Molecular Beam Epitaxy (MBE) is a method for growing a film or a stack of films on a substrate in ultra high vacuum (UHV). The particular advantage of this method is the good controllability of the growth process by in-situ analysis tools, which has a significant influence on the physical properties of the specific layers [1]. For analysis several techniques are used such as low energy electron diffraction (LEED), reflected high energy electron diffraction (RHEED), Auger electron spectroscopy, as well as scanning probe techniques. MBE is a particular important deposition method for the fabrication of single-crystalline thin-film structures.

For a typical MBE-deposition process the material that will be deposited is heated in UHV using thermal heating (Knudsen cells) or electron heating. For low enough pressures of a few 10^{-11} mbar the atoms of the heated metal can evaporate and form a molecular beam. When this beam is impinging on surface, the atoms start to adsorb on the surface. These atoms are referred to as ad-atoms. Interaction between the ad-atoms and the atoms of the surface take place during the deposition of the atoms (Fig. 1). This interaction depends on the ad-atoms, the used substrate, and the temperature of the substrate. It is responsible for the nucleation and the subsequent growth of thin layers on the substrate.

In general, depending on the growth parameters, one can distinguish between three different growth modes [2], (Fig. 2).

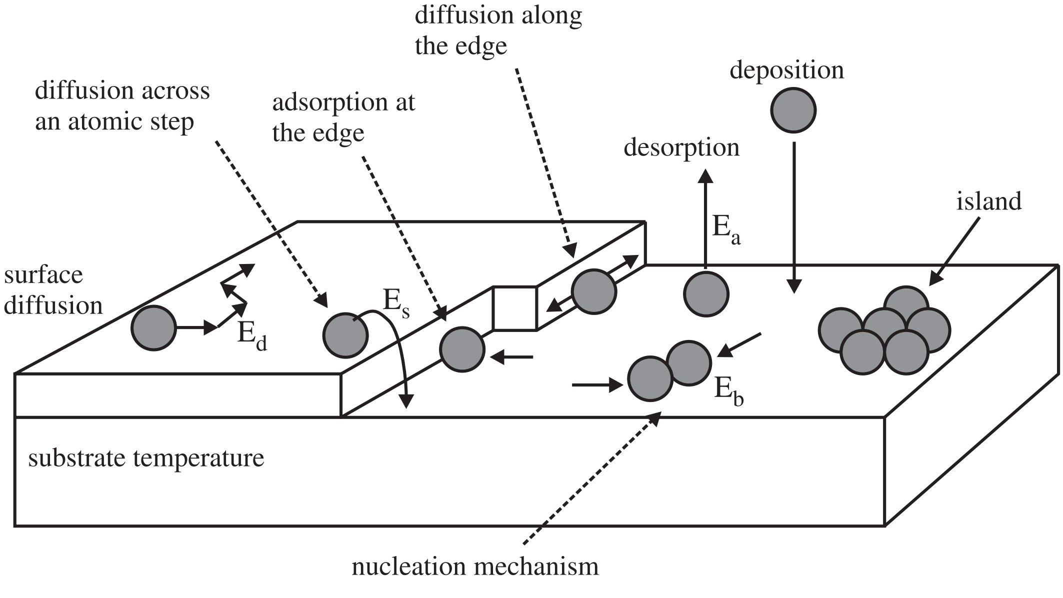

Fig. 1: Behavior of ad-atoms in the surface deposition process (diffusion until nucleation with other adatoms; deposition on edges).

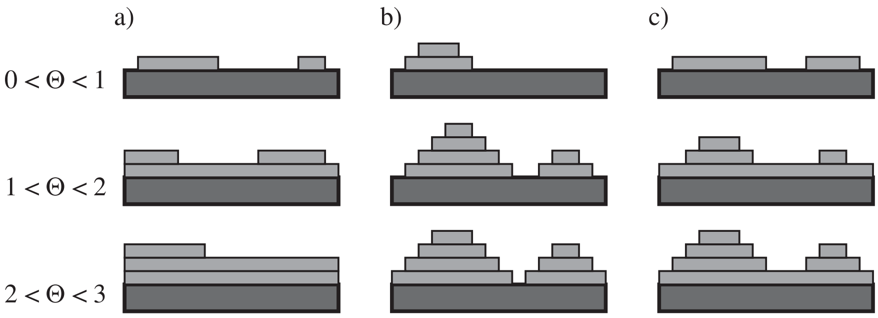

Fig. 2: Growth modes for layer development by MBE

1. Layer or Franck-van der Merwe growth mode: A new layer start to grow only after the preceding one is finished (Fig. 2a).
2. Island or Vollmer-Weber growth mode: The deposited atoms cannot diffuse past the island boundaries. Already after a light coverage multiple monolayers can be formed as high islands (Fig. 2b).
3. Layer plus island or Stranski-Krastanov growth mode: This type is a combination of layer and island growth mode (Fig. 2c).

MBE systems in our laboratory:

Multi-chamber UHV deposition system:

- deposition chamber (electron beam and Knudsen evaporation sources, RHEED, LEED, AES)
- scanning tunneling microscopy chamber with *in-situ* STM, Omicron)
- Brillouin light scattering and Kerr magnetometry chamber (magnetic field 1.2 T, temperature range 80-400 K)
- preparation chamber (optical coating, heating station 2300 °C)
- atom beam reactor chamber with *in-situ* four point probe resistance measurement stage

Two-chamber UHV multideposition system:

- deposition chamber (electron beam and Knudsen sources, LEED, AES)
- ion beam chamber with fine focus noble gas keV ion source (Omicron), ion beam oxidation module
- atom beam reactor chamber

References

[1] A.Y. Cho: Applied Physics Letters **19** 467, 1971.
[2] J.A. Venables, Reports on Progress in Physics **47**, 399 (1984).

Chapter 4: Reports on Experimental Results

A. Magnon Gases

In ferromagnetic materials atoms having unpaired electrons act as individual magnets. Their magnetism is mostly caused by the magnetic moments of the uncompensated electron spins. Since these atomic magnets tend to be oriented in the same direction due to specific quantum-mechanical exchange interaction, a macroscopic magnetic moment appears. As the atoms strongly interact a reversal of a single atomic magnetic moment is not spatially localized but spreads through the solid as a wave of discrete magnetic momentum transfer. This wave is known as a spin wave, and in frame of the second quantization it is associated with a quasi-particle called magnon. Weakly interacting magnons can be considered as a gas of magnetic bosonic quasi-particles, and therefore this is called a magnon gas.

This gas may serve as a model system for the investigation of interacting bosonic particles and for correlated systems in general. Its potential is based on the wide controllability of the magnon density as well as on the spectral properties influencing the magnon-magnon interaction. The recent observation of Bose-Einstein condensation of magnons at room-temperature in the minimum of the spin-wave spectrum demonstrates this clearly (see Nature 443, 430 (2006)).

The spectrum of a magnon gas can be easily controlled by change of orientation and strength of an external bias magnetic field. The most effective mechanism to inject magnons into the gas is microwave parametric pumping (see Gurevich and Melkov, Magnetization Oscillation and Waves, CRC, Cleveland, 1996). In the simplest case one photon of the pumping electromagnetic field excites two magnons with half the energy/frequency that propagate in the opposite directions. Such mechanism creates a huge quantity of phase correlated magnons, called condensate of photon-coupled magnon pairs. Among others, such magnon pairs serve as an energy source and as a strong disturbing factor the entire spin-wave system. Formation, thermalization and disintegration of this condensate as well as its interaction with the other magnonic states and especially with the Bose-Einstein condensate (BEC) of magnons constitutes a hot topic of research. To investigate these processes we use time- and wavevector-sensitive Brillouin light scattering spectroscopy in combination with conventional microwave techniques.

In Report 4.1 we demonstrate the recent results on the optical identification of spectral positions of a directly pumped condensate of exchange-dominant magnon pairs in a tangentially magnetized magnetic film. In Report 4.2 the storage and recovery of a microwave signal in a periodically structured ferrite film is presented. This experiment builds a bridge between the nonlinear dynamics of a magnon gas in uniform magnetic media and in hand-made metamaterials which properties are derived from an engineered mesoscopic (rather than atomic scale, or molecular) structuring. Particularly, it is shown that peculiarities of the restoration process are determined by behavior of magnons decelerated at the edges of artificially created spectral gaps. Finally, in Report 4.3, the anisotropic emission of spin-wave energy from the collapsing spin-wave bullet propagating in a two-dimension magnetic medium is studied both experimentally and theoretically.

A. Magnonengase

In ferromagnetischen Materialien treten Atome, die ungepaarte Elektronen haben, als einzelne Magnete auf. Ihr Magnetismus wird in der Regel durch die magnetischen Momente des nicht kompensierten Elektronenspins verursacht. Diese atomaren Magnete richten sich aufgrund der quantenmechanischen Austauschwechselwirkung in einem Ferromagneten parallel zueinander aus. Daher beobachtet man ein makroskopisches magnetisches Moment. Da die Atome stark miteinander wechselwirken, wird das Umklappen eines einzelnen atomaren Moments nicht räumlich lokalisiert sein, sondern breitet sich als Welle mit einem diskreten magnetischen Moment über den gesamten Festkörper aus. Diese Welle wird als Spinwelle bezeichnet und ist im Rahmen der zweiten Quantisierung mit einem Quasiteilchen, dem so genannten Magnon, verbunden. Schwach miteinander wechselwirkende Magnonen können als Gas von magnetischen bosonischen Quasiteilchen angesehen werden. Daher werden sie auch als Magnonengas bezeichnet.

Dieses Gas kann als Modellsystem für die Untersuchung von wechselwirkenden bosonischen Teilchen und von korrelierten Systemen im allgemeinen dienen. Sein Potenzial liegt dabei in der guten Kontrollierbarkeit der Magnonendichte und den Eigenschaften des Spektrums, welche die Magnon-Magnon-Wechselwirkung beeinflussen. Die kürzlich erfolgte Beobachtung der Bose-Einstein-Kondensation von Magnonen bei Raumtemperatur im Minimum des Spinwellen-Spektrums zeigt dies deutlich (s. Nature 443, 430 (2006)).

Das Spektrum des Magnonengases kann leicht durch eine Änderung der Richtung oder der Stärke eines externen Magnetfelds kontrolliert werden. Der wirkungsvollste Mechanismus, Magnonen in ein Magnonengas einzufüllen, ist parametrisches Pumpen mittels Mikrowellen (s. Gurevich and Melkov, Magnetization Oscillation and Waves, CRC, Cleveland, 1996). Im einfachsten Fall erzeugt ein Photon des elektromagnetischen Pumpfeldes zwei Magnonen mit je der Hälfte der Energie des Photons, die sich in entgegengesetzte Richtungen ausbreiten. Dieser Mechanismus erzeugt eine große Anzahl von phasenkorrelierten Magnonen, ein Kondensat von photonengekoppelten Magnonenpaaren. Unter anderem dienen solche Magnonenpaare als Energiequelle und als starke Störung des gesamten Spinwellensystems. Erzeugung, Thermalisierung und Zerfall dieses Kondensats sowie seine Wechselwirkung mit anderen Magnonenzuständen und besonders mit dem Bose-Einstein-Kondensat von Magnonen sind ein aktuelles Thema der Forschung. Zur Untersuchung dieser Prozesse verwenden wir zeit- und wellenvektoraufgelöste Brillouin-Lichtstreuspektroskopie in Verbindung mit konventioneller Mikrowellentechnik.

In Bericht 4.1 stellen wir neue Resultate über die optische Identifizierung der spektralen Position eines direkt gepumpten Kondensats von austauschdominierten Magnonenpaaren in einem tangential magnetisierten Film vor. In Bericht 4.2 beschreiben wir die Speicherung und Wiedergewinnung eines Mikrowellensignals in einem periodisch strukturierten Ferritfilm. Dieses Experiment verbindet die nichtlineare Dynamik von Magnonengasen in einer homogen magnetisierten Umgebung mit künstlich hergestellten Metamaterialien, deren Eigenschaften durch die Strukturierung auf der mesoskopischen Skala (statt auf der atomaren oder molekularen Skala) modifiziert sind. Speziell zeigen wir, dass die Besonderheiten des Wiederherstellungsprozesses durch das Verhalten der Magnonen an den Kanten der künstlich erzeugten spektralen Lücken gegeben sind. Hier geht die Gruppengeschwindigkeit zu Null. Abschließend präsentieren wir in Bericht 4.3 die anisotrope Emission von Spinwellenenergie durch ein kollabierendes Spinwellen-Bullet, welches sich in einem zweidimensionalem Film ausbreitet, und vergleichen Experiment mit numerischen Simulationen.

4.1 Brillouin light scattering spectroscopy of parametrically excited exchange magnons

C.W. Sandweg, V.I. Vasyuchka, M.B. Jungfleisch, A.A. Serga, and B. Hillebrands[1]

Parallel pumping, the parametric excitation of spin waves by means of a linearly polarized microwave magnetic field parallel to an external bias magnetic field, was first described in 1960 [1,2]. The technique was used in the last five decades to investigate a various number of interesting phenomena such as the excitation of magnetoelastic waves in ferromagnets [3], the spin wave instability absorption [2,4], and the investigation of high-density magnon gases and condensates [7–10]. The parallel pumping has two essential advantages in comparison with the direct excitation of spin waves. Firstly, when exciting spin waves directly with a microstrip antenna using the alternating Oerstedfield, the wavenumber of the efficiently excited spin waves is rather small, in the range of 10^3 rad/cm due to the finite width of the antenna. Therefore, the direct excitation of short-wavelength spin waves can be hardly realized. Secondly, since parallel pumping is a threshold process, i.e. the amplitude h of the pumping field has to exceed a certain threshold h_{crit} [5,6], the pumping efficiency is much higher than for the direct excitation once the threshold is overcome.

During the process of parallel parametric amplification, spin waves with a frequency $\omega_p/2$ are excited at half of the initial microwave pumping frequency ω_p. In terms of energy quanta, a microwave photon splits into two magnons, the quasi-particles of the dynamic magnetization. Different magnon groups with the same frequency $\omega_p/2$ are pumped at the same time and only the one with the lowest damping survives. The determination of the spectral position of the surviving group, i.e. the dominant group, is of crucial importance not only for the investigation of these primarily pumped magnons but for all the magnon groups which get their energy in a subsequent transition process from the dominant group. Here we present the direct observation of the

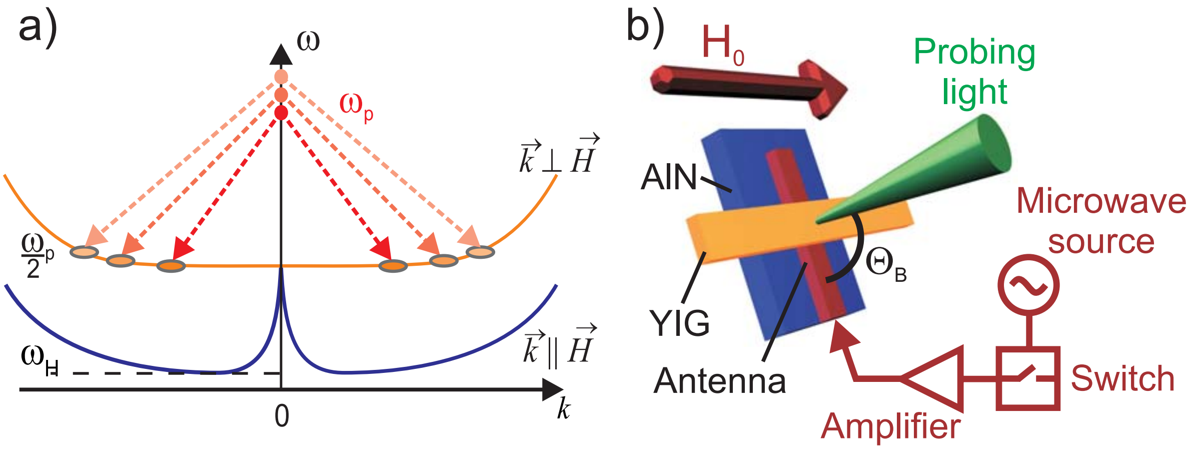

Fig. 1: a) Schematic illustration of the parallel pumping process where one microwave photon with ω_p splits into two magnons with $\omega_p/2$. By changing the pumping frequency, the position of the created magnon pair can be changed. b) Experimental setup. The YIG sample is placed on top of a microstrip antenna which serves as a fed line for the parallel pumping realized by a combination of microwave source, switch and amplifier. The incident angle Θ_B of the probing light determines the selected wavevector.

---

[1] In collaboration with A. Kreisel, Prof. P. Kopietz, Institut für Theoretische Physik, Universität Frankfurt, Germany.

dominant group for different pumping frequencies and powers on a wide wavevector range up to $1.6 \cdot 10^5$ rad/cm using Brillouin light scattering spectroscopy (BLS). We show that the primarily excited spin waves of the dominant group are always located at the $90^\circ-$branch of BVMSW having the lowest energy. Previous works on this topic have been performed by Kabos et al. [12], but only for dipolar-dominated spin waves with a wave number up to $4 \cdot 10^4$ rad/cm. In our present work we complete the picture for dipolar-dominated as well as exchange-dominated BVMSW. By changing the pumping frequency ω_p in sufficiently small step sizes, as shown in Fig. 1a, it is possible to move along the dispersion branch of the BVMSW and determine the spectral position of the dominant group. In addition, theoretical calculations of the dispersion relation have been performed which are in excellent accordance with the experimentally obtained results.

The measurements were achieved using a combined microwave and BLS setup where the magnon system is parametrically pumped by the microwave part and the response of the magnon system is analyzed by BLS spectroscopy. Parallel pumping was realized by a microwave setup comprising source, switch, and amplifier, see Fig. 1b. The switch generated a pulse of 2 µs width and 20 µs repetition time. Therefore, any heating effects were reduced to the minimum. For the same reason, a metalized aluminum nitride substrate served as a ground plate due to its high thermal conductivity. On top, a 50 µm wide microstrip antenna was fabricated which worked as a fed line for the parallel pumping. In order to excite dipolar as well as exchange-dominated magnons, the frequency of the microwave source was varied from 13.6 GHz up to 14.6 GHz in a step size of 20 MHz, which corresponds to $\omega_\mathrm{p}/2$ from 6.8 GHz to 7.3 GHz in steps of 10 MHz. Thus, according to the magnon spectrum, a wide range of wave numbers up to $1.6 \cdot 10^5$ rad/cm was investigated by means of BLS spectroscopy. The experiments were performed for different microwave powers from 100 mW to 10 W.

The investigated sample was a 15 mm long and 3 mm narrow yttrium iron garnet (YIG) film with a thickness of 5 µm. An external bias field H_0 was applied parallel to the long side of the YIG film and was held constant at 1750 Oe during the measurements. In order to analyze the parametrically pumped magnons, BLS measurements were performed in backscattering geometry. A single-mode solid state laser with 532 nm wavelength was focused onto the sample by an objective with a high numerical aperture. The back-scattered light was collected with the same objective and sent to the interferometer.

In a classical description, the inelastic BLS process can be interpreted as the diffraction of the probing light from a moving Bragg-grating due to magneto-optical coupling. The diffraction from the grating leads to a transfer of momentum during this process. By changing the angle Θ_B between the sample and the incident light, the wavevector selection can be realized as shown in Fig. 1b [11]. The incident angle Θ_B of the probing light determines the selected wave vector.

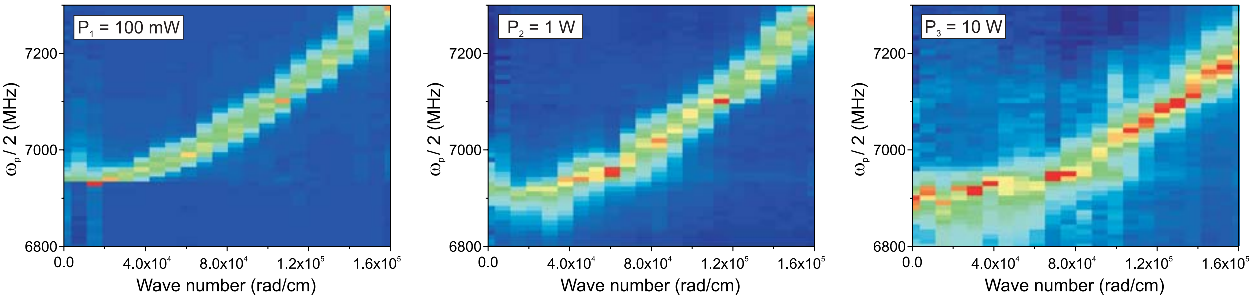

Fig. 2: Color-coded BLS intensity maps of parametrically injected magnons with $\omega_\mathrm{p}/2$ for different pumping powers of 100 mW, 1 W and 10 W. Blue color denotes to low intensities and red color to higher intensities.

Figure 2 shows the integrated BLS intensity of parametrically injected magnons at $\omega_\mathrm{p}/2$ for different pumping powers. The color-coded intensity maps, where blue denotes to low intensities and red to higher intensities, were achieved by changing the pumping frequency, and at the same time, the incident angle Θ_B of the probing light (see Fig. 1) was systematically changed, so that the selected wave number varied from 0 to $1.6 \cdot 10^5$ rad/cm in steps of $8.2 \cdot 10^3$ rad/cm.

At $\mathrm{P}_1 = 100\,\mathrm{mW}$, which is slightly above the threshold power of the parametric excitation, the BLS intensity of the pumped magnons is modest compared to the higher powers P_2 and P_3. It is clearly visible that the magnons are located along one mode while other regions of the spectrum show no increase of the BLS intensity at all. This behavior can be attributed to the fact that of all magnon groups pumped at the same time only the dominant group with the lowest damping is significantly populated. Nevertheless, for $\mathrm{P}_2 = 1\,\mathrm{W}$, more magnons were injected into the system and a broadening of the populated area can be observed. This broadening of the parametrically injected magnons is significantly pronounced for $\mathrm{P}_3 = 10\,\mathrm{W}$. Since parallel pumping is a strongly non-linear process, magnon groups with damping higher than the dominant group can be excited, which leads to the observed spreading of the BLS intensity signal.

In order to characterize the exact spectral position of the parametrically injected magnons, calculations have been performed using a recently developed microscopic approach [13]. The magnetic properties of the relevant magnon modes in YIG films of finite thickness can be derived form the microscopic model Hamiltonian which contains both exchange and dipole-dipole interactions as well as a Zeeman term due to the external bias magnetic field $\mathbf{H}_0$:

$$\begin{aligned} \hat{H} &= -\frac{1}{2}\sum_{ij} J_{ij}\mathbf{S}_i \cdot \mathbf{S}_j - \mu \mathbf{H}_0 \cdot \sum_i \mathbf{S}_i \\ &\quad -\frac{1}{2}\sum_{ij,i\neq j} \frac{\mu^2}{|\mathbf{R}_{ij}|^3}\left[3(\mathbf{S}_i \cdot \hat{\mathbf{R}}_{ij})(\mathbf{S}_j \cdot \hat{\mathbf{R}}_{ij}) - \mathbf{S}_i \cdot \mathbf{S}_j\right]. \end{aligned} \tag{1}$$

While the bias magnetic field is held constant at 1750 Oe, the saturation magnetization M_s can be changed since strong pumping lead to rather large magnon densities and each magnon reduces M_s by about one Bohr magneton μ_B. For the theoretical calculations, M_s is therefore used as a fit parameter. Consequently, the relevant spin stiffness

$$D = \frac{JM_\mathrm{s}a^5}{\mu^2}, \tag{2}$$

which determines the slope of the spectrum actually also depends on the saturation magnetization and has to be adjusted to the experimental data as well. J is the exchange coupling of neighboring spins, a is the lattice spacing and $\mu = g\mu_\mathrm{B}$ is the effective magnetic moment.

Figure 3a demonstrates the color-coded BLS-intensity map for $\mathrm{P}_2 = 1$ W in combination with the theoretical calculations of the relevant modes of the magnon spectrum. The lowest mode denotes the BVMSW. Modes with higher frequencies belong to high BVMSW modes, quantized perpendicular to the film plane over the thickness of the film. The comparison of the measured distribution of the parametrically excited magnons in k-space and the calculated modes leads to the conclusion that the dominant group stays at the lowest energy mode of the spectrum. At lower pumping powers an occupation of higher standing modes does not occur. The existence of a fine structure as presented in ref. [4] at the beginning of the magnon spectrum caused by quantized standing modes can not be observed in the magnon distribution. For the investigation of the fine

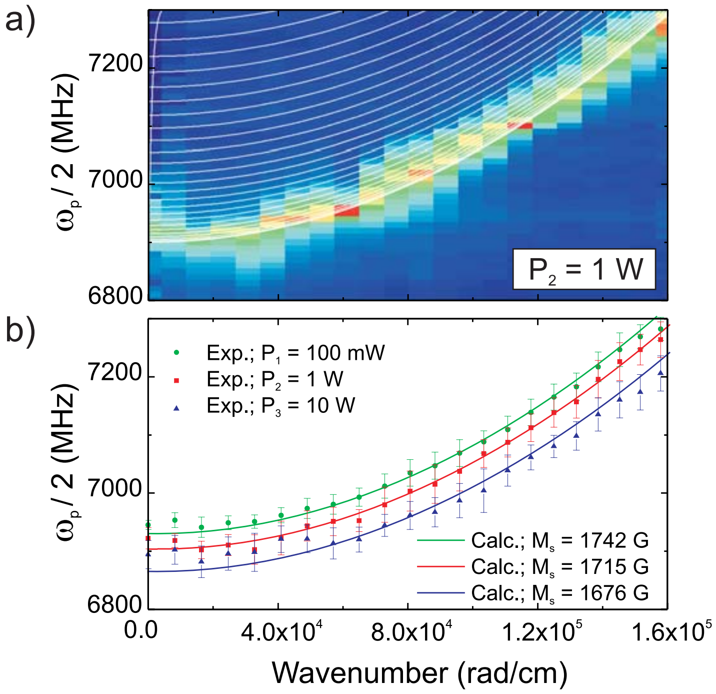

Fig. 3: a) Color-coded BLS-intensity map for $P_2 = 1$ W in combination with the theoretical calculations of the relevant modes of the magnon spectrum. b) Position of the maximal BLS intensity values extracted from the color-maps. The solid lines correspond to the calculations of the BVMSW modes having the lowest energy.

structure, one would need to decrease the stepsize of the pumping frequency. However, the measurement time would be disproportionate to the achieved results. Figure 3b shows the position of the maximal BLS intensity values extracted from the color-maps. The solid lines correspond to calculation of the BVMSW modes having the lowest energy. The saturation magnetization M_s was varied to fit the experimental data. With increasing pumping power, M_s is decreasing significantly in accordance with the theoretical expectations.

In conclusion, we have completed the picture of parallel pumped magnons at half of the pumping frequency $\omega_p/2$ for a large range of wave numbers up to $1.6 \cdot 10^5$ rad/cm. We demonstrated that the primarily pumped magnons are located along the mode having the lowest energy. In addition, the saturation magnetization M_s showed a significant decrease for higher pumping powers which is attributed to the creation of large quantities of magnons during the parallel pumping.

Financial support by the Deutsche Forschungsgemeinschaft (DFG, SFB/TRR 49) is gratefully acknowledged.

References

[1] F.R. Morgenthaler, J. Appl. Phys. **31**, S95 (1960).
[2] E. Schlömann, J.J. Green, U. Milano, J. Appl. Phys. **31**, S386 (1960).
[3] E. Schlömann, J. Appl. Phys. **40**, 2164 (1969).
[4] G. Wiese, L. Buxman, P. Kabos, C.E. Patton, J. Appl. Phys. **75**, 1041 (1994).
[5] H. Suhl, J.Phys.Chem. Solids **1**, 209 (1957).
[6] V.S. L'vov, *Wave Turbulence Under Parametric Excitation. Applications to Magnets.* (Springer, Berlin, 1994).
[7] S.O. Demokritov, V.E. Demidov, G.A. Melkov, A.A. Serga, B. Hillebrands, A.N. Slavin, Nature, **443**, 430 (2006).
[8] V. Demidov, O. Dzyapko, M. Buchmeier, T. Stockhoff, G. Schmitz, G. Melkov, S. Demokritov, Phys. Rev. Lett. **101**, 257201 (2008).
[9] T. Kloss, A. Kreisel, P. Kopietz, Phys. Rev. B **81**, 104308 (2010).
[10] T. Neumann, A.A. Serga, B. Hillebrands, Appl. Phys. Lett. **93**, 252501 (2008).
[11] C.W. Sandweg, M.B. Jungfleisch, V.I. Vasyucka, A.A. Serga, P. Clausen, H. Schultheiss, B. Hillebrands, A. Kreisel, P. Kopietz Rev. Sci. Instrum. **81** 073902 (2010)
[12] P. Kabos, M. Mendik, G. Wiese, C.E. Patton Phys. Rev. B **55**, 11457 (1997).
[13] A. Kreisel, F. Sauli, L. Bartosch, P. Kopietz, Eur. Phys. J. B **71**, 59 (2009).

4.2 Parametrical recovery of a spin-wave signal stored in a magnonic crystal

V.I. Vasyuchka, A.V. Chumak, A.A. Serga, and B. Hillebrands[1]

In the last years the storage and recovery of microwave signals in a tangentially magnetized magnetic ferrite film using standing dipole-exchange spin-wave modes have been experimentally discovered and theoretically interpreted [1, 2]. The inherent standing spin-wave modes exist in magnetic films due to the spatial confinement of the spin waves caused by the finite film thickness. Interaction between propagating surface magnetostatic spin waves and discrete standing spin-wave modes was used for the storage of a microwave signal in the magnetic film. The storage mechanism can take place only for the case of nonreciprocal surface spin waves, which have a natural hybridization with standing spin-wave modes in the plane film. Within this condition, the storage and recovery of a microwave signal are possible only if the signal frequency is equal to one of a standing wave modes.

In order to overcome this feature and to make storage-recovery effects more general, we proposed to utilize an artificial medium with periodic lateral variations in their magnetic properties - magnonic crystals (MCs) [3–5]. Spin-wave spectra in such structures are significantly different from those of uniform media and exhibit features such as band gaps, where spin wave propagation is prohibited. Traveling spin waves that satisfy the Bragg condition for the MC lattice constant are not allowed to propagate and will be reflected. In the case of an ideal MC, the group velocity of propagating spin waves with the frequency at the edges of the band gap is going to zero and the respective spin waves will be “trapped” inside the MC. This effect can be used to store a spin-wave signal in the MC. This phenomenon has been under consideration in photonic crystals [6, 7] but was never studied in strongly dissipative spin-wave systems.

In this report we present experimental results on storage and recovery of microwave signals realized in a thin film based MC. We demonstrate that the storage of the signal takes place only at the edges of the band gaps of MC. The amplitude, the duration and the recovery time of restored signals are mainly determined by the parametric pumping used in the recovery process.

The experiments were performed using one-dimensional MC, produced by etching a grating of shallow grooves into the surface of single-crystal yttrium iron garnet (YIG) ferrite film [3]. It consists of 10 grooves of 30 μm width and 300 nm depth etched into the surface of a YIG film of 5.5 μm thickness. A bias magnetic field H_0 was applied in the plane of the YIG waveguide, along its width. The excitation and detection of spin waves was done using input and output microstrip transducers placed 8 mm apart, in front and behind of the grating. Within this geometry reciprocal backward volume magnetostatic waves (BVMSW) are excited in the MC. BVMSWs were chosen in order to avoid an influence on the storage-recovery effects from natural spin-wave standing modes.

At the input transducer rectangular microwave pulses of $\tau_s = 100\,\mathrm{ns}$ duration and a carrier frequency $f_s = 7.212\,\mathrm{GHz}$ were applied. These pulses excite traveling BVMSW packets in a frequency range ($f_s \pm 5\,\mathrm{MHz}$) which were detected by the output antenna after a time delay of about 300 ns. The waves with frequencies at the edges of the band gaps of the MC have been decelerated and trapped inside the MC.

---

[1] In collaboration with Prof. M.P. Kostylev, School of Physics, University of Western Australia, Crawley, WA, Australia

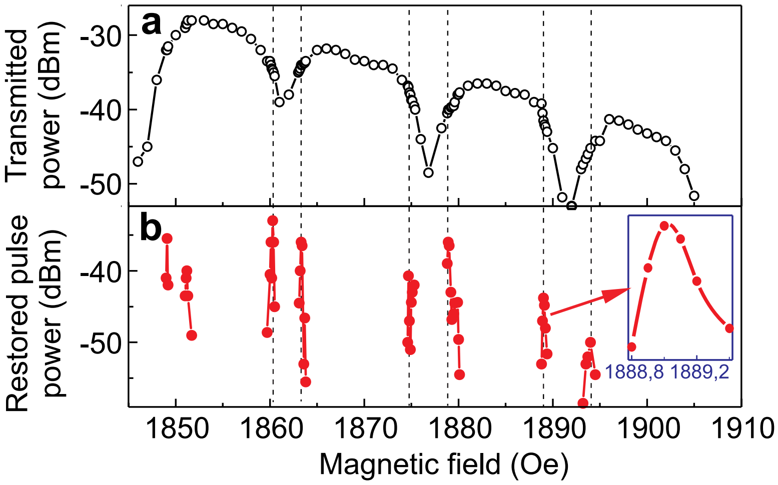

Fig. 1: a) Measured microwave signal transmitted by BVMSW through the magnonic crystal. b) Dependence of the restored pulse power on the bias magnetic field. Restoration of the spin-wave signal takes place only in a small range of fields (or frequencies) close to the MC rejection band edges. Inset: detailed profile of the recovered signal power on the magnetic field for one particular band-gap edge.

In order to restore the trapped signal we used parallel parametric pumping [8]. An open dielectric resonator placed in the middle of the MC and excited by an external microwave source was used to produce a pumping magnetic field parallel to the static bias magnetic field. The resonance frequency of the resonator was chosen to be twice the carrier frequency of the input microwave signal $f_\text{p} = 14.424\,\text{GHz}$. The pumping pulse of duration $\tau_\text{p} = 10\,\mu\text{s}$ was applied after the propagating spin-wave packet has left the dielectric resonator area.

The power of the transmitted signal (pumping was switched off) as a function of the applied magnetic field is shown in the Fig. 1(a). Three band gaps were clearly observed in the transmission characteristics. Their depth is limited due to the finite spectral width of the input microwave signal (10 MHz). After the transmitted signal has been detected at the output antenna, the pumping pulse was applied at the resonator. The restored signal was observed at the output antenna after a certain time called recovery time. The dependence of the restored pulse power on the bias magnetic field is presented in Fig. 1(b). One can see the sharp maxima of the recovered pulse power which correspond exactly to the band gap edges. This fact confirms our assumption that storage and recovery of the spin-wave signals take place only at the edges of the MC rejection bands. The typical width of the recovered signal is about 0.5 Oe which is comparable to the ferromagnetic resonance linewidth of the YIG film. As a side note, the first two maxima in the restored pulse power correspond to the standing spin-wave modes, observed in the plane YIG film as well.

Typical measured oscillograms showing normalized waveforms of the restored pulses from the MC for different values of the pumping power are presented in Fig. 2(a). The bias magnetic field $H_0 = 1860.3\,\text{Oe}$ was chosen in such a way that the carrier frequency is at the first gap edge of the MC. One can see that an increase of the pumping power P_p leads to a decrease of both the restored pulse duration and the recovery time. The recovery time of the restored pulse is much larger than the time of the spin wave propagation between the input and output transducers. This means that only slow MC spin-wave modes participate in processes of signal storage and recovery. Fig. 2(b) shows the dependence of the output power and the restoration time of the restored pulse on the pumping power. Both these characteristics have the tendency to reach constant values with increasing pumping power.

In order to clarify these dependencies we used the parametric recovery mechanism studied in details in [2]. This mechanism is based on the competitive interaction of both signal-induced standing spin-wave modes and high-wavevector thermal spin waves (dominant group) with the parametric pumping field. In our case, instead of standing spin-wave modes we are dealing with

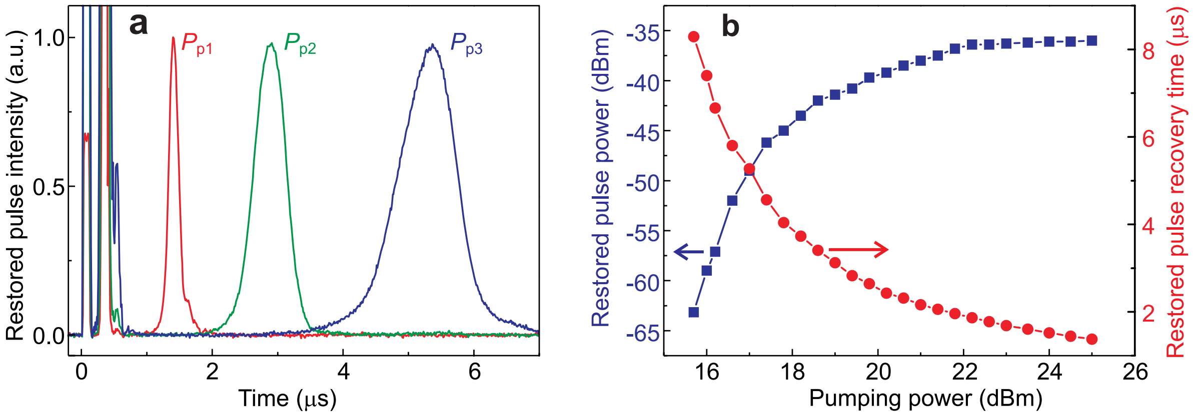

Fig. 2: a) Experimental waveforms of the delayed and restored pulses from the one-dimensional magnonic crystal for different values of the pumping power P_p: $P_{p1} = 316\,\mathrm{mW}$, $P_{p2} = 87\,\mathrm{mW}$, $P_{p3} = 50\,\mathrm{mW}$. b) Dependence of the power (rectangles) and the restoration time (circles) of the restored pulse on the pumping power.

slow spin-wave modes trapped in the MC. Thus, when the pumping signal is applied, it starts to amplify both the slow MC modes and the short-wavelength exchange spin waves from the dominating group. The amplitude of the recovered microwave pulse, formed from the amplified trapped spin waves in the MC, will reach the maximum value at the moment of time when the amplitude of the dominating spin wave group reaches a certain critical value which is sufficient to stop the parametric amplification of the MC modes.

Previous experiments with standing spin-wave modes demonstrate that the increase in the input signal power leads to a decrease in the recovery time and to an increase in the restored pulse power [2]. In contrast, for the MC due to the higher efficiency of the signal storage in comparison to the standing spin-wave modes, two different regimes of restoration were found. They are determined by the input signal power (see Fig. 3). In the first regime, the parametric amplification is saturated by the thermal magnons, the restored signal power is proportional to the power of the input signal and the recovery time is constant. In the second regime, for higher values of the input signal, slow MC modes reach their critical level before the thermal magnons saturate the parametric amplification. As a result the restored pulse power remains constant whereas the recovery time decreases with further increasing input power.

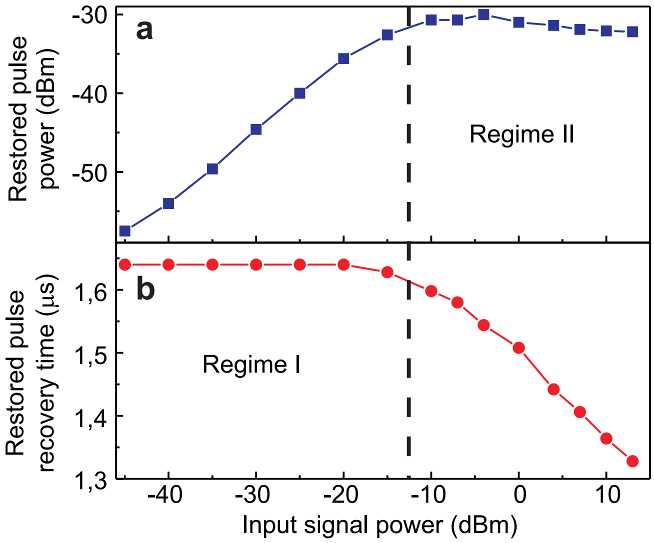

Fig. 3: Dependence of the restored pulse power a) and the restoration time b) on the input signal power. Two different regimes of restoration are determined by the input signal power. Regime I: parametric amplification is saturated by the thermal magnons. Thus, the restored signal power is proportional to the power of the input signal. Regime II: parametric amplification is saturated by the signal-induced spin-wave mode. Thus, the restored signal power does not depend on the input signal power and is determined by the critical spin-wave amplitude level.

In conclusion we have shown the storage-recovery effects in a one-dimensional magnonic crystal. This mechanism takes place only at the edges of the MC band gaps, where the group velocity of traveling spin waves goes to zero. Due to the high efficiency of the signal storage process inside the magnonic crystal two different regimes of restoration were observed depending on the input pulse power. In the first regime the restored signal power is proportional to the small power of the input signal, and the recovery time remains constant. For the second regime of large input signal power the output restored power is constant whereas the recovery time decreases.

Financial support by the Deutsche Forschungsgemeinschaft (DFG, SFB/TRR 49 and SE 1771/1-1) is gratefully acknowledged.

References

[1] A.A. Serga, A.V. Chumak, A. André, G.A. Melkov, A.N. Slavin, S.O. Demokritov, B. Hillebrands, Phys. Rev. Lett. **99**, 227202 (2007).

[2] A.V. Chumak, A.A. Serga, G.A. Melkov, A.N. Slavin, V. Tiberkevich, B. Hillebrands, Phys. Rev. B **79**, 014405 (2009).

[3] A.V. Chumak, A.A. Serga, B. Hillebrands, M.P. Kostylev, Appl. Phys. Lett. **93**, 022508 (2008).

[4] A.V. Chumak, P. Pirro, A.A. Serga, M.P. Kostylev, R.L. Stamps, H. Schultheiss, K. Vogt, S.J. Hermsdoerfer, B. Laegel, P.A. Beck, B. Hillebrands, Appl. Phys. Lett. **95**, 262508 (2009).

[5] A.A. Serga, A.V. Chumak, B. Hillebrands, J. Phys. D: Appl. Phys. **43**, 264002 (2010).

[6] Y.A. Vlasov, M. O'Boyle, H.F. Hamann, S.J. McNab, Nature **438**, 65 (2005).

[7] H. Gersen, T.J. Karle, R.J.P. Engelen, W. Bogaerts, J.P. Korterik, N.F. van Hulst, T.F. Krauss, L. Kuipers, Phys. Rev. Lett. **94**, 073903 (2005).

[8] A.G. Gurevich, G.A. Melkov, *Magnetization Oscillations and Waves*, CRC Press, New York, (1996).

4.3 Radiation of caustic beams from a collapsing bullet

A.A. Serga and B. Hillebrands[1]

Solitons while perturbed are able to emit small-amplitude radiation with frequency detuned far from the soliton frequency [1–3]. This ability, generally recognized as striking evidence of soliton's wave nature [4], has gained dramatically in importance in recent years with the discovery of supercontinuum generation in photonic crystal fibres whose applications for frequency comb generation in metrology, spectroscopy and imaging are more than just impressive (see e.g. [5]).

One has to note that small-amplitude radiation from solitons is possible, provided the dispersion relation for the medium deviates from the parabolic law $\omega(k) = \omega_0 + v(k-k_0) + D/2(k-k_0)^2$ built-in to the standard (i.e. parabolic) Cubic Nonlinear Schrödinger Equation (CNSE):

$$\frac{\partial a}{\partial t} + i\omega_0 a + v\frac{\partial a}{\partial z} - i\frac{D}{2}\frac{\partial^2 a}{\partial z^2} + iN \mid a \mid^2 a = 0 \quad . \tag{1}$$

Here a is the envelope function for the propagating wave packet, z is the direction of propagation, and N is the nonlinear coefficient (the term $iN|a|^2a$ is called "cubic nonlinearity" and gives rise to the equation name). The dispersion law is expressed as a series expansion of the frequency ω in terms of the wave number k of plane linear waves supported by the medium. The sign of the second-order dispersion coefficient $D = \partial^2\omega(k)/\partial k^2$ is of paramount importance for soliton formation: solitons are formed provided $DN < 0$.

Karpman [6] theoretically predicted that in the same CNSE framework the fourth-order two-dimensional (2D) dispersion $\omega(k_y, k_z)$ with a set of coefficients of proper signs should lead to wave irradiation from (2+1)-dimensional wave packets $a(x,y,t)$ as well. He considered an axially symmetric wave packet in an isotropic medium. In his work and in subsequent numerical simulations [7] it was shown that an axially symmetric wave packet in an isotropic medium is destroyed by radiating energy into a non-trapped circular wave.

In contrast to the isotropic case considered by Karpman [6] here we demonstrate that in a medium with uniaxial anisotropy this radiation takes the form of two narrow-aperture beams. This phenomenon is found for a spin-wave bullet propagating in a thin magnetic film.

Stable (2+1)D localized nonlinear spin-wave excitations, termed spin-wave bullets, have been previously observed in thin ferrimagnetic films of yttrium iron-garnet (YIG) magnetized along the propagation direction [8–11]. The waves propagating along the field are called backward volume magnetostatic spin waves. They are waves of backward nature, which means that their group velocity and wave vector point in opposite directions.

Two-dimensional pulses are intrinsically unstable and undergo nonlinear narrowing leading to collapse as nonlinearity overcompensates linear broadening due to 2D parabolic dispersion. Weak magnetic losses in a real magnetic film may balance the nonlinear narrowing. This results in a quasi-2D spatially localized bell-shaped waveform called a bullet and ensures its stability for some distance of propagation [8]. This regime is well described by the (2+1)D CNSE.

Stable bullets are observed in a certain range of initial powers for the wave packets. For larger input powers waveform collapse is unavoidable [8]. The advanced stage of the collapse is beyond

---

[1] In collaboration with M.P. Kostylev, School of Physics, M013, University of Western Australia, Crawley, WA 6009, Australia.

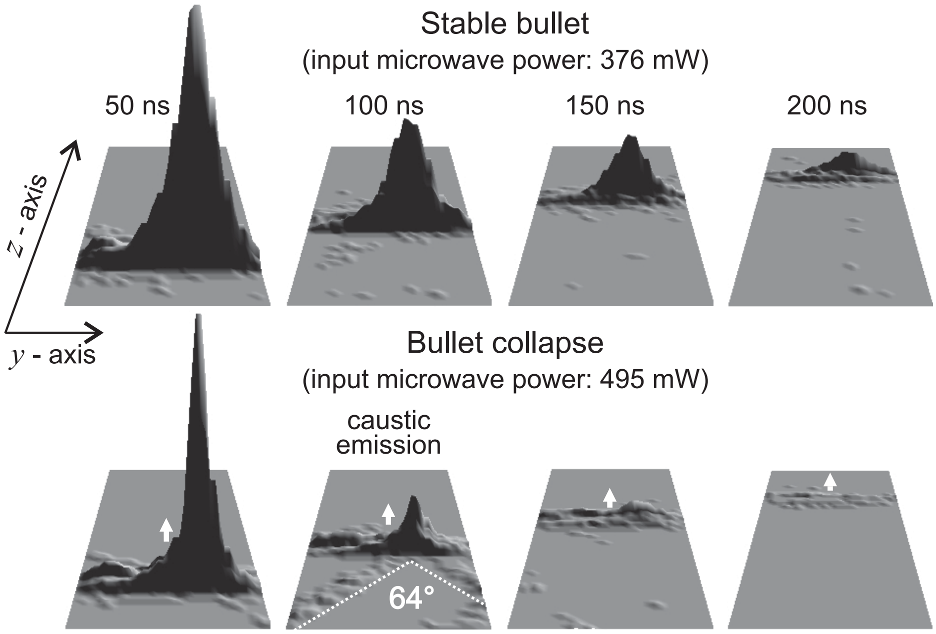

Fig. 1: Snapshots of spin-wave packets measured at different input powers and at 50 ns time intervals. Arrows show the bullet propagation direction. It coincides with the direction of the bias magnetic field $\mathbf{H}$ and the coordinate axis $\mathbf{z}$.

the limit of applicability of the CNSE, and the specific scenario for destruction of the collapsing wave packet ("collapse scenario") should be governed by processes of higher-order.

In this work we experimentally study the behavior of spin-wave bullets beyond the power range of their stability. The experiment is carried out using a longitudinally magnetized yttrium iron garnet (YIG) film stripe which is 2.5 mm wide ($w = 2.5$ mm) and 5 µm thick. The magnetizing field H is 1831 Oe. The spin waves are excited by a rf magnetic field created with a 25 µm wide microstrip antenna placed across the stripe and driven by 20 ns long microwave current pulses at a carrier frequency of 7.125 GHz. The spatio-temporal behavior of the traveling spin-wave packets is probed by means of space- and time-resolved Brillouin light scattering spectroscopy [12]. For relatively small input powers we observe formation of quasi-stable (2+1)D wave packets - guided spin-wave bullets (Fig. 1, upper row) - reported previously for the same geometry [11]. If we increase the power beyond the range of bullet stability the wave packet collapses (Fig. 1, lower row). The most prominent feature of the collapse is the pair of rays irradiated from the packet in the backward direction (second panel in the lower row of Fig. 1). One clearly sees that the rays have narrow apertures and are directed at well defined angles to the longitudinal axis of the ferromagnetic stripe: the value of the angle between the rays is 64°.

In order to understand the particular value of the angle between the two irradiated beams it is appropriate to consider the phenomenon of caustics which will play a central role in the following.

In an anisotropic medium with a dispersion law $\omega(\mathbf{k})$, the direction of the wave group velocity $\mathbf{v}_g = \partial\omega(\mathbf{k})/\partial\mathbf{k}$ indicating the direction of energy flow does not, in general, coincide with the direction of the wave vector $\mathbf{k}$. When the medium anisotropy is sufficiently strong, the direction of the group velocity of the waves in the vicinity of a certain wave vector $\mathbf{k}_c$ may become practically independent of their wave vectors. In this case the energy of the waves is channeled along this specific direction, which is called *caustic direction*, and forms a so-called *caustic beam*.

In a YIG film magnetocrystalline anisotropy is negligible; application of an external static field $\mathbf{H}$ in the film plane orients the static magnetization along the field direction and thus imposes a uniaxial symmetry necessary for the formation of caustics. Thus, two pairs of spin-wave caustic beams are directed at specific angles with $\mathbf{H}$. The angles depend on the magnitude of the applied field, film saturation magnetization, film thickness, and spin wave frequency [8, 13–17]. For an immobile excitation source and for the conditions of our current experiment the angle ϕ_I between the beams in each pair should amount to 84° as our calculation based on the theory in [15] shows. Note that this value is significantly different from the angle seen in Fig. 1.

To reveal the origin of the irradiation we carry out numerical simulations. An original reciprocal-space approach is used which effectively accounts for all dispersion orders of the real spin-wave dispersion [11, 18]. In the reciprocal space CNSE takes the form of a system of coupled equations for the amplitudes of the wave packet's spatial Fourier components:

$$i\frac{\partial F_{n,k}(a)}{\partial t}+(\omega_{n,k}+i\Gamma-\omega_0)F_{n,k}(a)+NF_{n,k}(|a|^2a)=f_{n,k}(t) \quad , \tag{2}$$

where $a=a(y,z,t)$ is the spin-wave scalar amplitude and

$$F_{n,k}(a)=\frac{1}{2\pi w}\int_{-w/2}^{w/2}\sin\left(\frac{n\pi y}{w}\right)dy\int_{-\infty}^{\infty}ae^{-ik_zz}dz \tag{3}$$

denotes a 2D Fourier transform which is continuous along the stripe (k_z takes continuous values in the model) and discrete in the transverse direction ($k_y=n\pi/w, n=1,2,3,\ldots$). This term is responsible for nonlinear coupling of Fourier components with different values of n and k_z. Γ denotes the coefficient of spin-wave linear damping for the medium and $f_{n,k}(t)$ is the Fourier transform of the time envelope of the driving microwave field which excites the spin-wave packet at the entrance into the waveguide medium. Similar to the experiment, $f_{n,k}(t)$ is taken in the form of a 20 ns-long rectangular pulse. The carrier frequency of this driving pulse is $\omega_0/2\pi$ (see Fig. 2).

The term $\omega_{n,k}=\omega(k_y,k_z)$ is the 2D spectrum of spin waves, shown in Fig. 2 as k_z-dependence of frequency for a family of different discrete values of k_y which we take here equal to $n\pi/w$. The calculated dispersion corresponds to the conditions of our experiment. Physically this (n,k_z)-representation describes a family of guided modes for a film waveguide. The transverse profiles of the width modes are given by $\sin(n\pi y/w)$ with the integer number n indicating each particular mode. One sees that the dispersion slope $\partial\omega_{n,k}/\partial|k_z|$ is negative for all the modes. This reflects the fact that the modes are of backward type. Consequently, a localized wave packet which propagates in the positive direction of the axis z has a carrier wave number $k_z<0$.

As previously shown for both 1D [2] and isotropic 2D media [6], to ensure radiation from nonlinear waveforms it is important to have a dispersion law for a medium which contains terms higher than parabolic. More precisely, the curvature $\partial^2\omega/\partial k^2$ should change sign along the dispersion curve. From Fig. 2 one sees that, on one hand, for each particular width mode the sign of $\partial^2\omega_{n,k}/\partial k_z^2$ changes from negative to positive in the vicinity of $k_z=0$. On the other hand, the spectrum in Fig. 2 is quite dense. Considering this spectrum as quasi-continuous one retrieves the 2D continuous dispersion of plane spin waves in ferromagnetic films [19] which is characterized by the variation of the dispersion sign $\partial^2\omega/\partial k^2$ as a function of the propagation angle with respect to the direction of the applied field $\mathbf{H}$ ($k^2=k_y^2+k_z^2$, $\phi=\arctan(k_y/k_z)$). Waves excited in this medium by an immobile point source are prone to forming caustics [13]. All this suggests that irradiation from a bullet may indeed be possible and may take the form of narrow beams at particular angles to the bullet propagation direction.

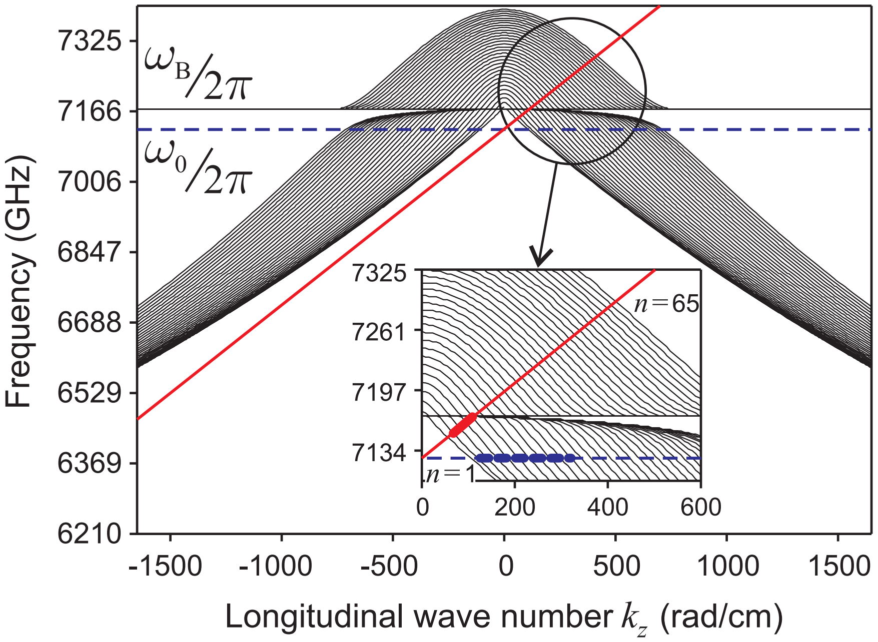

Fig. 2: Spectrum of the guided modes for the longitudinally magnetized film waveguide. The calculation assumes pinned spins at the stripe edges. The family of symmetric modes $n = 1, 3, \ldots 65$ is shown. The mode which is the lowest in frequency is the fundamental width mode for the waveguide $n = 1$. Inset: a section of the spectrum close to the frequency $\omega_B/2\pi$. The horizontal dashed lines in the main field of the figure and in the inset show the carrier frequency $\omega_0/2\pi$ of the input microwave pulse. The oblique lines show the Doppler-shifted frequencies of an excitation source which moves in the positive direction. The bold sections of these lines show the modes responsible for formation of the respective caustics.

Our simulations confirm the validity of Karpman's idea that the sign of dispersion should vary along the dispersion curve in order to generate a wave which is not trapped by the original nonlinear wave packet. The result is shown in Fig. 3a (same parameters as for Fig. 2 and standard for YIG films have been used in this calculation.) One sees good agreement with the experiment. In particular, we obtain the same radiation angle of 64° as in the experiment. Important here is that in order to obtain the correct collapse scenario we have to include all the modes shown in Fig. 2 into the simulation. Since in our experiment the carrier frequency for the excitation pulse is located about 45 MHz below the frequency of the in-plane ferromagnetic resonance $\omega_B/2\pi$ (Fig. 2), it would be natural to exclude the modes located above the gap $\omega = \omega_B$ from the calculation. However, if we limit the wave packet spectrum in this way the simulation delivers a completely different collapse scenario. In particular, in this case the velocity of the collapsing bullet is zero and beams are irradiated at quite different angles. This fundamental difference in simulated scenarios evidences the crucial importance of the specific form of the 2D dispersion relation for the collapse dynamics.

Now let us understand the specific angle for the radiation indicated both in Fig. 1 and in Fig. 3a. In the following we will show that the respective directions are the caustic angle directions which have been rotated because the excitation source is moving. First one notices that a collapsing spin-wave bullet in a magnetically saturated ferromagnetic film meets the size criterion $d < 2\pi/k_c$ for a quasi-point source of linear excitation of caustic waves. The source moves with the velocity of the bullet $v = 2.5$ cm/µs. A point source located on the axis of the waveguide will excite all waveguide modes which have an anti-node on the axis. These are the symmetric modes $n = 1, 3, 5, \ldots$ If the source were immobile, the frequency of the excited waves would be equal to the frequency of the source. This condition is indicated by the dashed horizontal line in Fig. 2: all the symmetric modes whose dispersion lines cross the dashed line will be excited with the frequency given by the

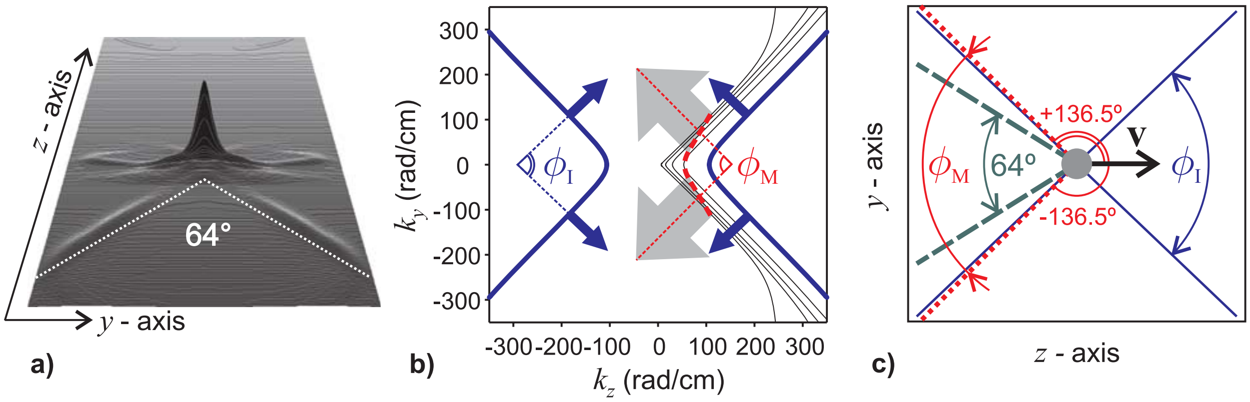

Fig. 3: Numerical simulation of irradiation of caustic beams from the collapsing bullet a), slowness curves for the immobile and the mobile excitation sources b) and the respective angles c). In b): bold solid lines are the slowness curves for the frequency given by the horizontal dashed line in Fig. 2. Thin solid lines are the slowness curves for the Doppler-shifted frequencies, as explained in the text. The bold dashed line connects zero-curvature points of the thin solid lines. Dark arrows normal to the thick solid line show the caustic directions for excitation by an immobile source. Grey arrows normal to the family of the thin solid lines show the directions of irradiation by the moving source. The arrows are located at the points of the slowness curves, where their curvature vanishes. In c): the arrow indicates the direction of source motion. Thin solid lines: caustic directions for the immobile source. Dotted lines: directions of energy radiation by the moving source. Dashed lines: instant directions along the irradiated beams.

ordinate of the point of the cross-section. It is a short exercise [14] to find which of the modes are responsible for formation of the standard caustics: those modes are shown by the bold part of the dashed horizontal line.

The moving source is described in Fig. 2 by the solid oblique line $\omega = \omega_0 + v k_z$ which can be considered as the time-space Fourier transform of the moving point source (see e.g. Eq. (14) in [20]). The term $v k_z$ is obviously the Doppler frequency shift for the excited modes. One sees that now each mode is excited with its own frequency. Furthermore, one sees that crossings are possible only for positive k_z values. Importantly, our calculations show that, similar to the previous case of the immobile source, the modes which satisfy the Doppler shift condition $\omega_{n,k}(k_z) = \omega_0 + v k_z$ are also able to form caustic beams. The family of modes which are found to be responsible for formation of the modified caustics is shown by the bold section of the oblique line.

The modified caustic angles are obtained by considering the family of slowness curves for the Doppler-shifted frequencies. A slowness curve is a constant-frequency line in the (k_y, k_z) plane (Fig. 3b) calculated for a film which is continuous in both in-plane directions [15]. The group velocities of all plane waves which exist at the respective frequency are directed perpendicular to this curve. For this reason the caustic direction is given by the normal to the slowness curve at the point where its curvature is zero. A range of frequencies for which the slowness directions are close to each other will contribute to formation of the modified caustics. The thin solid lines in Fig. 3b are the slowness directions for the frequencies which correspond to the crossing points of the oblique solid line with the dispersion lines in Fig. 2. The bold dashed line runs across zeros of curvature for these curves. One sees that normals to the thin solid lines at these points point in the same direction which suggests that this direction is the modified caustic direction. By calculating the direction of the maximum energy flow [15] for this set of slowness curves one finds a rigorous value for the angles between the caustic beams and the bullet velocity: $\pm 136.5^\circ$ (Fig. 3c).

First one sees that the angles exceed 90° which reflects the fact that the carrier waves are the waves of backward nature. (Note that the Doppler frequency shift for backward waves is anomalous [21,22].) Second one notices that the angle between the two caustics $\phi_{\mathrm{M}} = 87^\circ$ is increased by just 3° with respect to $\phi_{\mathrm{I}} = 84^\circ$ for the excitation by an immobile source (Fig. 3c). However, this is not the full story yet, since ϕ_{M} is the angle at which the energy is irradiated by the moving source, but not the instant direction along the irradiated beam. The angle correction due to this effect depends on the source velocity $\mathbf{v}$ solely, and is the same for waves of backward and forward types. Upon introducing this correction one finds a net angle between the two backwards-irradiated beams. The net angle is 64° which is in the excellent agreement with the experimental data and results of numerical simulation shown in figures 1 and 3a, respectively.

In conclusion, we experimentally studied the collapse scenario for an intense two-dimensional wave packet in a ferromagnetic medium with cubic nonlinearity and induced uniaxial anisotropy. We showed that before being self-destroyed the wave packet irradiates narrow-aperture beams of continuous waves at very specific angles to its propagation direction. We believe that this effect is of fundamental importance for physics of nonlinear waves and may exist for other types of wave excitations in other materials. Nonlinear 2D-media from a broad class which is characterized by cubic nonlinearity and 2D-dispersion of an order higher than parabolic, provided uniaxial anisotropy of dispersion is available or induced in the medium should be suitable candidates to observe the effect.

Financial support by the Deutsche Forschungsgemeinschaft (DFG, SFB/TRR49) and the Australian Research Council is gratefully acknowledged. The authors also thank A.N. Slavin for fruitful discussions.

References

[1] N. Akmediev, M. Carson, Phys. Rev. A **51**, 2602 (1995).
[2] V.I. Karpman, Phys. Rev. B **47**, 2073 (1993).
[3] P.K.A. Wai, H.H. Chen, Y.C. Lee, Phys. Rev. A **41**, 426(1990).
[4] D.V. Skryabin, A.V. Gorbach, Rev. Mod. Phys. **82**, 1982 (2010).
[5] J.M. Dudley, J.R. Taylor, Nature Photonics **3**, 85.
[6] V.I. Karpman, Physics Lett. A **160**, 531 (1991).
[7] V.I. Karpman, A.G. Shagalov, Physics Lett. A **160**, 538 (1991).
[8] O. Büttner, M. Bauer, S.O. Demokritov, B. Hillebrands, Yu.S. Kivshar, V. Grimalsky, Yu. Rapoport, A.N. Slavin, Phys. Rev. B **61**, 11576 (2000).
[9] A.A. Serga, S.O. Demokritov, B. Hillebrands, A.N. Slavin, Phys. Rev. Lett. **92**, 117203 (2004).
[10] A.A. Serga, B. Hillebrands, S.O. Demokritov, A.N. Slavin, P. Wierzbicki, V. Vasyuchka, O. Dzyapko, A. Chumak, Phys. Rev. Lett. **94**, 167202 (2005).
[11] A.A. Serga, M.P. Kostylev, B. Hillebrands, Phys. Rev. Lett. **101**, 137204 (2008).
[12] S.O. Demokritov, B. Hillebrands, A.N. Slavin, Phys. Rep. **348**, 441 (2001).
[13] T. Schneider, A.A. Serga, A.V. Chumak, C.W. Sandweg, S. Trudel, S. Wolff, M.P. Kostylev, V.S. Tiberkevich, A.N. Slavin, B. Hillebrands, Phys. Rev. Lett. **104**, 197203 (2010).
[14] A.B. Valyavsky, A.V. Vashkovsky, A.V. Stal'makov, V.A. Tyulyukin, Sov. Tech. Phys. Lett. **34**, 616 (1989).
[15] V. Veerakumar, R.E. Camley, Phys. Rev. B **74**, 214401 (2006).
[16] V.E. Demidov, S.O. Demokritov, D. Birt, B. O'Gorman, M. Tsoi, X. Li, Phys. Rev. B **80**, 014429 (2009).
[17] V. Veerakumar, R.E. Camley, Phys. Rev. B **81**, 174432 (2010).
[18] M. Kostylev, V.E. Demidov, U.-H. Hansen, S.O. Demokritov, Phys. Rev. B **76**, 224414 (2007).
[19] R.W. Damon, J.R. Eshbach, J. Phys. Chem. Solids **19**, 308 (1961).
[20] H.A. Haus, Am. J. Phys. **54**, 1126 (1986).
[21] D.D. Stancil, B.E. Henty, A.G. Cepni, J.P.V. Hof, Phys. Rev. B **74**, 60404 (2006).
[22] A.V. Chumak, P. Dhagat, A. Jander, A.A. Serga, B. Hillebrands, Phys. Rev. B **81**, 140404(R) (2010).

B. Magnon Spintronics

Spintronics is the field of spin-based data storage and processing. In conventional spintronics the electron is used as a carrier of spin. A magnon, i.e. the quantum of a spin wave, carries an angular momentum or spin as well and can be used for storage, processing and transport of spin information, building on its outstanding properties such as long lifetime and potential for dissipationless transport. With "magnon spintronics" we refer to the use of spin in data storage and processing carried by magnons. The field is currently emerging. Some building blocks such as magnon generators (spin wave emitters) and detectors have been realized, others are in development.

In Report 4.4 the detection of magnons in an Yttrium Iron Garnet film using the inverse spin Hall effect is reported addressing time resolved measurements, which provide inside in details of the underlying mechanisms. Report 4.5 addresses a different approach, i.e. the use of micro- and nano-scale mechatronic elements to detect and manipulate magnon transport. Report 4.6 presents results on four-magnon scattering in spin-wave micro-conduits, a direct observation of intrinsic non-linear damping mechanisms. In Report 4.7 near- and far-field excitation of lateral standing spin waves in a magnetic microstripe are studied by means of phase resolved BLS microscopy. Finally, Report 4.8 addresses the enhancement of spin pumping efficiency for the inverse spin Hall effect using spin-wave mode selection.

B. Magnon-Spintronik

Die Spintronik ist das Feld der spin-basierten Datenspeicherung und -Verarbeitung. Während in der etablierten Spintronik das Elektron als Träger eines Spins benutzt wird, wurde bisher das Magnon, d.h. das Quant einer Spinwelle nur wenig als Spinträger betrachtet. Es kann ebenso für die Speicherung und Bearbeitung von Spininformation eingesetzt werden. Von Vorteil ist die vergleichsweise lange Lebensdauer eines Magnons und grundsätzlich das Vorhandensein des Potentials für verlustfreien Transport. Mit dem Ausdruck "Magnon-Spintronik" bezeichnen wir daher die Nutzung des Spins in Datenspeicherung und -Verarbeitung mit dem Magnon als Spinträger. Das Feld entwickelt sich derzeit. Einige Bausteine, wie z.B. Magnonengeneratoren (Spinwellenemitter) und -Detektoren wurden realisiert, andere sind in der Entwicklung.

Im Bericht 4.4 wird die Detektion von Spinwellen in einem Yttrium-Eisen-Granatfilm mit Hilfe des inversen Spin-Halleffektes vorgestellt und hierbei besonders das zeitliche Verhalten untersucht, welches Einblick in die Details der zugrundeliegenden Mechanismen erlaubt. Bericht 4.5 behandelt einen anderen Zugang, nämlich die Nutzung von mikro- und nanoskaligen Mechatronikelementen zur Detektion und Manipulation von Spinwellentransport. Bericht 4.6 stellt Vier-Magnonen-Streuung in Spinwellenmikroleitern vor, eine direkte Beobachtung eines intrinsischen nichtlinearen Dämpfungsmechanismus. In Bericht 4.7 werden die Ergebnisse der Untersuchung von Nah- und Fernfeldanregung stehender Spinwellen in magnetischen Mikrostreifen mittels phasenaufgelöster BLS Mikroskopie präsentiert. Abschließend stellt Bericht 4.8 die Verstärkung der Spinpumpeffizienz im inversen Spin-Halleffekt durch geeignete Modenselektion vor.

4.4 Temporal evolution of the inverse spin Hall voltage in a magnetic insulator-nonmagnetic metal structure

M.B. Jungfleisch, A.V. Chumak, V.I. Vasyuchka, A.A. Serga, B. Obry, H. Schultheiss, P.A. Beck, and B. Hillebrands[1]

Over the last decade, the field of spintronics has risen to some prominence. Spintronics is concerned with the development of devices which exceed the performance and energy efficiency of conventional charge-based electronics by exploiting the electron's spin degree of freedom [1–5]. The hard disc read head is perhaps the best known spintronic success [2] to date. Much effort is currently focussed on the development of spintronic (magnetic) memory, nano-sized microwave sources, galvanic isolators, voltage generators, spin-based transistors and logic devices.

Spin angular momentum, which is the information carrier in spintronics, can be transferred not only by the flow of electrons, but also by magnons: the quanta of spin waves. The utilization of spin waves introduces the possibility of insulator-based spintronic devices which operate with pure *spin* currents entirely decoupled from conventional *charge* currents [1, 6]. The propagation length of spin waves in magnetic insulators is many orders of magnitude longer than the spin diffusion length [7, 8]. Thus they are promising candidates for information transfer and processing [7, 9, 10]. Spin pumping, (which transforms spin waves into pure spin currents) and the inverse spin Hall effect (iSHE) (which converts spin currents into charge currents) are both of fundamental importance for spin-wave based spintronics. The temporal characteristics of these phenomena will ultimately determine the operational speeds of spin-wave spintronic devices.

In this report we investigate the temporal behavior of an inverse spin Hall voltage in a magnetic

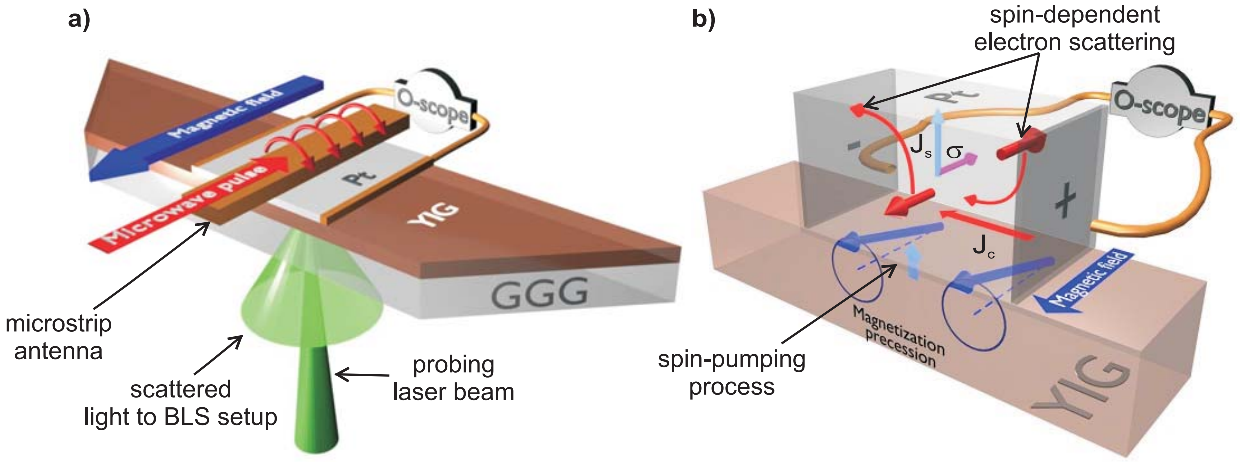

Fig. 1: a) Sketch of the experimental setup. The 2.1 μm thick YIG wavequide is 20 mm long and 3 mm wide. The 10 nm thick Pt layer is $3 \times 3\,\text{mm}^2$ in size and is deposited in the middle of the waveguide. The magnetic field is applied in the film plane perpendicular to the waveguide. A microwave signal is applied to a 600 μm wide copper microstrip antenna. A spin-wave induced iSHE voltage was detected using a voltmeter or a conventional oscilloscope. The Brillouin light scattering technique has been used to measure the spin-wave intensity. b) Spin pumping scheme and resulting inverse spin Hall effect. Details in the text.

---

[1] In collaboration with E. Saitoh, Institute for Materials Research, Tohoku University, Sendai 980-8577, Japan; A.D. Karenowska, Department of Physics, Clarendon Laboratory, University of Oxford, OX1 3PU Oxford, United Kingdom.

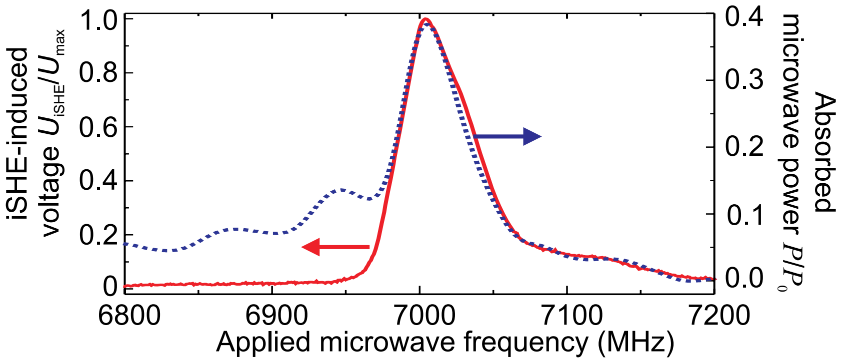

Fig. 2: The inverse spin Hall voltage (solid curve) and the absorbed microwave power (doted curve) as a function of the applied microwave frequency. The bias magnetic field was set to be $H_0 = 182\,\text{mT}$. The maximal iSHE voltage U_{max} is $60\,\mu\text{V}$.

insulator (yttrium iron garnet, YIG) – nonmagnetic metal (platinum, Pt) structure and compare it with the evolution of the (externally driven) spin-wave intensity from which it originates. We show that the iSHE voltage only partially mirrors the intensity of the externally driven spin-wave mode. The iSHE pulsed signal has a tail due to the pumping effect of *secondary* spin waves created by two-magnon scattering of the initially excited spin-wave mode. In our experimental study we were able to detect and distinguish between the spin pumping and iSHE contributions of externally excited coherent magnons and secondary, incoherent magnons. In doing so, we demonstrate that secondary spin waves play an important role in producing the iSHE signal.

We investigated a platinum (Pt) coated YIG film. YIG single crystal films have the smallest known spin-wave damping [7,8] and magnon spin currents can propagate in YIG over centimeter distances [1]. Platinum features strong spin-orbit interaction and is therfore an attractive material for iSHE measurements [11–14]. The experimental setup is shown in Fig. 1a. It comprises a $2.1\,\mu\text{m}$ thick YIG stripe with a $10\,\text{nm}$ thick $3 \times 3\,\text{mm}^2$ Pt layer deposited on the top. The Pt square was connected to a voltage measuring instrument (see Fig. 1a). A copper microstrip antenna of $600\,\mu\text{m}$ width placed above the Pt layer was used to excite spin waves. This antenna was isolated from the Pt coating by a non-magnetic dielectric.

Brillouin light scattering (BLS) spectroscopy [15] was used to observe the excited spin waves. The probing laser beam was focused on the YIG/Pt sample and the intensity of the inelastically scattered light was analyzed [16] on a 500 ps timescale. We used a wideband (DC to 200 MHz) voltage amplifier FEMTO DHPVA-200 and a 300 MHz bandwidth Agilent DSO6034A oscilloscope for the time-resolved voltage measurements.

We performed the experiment in the following way: an external magnetizing field $\mathbf{H}_0$ was applied perpendicular to the RF magnetic field $\mathbf{h}_{rf}$ induced by the microstrip antenna. When the carrier frequency f of the RF field fulfilled the the condition for ferromagnetic resonance in the YIG, spin waves were excited in the YIG stripe. Due to the spin pumping effect [17, 18] a spin current $\mathbf{J}_s$, originated by the precessing magnetization at the YIG-Pt interface, was caused to flow in the Pt layer. As a consequence of spin-dependent electron scattering (strong spin-orbit interaction in Pt) [11,12,19] a charge current $\mathbf{J}_c$ and thus a charge accumulation transverse both to $\mathbf{H}_0$ and $\mathbf{J}_s$ was brought about. Accordingly, an iSHE voltage U_{iSHE} appeared across the Pt square (see Fig. 1b). As $\mathbf{J}_c \propto \mathbf{J}_s \times \sigma$ the polarity of the iSHE voltage could be changed by changing the direction of a spin current polarization σ via the static magnetization of the YIG stripe.

In order to increase the dynamic range of our time-resolved iSHE and BLS measurements we supplied a moderately high microwave power to the spin-wave antenna of $P_0 = 100\,\text{mW}$. Microwave pulses of $1\,\mu\text{s}$ duration were applied with a repetition rate of $10\,\mu\text{s}$ to avoid possible caloric effects. The rise and fall times of these applied pulses were less than 5 ns.

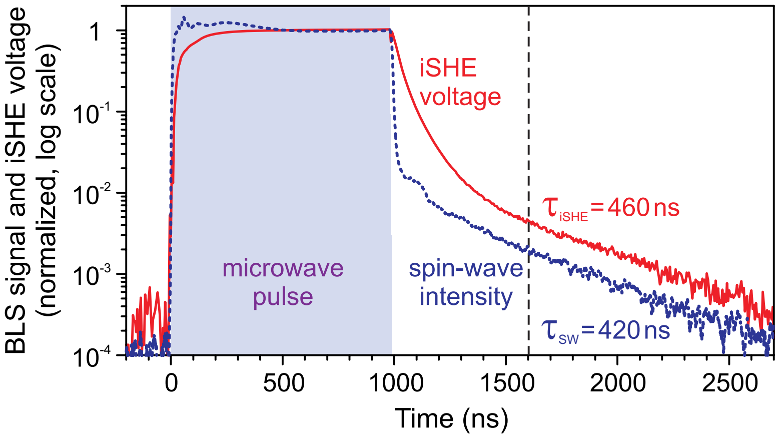

Fig. 3: Spin-wave intensity and iSHE voltage as a function of time in logarithmic scale. For $t > 1600$ ns the iSHE and spin-wave pulse fall times τ_{iSHE} and τ_{SW} are very close; 460 ns and 420 ns, respectively. This fact can be understood if one assumes that many modes contribute to the iSHE voltage. The maximal iSHE voltage U_{max} is 60 μV. Details in the text.

First of all, in order to confirm the origin of the observed voltage U_{iSHE}, we verified that its polarity was indeed dependent on the polarity of the magnetization direction. To additionally corroborate our results we also tested a control structure with a nonmagnetic insulator (gadolinium gallium garnet, GGG) in the place of the YIG. No voltage was detected. Thus, we are able to say with confidence that the voltages we observed were due to the iSHE.

After our control experiments, the absorbed microwave power (that is a quantity for the excited spin-wave intensity) and the iSHE voltage were measured as functions of the applied microwave frequency (see Fig. 2). For $H_0 = 182$ mT maximal absorption occured at $f_0 = 7$ GHz. It is known that for a microstrip antenna the highest excitation efficiency corresponds to a spin wave for which $k \rightarrow 0$. Thus, we know with certainty that f_0 corresponds to the frequency of ferromagnetic resonance (FMR). As the measured iSHE voltage originates directly from the spin-wave intensity (Fig. 2) a similar tail was expected to be observed on the U_{iSHE} pulse. However, the real temporal behavior both of the spin-wave intensity and iSHE voltage proved to be much more complex than this simple picture might suggest.

The time dependent measurements were performed at $H_0 = 182$ mT and $f_0 = 7$ GHz where the iSHE voltage was maximal. In Fig. 3 the time profiles of the spin-wave and voltage pulses are compared. The spin-wave waveform was detected by the BLS setup adjacent to the microstrip line. The spin-wave intensity (doted waveform in Fig. 3) increases rapidly when the microwave pulse is applied at $t = 0$ ns. After some oscillations corresponding to a nonlinear transition process, an equilibrium value is reached. When the microwave pulse is switched off at $t = 1000$ ns, the BLS signal decreases rapidly. The measured iSHE voltage is shown by a solid line in Fig. 3. Rise and fall times of the iSHE voltage are considerably longer than those corresponding to the spin-wave intensity.

We show the temporal evolution of the iSHE voltage and the spin-wave amplitude plotted on logarithmic scale in Fig. 3. The data of Fig. 3 has several features which will be discussed in detail.

Firstly, the rise and fall slopes both of the iSHE voltage and of the spin-wave pulse are non-exponential. Secondly, the measured iSHE voltage rises and decreases much more slowly than the spin-wave intensity. Thirdly, for $t > 1600$ ns the iSHE and spin-wave pulse fall times τ_{iSHE} (460 ns) and τ_{SW} (420 ns) are very close.

This can be understood if one assumes that – rather than simply the externally driven spin-wave mode – many modes contribute to the iSHE voltage. To illustrate how such a model fits with the experimental data we consider for simplicity two groups of modes. The first group are “long-wavelength" dipolar dominated modes excited directly by the microstrip line. The dynamic magnetization generated by this group features a strong amplitude and a high decay rate which is inversely proportional to the bandwidth of the microwave absorption (see Fig. 2). We assume that for these waves, the dominant dissipative mechanism is radiation loss at the microstrip antenna. The second mode group is much weaker and more long-lived; these "short-wavelength" dipolar-exchange modes are almost entirely decoupled from the microstrip line. They are excited indirectly via two-magnon scattering of the first group [20–22]. As the scattering occurs on inhomogeneities and impurities that are concentrated close to the YIG film surface, these modes are localized near the YIG/Pt interface. Since spin-wave scattering events are uncorrelated, unlike the directly excited group, this indirectly excited group is entirely incoherent.

The weak short-wavelength spin-wave group cannot be resolved by BLS on the background of the strong long-wavelength modes and thus is visible only after the microwave pulse is switched off and the fast-relaxing directly excited group has decayed. From this, it follows that the spin-wave fall time τ_{SW} of 420 ns is determined *only* by the relaxation time of the slow short-wavelength modes. For $t > 1600$ ns the short-wavelength modes are the sole contributors to the BLS signal and the iSHE voltage. As a result, the slopes τ_{iSHE} and τ_{SW} are approximately the same.

We propose that the short-wavelength modes, in spite of their small amplitude, make a proportionally higher contribution to the iSHE voltage than their directly-excited long-wavelength counterparts, due to their localization close to the YIG/Pt interface. As a result of the existence of these modes, after the excited spin-wave intensity maximum, the iSHE voltage continues to grow (for times $t < 200$ ns). The same effect is visible after the microwave pulse is switched off: the iSHE voltage continues to be generated by a long-lived group of short-wavelength dipolar-exchange modes long after the long-wavelength group has entirely decayed.

In summary, the iSHE voltage increases and decreases significantly more slowly than the amplitude of the externally driven spin waves from which it originates. The complex temporal behavior of both signals we have investigated allows us to conclude that indirectly excited short-wavelength dipolar-exchange spin waves as well as directly excited long-wavelength dipolar-dominated spin waves contribute to the effective spin pumping and thus the iSHE voltage. Moreover, we could demonstrate that the scattered dipolar-exchange spin-wave modes make− despite their small amplitude and incoherent character − a strong contribution to the iSHE signal due to their surface localization.

Financial support by Magdalen College, Oxford (to A. K.) and by Deutsche Forschungsgemeinschaft (DFG, GRK 792, to B. O.) is gratefully acknowledged. The Nano+Bio Center, TU Kaiserslautern, is gratefully acknowledged for technical support.

References

[1] Y. Kajiwara, K. Harii, S. Takahashi, J. Ohe, K. Uchida, M. Mizuguchi, H. Umezawa, H. Kawai, K. Ando, K. Takanashi, S. Maekawa, and E. Saitoh, Nature **464**, 262 (2010).

[2] S. A. Wolf, D. D. Awschalom, R. A. Buhrman, J. M. Daughton, S. von Molnár, M. L. Roukes, A. Y. Chtchelkanova, and D. M. Treger, Science **294** 5546 (2001).

[3] I. Žutic, J. Fabian, and S. Das Sarma, Rev. Mod. Phys. **76**, 2 (2004).

[4] J. F. Gregg, Nature Materials **6** (2007).

[5] S. D. Bader, and S. S. P. Parkin, Annual Review of Condensed Matter Physics **1** (2010).

[6] K. Uchida, J. Xiao, H. Adachi, J. Ohe, S. Takahashi, J. Ieda, T. Ota, Y. Kajiwara, H. Umezawa, H. Kawai, G. E. W. Bauer, S. Maekawa, and E. Saitoh, Nature Mat. **9**, 894 (2010)

[7] A. A. Serga, A. V. Chumak, and B. Hillebrands, J. Phys. D: Appl. Phys. **43**, 264002 (2010).

[8] V. Cherepanov, I. Kolokolov, and V. L'vov, Phys. Rep.—Rev. Sec. Phys. Lett. **229** 81 (1993).

[9] T. Schneider, A. A. Serga, B. Leven, B. Hillebrands, R. L. Stamps, and M. P. Kostylev, Appl. Phys. Lett. **92**, 022505 (2008).

[10] A. Khitun, M. Bao, J. Lee, K. Wang, D. W. Lee, and S. Wang, Materials Research **998** (2007).

[11] J. E. Hirsch, Phys. Rev. Lett. **83**, 1834 (1999).

[12] S. Zhang, Phys. Rev. Lett. **85**, 393 (2000).

[13] A. Brataas, Y. Tserkovnyak, G. E. W. Bauer, and B. I. Halperin, Phys. Rev. B **66**, 060404(R) (2002).

[14] Y. Tserkovnyak, A. Brataas, and G. E. W. Bauer, Phys. Rev. B **66**, 224403 (2002).

[15] S. O. Demokritov, B. Hillebrands, and A. N. Slavin, Phys. Rep. **348**, 441 (2001).

[16] O. Büttner, M. Bauer, S. O. Demokritov, B. Hillebrands, Y. S. Kivshar, V. Grimalsky, Yu. Rapoport, and A. N. Slavin, Phys. Rev. B **61**, 11576 (2000).

[17] R. H. Silsbee, A. Janossy, and P. Monod, Phys. Rev. B **19**, 4382 (1979).

[18] S. Mizukami, Y. Ando, and T. Miyazaki, Phys. Rev, B **66**, 104413 (2002).

[19] M. I. Dyakonov, and V. I. Perel, Phys. Lett. A **35**, 6 (1979).

[20] M. Sparks, *Ferromagnetic Relaxation Theory* (McGraw-Hill, New York, 1964).

[21] G. A. Melkov, V. I. Vasyuchka, Yu. V. Kobljanskyj, and A. N. Slavin, Phys. Rev. B, **70**, 224407 (2004).

[22] G. A. Melkov, A. D. Dzyapko, A. V. Chumak, and A. N. Slavin, J. Exp. and Theor. Phys. **99**, 1193 (2004).

4.5 Spin wave based information processing by micro- and nanoscale spin-mechatronics

A.A. Serga, A.V. Chumak, V.I. Vasyuchka, and B. Hillebrands[1]

The study of spin waves offers unique insight into the underlying physical mechanisms of static and dynamic magnetic phenomena and their potential to provide a platform for spintronic information transport is widely acknowledged (see for example [1,2] and references therein). However, to date, research in this area has focused on the development of purely magnetic thin-film transmission systems capable of logical operations; these typically exploit interference of waves driven and detected by microwave antennas and manipulated via low-frequency current-induced magnetic fields [3,4]. Whilst such topologies have clear device potential, their functionality is limited, and they make use of only a small fraction of the wide range of interesting and dynamic effects readily accessible in spin-wave systems. Moreover, they reflect a general and longstanding trend in the study of magnonic systems; the predominance of intrinsically inefficient (and therefore power demanding) inductive techniques for spin wave excitation, detection, and manipulation.

In this report, we suggest and demonstrate an alternative, non-inductive approach to spin-wave spin-information processing, involving the creation of functional spinmechatronic systems through the hybridization of spin-wave transmission structures with magnetic micro- or nano-mechanical elements. We propose that miniature magnetically loaded mechanical systems (for example magnetic cantilevers, beams and wires) may be used to (*i*) write information in the form of amplitude and phase perturbations onto traveling spin waves, (*ii*) function as read elements via spin wave driven mechanical displacements and (*iii*) provide the basis for current-free spin-wave sources. We demonstrate the feasibility of (*i*) and (*ii*) experimentally, and elaborate on how (*iii*) might, in future, be achieved.

The viability of mechanical coupling to short wavelength, highly spatially localized spin-wave excitations is well established in the context of magnetic resonance force microscopy (MRFM) (see for example [5–7] and references therein). However, mechanical coupling to traveling spin waves in transmission systems has until now remained unexplored.

At first glance, it may appear that the ability to mechanically detect localized spin-wave excitations using MRFM implies that the observation of traveling spin waves using a similar technique is a foregone conclusion. However, a closer inspection identifies important distinctions between the physics of the two situations and forces us to re-appraise this view.

The localized spin waves detected in conventional MRFM experiments are resonantly excited standing waves. These waves are driven by externally applied microwave magnetic fields and their frequencies are determined by the magnetic and geometric properties of the sample in which they are excited. Such systems have trapped spin-wave energy and thus a non-negligible quality factor (Q) which – for a given driving power input – enhances the amplitude of the stray field that one is hoping to mechanically detect.

In contrast, the viability of the spinmechatronic information processing system we propose is predicated on the ability to mechanically detect fast, propagating spin waves, excited by spatially localized sources under conditions in which the regions of the sample at which excitation and detection

---

[1] In collaboration with A.D. Karenowska, J.F. Gregg, Department of Physics, Clarendon Laboratory, University of Oxford, OX1 3PU Oxford, United Kingdom.

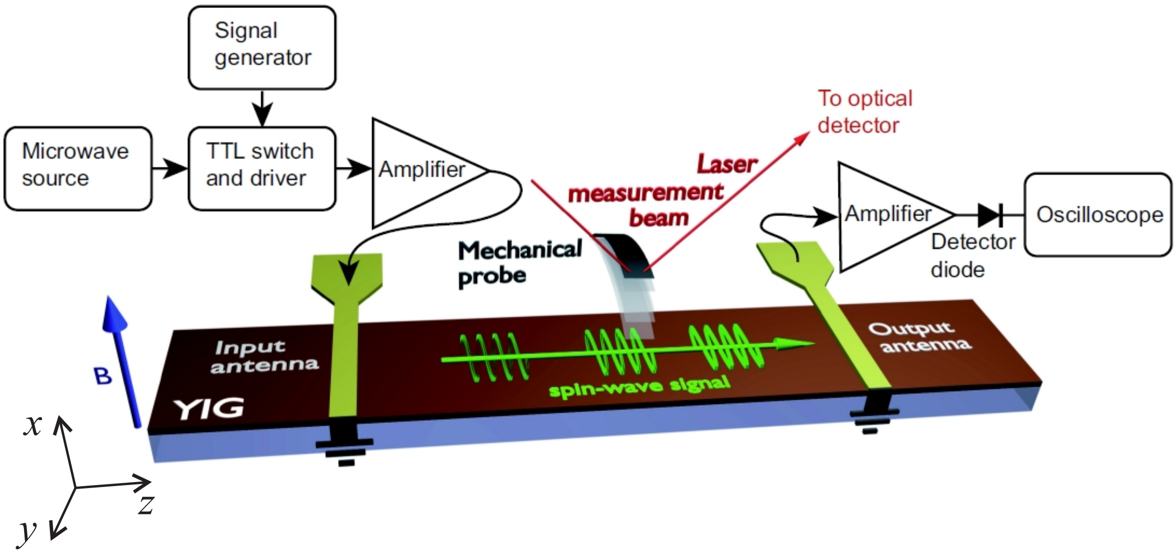

Fig. 1: Experimental setup.

are performed are entirely magnetically decoupled. Such a mechanical detection problem threatens to be significantly more challenging than an MRFM type measurement, owing to the lack of quality factor associated with a traveling wave, the low Q of the driving antenna, and a poor driving antenna to spin wave coupling coefficient.

In order to investigate the feasibility of the proposed spinmechatronic scheme, we employed a thin-film ferrimagnetic Yttrium Iron Garnet (YIG) waveguide as a spin-wave transmission structure, and a magnetic cantilever (nickel, diameter 10 µm) suspended above the film as a micromechanical probe (Fig. 1). The probe is moveable in the x-, y-, and z-directions (resolution ±2 µm over 10 mm). A nano-positioning stage provides additional precision in the x-direction (±2 nm over 100 µm). The YIG waveguide was biased by an out-of-plane magnetic field B so as to support the propagation of forward volume magnetostatic spin waves (FVMSW) [8] and a microwave drive signal, on/off modulated at 3 Hz by a switch, was supplied to a spin-wave input antenna (a short-circuited conducting wire, diameter 50 µm) on its surface. The signal from a second, receiving (output) antenna, 8 mm distant from the input was captured at an oscilloscope via an amplifier and negative polarity detector diode. An optical vibrometer (SIOS Meßtechnik GmbH, Nano Vibration Analyzer, resolution 0.1 nm) allowed displacements of the cantilever structure to be measured.

With the microwave source tuned to a frequency close to the spin-wave transmission maximum for the film (4300 MHz), a large transmitted envelope signal was measured at the oscilloscope (Fig. 2a) and a 3 Hz, 2.5 nm periodic displacement of the cantilever, driven by the stray magnetic field from the modulated spin waves traversing the YIG was observed (Fig. 2b). The spin-wave origin of the displacement signal was verified via a control measurement in which the microwave source was tuned to a frequency outside of the spin-wave transmission band (2000 MHz). Oscilloscope data from this control configuration of the experiment is shown in Fig. 2c (raw signal amplification identical to that applied to the data of Fig. 2a). It can be seen that only a low level residual signal due to direct electromagnetic interaction between the input and output spin-wave antennas is present (amplitude ~ 9 units) and – as anticipated – the 3 Hz peak of Fig. 2b is entirely absent from the corresponding displacement data set of Fig. 2d. Note that the structure around 4 Hz in Fig. 2b and Fig. 2d is an artifact originating from a low-level mechanical noise source in the experimental set-up and that in Fig. 2a and Fig. 2c the negative polarity of the signals reflects that of the detector diode.

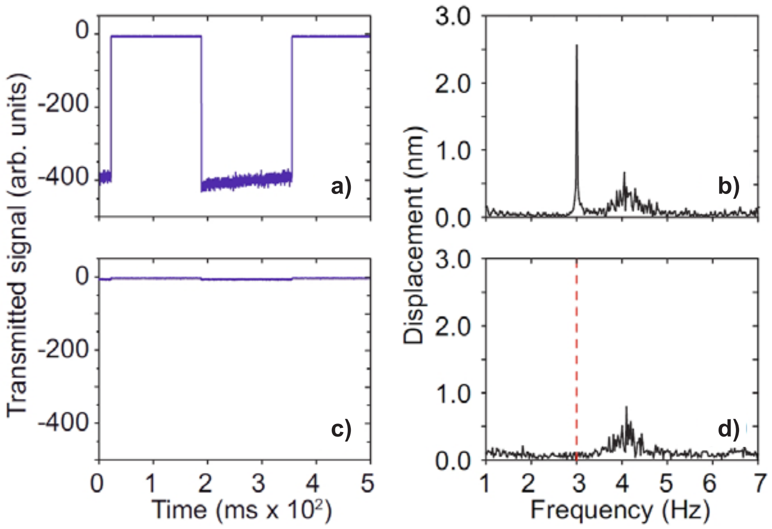

Fig. 2: Experimental results. a) and b): Propagating spin-wave excitations are driven via a 4300 MHz microwave carrier. c) and d): The modulated microwave signal which drives the input antenna is 2000 MHz.

In a separate investigation, it was established that magnetic cantilever movement could measurably perturb the spin-wave transmission through the waveguide; at sub-millimeter approach distances, the probe produced up to 6 dB influence on transmission amplitude and around 25 degrees of relative phase shift.

Our low-frequency mechanical detection measurements were undertaken non-resonantly; i.e. the mechanical cantilever was not resonant with the 3 Hz spin-wave modulation. This suggests that – given that the use of resonant mechanical detectors would afford a significant gain in sensitivity – the prospects for creating a practical information processing system based on this class of interaction may indeed be very favorable.

Miniature mechanical elements with resonant responses in the kHz to MHz range – together with the technology required to make them magnetic – are now readily available. Widely exploited in scanning-probe microscopy and spectroscopy techniques, including MRFM, the quality factors of these systems are several orders of magnitude in excess of the best achievable in electrical or magnetic systems. From an information processing perspective, their exceptional frequency selectivity makes them extremely attractive; they are capable of functioning both as sensitive, narrowband receivers, and as low power, operationally robust write elements.

Information platforms based on traveling spin waves compare favorably with established alternatives – notably optics and conventional electronics – in several important respects: The waves short wavelengths (in comparison with electromagnetic waves of the same frequency) and relatively slow speeds (typically of order $c/10^4$) allow classical wave phenomena to be exploited in small-scale structures; their dispersion properties can be tuned over a wide frequency and wavevector range via the application of modest external magnetic fields; and, unlike in optics, where the weak nonlinearity of practical materials presents a significant fundamental challenge to all-optical information processing, nonlinear dynamic effects are accessible in spin-wave systems at very low powers (see for example [9,10]). Artificial magnetic materials including magnonic crystals [11–13] (the spin-wave analogue of optical photonic crystals) open doors to further signal processing functionalities, and the possibility of storing information in geometrically defined spin-wave modes of magnetic elements [14], and/or exploiting nonlinear mechanisms of spin-wave information storage and recovery based on energy exchange between dynamically distinct magnon populations (see for example [15, 16] and references therein) enhance their potential further still.

On the evidence of our proof-of-concept experiments and the strengths and contemporary capabilities of the two constituent technologies outlined above, we suggest that an information processing platform operating via interactions between amplitude modulated traveling spin waves and miniature resonant magno-mechanical elements could provide an operationally robust, low-power route to capitalizing on the sophisticated spintronic signal processing potential of spin waves. Moreover – although at the forefront of development and yet to become widely available – mechanical elements with resonance frequencies well within range of GHz spin waves can now be manufactured [17]. In the context of the spinmechatronic concept we describe, such elements potentially enable phase-resolved spin-wave read and write, and perhaps even excitation operations to be performed entirely mechanically, with exceptional frequency selectivity, and at low energy cost.

Finally, we note that allied to the technological opportunity outlined in this paper is the promise of fresh fundamental physical insight into as yet unexplored spin wave/ mechanical coupling phenomena. In particular, recent successes in the observation of quantum-limited ground states of macroscopic resonant mechanical systems [18, 19] suggest that it could prove possible to investigate and exploit information exchange in coupled mechanical-magnon systems which straddle the boundary between the classical and quantum regimes.

Financial support by the Deutsche Forschungsgemeinschaft (DFG, SFB/TRR49) and the Institution of Engineering and Technology and Magdalen College, Oxford is gratefully acknowledged. SIOS Meßtechnik GmbH and Armstrong Optical Ltd are gratefully acknowledged for generous support.

References

[1] Y. Kajiwara, K. Harii, S. Takahashi, J. Ohe, K. Uchida, M. Mizuguchi, H. Umezawa, H. Kawai, K. Ando, K. Takanashi, S. Maekawa, E. Saitoh, Nature **464**, 262 (2010).

[2] A. Khitun, K.L. Wang, Superlattices and Microstructures **38**, 184 (2005).

[3] T. Schneider, A.A. Serga, B. Leven, B. Hillebrands, R.L. Stamps, M.P. Kostylev, Appl. Phys. Lett. **92**, 022505 (2008).

[4] M.P. Kostylev, A.A. Serga, T. Schneider, B. Leven, B. Hillebrands, Appl. Phys. Lett. **87**, 153501 (2005).

[5] B. Pigeau, G. de Loubens, O. Klein, A. Riegler, F. Lochner, G. Schmidt, L.W. Molenkamp, V.S. Tiberkevich, A.N. Slavin, Appl. Phys. Lett. **96**, 132506 (2010).

[6] O. Klein, G. de Loubens, V.V. Naletov, F. Boust, T. Guillet, H. Hurdequint, A. Leksikov, A.N. Slavin, V.S. Tiberkevich, N. Vukadinovic, Phys. Rev. B **78**, 144410 (2008).

[7] J.A. Sidles, Appl. Phys. Lett. **58**, 24 (1991).

[8] D.D. Stancil, *Theory of Magnetostatic Waves*, Springer-Verlag, New York (1993).

[9] S.O. Demokritov, A.A. Serga, V.E. Demidov, B. Hillebrands, M.P. Kostylev, B.A. Kalinikos, Nature **426**, 159 (2003).

[10] B.A. Kalinikos, N.G. Kovshikov, C.E. Patton, Phys. Rev. Lett. **80**, 4301 (1998).

[11] A.V. Chumak, T. Neumann, A.A. Serga, B. Hillebrands, M.P. Kostylev, J. Phys. D **42**, 205005 (2009).

[12] A.V. Chumak, A.A. Serga, B. Hillebrands, M.P. Kostylev, Appl. Phys. Lett. **93**, 022508 (2008).

[13] A.V. Chumak, P. Pirro, A.A. Serga, M.P. Kostylev, R.L. Stamps, H. Schultheiss, K. Vogt, S.J. Hermsdoerfer, B. Laegel, P.A. Beck, B. Hillebrands, Appl. Phys. Lett. **95**, 262508 (2009).

[14] K. Perzlmaier, M. Buess, C.H. Back, V.E. Demidov, B. Hillebrands, S.O. Demokritov, Phys. Rev. Lett. **94**, 057202 (2005).

[15] A.A. Serga, A.V. Chumak, B. Hillebrands, J. Phys. D **43**, 264002 (2010).

[16] A.A. Serga, A.V. Chumak, A. André, G.A. Melkov, A.N. Slavin, S.O. Demokritov, B. Hillebrands, Phys. Rev. Lett. **99**, 227202 (2007).

[17] X.M.H. Huang, C.A. Zorman, M. Mehregany, M.L. Roukes, Nature **421**, 496 (2003).

[18] A.D. O'Connell, M. Hofheinz, M. Ansmann, R.C. Bialczak, M. Lenander, E. Lucero, M. Neeley, D. Sank, H. Wang, M. Weides, J. Wenner, J.M. Martinis, A.N. Cleland, Nature **464**, 697 (2010).

[19] T. Rocheleau, T. Ndukum, C. Macklin, J.B. Hertzberg, A.A. Clerk, K.C. Schwab, Nature **463**, 72 (2010).

4.6 Four-magnon scattering in spin-wave micro-conduits

H. Schultheiss, K. Vogt, P. Pirro, T. Brächer, P.A. Beck, and B. Hillebrands

The transport of spin information is one of the great challenges in condensed matter physics and of fundamental importance for the development of spintronic devices. Due to the rather high spin relaxation rates in metals, a pure diffusive transportation of spin angular momentum cannot fulfill the needs of future applications. The information encoded in the spin polarization is typically lost in metals within distances of less than one micrometer at room temperature. The recent discovery that a spin current can be transmitted over macroscopic distances even through a ferrimagnetic insulator utilizing spin waves [1] has put great attention to the transport properties of spin waves. But there are plenty of obstacles that need to be overcome for utilizing spin waves as a carrier of information. In conventional ferromagnetic materials such as $Ni_{81}Fe_{19}$, the spin-wave lifetime is of the order of a few nanoseconds and the group velocity, which corresponds to the speed of information transport, does not exceed a few micrometer per nanoseconds for reasonable geometries. As a result, the operating distance of a spin-wave driven information transport is limited to a few micrometer. This is still above the spin diffusion length but, obviously, a further increase of the operating distance would be beneficial for future applications.

Possible solutions for this problem are either new mechanisms for a more efficient excitation of spin waves in microstructures or the development of novel materials with a reduced magnetic damping such as Heusler compounds. However, the intrinsic nonlinear character of spin waves might pose a limitation to these approaches and might cause instabilities of the excited spin waves, which are generally known under the term magnon-magnon scattering [2]. Both, the excitation of higher spin-wave amplitudes as well as the reduction of the magnetic damping will decrease the power thresholds for magnon-magnon scattering processes. As a result, these processes might ultimately define the limitations of spin-wave currents in magnetic materials.

Experimental evidence for these nonlinear phenomena was indirectly seen in previous experiments by an increase of the resonance linewidth in ferromagnetic resonance measurement experiments [3] and in the reduction of the amplitude of spin-wave pulses in the time domain, as recently reported in [4]. Here, we report on the direct observation of intrinsic nonlinear damping mechanisms. In particular, we discuss the process of four-magnon scattering which, in many experimental geometries, is the lowest order magnon-magnon scattering process due to reasons discussed in the following. A consistent theoretical description of magnon-magnon scattering is tedious and was only developed for continuous thin films so far [2, 5]. For more complex magnetization dynamics in finite magnetic elements, a basic understanding of the restrictions for magnon-magnon scattering can be derived from the energy and momentum conservation laws:

$$\sum_{i}^{N} \hbar\omega_i = \sum_{j}^{M} \hbar\omega_j \tag{1}$$

$$\sum_{i}^{N} \hbar\mathbf{k}_i = \sum_{j}^{M} \hbar\mathbf{k}_j \tag{2}$$

The left (right) part of the equations summarizes over the initial (final) magnons with indices i (j) which are present before (after) the scattering process, respectively. The spin-wave frequencies

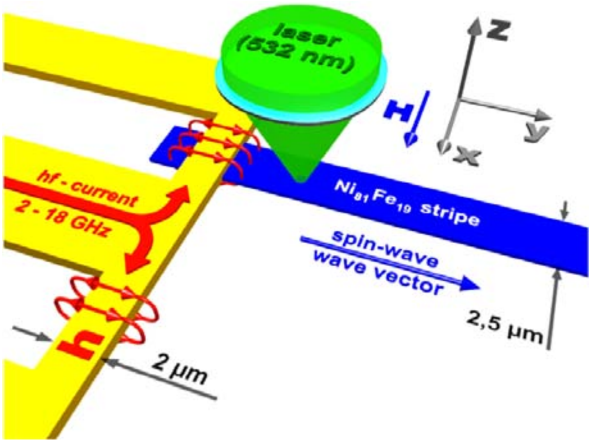

Fig. 1: Schematic layout of the sample. A 2.5 μm wide $Ni_{81}Fe_{19}$-microstripe acts as a spin-wave conduit and is placed under the shorted end of a coplanar waveguide (CPW). A microwave current flowing through the CPW creates a dynamic Oersted field **h** which excites propagating spin waves. The spin-wave spectra are locally probed by analyzing the Brillouin light scattering of a focused laser beam.

$\omega_{i,j}$ and wavevectors $\mathbf{k}_{i,j}$ are connected via the spin-wave dispersion relation $\omega_{i,j}(\mathbf{k_{i,j}})$ which has a non-zero minimum frequency $\omega_0 = 2\pi\nu_0$ for a non-vanishing externally applied magnetic field [6, 7]. Below this frequency ω_0, no spin-wave eigenmodes exist which immediately prohibits 3-magnon scattering processes with $i = 1$ and $j = 2$ for $\omega_i < 2\omega_0$. Direct magnon-magnon scattering processes with $i = 1$ and $j = 1$ are forbidden due to momentum conservation and are only possible in the presence of defects breaking the translational symmetry. Similar considerations lead to the conclusion that four-magnon scattering processes with $i = 2$ and $j = 2$ are the lowest order processes allowed in the frequency range $\omega_0 < \omega_i < 2\omega_0$ considering Eq. (1).

The sample under investigation is a spin-wave micro-conduit consisting of a 2.5 μm wide $Ni_{81}Fe_{19}$-stripe as shown in Fig. 1. The stripe has a thickness of 40 nm and was deposited in an ultra high vacuum chamber via molecular beam epitaxy. The patterning was made by means of electron beam lithography and chemical lift-off. One end of the spin-wave conduit is placed beneath the shorted end of a coplanar waveguide (CPW) with a thickness of 500 nm and a lateral width of 2 μm at the shorted end. Spin waves in the $Ni_{81}Fe_{19}$-stripe are excited by the dynamic magnetic Oersted field which is generated from a microwave current transmitted through the CPW. At the position of the shorted end of the CPW, the electric field is zero and therefore the microwave current reaches its maximum just above the spin-wave conduit. This allows for the excitation of spin waves with very high amplitudes driving the magnetic system into the strongly nonlinear regime. The spin-wave intensity is locally probed by a Brillouin light scattering (BLS) microscope [8] with an active stabilization of the lateral sample position. The lateral position stability of the sample stage with respect to the probing laser spot is better than 20 nm for long-time acquisition. This precision allows for a quantitative analysis of extremely power and position dependent processes and, thus, is well suited for an extensive investigation of nonlinear magnetization dynamics on the micrometer scale.

The spin-wave conduit was saturated by an externally applied magnetic field of 51.1 mT perpendicular to the conduits long axis. In this geometry, the spin-wave dispersion relation for the first width mode is monotonously increasing as depicted by the solid line in Fig. 2. The dispersion relation was calculated following the procedure given in [9] using standard material parameters for $Ni_{81}Fe_{19}$ as summarized in [10]. The minimum frequency ν_0 for this specific geometry and magnetic field is 6.3 GHz. In the same figure, the normalized excitation efficiency of the 2 μm wide antenna is given as a function of the spin-wave wavevector component parallel to the spin-wave conduit (dashed line). The excitation efficiency is decreasing for higher wavevectors and has a local minimum at a wavevector of $\pi\,\mu m^{-1}$ which corresponds to a spin-wave frequency of 9.2 GHz.

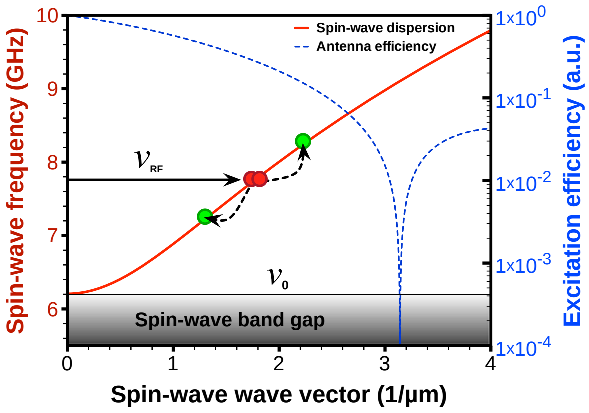

Fig. 2: Spin-wave frequencies (solid line) in the $Ni_{81}Fe_{19}$-microstripe with a magnetic field applied perpendicular to the stripe's long axis are shown together with the excitation efficiency of the shorted CPW (dashed line) as a function of the wavevector k along the stripe. The dispersion has a non-zero frequency minimum ν_0 at $k = 0$ which defines the upper limit of the spin-wave band-gap. The circles illustrate a four-magnon scattering process when two spin waves, pumped by the applied microwave current with ν_{RF}, annihilate and create two spin waves within the spin-wave band.

Hence, within the frequency range $6.3\,\mathrm{GHz} < \nu_{RF} < 9.2\,\mathrm{GHz}$ spin waves are efficiently excited by a RF current transmitted through the shorted CPW. As indicated by the circles and arrows in Fig. 2, two of the directly excited spin waves with frequency ν_{RF} can scatter and create two new spin waves with frequencies $\nu_{RF} \pm \Delta\nu$ in case the restriction $\Delta\nu < \nu_{RF} - \nu_0$ is fulfilled. If that was not the case, one of the scattered spin waves would have a frequency below ν_0. Except for the part close to $\mathbf{k} = 0$, the dispersion relation is approximately linear. Consequently, the momentum conservation holds for four-magnon scattering processes with $i = 2$ and $j = 2$ and $\omega_i = 2\pi\nu_{RF}$.

To track down these nonlinear processes experimentally, we locally measured the spin-wave spectra close to the shorted end of the CPW using BLS microscopy as a function of the applied microwave frequency ν_{RF} for microwave powers between $0 - 33\,\mathrm{dBm}$. The experimental results are shown in Fig. 3 as intensity graphs. For each excitation frequency ν_{RF} (x-axis), we acquired a spin-wave spectrum for a couple of minutes. The measured spin-wave frequencies are plotted on the y-axis whereas the spin-wave intensity is given by the color coded z-axis. Between the measurements for 3 dBm and 33 dBm the applied power differs by a factor of $2^{10} = 1024$. For a direct quantitative comparison of all measurements, the color scale is logarithmic to the base 10 and covers the same absolute range for all graphs shown.

For powers from 0 to 9 dBm, the response of the spin-wave conduit to the applied microwave current is simply the identity function. But starting from a power level of 12 dBm, a significant broadening of the measured spin-wave spectra is observed. Apparently, the broadening of the spectrum does not cover the entire excitation frequency range for the intermediate power levels but is only visible up to a certain threshold excitation frequency marked with black arrows in the middle and lower row of Fig. 3. The reason for this frequency threshold and the fact that for some graphs a vertical spike pattern is observed is a combination of the inherent nonlinear character of four-magnon scattering processes and the wavevector dependent excitation efficiency of the shorted CPW (see Fig. 2). The interaction of spin waves due to their intrinsic nonlinearity only takes place above a certain amplitude. But since we keep the output power of the microwave generator fixed when changing the excitation frequency, the intensity of the excited spin waves decreases with increasing ν_{RF} because of the reduced excitation efficiency of the CPW. The sharpness of the threshold frequency for the appearance of the magnon-magnon scattering is directly related to the slope of the excitation efficiency. For smaller wavevectors, i.e. for smaller spin-wave frequencies, the excitation efficiency changes drastically as a function of the wavevector, whereas for higher frequencies the relative change in the excitation efficiency is much smaller. As a consequence, the transition from line-broadening to sharp resonance spectra happens very fast for a power of 18 dBm and gets smoother for increasing power values.

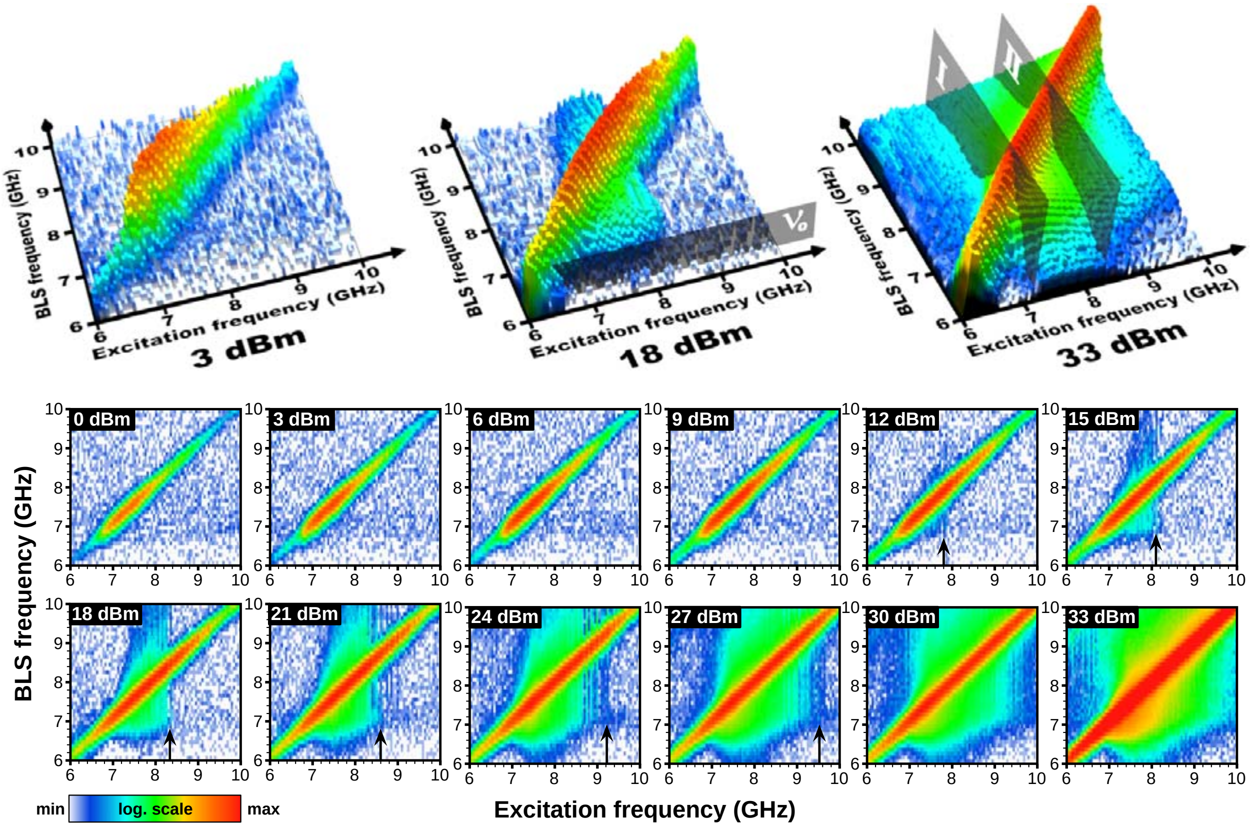

Fig. 3: **Top row:** Spin-wave excitation spectra as a function of the applied microwave frequency ν_{RF} for three different power values: 3 dBm, 18 dBm, and 33 dBm. For each excitation frequency (abscissa), a spin-wave spectrum is locally measured close to the CPW by means of BLS microscopy. The spin-wave intensity (z-axis) is color coded corresponding to the color scale shown at the bottom of the figure. In the middle graph the cutting plane depicts the minimum frequency of the spin wave band. The planes (I) and (II) in the right graph display the frequencies for the power analysis of the spin-wave spectra in Fig. 4. **Middle/bottom row:** 2D projections of the spin-wave spectra as a function of the excitation frequency for various input powers; a power increase of 3 dBm corresponds to doubling the power. Arrows on the abscissa mark the frequencies up to which 4-magnon scattering can be observed. **Note:** The logarithmic color scale covers exactly the same intensity range for all graphs shown which allows for a direct comparison of the spin-wave spectra for all applied microwave powers.

The vertical spike pattern in the data is a result of the frequency transmission characteristic of the CPW. Due to small impedance mismatches at the electrical contacts of the waveguide, the transmitted power varies as a function of ν_{RF}. In cases when the system is close to the threshold power for four-magnon scattering, these small variations play an important role and become visible when ν_{RF} is changed.

For a direct comparison of the spin-wave spectra as a function of the applied microwave power, we plotted the spin-wave spectra for 7.1 GHz and 8.3 GHz in Fig. 4. These frequencies correspond to the planes (I) and (II) indicated in the 3D graph at the right side of the upper row of Fig. 3. For both applied frequencies ν_{RF}, the broadening is clearly visible and one can see that the main part of the scattered spin waves is concentrated within the frequency interval $[\nu_0, 2\nu_{\mathrm{RF}} - \nu_0]$. For the lower excitation frequency of $\nu_{\mathrm{RF}} = 7.1\,\mathrm{GHz}$, an increase of the spin-wave intensities for frequencies even above $2\nu_{\mathrm{RF}} - \nu_0$ is observed. Within the presented framework of four-magnon scattering this can be understood when taking repetitive scattering processes into account.

In conclusion, we have demonstrated that the intrinsic nonlinear damping of spin waves via four-magnon scattering plays an important role for spin dynamics in small magnetic elements. A deeper

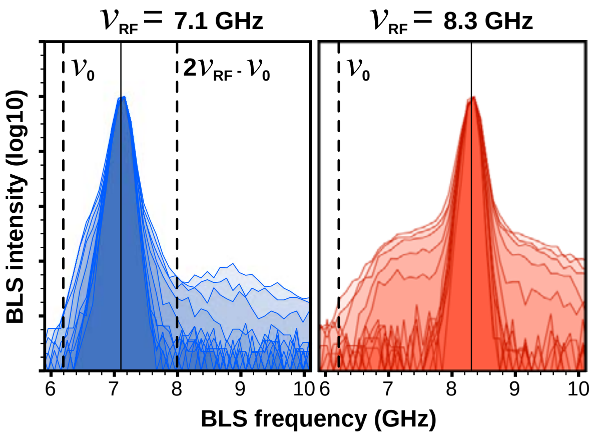

Fig. 4: Spin-wave spectra for fixed excitation frequencies of 7.1 GHz and 8.3 GHz corresponding to the planes (I) and (II) shown in Fig. 3. Different lines represent different applied microwave powers. The broadening of the spin-wave resonance due to four-magnon scattering covers the accessible range of the spin-wave band and no spin-waves are detected below the minimum frequency ν_0.

understanding of these effects is of crucial importance for future applications of spin waves in spintronic devices since they will be even more pronounced in novel magnetic materials with a reduced magnetic damping.

Financial support by the Carl-Zeiss-Stiftung, and the Deutsche Forschungsgemeinschaft (DFG, Graduate School of Excellence *Materials Science in Mainz*) is gratefully acknowledged. The authors thank the Nano+Bio Center, TU Kaiserslautern for assistance in sample preparation.

References

[1] Y. Kajiwara, K. Harii, S. Takahashi, J. Ohe, K. Uchida, M. Mizuguchi, H. Umezawa, H. Kawai, K. Ando, K. Takanashi, S. Maekawa, E. Saitoh, Nature **464**, 262 (2010).
[2] H. Suhl, Journal of Physics and Chemistry of Solids **1** 209-227 (1957).
[3] M. Sparks, R. Loudon, C. Kittel, Phys. Rev. **122** 791 (1961).
[4] V.E. Demidov, J. Jersch, K. Rott, P. Krzysteczko, G. Reiss, S.O. Demokritov, Phys. Rev. Lett. **102** 177207 (2009).
[5] A. Dobin, R. Victora, Phys. Rev. Lett. **90** 167203 (2003).
[6] C. Kittel, Phys. Rev. **110** 1295 (1958).
[7] B.A. Kalinikos, A.N. Slavin, J. Phys. C Solid State **19** 7013 (1986).
[8] H. Schultheiss, S. Schäfer, P. Candeloro, B. Leven, B. Hillebrands, Phys. Rev. Lett. **100** 047204 (2008).
[9] K. Vogt, H. Schultheiss, S.J. Hermsdoerfer, P. Pirro, A.A. Serga, B. Hillebrands, Appl. Phys. Lett. **95** 182508 (2009).
[10] The material parameters used for the calculation of the spin-wave dispersion are:
saturation magnetization $M_S = 860\,\mathrm{kA/m}$
gyromagnetic ratio: $\gamma = 28\,\mathrm{GHz/T}$
exchange stiffness constant: $A = 1.3 \cdot 10^{-9}\,\mathrm{J/m}$

4.7 Near- and far-field excitation of lateral standing spin waves in a magnetic microstripe

K. Vogt, H. Schultheiss, S. Schäfer, P. Pirro, P.A. Beck, B. Leven, and B. Hillebrands

A challenging task in the field of spintronics is the realization of spin-based data processing. For this purpose, an efficient mechanism for the transportation of spin-encoded information is needed to interconnect spintronic devices with a spin-bus [1]. The straight forward solution - transport of spin information by electrons - has the disadvantage of very small operating distances below one micrometer due to the small spin diffusion length in nonmagnetic metallic materials [2]. Another promising approach is the conversion of spin information into spin waves in ferromagnetic materials [3]. Spin waves have the advantage of exhibiting operating distances up to two orders of magnitude larger compared to typical spin diffusion lengths in metals [4, 5]. Moreover, spin waves benefit from well known amplification mechanisms for the compensation of losses, e.g. parametric pumping [6] or spin torque [7], and they are well suited for realizing fundamental logic elements [8]. Therefore, spin waves as the carrier of information show a high potential for future spintronic devices.

The excitation of spin waves via microwave strip lines and coplanar waveguides as well as the propagation and manipulation of spin waves in $Ni_{81}Fe_{19}$-microstripes has already been widely discussed [4, 5, 9–12]. However, in all these studies, the influence of the far field from the exciting antenna structure on the spin-wave properties has not been addressed. In this report, we focus on this particular problem. We define the far field as the long range Oersted field generated by the given antenna geometry, whereas the near field is limited to the region directly at the antenna where spin waves are excited. As a model system, we investigate the ramifications such a far field can have on lateral standing spin waves. In the case of a standing spin wave, all the magnetic moments between two neighboring nodes precess in phase, whereas two adjacent antinodes oscillate 180 degree out of phase. Depending on the relative phase between the spin-wave antinodes and the microwave field of the antenna, one should observe an amplification or suppression of the spin-wave amplitude, respectively.

The experimental method we employ is phase-resolved Brillouin light scattering (BLS) microscopy [4]. This method allows us to determine the spin-wave intensity distribution and to reconstruct the phase profile of propagating as well as of standing spin waves.

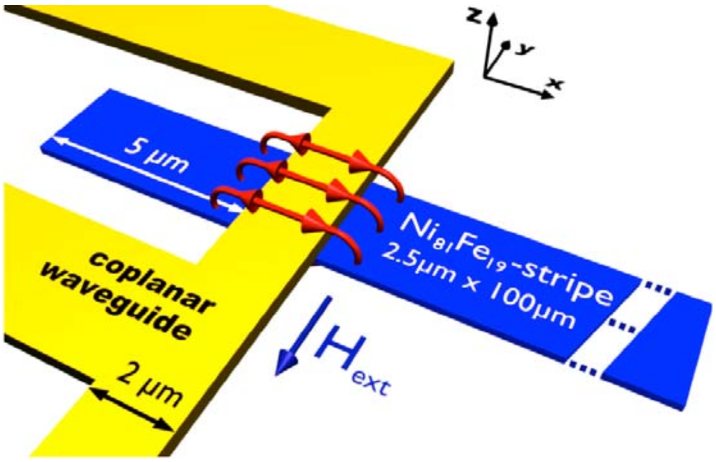

Fig. 1: Schematic drawing of the sample layout. The Oersted field (indicated by red arrows) generated by a microwave current flowing through the shorted end of a coplanar waveguide excites spin waves in a 2.5 μm wide and 40 nm thick $Ni_{81}Fe_{19}$-stripe.

Figure 1 gives a schematic description of the sample geometry. A microwave current flowing through the shorted end of a coplanar waveguide (CPW) is employed to excite spin waves in a 40 nm thick $Ni_{81}Fe_{19}$-microstripe with dimensions of $2.5 \times 100\,\mu m^2$. The $Ni_{81}Fe_{19}$-stripe has been fabricated onto a thermally oxidized silicon substrate using electron beam lithography. The shorted end of the CPW made of 500 nm thick copper is produced on top of the $Ni_{81}Fe_{19}$-stripe and acts as an antenna. With a width of $w = 2\,\mu m$, this antenna allows for efficient excitation of spin waves with wavevectors up to a maximum value of $k_{max} = 2\pi/w \approx 3.14\,\mu m^{-1}$. The antenna divides the $Ni_{81}Fe_{19}$-waveguide in two optically accessible sections, of which the one under investigation is only 5 µm long and is positioned between the signal and ground line of the CPW. Spin waves, which are generated by the Oersted field of the electric microwave-frequency current flowing through the antenna, propagate along the stripe and are reflected at its end. The length of the stripe is short enough to ensure that the intensity of the reflected spin waves is sufficiently high to effectively interfere with the incident spin waves. As a result, lateral standing spin waves are created. The static magnetic field H_{ext} is applied parallel to the short axis of the $Ni_{81}Fe_{19}$-stripe. In this case the Damon-Eshbach (DE) geometry for spin waves propagating along the waveguide is realized, i.e. the spin-wave wavevector is perpendicular to the magnetization direction.

In the experiments described in the following, we keep the microwave frequency of the electrical current, which is flowing through the CPW, fixed at 7.13 GHz since the electro-optical modulator used for phase-resolved BLS microscopy is designed for this particular frequency [4]. The wavelength of the spin waves is tuned by varying the magnitude of the static magnetic field. As can be seen from Fig. 2a, an increase of the magnetic field leads to a shift of the spin-wave dispersion curve to higher frequencies. For a fixed excitation frequency, this results in a decrease of the spin-wave wavevector and, thus, in an increase of the spin-wave wavelength. In order to determine the field range in which lateral standing spin waves appear, we measured the spin-wave intensity along the center of the 5 µm long part of the stripe (see dashed line in Fig. 3a) as a function of the applied magnetic field. The results are shown in Fig. 2b. Each horizontal line corresponds to a scan of the BLS intensity along a line in the middle of the stripe for a given externally applied magnetic field in the range between 10 and 40 mT. The detected spin-wave intensity is color coded where red (white) indicates maximum (minimum) signal, respectively. The formation of lateral standing spin waves is evident from clear modulations of the detected spin-wave intensity. The periodicity is determined by the wavelength of the spin wave. As already mentioned above, the increase of the modulation length with rising magnetic field can be understood when calculating the spin-wave dispersion for different applied fields as shown in Fig. 2a. For higher fields, the dispersion relation is shifted to higher frequencies leading to a decrease in the wavevector of the excited spin wave. As a result, the spin-wave wavelength is larger at higher external magnetic fields, and less nodes of the standing spin wave fit into the 5 µm long part of the stripe.

Below magnetic fields of 15 mT hardly any spin-wave intensity is visible in Fig. 2b, because of the limited excitation efficiency of the antenna for high wavevectors. As indicated in Fig. 2a, the intersection between the dispersion relation for an externally applied field of 14 mT and the fixed excitation frequency of 7.13 GHz yields a wavevector of $k = 3.15\,\mu m^{-1}$. This value is of the order of the maximum wavevector $k_{max} \approx 3.14\,\mu m^{-1}$ which can be efficiently excited with the given antenna geometry. The dispersion relations shown in Fig. 2a were calculated as described in [13] and taking into account the finite width of the spin-wave waveguide. We used standard material parameters for $Ni_{81}Fe_{19}$, which are summarized in the reference section [14].

In order to analyze the consequences of the far field generated by the shorted end the CPW on laterally standing spin waves, we investigated the case for an applied magnetic field of $\mu_0 H_{ext} = 26\,mT$

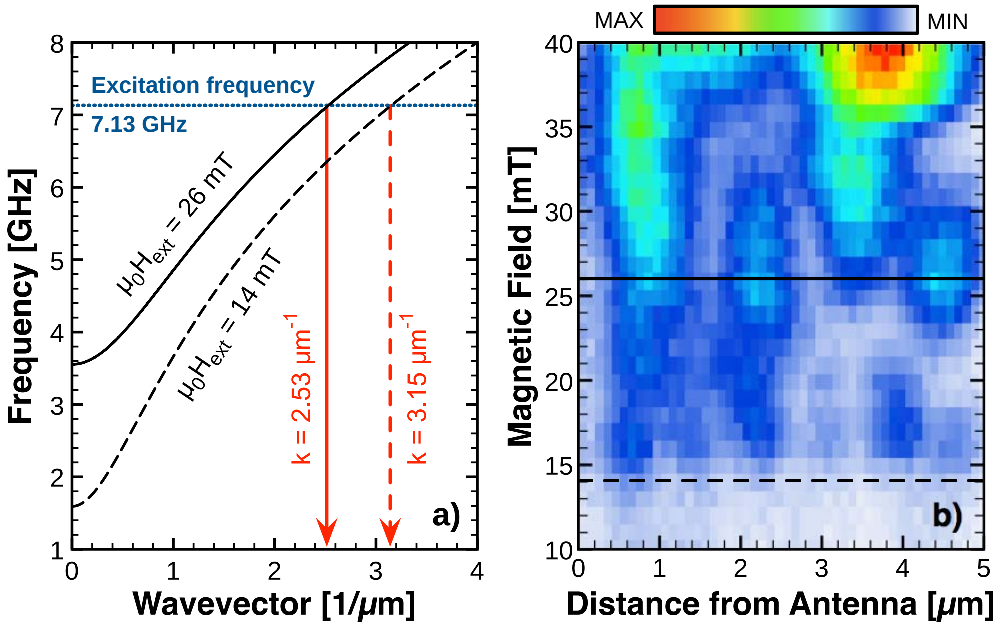

Fig. 2: a) Theoretical spin-wave dispersion relations calculated for two different magnetic fields. b) Standing spin waves for different applied magnetic fields. Each horizontal line represents a scan of the BLS intensity along a line in the middle of the 5 µm long part of the stripe for one fixed external magnetic field in the range between 10 and 40 mT. The BLS intensity is color coded where white (red) indicates minimum (maximum) signal.

in more detail. As can be seen from the measured two-dimensional BLS intensity distribution in Fig. 3a, a standing spin wave with four distinct intensity maxima along the stripe's long axis and only one maximum across the stripe's width is observed for this particular magnetic field. Red (white) represents maximum (minimum) intensity, respectively. The wavelength of the spin waves is 2.5 µm which corresponds to a wavevector of 2.51 µm^{-1}, which is in agreement with the wavevector calculated using the spin-wave dispersion relation for $\mu_0 H_{\mathrm{ext}} = 26\,\mathrm{mT}$ as shown in Fig. 2a.

The phase profile of this lateral standing spin wave was measured along a line in the center of the stripe as indicated by the dashed line in the intensity distribution in Fig. 3a. For reconstructing the phase profile, we followed the procedure as described in [4, 8]. The resulting phase profile is shown by red squares in Fig. 3b, whereas blue circles represent the corresponding BLS intensity.

The measured phase profile resembles many of the characteristics one would expect for a standing wave. Every time the BLS intensity (blue circles) reaches a minimum, which corresponds to a node of the standing spin wave itself, a phase shift of π is detected (red squares). In the regions between two nodes, the phase has a constant value leading to an overall steplike behavior of the spin-wave phase profile.

The impact of the far field of the antenna is evident from the fact that every second maximum of the standing spin wave under investigation shows a higher intensity than the maxima in between. This is a direct consequence of the excitation geometry. Whenever the far field of the antenna and the precession of the magnetic moments between two nodes are in phase, the precessional motion and the according antinode of the standing spin wave is amplified. In case of each neighboring antinode, the precession of the magnetic moments is 180 degree out of phase with the Oersted field, which leads to a suppression of the oscillation of these antinodes. This interplay induces the alternating strength of adjacent maxima in the intensity of the lateral standing spin wave. From

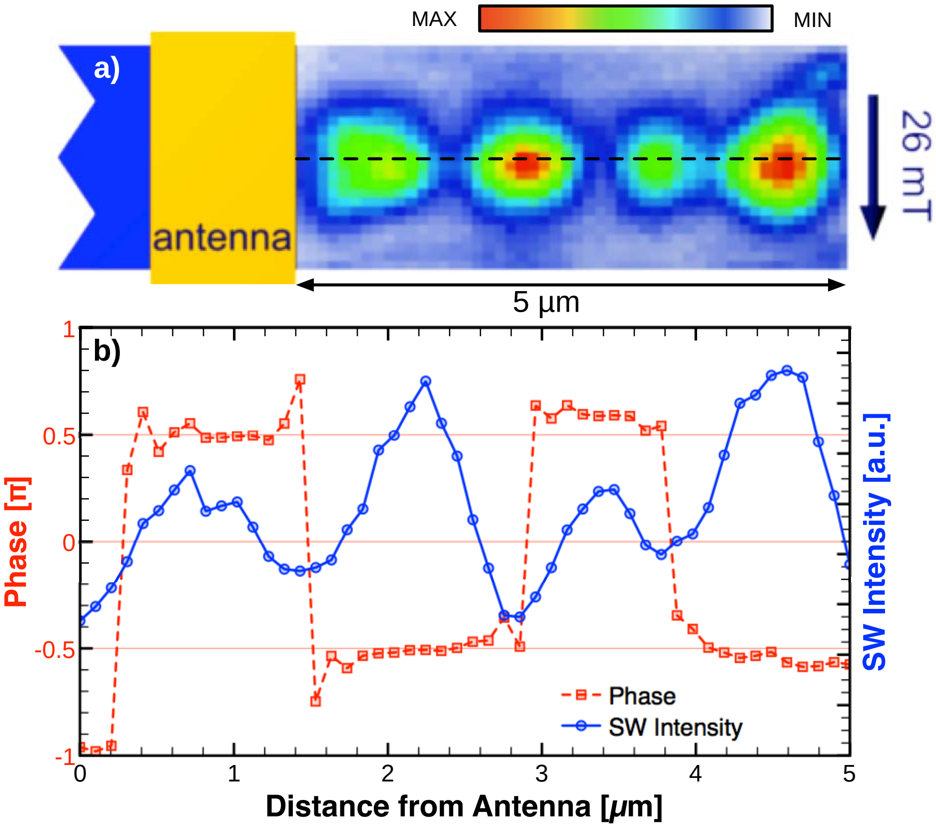

Fig. 3: a) Measured two-dimensional intensity distribution of a standing spin wave for an external magnetic field of 26 mT. b) Red squares show the reconstructed phase profile of the standing spin wave measured along the 5 µm long part of the stripe as indicated by the dashed line in a). Blue circles represent the according spin-wave intensity.

this analysis, we can conclude that the second and fourth antinode, as counted from the antenna, oscillate in phase with the Oersted field generated by the antenna and are thus amplified, whereas the other two oscillate with a phase shift of 180 degree.

The amplification and suppression of the spin-wave antinodes is not only visible in the intensity distribution, but also in the phase profile of the standing spin waves in Fig. 3b. The areas with a phase of -0.5π, where the intensity of the spin wave is increased, are extended at the expense of the areas with a phase of 0.5π having a reduced spin-wave intensity. Thus, besides the manipulation of the amplitude ratio of adjacent antinodes, the far field is modifying even the spatial profile of the standing spin wave.

In conclusion, we studied the effect of the dynamic far field of an antenna structure on the profile of lateral standing spin waves. It should be mentioned, that this kind of manipulation is only possible in case of standing spin waves. The phase of a propagating spin wave is a continuous function of the position so that there are no designated areas which are always in phase with the exciting microwave field. We believe that the effect described in this report is of great importance for spin-wave propagation in magnetic microstructures with an artificial periodicity. In these structures, standing spin waves are observed, either due to the reflection at artificial boundaries or in spin-wave wells as in recently reported antidot lattices [15,16]. Here, the far field of the exciting antenna might cause a drastic change of the mode profiles and thus modify the transmission properties of the artificially designed material.

Financial support by the Carl-Zeiss-Stiftung, and the Deutsche Forschungsgemeinschaft (DFG, Graduate School of Excellence *Materials Science in Mainz*) is gratefully acknowledged. The authors thank the Nano+Bio Center, TU Kaiserslautern for assistance in sample preparation.

References

[1] I. Žutić, J. Fabian, S. Das Sarma, Rev. Mod. Phys. **76** 323 (2004).
[2] F.J. Jedema, A.T. Filip, B.J. van Wees, Nature **410**, 345 (2001).
[3] Y. Kajiwara, K. Harii, S. Takahashi, J. Ohe, K. Uchida, M. Mizuguchi, H. Umezawa, H. Kawai, K. Ando, K. Takanashi, S. Maekawa, E. Saitoh, Nature **464**, 262 (2010).
[4] K. Vogt, H. Schultheiss, S.J. Hermsdoerfer, P. Pirro, A.A. Serga, B. Hillebrands, Appl. Phys. Lett. **95** 182508 (2009).
[5] V.E. Demidov, S.O. Demokritov, K. Rott, P. Krzysteczko, G. Reiss, Appl. Phys. Lett. **92** 232503 (2008).
[6] A.A. Serga, S.O. Demokritov, B. Hillebrands, S.G. Min, A.N. Slavin, J. Appl. Phys. **93** 8585 (2003).
[7] S. Seo, K. Lee, H. Yang, T. Ono, Phys. Rev. Lett. **102**, 147202 (2009).
[8] T. Schneider, A.A. Serga, B. Leven, B. Hillebrands, R.L. Stamps, M.P. Kostylev, Appl. Phys. Lett. **92**, 022505 (2008).
[9] V. Vlaminck, M. Bailleul, Science **322**, 410 (2008).
[10] V.E. Demidov, S. Urazhdin, S.O. Demokritov, Appl. Phys. Lett. **95**, 262509 (2009).
[11] D.R. Birt, B. O'Gorman, M. Tsoi, X. Li, V.E. Demidov, S.O. Demokritov, Appl. Phys. Lett. **95**, 122510 (2009).
[12] K. Perzlmaier, G. Woltersdorf, C.H. Back, Phys. Rev. B **77**, 054425 (2008).
[13] B.A. Kalinikos, A.N. Slavin, J. Phys. C: Solid State Phys. **19**, 7013 (1986).
[14] The material parameters used for the calculation of the spin-wave dispersion are:
Saturation magnetization $M_S = 860\,\mathrm{kA/m}$
Gyromagnetic ratio: $\gamma = 28\,\mathrm{GHz/T}$
Exchange stiffness constant: $A = 1.3 \cdot 10^{-9}\,\mathrm{J/m}$
[15] H. Ulrichs, B. Lenk, M. Münzenberg, Appl. Phys. Lett. **97**, 092506 (2010).
[16] S. Tacchi, M. Madami, G. Gubbiotti, G. Carlotti, A.O. Adeyeye, S. Neusser, B. Botters, D. Grundler, IEEE Trans. Magn. **46** 172 (2010).

4.8 Enhancement of the spin pumping efficiency by spin-wave mode selection

C.W. Sandweg, A.A. Serga, A.V. Chumak, and B. Hillebrands[1]

The prospering field of spintronics has become of great interest throughout the last decade. The aim of a future spintronics device is to overcome the limits of ordinary electronics devices by controlling the magnetization dynamics. A promising approach for forcing this new technology is the precise control as well as the accurate manipulation of spin current. [1]

Therefore, the spin pumping mechanism [2–4] is of great importance for the generation of a spin current in paramagnetic materials because it is emitting a pure spin current at the interface between a ferromagnet or a ferrimagnet and a paramagnet. An immense advantage in comparison with other methods generating a spin current is the absence of an electrical current driven through the interface. This important aspect of spin pumping reveals a completely new field of innovative electrical circuit designs and components, especially in combination with magnetic and paramagnetic metals as well as magnetic insulators. [5] The spin pumping mechanism can be observed directly via inverse spin-Hall effect (ISHE). [6–13] This effect describes the induction of an electromotive force in the paramagnetic metal which can be detected using a sensitive voltmeter.

In previous investigations, the pumping of the uniform precession mode was in the focus, but also the study of the spin wave spectrum and the corresponding spin pumping efficiencies is of immense importance for a successful design of a future spintronics device involving spin pumping.

In this report we show that surface spin-wave modes, hybridized with standing thickness modes, exhibit significantly greater efficiencies of spin pumping in $Y_3Fe_5O_{12}$ compared to volume spin waves. The experiments have been performed during a visit of C.W.S. in Sendai.

Figure 1a shows a sketch of the sample used in the present study. The sample consists of a 2.1 µm thick (111)-oriented single-crystal $Y_3Fe_5O_{12}$ (YIG) film grown on a $Gd_3Ga_5O_{12}$ single-crystal

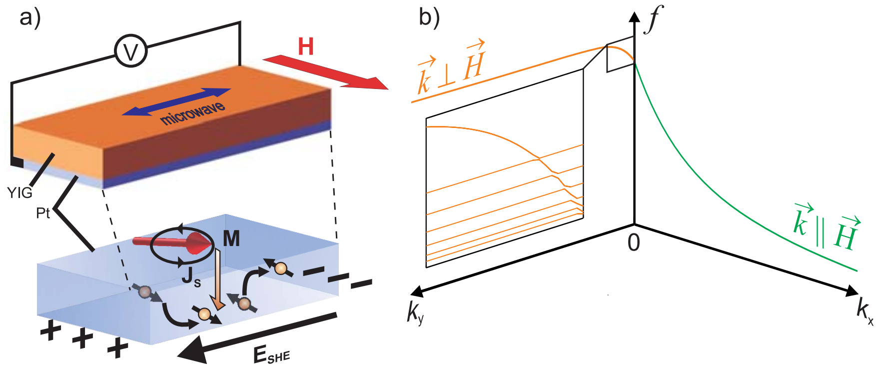

Fig. 1: a) Schematic illustration of the spin pumping and inverse spin-Hall effect in a YIG/Pt sample. The electromotive force is measured by attaching a nanovoltmeter to the Pt layer. b) Dispersion relation of magnetostatic surface modes (MSSW) and backward-volume magnetostatic waves (BVMSW) in YIG. The inset shows the hybridization of the surface modes with standing thickness modes at the beginning of the dispersion relation.

---

[1] In collaboration with Y. Kajiwara, Prof. E. Saitoh, Institute for Materials Research, Tohoku University, Sendai 980-8577, Japan.

substrate by liquid phase epitaxy. A 10 nm thick Pt layer was sputtered onto the YIG film. The sample has a rectangular shape with a width of $x = 1$ mm and a length of $y = 4$ mm. In addition, two electrodes are attached to the ends of the Pt layer and wired to a Keithley 2182A Nanovoltmeter (see Fig. 1a) for a precise and stable measurement of the electromotive force V generated by the ISHE.

For the measurement the sample is placed in a JEOL JES-FA200 microwave absorption spectrometer so that it is in the center of a TE_{011} microwave cavity. Thus, the magnetic-field component of the mode is maximized and the electric field component is minimized respectively. A microwave mode with $f = 9.441$ GHz is excited and sent to the cavity and, in addition, a tunable external magnetic field H is applied at the same time. During the measurement, the microwave magnetic field and the bias magnetic field are aligned in-plane of the investigated sample. The microwave absorption spectrometer comprises a lock-in amplifier, and therefore the derivative of the microwave absorption intensity I with respect to the magnetic field dI/dH is measured. When H and f fulfill the resonance condition of a magnetic mode, a spin current is resonantly injected into the Pt layer by the mechanism of spin pumping. Afterwards, the injected spin current is converted into a charge current by the ISHE and can be detected using the voltmeter. Thus, we measured simultaneously the microwave absorption signal and the electromotive force V between the electrodes connected to the Pt layer.

Figure 1b shows the schematic illustration of the dispersion relation for an in-plane magnetized YIG film. [14, 15] At $k = 0$ the mode of the uniform precession, the ferromagnetic resonance (FMR), is located. If the wavevector is non-zero, two different types of propagating spin waves can be distinguished. Magnetostatic surface spin waves (MSSW) have a wavevector which is oriented perpendicular to the external bias magnetic field. The dynamic magnetization is localized at the surface. Another key property of these modes is the hybridization with standing thickness modes [14, 15], as shown in the inset of Fig. 1b. In contrast, the wavevector of backward-volume magnetostatic spin waves (BVMSW) is oriented parallel to the bias magnetic field and their dynamic magnetization is distributed over the whole sample and it is small at the surface. In the present case, both types of spin waves are propagating in a rectangular YIG film of finite dimensions $x \times y$ and are reflected from the edges. If their wavevectors fulfill the conditions $k_x = n_x\pi/x$ and $k_y = n_y\pi/y$ with integers for n_x and n_y, standing waves (n_y,n_x) are formed. [16–18] They can be observed in the spin wave resonance (SWR) spectrum for odd integers of (n_y,n_x) only since the net magnetic moment is very close to zero for even numbers.

Figure 2a shows the spin wave resonance spectrum of the YIG/Pt sample for a microwave power of 2 mW, a fixed frequency of 9.441 GHz and a magnetic field range from 254.3 mT to 261.3 mT. In the spectrum dI/dH refers to the derivative of the microwave absorption intensity with respect to the magnetic field. Next to the main peak, which corresponds to the FMR, multiple resonance signals appear in the spectrum. These signals correspond to standing spin waves which exist due to the confinement of the investigated rectangular sample. In order to examine the microwave absorption intensity which has been absorbed by each mode, the SWR spectrum has been integrated, as shown in Fig. 2b. In the inset the integral intensity S of the I-spectrum is drawn as a function of the square root of the microwave power. The linear slope proves that the microwave absorption is not saturated and therefore nonlinear effects will not influence the measurement. [19]

Using the dispersion relations for hybridized MSSW and BVMSW it is possible to identify the resonance signals to the left and to the right of the FMR signal. As shown in Fig. 2c, hybridized MSSW have frequencies above the FMR and BVMSW below the FMR. By changing the magnetic field at a fixed frequency, the whole dispersion relation is shifted up or down. In this way, magnetic

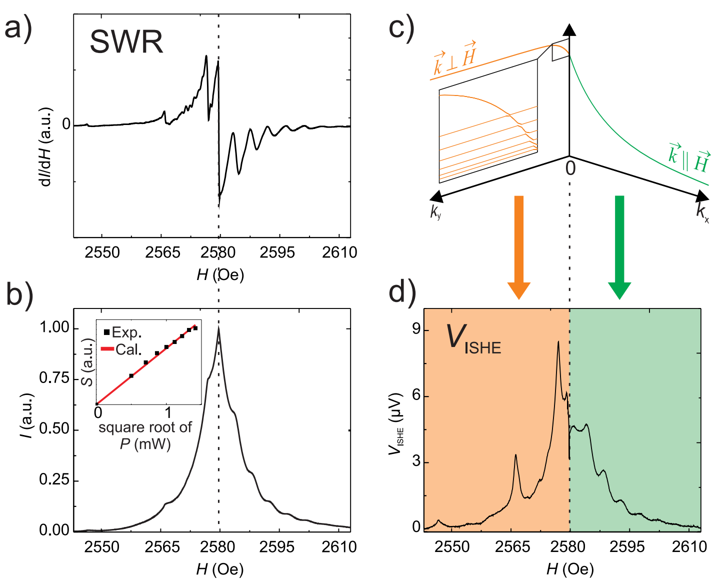

Fig. 2: a) Spin wave resonance (SWR) spectrum of the YIG/Pt sample at 2 mW. The dashed line shows the magnetic field position (H) of the ferromagnetic resonance (FMR). b) Integrated SWR spectrum at 2 mW. I denotes the microwave absorption intensity. In the inset, the integral intensity S of the I-spectrum is drawn as a function of square root of the microwave power. c) The schematic dispersion relation illustrates the positions of the MSSW and the BVMSW in the resonance spectrum d) Spectrum of the electromotive V_{ISHE} as a function of the bias magnetic field. The dashed line indicates the position of the FMR.

resonances lower than the FMR position corresponds to MSSW modes and higher field positions to BVMSW modes in accordance with the dispersion relation. The electromotive force V_{ISHE} measured with a nanovoltmeter is presented in Fig. 2d. The dashed line indicates the peak position of the FMR. To the left of this line the resonant electromotive force signals from the MSSW appear and on the right, the signals from the standing BVMSW modes are located.

The main aim of the presented work is to evaluate the spin pumping efficiency for the different lateral standing spin wave modes. The peaks of the spectrum of the electromotive force can be unambiguously identified by analytical calculations of the spin-wave spectrum. [14, 15] Three of these peaks correspond to standing MSSW modes with $(n_y,n_x) = (3,1)$, (5,1) and (7,1) (see **A**, **B**, **C** in Fig. 3b), which are significantly pronounced but barely detectable in the SWR spectrum, as presented in Fig. 3a. The standing modes (1,3), (1,5) and (1,7) of the BVMSW are also clearly observable in the ISHE spectrum but not with such a significance as in the MSSW case. This indicates that the spin pumping efficiency is greater for hybridized MSSW standing modes as for BVMSW standing modes.

In order to analyze the different spin pumping efficiencies in a more quantitative manner, the resonant electromotive force spectrum V_{ISHE} is divided by the integral intensity of the SWR spectrum I, which reflects the microwave absorption intensity by each spin wave mode. Figure 3c shows the obtained spin pumping efficiency V_{ISHE}/I in logarithmic scale. The efficiency of the standing BVMSW modes remains constant, nearly independent of higher mode numbers. This demonstrates that the spin pumping efficiency of volume modes is not sensitive to the mode numbers in accordance with previous results. [8] On the other hand, the efficiency V_{ISHE}/I is clearly enhanced for hybridized MSSW modes (see the left branch of Fig. 3c). The efficiency curve also clarifies that the spin pumping efficiency increases with higher mode numbers of the hybridized MSSW.

This behavior can be attributed to different distributions of the dynamic magnetization over the sample thickness for the different standing spin waves. Hybridized MSSW are strongly located at the surface and the dynamic magnetization is significantly lower in the volume area of the sample. Thus, the coupling of the conduction electrons to the spin wave modes is enhanced. In contrast, the BVMSW are volume waves with a dynamic magnetization distributed over the whole sample and therefore the amplitude of the interface is smaller than for surface waves. Consequently, the ratio between the electromotive force signal and the microwave absorption intensity is even enhanced

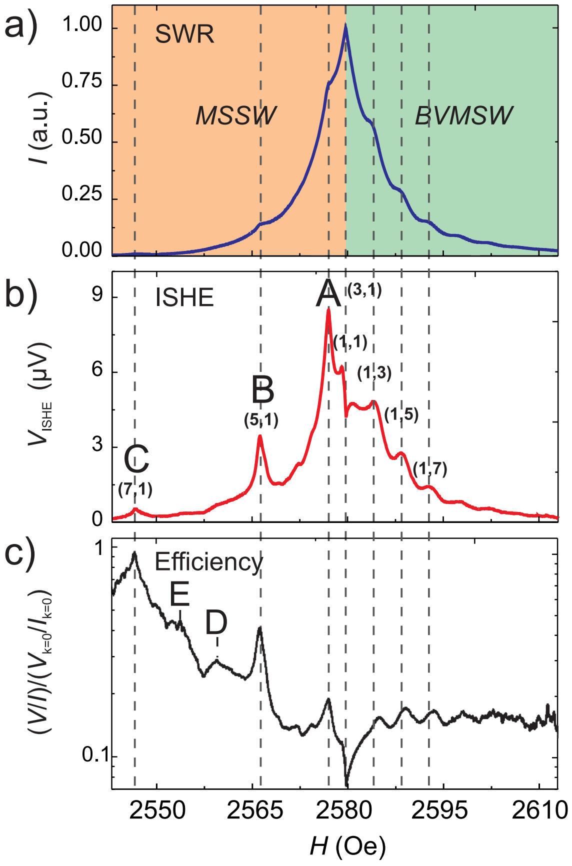

Fig. 3: Comparison between the SWR and the V_{ISHE} spectrum. The V_{ISHE} spectrum shows resonant signals from MSSW modes $(n_y,n_x) = (3,1)$, (5,1) and (7,1), which are hardly observable in the SWR spectrum. On the other hand, the BVMSW modes (1,3), (1,5) and (1,7) are visible in both spectra. The figure below shows the spin pumping efficiency which confirms this observation.

for higher MSSW modes. Owing to this enhanced sensitivity for the surface mode detection, we recognize two additional peaks in the V_{ISHE} spectrum, i.e. peak **D** and **E** in Fig. 3c, which are not detectable in the conventional microwave absorption measurement (see Fig. 2a and Fig. 3a). They are likely modes with both $(n_y,n_x) > 1$. This suggests that the ISHE method may provide a powerful tool for surface spectroscopy of spin dynamics.

In summary, we demonstrate that hybridized standing surface spin waves have a extensively higher spin pumping efficiency rather than backward-volume waves. Thus, the efficiency of a spin-current generator can be increased by selecting the spin wave modes.

Financial support by the Deutsche Forschungsgemeinschaft (DFG, SFB/TRR49) and MEXT, Japan (Grant-in-Aid for Scientific Research Priority Area: Creation and control of spin current (19048009, 19048028), a Grant-in-Aid for Scientific Research (A), global COE for the Materials Integration International Centre of Education and Research) and NEDO, Japan (grant for Industrial Technology Research) from. M.P. Kostylev is gratefully acknowledged for valuable discussions.

References

[1] K. Ando, S. Takahashi, K. Harii, K. Sasage, J. Ieda, S. Maekawa, E. Saitoh Phys. Rev. Lett. **101**, 036601 (2008).
[2] Y. Tserkovnyak, A. Brataas, G.E.W. Bauer, Phys. Rev. Lett. **88**, 117601 (2002).
[3] S. Mizukami, Y. Ando, T. Miyazaki, Phys. Rev. B **66**, 104413 (2002).
[4] M.V. Costache, M. Sladkov, S.M. Watts, C.H. van der Waal, B.J. van Wees Phys. Rev. Lett. **97**, 216603 (2006).
[5] Y. Kajiwara, K. Harii, S. Takahashi, J. Ohe, K. Uchida, M. Mizuguchi, H. Umezawa, H. Kawai, K. Ando, K. Takanashi, S. Maekawa, E. Saitoh, Nature, **464**, 262 (2010).
[6] E. Saitoh, M. Ueda, H. Miyajima, G. Tatara, Appl. Phys. Lett. **88**, 182509 (2006).
[7] S.O. Valenzuela, M. Tinkham, Nature **442**, 176 (2007).

[8] K. Ando, J. Ieda, K. Sasage, S. Takahashi, S. Maekawa, E. Saitoh, Appl. Phys. Lett. **94**, 2625005 (2009).
[9] T. Kimura, Y. Otani, T. Sato, S. Takahashi, S. Maekawa, Phys. Rev. Lett. **101**, 156601 (2007).
[10] S. Takahashi, S. Maekawa, Phys. Rev. Lett. **88**, 116601 (2002).
[11] K. Ando, Y. Kajiwara, S. Takahashi, S. Maekawa, K. Takemoto, M. Takatsu, E. Saitoh, Phys. Rev. B **78**, 014413 (2008).
[12] K. Ando, T. Yoshino, E. Saitoh, Appl. Phys. Lett. **94**, 152509 (2009).
[13] A. Takeuchi, G. Tatara, J. Phys. Soc. Jpn. **77**, 074701 (2008).
[14] B.A. Kalinikos, A. N. Slavin, J. Phys. C: Solid State Phys. **19**, 7013 (1986).
[15] A.A. Serga, A.V. Chumak, B. Hillebrands, J. Phys. D: Appl. Phys. **43** 264002 (2010).
[16] J. Barak, R. Ruppin, J.T. Suss, Phys. Lett. **108A**, 423 (1985).
[17] S.O. Demokritov, B. Hillebrands, A.N. Slavin, Phys. Rep. **348**, 442 (2001).
[18] J. Jorzick, S.O. Demokritov, C. Mathieu, B. Hillebrands, B. Bartenlian, C. Chappert, F. Rousseaux, A.N. Slavin, Phys. Rev. B **60**, 15194 (1999).
[19] J.W.H. Schreurs, G.K. Fraenkel, J. Chem. Phys. **34**, 756 (1961).

C. Magnonic Crystals and Spin Waves in Anisotropic Media

Magnonic crystals are defined as magnetic structures in which the magnetic properties vary periodically in one, two or three dimensions. With spin waves as their dynamic excitations, they are the magnetic analogue to photonic and sonic crystals, suitable to work in the microwave frequency range. Magnonic crystals can exhibit full band gaps, where spin waves are not allowed to propagate.

They are interesting for microwave and signal processing applications due to their potential ability to efficiently localize and guide spin waves along a waveguide constructed in the crystal as well as due to a wide tuneability of their characteristic parameters. The simplest type of a magnonic crystal is a one-dimensional diffraction grating created in a spin-wave waveguide by modulating periodically the internal magnetic field along the propagation direction. The waveguide typically has the form of a thin and narrow strip of a magnetically ordered material. When the spin wave is channeled along the main axis of such a waveguide, this grating behaves like a one-dimensional magnonic crystal.

Such structures can be created using single crystalline ferrimagnetic films of yttrium-iron-garnet (YIG) as well as by patterning of a thin ferromagnetic metal film. The first material is the most suitable one for the investigation of fundamentals of spin-wave dynamics because it has very low propagation losses for dipole-dominated spin waves (also called magnetostatic waves). Single crystalline ferromagnetic films possess large potential for further miniaturization, and thus, for practical application of the magnonic crystals.

Results on rejection band formation in a full-metallic micro-structured magnonic crystal prepared in the form of a Permalloy stripe of varying width are presented in Report 4.9. The understanding of spin-wave scattering on a single structural element of a magnonic crystal is of crucial importance for design of such a crystal. In Report 4.10 we present the results on spin-wave tunneling through the a mechanical gap etched in a YIG-film waveguide. The fundamental aspects of a wave dynamics has been revealed in our experiments with dynamically controlled magnonic crystal formed by periodic magnetic potential in a YIG film. This potential was created by the Oersted field of the electric current flowing near the YIG film surface. The Report 4.11 presents the first realization of time reversal and frequency inversion in an all-linear system. The shown results of evidence that dynamic phenomena in artificial crystals can provide a substitute for the nonlinear mechanisms traditionally used to perform complex spectral transformations such as time reversal.

C. Magnonische Kristalle und Spinwellen in anisotropen Medien

Magnonische Kristalle sind magnetische Strukturen, deren magnetische Eigenschaften sich periodisch in ein, zwei oder drei Dimensionen ändern. Mit ihren dynamischen Anregungen, den Spinwellen, sind sie die im Mikrowellenbereich arbeitenden, magnetischen Entsprechungen zu photonischen und phononischen Kristallen. Magnonische Kristalle können Bandlücken aufweisen, in denen Spinwellen nicht propagieren können.

Aufgrund ihrer Eigenschaft, Spinwellen innerhalb des Kristalls zu führen oder auch zu lokalisieren und der weiten Einstellbarkeit ihrer Parameter sind sie für Mikrowellen- und Signalverarbeitungsanwendungen interessant. Der einfachste Typ eines magnonischen Kristalls ist ein eindimensionales Gitter, das in einem Spinwellen-Wellenleiter durch periodische Modulation des internen Magnetfelds entlang der Propagationsrichtung erzeugt wird. Der Wellenleiter hat üblicherweise die Form eines dünnen, schmalen Streifens aus einem magnetisch geordneten Material. Wenn eine Spinwelle entlang der Achse dieses Wellenleiters propagiert, wirkt das Gitter als eindimensionaler magnonischer Kristall.

Solche Strukturen können aus einkristallinen ferrimagnetischen Yttrium-Eisen-Granat (YIG) Filmen, sowie durch das Strukturieren eines dünnen ferromagnetischen Metallfilms erzeugt werden. Das erstgenannte Material ist aufgrund seiner sehr niedrigen Dämpfung für dipolare Spinwellen hervorragend geeignet. Metallische ferromagnetische Filme haben ein großes Potential für weitere Miniaturisierung, und damit für die technische Anwendung von magnonischen Kristallen.

Resultate zu den gemessenen Sperrbändern in einem metallischen, mikrostrukturierten magnonischen Kristall präpariert als ein schmaler Permalloy-Streifen mit periodisch variierender Breite werden in Bericht 4.9 vorgestellt. Das Verständnis der Spinwellenstreuung an einer einzelnen Inhomogenität eines magnonischen Kristalls ist von großer Wichtigkeit für den Entwurf von magnonischen Kristallen. In Bericht 4.10 stellen wir die Resultate von Spinwellen-Tunnelexperimenten über eine mechanische Lücke vor, die in einen YIG-Film geätzt wurde. Die fundamentalen Aspekte der Wellendynamik in dynamisch schaltbaren magnonischen Kristallen sind von besonderer Bedeutung. Solche Strukturen können durch einen mäanderförmigen stromtragenden Draht auf einem YIG-Streifen erzeugt werden. Im Bericht 4.11 zeigen wir die Realisation von Zeitumkehr und Frequenzinversion in einem solchen, vollständig linearen System. Die Ergebnisse belegen, dass dynamische Phänomene in künstlichen Kristallen einen Ersatz für die bisher eingesetzten nichtlinearen Mechanismen darstellen können, um so besonders elegant komplexe spektrale Transformationen wie z.B. die Zeitumkehr experimentell realisieren zu können.

4.9 Spin-wave propagation in a microstructured magnonic crystal

A.V. Chumak, P. Pirro, A.A. Serga, H. Schultheiss, K. Vogt, S.J. Hermsdörfer, P.A. Beck, and B. Hillebrands[1]

Magnonic crystals (MCs) operate with spin waves (SW) in the microwave frequency range [1–8] and are the magnetic counterpart of photonic and sonic crystals. The greatest success in MC making has been achieved with yttrium-iron-garnet (YIG) film based structures due to the extremely small magnetic loss [1–3]. However, comparatively large sizes of these devices (hundreds of microns) and the incompatibility of the YIG film growing process with modern complementary metal-oxide semiconductor (CMOS) technology inhibit their wide practical use. Applications in microelectronics require downscaling to sub-micron sizes and a replacement of YIG films by thin ferromagnetic metallic layers.

Previous studies of metal film based microstructured magnonic crystals (micro-MCs) were mostly focused on their thermal SW spectrum [4, 5], or were purely theoretical [6, 7]. Here we report on the experimental observation and characterization of spin-wave propagation in a metal micro-MC [8]. The crystal was fabricated as a SW-waveguide made from a permalloy (Py) stripe with a periodically varying width [6, 8].

Electron beam lithography, molecular beam epitaxy, and lift-off process were used to fabricate the magnonic crystal in the form of a notched permalloy stripe on thermally oxidized Si(001) substrate (see Fig. 1). The width of the 40 nm thick Py ($\mathrm{Ni_{81}Fe_{19}}$) stripe varies periodically between $w_0 = 2.5\,\mu\mathrm{m}$ and $w_0 = 1.5\,\mu\mathrm{m}$. The length of the $2.5\,\mu$m-wide sections is $0.75\,\mu$m and the length of the $1.5\,\mu$m-wide sections ("notches") is $0.25\,\mu$m. This forms a magnonic crystal with a lattice constant $a = 1\,\mu\mathrm{m}$. As a reference a second waveguide with a uniform $w_0 = 2.5\,\mu\mathrm{m}$ width was also patterned on the same substrate $6\,\mu$m apart from the magnonic crystal (see Fig. 1).

Spin waves are excited by the microwave Oersted field created by a $0.5\,\mu$m thick and $w_\mathrm{a} = 1\,\mu$m-wide copper antenna, which is placed across the both Permalloy waveguides (see Fig. 1). In order to detect spin waves the space-resolved Brillouin light scattering microscopy technique is used [9]: a focused laser beam probes spin waves with a spatial resolution of 250 nm and a frequency resolution of 300 MHz [9, 10].

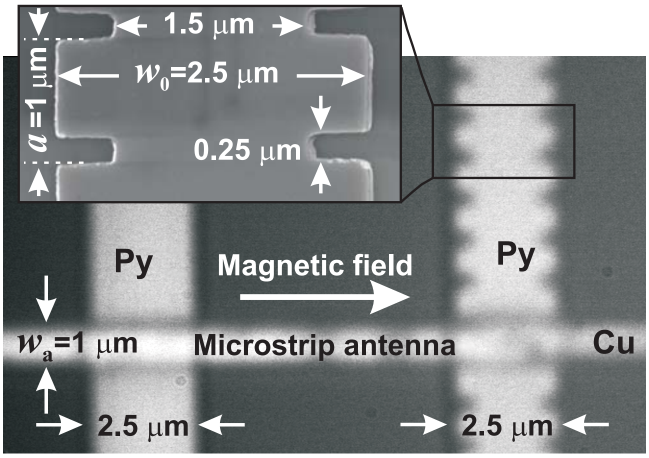

Fig. 1: Scanning electron microscopy and optical images of the structure under study. The uniform reference waveguide is shown on the left and the magnonic crystal on the right.

---

[1] In collaboration with M.P. Kostylev, School of Physics, University of Western Australia, Crawley, Western Australia 6009, Australia.

The calculated dispersion for the lowest (fundamental) width mode of a $w_0 = 2.5\,\mu$m-wide uniform waveguide is shown in Fig. 2a as solid line. For comparison, in this panel we also show the dispersion for a $w_0 = 1.5\,\mu$m-wide uniform waveguide which corresponds to the narrow sections of the magnonic crystal. The calculation was carried out by numerically solving the integro-differential equation derived in Ref. [11].

The experimentally measured SW intensity for the reference waveguide is shown in Fig. 2b (dotted line) as a function of the applied microwave frequency. The maximum intensity corresponds to spin waves with wavenumbers slightly larger than $k = 0$ because of the highest excitation efficiency and the highest SW group velocity. With increasing frequency (and increasing spin-wave wavenumber, respectively) the excitation efficiency drops. For the used antenna it gets close to zero above 11 GHz. A weak oscillatory intensity variation with frequency can be understood as beating of the fundamental width mode with the third one, which is also excited by the antenna but less efficiently [10].

The solid line in Fig. 2b shows the measured SW intensity for the magnonic crystal. A pronounced rejection band (where spin waves are not allowed to propagate) is clearly observed for frequencies close to 8 GHz. One can see that the rejection frequency is slightly shifted down with respect to the frequency expected from the simple Bragg analysis of the SW dispersion for the uniform 2.5 μm-wide waveguide ($k_{\mathrm{rej1}} = \pi/a = 3.14\,\mathrm{rad}/\mu\mathrm{m}$). We suppose that this is due to inhomogeneity of the internal magnetic field within the crystal. The decrease in the internal field between the opposite notches shifts the dispersion curve downwards in frequency. As a result the condition $k_{\mathrm{rej2}} = \pi/a = 6.28\,\mathrm{rad}/\mu\mathrm{m}$ is fulfilled for a smaller frequency value. It is worth noting that the rigorously calculated SW intensity (see for the details [8]), which is also shown in Fig. 2b, is in good agreement with the experiment. The second rejection band $k_{\mathrm{rej2}} = 2\pi/a = 6.28\,\mathrm{rad}/\mu\mathrm{m}$ is visible in Fig. 2b as well. However, it is not well pronounced because k_{rej2} coincides with the edge of the antenna excitation band $k_{\mathrm{max}} = 2\pi/a = 6.28\,\mathrm{rad}/\mu\mathrm{m}$.

To obtain a closer insight into the wave scattering mechanisms we performed a simulation based on a phenomenological approach from [2, 12]. For this purpose we consider the micro-MC as a periodical sequence of sections of regular transmission lines with different propagation constants (different k-values) for the same carrier frequency. The rejection coefficient at the junction of wider-to-narrower waveguide can then be written as $\Gamma_{0-1} = (k_1 - k_0)/(k_1 + k_0) + \Gamma'$, where k_0 and k_1 are the wavenumbers for w_0-wide and w_1-wide waveguide sections, respectively [12]. As it was mentioned above, the spin wave is scattered back not only due to the difference in k, which is

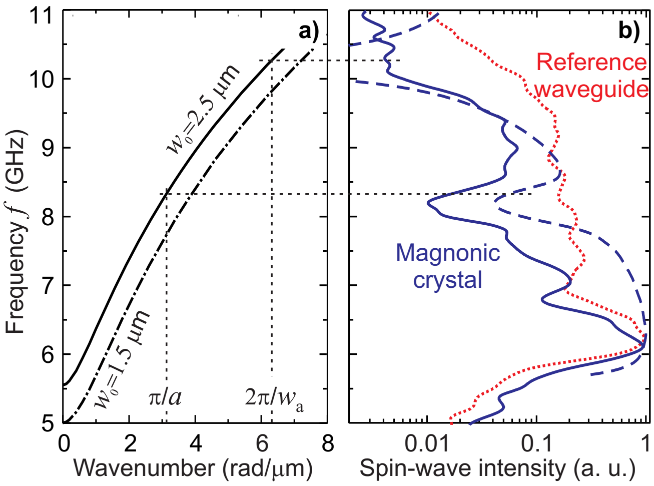

Fig. 2: a) Calculated SW dispersion curves for uniform waveguides with $w_0 = 2.5\,\mu$m (solid line) and 1.5 μm (dash-dotted line). b) Normalized SW intensity measured at the distance $x = 8\,\mu$m from the antenna versus the applied frequency. Solid line – the magnonic crystal; dotted line – the reference waveguide. The dashed line represents the calculation for the magnonic crystal. For both panels the bias magnetic field and the saturation magnetization are 500 Oe and $M_s = 770$ G.

accounted by first summand Γ_{0-1}, but also because its initial transverse profile does not fit into the width w_1. To account for this additional reflection mechanism we phenomenologically introduce Γ'. The rejection coefficient for the waveguide junction narrower-to-wider contains only one term $\Gamma_{1-0} = -(k_1 - k_0)/(k_1 + k_0)$.

The theoretical dependence of the SW intensity on the applied frequency is shown in Fig. 2b with a dashed line. It was calculated as $(F(k_0)/|T_{11}|)^2$, where $F(k_0) \propto \sin(k_0 \cdot w_\mathrm{a}/2)/k_0$ is the efficiency of the antenna excitation. T_{11} is the element (1,1) of the MC transmission matrix (see [2, 12]) which includes Γ_{1-0}, Γ_{0-1}, and the experimentally measured spatial SW damping corresponding to a Gilbert damping parameter $\alpha \approx 0.007$ [13]. This best fit is obtained for $\Gamma' = 0.12$. It means that 12 percent of incident beam energy is reflected back due to the geometrical mismatch between the waveguide sections. We should also emphasize that the reflection caused by the change of the SW wavenumbers is of the same order.

The transmission characteristic for the micro-MC shown in Fig. 2b has been also measured for different bias magnetic fields [8]. The first rejection band has been clearly observed for all the fields higher than 150 Oe. It has been shown that variation of the applied bias magnetic field in the range from 150 Oe to 700 Oe makes it possible to control the band gap frequency in the range from 6.5 to 9 GHz. The value of 150 Oe corresponds to the demagnetizing field calculated across a long ellipsoidal Py stripe of 2.5 µm width and 40 nm thickness. Thus, the experimentally obtained value of 150 Oe is the minimum field one has to apply in order to saturate the magnonic crystal.

In conclusion, a micro-sized magnonic crystal operational at microwave frequencies has been fabricated in the form of a notched permalloy waveguide. Formation of pronounced magnonic band gaps was observed. They are seen as considerable decrease in SW transmission caused by the resonant backscattering from a periodical lattice. The band gap frequency can be tuned in a wide range by varying the applied magnetic field.

Financial support by the Deutsche Forschungsgemeinschaft (DFG, SE 1771/1-1) is gratefully acknowledged. B. Laegel (Nano+Bio Center, TU Kaiserslautern) is gratefully acknowledged for electron beam lithography.

References

[1] S.L. Vysotskii, S.A. Nikitov, Yu.A. Filimonov, JETP **101**, 636 (2005).

[2] A.V. Chumak, A.A. Serga, B. Hillebrands, M.P. Kostylev, Appl. Phys. Lett. **93**, 022508 (2008).

[3] A.V. Chumak, T. Neumann, A.A. Serga, B. Hillebrands, M.P. Kostylev, J. Phys. D **42**, 205005 (2009).

[4] G. Gubbiotti, S. Tacchi, G. Carlotti , N. Singh , S. Goolaup, A.O. Adeyeye, M. Kostylev, Appl. Phys. Lett. **90**, 092503 (2007).

[5] Z.K. Wang, V.L. Zhang, H.S. Lim, S.C. Ng, M.H. Kuok, S. Jain, A.O. Adeyeye, Appl. Phys. Lett. **94**, 083112 (2009).

[6] K.S. Lee, D.S. Han, S.K. Kim, Phys. Rev. Lett. **102**, 127202 (2009).

[7] M. Krawczyk, H. Puszkarski, Phys. Rev. B **77**, 054437 (2008).

[8] A.V. Chumak, P. Pirro, A.A. Serga, M.P. Kostylev, R.L. Stamps, H. Schultheiss, K. Vogt, S.J. Hermsdoerfer, B. Laegel, P.A. Beck, B. Hillebrands, Appl. Phys. Lett. **95**, 262508 (2009).

[9] V.E. Demidov, S.O. Demokritov, B. Hillebrands, M. Laufenberg, Appl. Phys. Lett. **85**, 2866 (2004).

[10] V.E. Demidov, S.O. Demokritov, K. Rott, P. Krzysteczko, G. Reiss, Phys. Rev. B **77**, 064406 (2008).

[11] M.P. Kostylev, G. Gubbiotti, J.-G. Hu, G. Carlotti, T. Ono, R.L. Stamps, Phys. Rev. B , **76**, 054422 (2007).

[12] A.V. Chumak, A.A. Serga, S. Wolff, B. Hillebrands, M.P. Kostylev, J. Appl. Phys. **105**, 083906 (2009).

[13] S.S. Kalarickal, P. Krivosik, M. Wu, C.E. Patton, M.L. Schneider, P. Kabos, T.J. Silva, J.P. Nibarger, J. Appl. Phys. **99**, 093909 (2006).

4.10 Spin-wave tunneling through a mechanical gap

T. Schneider, A.A. Serga, A.V. Chumak, and B. Hillebrands[1]

Scattering of dipole-dominated spin waves from magnetic inhomogeneities has attracted a lot of attention recently (see e.g. [1–5] and references therein). One of the observed effects was spin-wave tunneling through an area in which the propagation of traveling spin waves is prohibited [6]. This zone was formed due to a spatial inhomogeneity of the internal field thus locally shifting the spin-wave frequency out of the allowed spin-wave band. The same can be achieved by locally changing the saturation magnetization M_S, for example by local reduction due to local heating the sample, by injecting magnons using parametric pumping [7] or by ion implantation [8, 9]. The precession of magnetization in this area is non-resonantly excited by the long-range dynamic dipole field created by the long-wavelength spin waves in the regions outside. Since the existence of the dipole field is not bounded to the presence of a magnetic material, tunneling can also be realized through an area where $M = 0$, i.e. through a mechanical gap.

In the present work we use an yttrium iron garnet (YIG) waveguide to study the tunneling of spin waves through a mechanical gap. Due to its extremely small magnetic losses this material allows for spin-wave propagation over centimeter distances and thus gives the possibility to conveniently observe spin-wave dynamics with high phase resolution with respect to the spin-wave wavelength. We use backward volume magnetostatic spin waves (BVMSW) [10] which propagate parallel to the applied field in an in-plane magnetized film. It should be noted that these waves are characterized by a negative group velocity $\mathrm{d}\omega/\mathrm{d}k$ for small wavenumbers k (where ω is the spin-wave frequency). Therefore one can expect features in the phase characteristics of tunneling arising from the fact that a BVMSW pulse which propagates in a positive direction has a negative carrier wavenumber k.

The spin-wave tunneling process is investigated using a microwave technique. The setup is shown in the upper inset of Fig. 1. It consists of three equally spaced, lithographically produced antennas

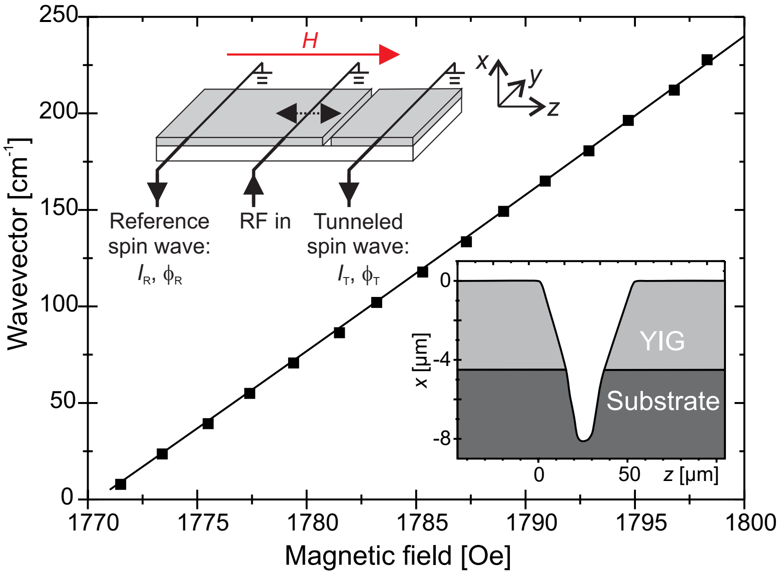

Fig. 1: Spin-wave field dependence $k(H)$ for $\omega = 2\pi \cdot 7\,\mathrm{GHz}$. The measurement (squares) are in excellent agreement with the theoretical dispersion for $L = 4.3\,\mu\mathrm{m}$ and $4\pi M_\mathrm{S} = 1760\,\mathrm{G}$. Upper inset: sketch of the setup. Spin waves are excited by a microwave pulse. Two output antennas allow to measure the tunneled signal as well as a reference signal. Lower inset: Profilometer measurement of the gap with the (nominal) width of $20\,\mu\mathrm{m}$. To take into account the trapezoidal shape, the width at the half-height is used in all calculations.

---

[1] In collaboration with M.P. Kostylev, School of Physics, M013, University of Western Australia, Crawley, Australia

placed across a YIG waveguide. The distance between neighboring microstrip spin-wave antennas is 4 mm. The nominal film thickness is 4.5 µm. A mechanical gap with the width w_g is formed in the film by chemical etching and is located between the central antenna and one of the outer antennas. The continuous film between the central antenna and the second outer antenna serves as a reference spin-wave waveguide. Three samples were fabricated using lithographic masks with 20, 50 and 100 µm wide gaps. Profilometer measurements of the fabricated samples showed that the gap edges are not perpendicular to the film substrate (see lower inset of Fig. 1). The gaps have trapezoidal cross-sections with the gap widths at the half-height ("average widths") larger by 18 µm micron than the nominal ones for all three samples. In the following presentation of our results we use these average gap width values (38, 68, and 118 µm). We also utilize them in our quasi-1D calculations.

First, by using the reference arm the dispersion of the spin waves in the film has been measured. For this purpose interference of two microwave signals, one traveling as a spin wave through the reference arm and the second along a microwave cable connecting the arm's spin wave antennas (see e.g. [11] for details), was used. The resulting interference signal varies as a function of the applied magnetic field H. Between two neighboring interference minima the spin-wave wavevector changes by $2\pi/(4\,\text{mm})$. This allows for tracing the spin-wave dispersion $k(H)$. For small wavenumbers $kL \ll 1$ (where L is the film thickness) the BVMSW dispersion is practically linear with its slope linearly proportional to L (see e.g. Eqs. (B11) and (B13) in [5]). As shown in Fig. 1, it is in excellent agreement with the theoretical dispersion for $L = 4.3\,\mu\text{m}$ and $4\pi M_s = 1760\,\text{G}$.

In the next stage, by using the middle antenna as an input and the two outer antennas as outputs, we measure both the intensity of the tunneled spin wave (I_T) as well as a the intensity of the reference spin wave (I_R). To avoid the interference between the picked up spin-wave signal and the direct electromagnetic leakage from the input to the output antenna antennas, a pulsed spin-wave signal was used. Due to the reciprocity of BVMSW propagation [12] and to the fact that both signals travel the same distance in the YIG film, their spatial damping as well as the phases accumulated on the length of the propagation distance is identical outside the gap. Thus one can easily extract the transmission coefficient through the gap as a function of the applied magnetic field $T(H) = I_T/I_R$. In addition, by using interference between the reference and the spin-wave signal and following the algorithm given in [13] it is possible to calculate the phase difference $\Delta\phi(H) + \phi_0$ between both channels. We are interested in the field dependent part of the phase difference $\Delta\phi(H)$, as the magnetic field independent part ϕ_0 is obviously connected to the difference in microwave cables and connections for both signal and reference channels.

Figure 2 shows the measured transmission $T(H)$ for different gap widths as a function of the applied bias magnetic field. One clearly observes, that the transmission through the gap decreases with increasing field. As the BVMSW wavelength for a fixed frequency decreases with increase in the applied field (see Fig. 1) the transmission is dependent on the spin-wave wavelength. It can be understood taking into consideration that the long range dynamic stray fields created by the spin-wave are responsible for the tunneling process. The shorter the spin-wave wavelength, the less far-reaching is the wave dipole field, since for a smaller wavelength spins with antiparallel orientation are positioned closer to each other. This peculiarity of the dipole field was previously seen indirectly in the experiments on formation of collective modes on arrays of dipole-coupled stripes [14]. It manifested itself as a decrease in the frequency width of the magnonic bands for collective modes with an increase in mode number. Our present experiment is the direct evidence of this property of the dynamic dipole field.

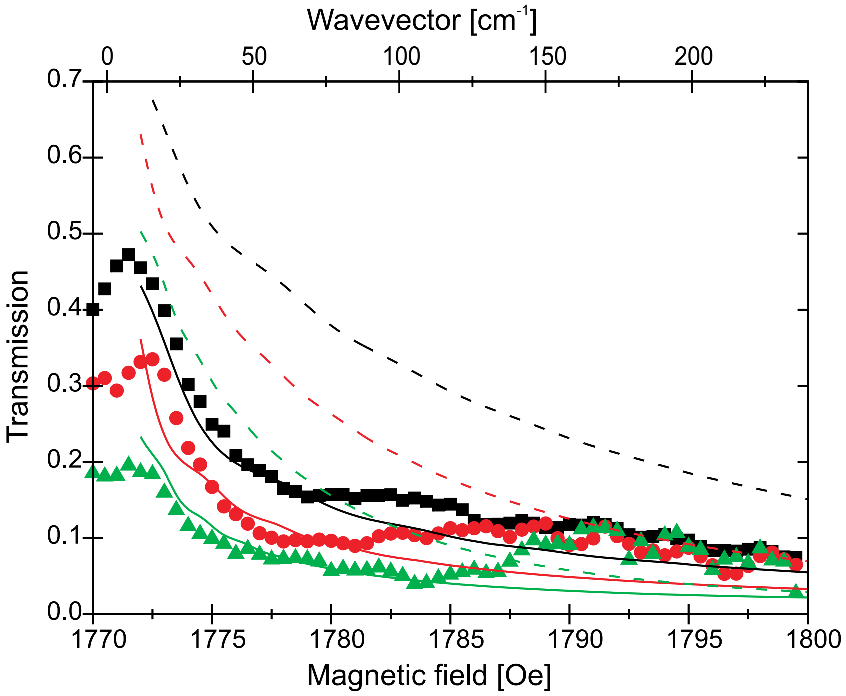

Fig. 2: Measured and calculated transmission as a function of the applied magnetic field. Squares: $w_\mathrm{g} = 38\,\mu\mathrm{m}$; circles: $w_\mathrm{g} = 68\,\mu\mathrm{m}$; triangles: $w_\mathrm{g} = 118\,\mu\mathrm{m}$. Dashed line: calculation without including inhomogeneity of the internal field; solid line: calculation which includes inhomogeneity of the internal field. Spin-wave frequency $\omega = 2\pi \cdot 7\,\mathrm{GHz}$.

Interestingly, $T(H)$ dependencies for all the gap widths show a decrease in the transmission for the smallest applied fields $H < 1775\,\mathrm{Oe}$, i.e. when approaching zero wavenumber $k = 0$. This decrease is not easy to explain. Supposedly it is connected with a distortion of the spin-wave pulse shape for very long-wave spin waves excited in a ferromagnetic film near the upper frequency band edge which is usually observed in spin wave experiments.

Figure 3 demonstrates the phase difference $\Delta\phi$ between the tunneled wave and the reference wave as a function of the applied bias magnetic field for different gap widths. The phase difference is positive which reflects the backward character of BVMSW [12]. Indeed, the phase accumulation of a backward wave $k \cdot l$ on a propagation path l is negative, as the phase velocity is negative and thus $k < 0$. In a simple model one can assume that the phase shift is due to the lack of phase accumulation in the gap $\Delta\phi(H) = -k(H) \cdot w_\mathrm{g}$ which is positive for negative k values. One can then expect that the shift increases with an increase in both H and the gap width w_g. This idea is clearly confirmed by the measurements.

The same theoretical model can be used to describe spin waves tunneling through an area with decreased saturation magnetization [7, 15–17] and through an air gap [14, 18]. The latter can be considered as the limiting case $M = 0$ and thus the approximate quasi-1D theory of spin-wave scattering from 1D inhomogeneities developed in [5] can be applied. In that work we considered scattering of spin waves from an inhomogeneity of the microwave magnetic permeability tensor $\hat{\chi}$. For BVMSW, only the diagonal component of this tensor

$$\chi = H_\mathrm{i} M / (H_\mathrm{i}^2 - (\omega/\gamma)^2) \tag{1}$$

is important ($\gamma = 2\pi \cdot 2.8\,\mathrm{rad}/(\mathrm{s} \cdot \mathrm{Oe})$ is the gyromagnetic ratio, and H_i is the internal field of the film). Thus, spin-wave tunneling through a mechanical gap is described by the solution of an equation which is another form of Eq. (5) in [5]:

$$\begin{aligned} \chi(z) h_{dx}(z) &= \int_0^{w_\mathrm{g}} G_{xx}(z - z') \frac{\chi(z')}{\chi_0 - 1} h_{dx}(z') dz' \\ &+ \exp(-ikz) \quad . \end{aligned} \tag{2}$$

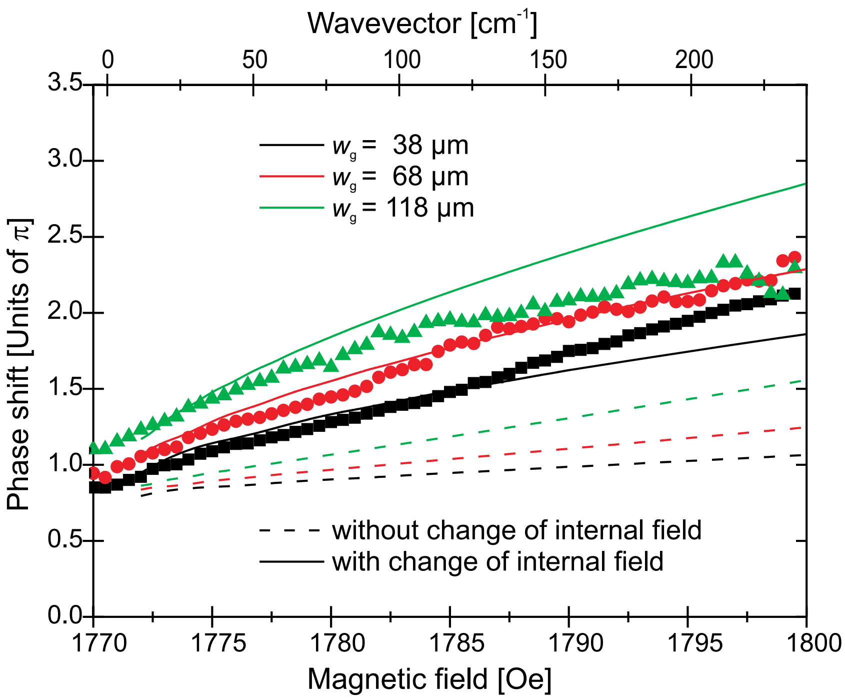

Fig. 3: Measured and calculated phase-shift as a function of the applied field. Squares: $w_g = 38\,\mu$m; circles: $w_g = 68\,\mu$m; triangles: $w_g = 118\,\mu$m. Dashed line: calculation without including inhomogeneity of the internal field; solid line: calculation which includes inhomogeneity of the internal field. Theoretical curves are shifted by $\phi_0 = 0.6\cdot\pi$ to compensate for the field independent phase shift due to the differences in reference and signal channel. Spin-wave frequency $\omega = 2\pi\cdot 7\,$GHz.

In this equation z and z' are the coordinates along the spin-wave propagation path (perpendicular to the antennas and the gap), $h_{dx} = \chi^{-1} m_x$ is the out-of-plane component of the dynamic dipole field produced by the dynamic magnetization m_x, $\chi_0 = \chi(z \ll 0, z \gg w_g)$ is the value of χ far away from the gap, and G_{xx} is the component of the Green's function of spin-wave excitation [5].

The complex transmission coefficient through the gap then reads

$$T = m_x(z)/\exp(-ikz) \quad \text{for} \quad z \gg w_\text{g} \quad . \tag{3}$$

In the gap $\chi = 0$ as M=0 (see Eq. (1)). Then for the gap Eq. (2) reduces to

$$\int_0^{w_\text{g}} G_{xx}(z-z')h_{dx}(z')\mathrm{d}z' + \mathrm{e}^{ikz} = 0 \quad . \tag{4}$$

Once the spatial distribution of the dipole field inside the gap has been found by solving this equation one can calculate the dynamic magnetization $m_x = \chi \cdot h_d$ outside the gap by using the equation as follows

$$m_x(z) = \int_0^{w_\text{g}} G_{xx}(z-z')h_{dx}(z')dz' + \exp(-ikz) \tag{5}$$

and then the transmission coefficient by using Eq. (3).

However, this approach does not account for an effect which can be important in our case. The static magnetic field is applied in the film plane perpendicular to the gap edge. Therefore, one has to expect inhomogeneities of the internal field and of the static magnetization in the film near the gap edges. As it was previously shown [19, 20], it is sufficient to account for the inhomogeneity of the static field and to neglect inhomogeneity of the static magnetization in order to get a valid description of the magnetization dynamics in patterned media. For simplicity we use here the same approach.

In the approximation of a homogeneous static magnetization inside the film, the inhomogeneity of the internal field due to the gap can be calculated as the stray field of an effective homogeneously magnetized rod of a rectangular cross-section $w_\mathrm{g} \cdot L$ with a negative value of saturation magnetization $-M_S$. The internal field H_i is the sum of the applied field H and the stray field of the rod H_S outside of the gap. The stray field is easily obtained by using the approximate 1D Green's function of the dipole field [21]. In doing so one obtains

$$H_i(z) = H - 2M_S \int_0^{w_\mathrm{g}} \ln\left(\frac{(z-z')^2}{(z-z')^2 + L^2}\right) \mathrm{d}z' \quad . \tag{6}$$

This $H_i(z)$ profile must be included in Eq. (1), and Eq. (2) must be solved to obtain the transmission coefficient for the gap.

We solved Eq. (2) and (4) numerically to produce the lines in Figs. 2 and 3. One sees very poor agreement with the experiment of the homogeneous H_i approximation (Eq. (4)). The agreement between the experiment and the solution of Eq. (2) with the included inhomogeneity of H_i is much better, which suggests that the real width of the barrier is actually larger than the gap width due to static demagnetization. However some deviation of the experimental data from the theory is still noticeable. We assume that they can be attributed to the trapezoidal shape of the gap and a not fully perpendicular incidence of the spin waves on the gap.

In conclusion, tunneling of dipole-dominated spin waves through mechanical gaps has been experimentally studied. Transmission properties of the gap have been measured as a function of the applied field and the gap width. It was shown that an increase of the gap width or the magnetic field leads to a reduced transmission as well as to a larger phase shift. Field dependencies could be explained by the characteristics of the dynamic dipolar field formed by the spin wave. Comparisons with theoretical calculations showed that the additional demagnetization field due to the gap leads to an effective increasing of the gap width. We believe, that the presented results will be useful for the full understanding and thus for the improvement of magnonic crystals that are based on periodically grooved ferromagnetic films [22] and arrays of ferromagnetic nanostripes.

Financial support by the Deutsche Forschungsgemeinschaft (DFG, GRK 792 and SE 1771/1-1) and the Australian Research Council, is gratefully acknowledged.

References

[1] R.L. Stamps, R.E. Camley, B. Hillebrands, G. Güntherodt, Phys. Rev. B **47**, 5072 (1993).

[2] U.-H. Hansen, M. Gatzen, V.E. Demidov, S.O. Demokritov, Phys. Rev. Lett. **99** 127204 (2007).

[3] V.E. Demidov, U.-H. Hansen, S.O. Demokritov, Phys. Rev. B **78** 054410 (2008).

[4] D.R. Birt, B. O'Gorman, M. Tsoi, X. Li, V.E. Demidov, S.O. Demokritov, Appl. Phys. Lett. **95**, 112510 (2009).

[5] M.P. Kostylev, A.A. Serga, T. Schneider, T. Neumann, B. Leven, B. Hillebrands, R.L. Stamps, Phys. Rev. B **76**, 184419 (2007).

[6] S.O. Demokritov, A.A. Serga, A. Andre, V.E. Demidov, M.P. Kostylev, B. Hillebrands, A.N. Slavin, Phys. Rev. Lett. **93**, 047201 (2004).

[7] T. Neumann, A.A. Serga, B. Hillebrands, Appl. Phys. Lett. **93** 252501 (2008).

[8] J. Fassbender, J. von Borany, A. Muecklich, K. Potzger, W. Moller, J. McCord, L. Schuktz, R. Mattheis, Phys. Rev. B **73**, 184410 (2006).

[9] J. Fassbender, J. McCord, Appl. Phys. Lett. **88**, 252501 (2006).

[10] R.W. Damon, J.R. Eshbach, J. Phys. Chem. Solids **19**, 308 (1961).

[11] M.P. Kostylev, A.A. Serga, T. Schneider, B. Leven, B. Hillebrands, Appl. Phys. Lett. **87**, 153501 (2005).

[12] T. Schneider, A.A. Serga, T. Neumann, B. Hillebrands, M.P. Kostylev, Phys. Rev. B **77**, 214411 (2008).

[13] A.A. Serga, T. Schneider, B. Hillebrands, S.O. Demokritov, M.P. Kostylev, Appl. Phys. Lett. **89** 063506 (2006).

[14] G. Gubbiotti, S. Tacchi, G. Carlotti, P. Vavassori, N. Singh, S. Goolaup, A.O. Adeyeye, A. Stashkevich, M. Kostylev, Phys. Rev. B **72**, 224413 (2005).

[15] Z.K. Wang, V.L. Zhang, H.S. Lim, S.C. Ng, M.H. Kuok, S. Jain, A.O. Adeyeye, Appl. Phys. Lett. **94**, 083112 (2009).

[16] N.I. Polushkin, S.A. Michalski, L. Yue, R.D. Kirby, Phys. Rev. Lett. **97**, 256401 (2006).

[17] M.P. Kostylev, N.A. Sergeeva, in G. Gubbiotti (Ed.), *Magnetic properties of laterally confined nanometric structures*, Transworld Research Network, Kerala, India (2006).

[18] M. Kostylev, P. Schrader, R.L. Stamps, G. Gubbiotti, G. Carlotti, A.O. Adeyeye, S. Goolaup, N. Singh, Appl. Phys. Lett. **92**, 132504 (2008).

[19] C. Bayer, J. Jorzick, S.O. Demokritov, A.N. Slavin, K.Y. Guslienko, D.V. Berkov, N.L. Gorn, M.P. Kostylev, B. Hillebrands, in B. Hillebrands, K. Ounadjela (Eds.), *Topics in Applied Physics: Spin dynamics in confined magnetic structures III*, Springer, Berlin (2006).

[20] M.P. Kostylev, G. Gubbiotti, J.-G. Hu, G. Carlotti, T. Ono, R.L. Stamps, Phys. Rev. B **76**, 054422 (2007).

[21] K.Yu. Guslienko, S.O. Demokritov, B. Hillebrands, A.N. Slavin, Phys. Rev. B **66**, 132402 (2002).

[22] A.V. Chumak, A.A. Serga, B. Hillebrands, M.P. Kostylev, Appl. Phys. Lett. **93**, 022508 (2008).

[23] T. Schneider, A.A. Serga, A.V. Chumak, B. Hillebrands, R.L. Stamps, M.P. Kostylev, Europhys. Lett. **90**, 27003 (2010).

4.11 All-linear time reversal and frequency inversion by a dynamic magnonic crystal

A.V. Chumak, A.A. Serga, and B. Hillebrands[1]

Mathematically, conversion between a time-dependent process $f(t)$ and a time-reversed version of this process $f(-t)$ is a matter of trivial substitution; but the physical realization of such a transformation has profound significance. Not only are time-reversal mechanisms immensely powerful technological tools, but their existence challenges our understanding of such fundamental notions as thermodynamic irreversibility, causality, and the perceived "arrow" of time.

The time-reversal mechanism proposed in this report is a linear, nonstationary coupling process, entirely distinct from known nonlinear mechanisms of time reversal (for example optical four-wave mixing [1, 2]). This mechanism – which is a principle of universal application to waves of any nature – is demonstrated with spin waves in a dynamic magnonic crystal (DMC) [3, 4]. Magnon systems have long been established as excellent environments for the observation of general wave and quasi-particle phenomena [5].

The experimental one-dimensional DMC comprises a planar metallic meander structure [3] with lattice constant a, positioned close to the surface of an Yttrium Iron Garnet (YIG) ferrimagnetic thin-film spin-wave waveguide (Fig. 1a). A current pulse $I_0(t)$ applied to the meander structure creates a periodic Oersted field of amplitude $\mu_0 \Delta H \sim 1\,\text{mT}$ which spatially modulates the waveguide's static magnetic bias field $\mu_0 H_0 = 180\,\text{mT}$. Two microstrip antennae are positioned approximately 1 mm from each end of the DMC: an input antenna to launch a spin-wave signal $A_\text{S}(t)$ and to

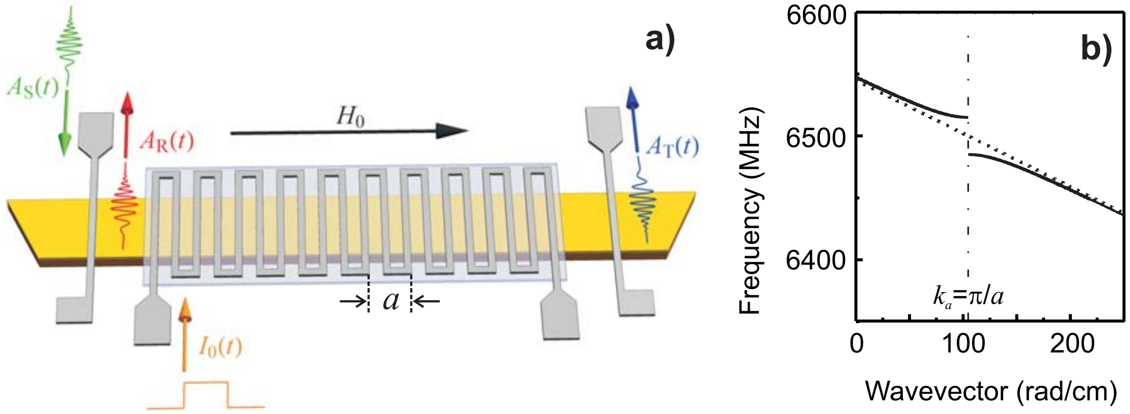

Fig. 1: Experimental dynamic magnonic crystal system. a) The dynamic magnonic crystal (DMC) comprises a planar current-carrying meander structure with 20 periods of lattice constant $a = 300\,\mu\text{m}$ (10 shown) positioned close to the surface of an YIG thin-film spin-wave waveguide (thickness $5\,\mu\text{m}$). Two spin-wave antennae are arranged on the surface of the film 8 mm apart: one to launch a spin-wave signal, amplitude $A_\text{S}(t)$ and to detect the signal $A_\text{R}(t)$ reflected by the DMC, and a second to detect the signal $A_\text{T}(t)$ transmitted through it. b) Theoretical spin-wave dispersion relationship for the waveguide with no applied current (dotted) and with a static current of 1 A in the meander structure (solid curve). The application of the current leads to the formation of a band gap of width approximately $\Delta f_a \approx 30\,\text{MHz}$, centred on $f_a = 6500\,\text{MHz}$.

---

[1] In collaboration with V.S. Tiberkevich, A.N. Slavin Department of Physics, Oakland University, Rochester, USA; A.D. Karenowska, J.F. Gregg Department of Condensed Matter Physics, Clarendon Laboratory, University of Oxford, UK.

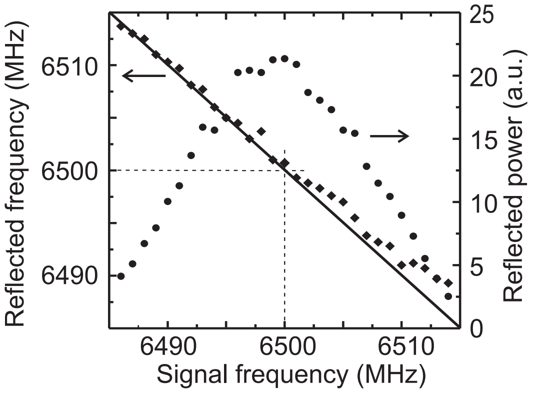

Fig. 2: Experimental demonstration of frequency inversion by the dynamic magnonic crystal. When the carrier frequency of the incident spin-wave signal packet is detuned from the resonant value of 6500 MHz, the frequency of the reflected signal is shifted (left ordinate axis, diamonds). The solid line is the theoretical curve of Eq. (1). The efficiency of the reflection process (right ordinate axis, circles) is maximum at the resonance condition and decreases symmetrically with detuning.

detect the signal $A_{\mathrm{R}}(t)$ reflected by the DMC, and an output antenna to receive the signal $A_{\mathrm{T}}(t)$ transmitted through it.

The in-plane, on-axis orientation of the static magnetic bias field (Fig. 1a) corresponds to the propagation of backward volume magnetostatic spin waves (BVMSW) [5]. BVMSW feature a dispersion curve $f(k)$ with a negative slope as indicated in Fig. 1b, but it is stressed that this practical detail has no bearing on the entirely general result we describe. BVMSW were used in the experimental investigations as they are reciprocal waves and are readily excited and received by microstrip antennae.

In the absence of an applied current, the meander structure has negligible influence on spin-wave transmission, the application of a static DMC current of 1 A results in the formation of a magnonic band-gap of width approximately $f_a = 30\,\mathrm{MHz}$, centred on the characteristic Bragg resonance frequency $f_a = 6500\,\mathrm{MHz}$ which corresponds to the Bragg wavevector $k_a = \pi/a = 105\,\mathrm{cm}^{-1}$ (see [3]). This band gap appears as a discontinuity in the dispersion relationship (Fig. 1b).

Time reversal is equivalent – in the frequency domain – to an inversion of a waveform's spectrum about a certain reference frequency [6]. In our experiments, we were able to successfully demonstrate both frequency inversion of quasi-monochromatic signals and time reversal of complex waveforms [4].

Frequency inversion was studied in the following manner. With the DMC off, a spin-wave signal packet of carrier frequency f_{S}, duration 200 ns (bandwidth 5 MHz), and amplitude $A_{\mathrm{S}}(t)$ was launched into the waveguide. After a delay, a rectangular current pulse $I_0(t)$ of duration 25 ns was supplied to the DMC meander structure (Fig. 1a). Timing parameters were chosen so that the packet was contained within the magnonic crystal at the time of DMC activation, and its spectrum lay entirely within the band gap. The carrier frequency f_{S} of the packet was varied over a range $\pm 15\,\mathrm{MHz}$ about the resonance frequency $f_a = 6500\,\mathrm{MHz}$, whilst its power was maintained at $< 1\,\mathrm{mW}$ (two orders of magnitude below that known to be required to observe the effects of nonlinear terms in YIG's microwave susceptibility). The spectrum of the reflected wave packet $A_{\mathrm{R}}(t)$ was captured.

The spatially periodic magnetic field created in the DMC by the current pulse $I_0(t)$ leads to a strong coupling between (initially independent) spin waves having wavevectors k and $k' = k \pm 2k_a$. This coupling is especially efficient for $k \approx k_a$, $k' = k - 2k_a \approx -k_a$ when the frequencies of the coupled waves are close to each other, and lie within the band-gap of the DMC. By analogy with a system of two coupled oscillators (see for example [7]), the DMC-induced coupling between two waves leads to a transfer of energy between the initially excited signal wave of wavevector k_{S} and a reflected wave of wavevector $k_{\mathrm{R}} = k_{\mathrm{S}} - 2k_a$.

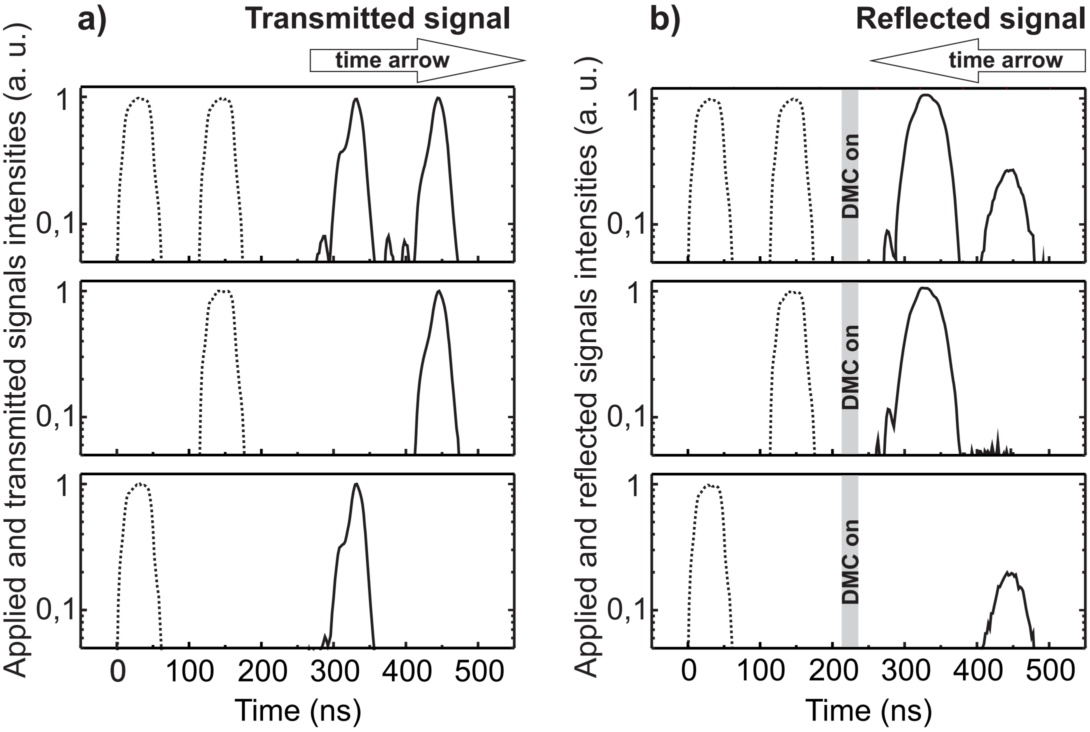

Fig. 3: Experimental demonstration of time reversal by the dynamic magnonic crystal. A train of two pulses (70 ns wide and spacing 40 ns) with carrier frequency $f_S = 6500\,\mathrm{MHz}$ was applied to the input antenna. The applied signals shown (dotted line) are the envelopes of those supplied by the microwave generator. a) The transmitted spin-wave signals with no current applied to the DMC appear after a delay of approximately 300 ns (solid line, upper frame). When the first of the two input pulses is switched off, the first transmitted pulse is absent (middle frame) and the same is true for the second pulse (lower frame). b) The reflected spin wave signals obtained when the DMC has been briefly activated (shaded area shows the activation interval). In the case that two pulses are applied, two corresponding reflected pulses are observed (upper frame, right ordinate axis). When the first of the two pulses is switched off, the second reflected pulse is absent (middle frame), and vice versa (lower frame), confirming time reversal.

After a certain time ($\sim 25\,\mathrm{ns}$ under the conditions of our experiment), a substantial fraction of the energy is transferred from the signal k_S to the reflected k_R wave. If the current pulse is switched off at this time, removing the coupling, the two waves become once again independent, and the reflected wave propagates back towards the input antenna.

The reflected frequency $f_R = f(k_R)$ can be determined using a linear Taylor expansion of the dispersion relationship $f(k)$ about $k_S \approx k_a$. The incident signal frequency is given by $f_S = f(k_S) \approx f_a + v(k_S - k_a)/(2\pi)$ where $f_a = f(k_a)$ is the centre frequency of the DMC band gap and $v = 2\pi \cdot df(k_a)/dk_a$ is the group velocity. Using obtained before equation for the k_R and the inversion symmetry of the dispersion curve, the frequency of the reflected wave can be written as $f_R \approx f_a - v(k_S - k_a)/(2\pi)$. Thus, the frequencies of the counter-propagating incident and reflected waves are connected by the simple relation

$$f_R = 2f_a - f_S, \tag{1}$$

i.e. they are inverted with respect to the centre of the band-gap f_a.

Experimental demonstration of frequency inversion in the DMC system is shown in Fig. 2. The efficiency of the process is maximal in the case of $f_S = f_a$, and decreases symmetrically with positive and negative detuning (Fig. 2a).

The frequency inversion described by Eq. (1) directly implies reversal of the time profile of the signal packet [6]. This can be seen by writing the time profile of the incident waveform as a Fourier series $A_\mathrm{S} \sim \sum_{\Delta f} \exp(i2\pi\Delta f t)$, where $\Delta f = f - f_a$ is the frequency detuning of a given spectral component. In the process of frequency inversion, the sign of the detuning Δf inverts, and thus the dynamically reflected signal has a reversed time profile $A_\mathrm{R} \sim \sum_{\Delta f} \exp(-i2\pi\Delta f t) \sim A_\mathrm{S}(-t)$.

In order to observe the effect of time reversal experimentally, a train of two input pulses with carrier frequency $f_\mathrm{S} = f_a = 6500\,\mathrm{MHz}$, 70 ns duration and spacing 40 ns was employed. Figure 3a shows – for reference – time profiles of input and transmitted signals detected in the absence of DMC activation. Here, if the first pulse is switched off (middle frame) the first pulse in the transmitted signal disappears. Similarly, the switching off of the second pulse (lower frame) leads to the disappearance of the second transmitted envelope. The signal reflected by the DMC is shown in Fig. 3b. When both pulses are applied, two corresponding reflected pulses are observed (upper frame). Here however, unlike in the case of the transmitted signal, the switching off of the first pulse results in the disappearance of the second reflected signal (middle frame). The corresponding situation when the second pulse is absent – the disappearance of the first reflected signal – is indicated in the lower frame. This behavior provides direct evidence of time reversal.

The work reported here demonstrates that dynamic phenomena in artificial crystals can provide a substitute for the nonlinear mechanisms traditionally used to perform complex spectral transformations such as time reversal. Since the overwhelming majority of real materials exhibit only weak nonlinearity, we suggest that this capability may provide an enabling route toward the development of low-power signal and information processing systems with complex functionalities.

Financial support by the Deutsche Forschungsgemeinschaft (DFG, SE 1771/1-1) is gratefully acknowledged.

References

[1] Ya.B. Zel'dovich, N.F. Pilipetsky, V.V. Shkunov, Principles of Phase Conjugation (Springer-Verlag, 1985).

[2] E.G. Sauter, Nonlinear Optics (Wiley, 1996).

[3] A.V. Chumak, T. Neumann, A.A. Serga, B. Hillebrands, M.P. Kostylev, J. Phys. D **42**, 205005 (2009).

[4] A.V. Chumak, V.S. Tiberkevich, A.D. Karenowska, A.A. Serga, J.F. Gregg, A.N. Slavin, B. Hillebrands, Nature Comm., *in press* (2010).

[5] A.A. Serga, A.V. Chumak, B. Hillebrands, J. Phys. D **43**, 264002 (2010).

[6] M.F. Yanik, S. Fan, Phys. Rev. Lett. **93**, 173903 (2004).

[7] I.G. Main, Vibrations and Waves in Physics, 2nd Edition, Ch. 8 (Cambridge University Press, 1984).

D. Dynamics in Nanostructures and Domain Walls

Magnetization dynamics in magnetic nanostructures exhibits specific features caused by the strong influence of the surface and demagnetization effects. The manipulation of spin currents in nanostructures has potential applications in computing devices and magnetic memory. It is determined by the possibility to use not only the charge of the electron as done in conventional electronics but also its spin orientation for information processing. For the successful utilization of spin information, e.g. for spin electronics, difficulties like the short distance over which an electron retains memory of its spin direction have to be overcome. This propagation distance through a material is referred to as spin diffusion length. The problem of the short spin diffusion length can be solved by combining standard spintronic approaches with spin-wave dynamics resulting in magnon spintronics (see Section B.). It is known that spin waves in ferromagnetic materials can propagate over distances many orders of magnitude larger than the spin-diffusion length. Spin waves, in this case, can serve as an information carrier for spintronic devices. Thus, detailed investigations of spin-wave propagation in magnetic stripes of submicron size are required. The phase-resolved Brillouin light scattering (BLS) microscopy technique, which was developed in our group, opens new possibilities for the research on linear and nonlinear spin-wave dynamics in nanostructures. The BLS investigations of spin dynamics in nanostructures is supported by micromagnetic simulations.

The investigation of the spin-wave interaction with locally pinned domain walls in nanostructures is also a focus of our interest. The ability to move domain walls by spin-waves can be used to fabricate memory devices, where domain walls serve as a carrier of information (see Annual Report 2008 and APL 94, 112502 (2009), APL 94, 223510 (2009)).

In this Annual Report results on the study of static and dynamic phenomena in nanostructures are presented. Report 4.12 discusses the influence of vortex-domain walls on the spin-wave spectrum in magnetic stripes studied by means of MFM as well as BLS microscopy. Report 4.13 is devoted to the demonstration of interference of spin waves in magnetic microstripes using phase-resolved BLS microscopy. The optical detection of spin transport in the high frequency regime in non-magnetic metals is addressed in Report 4.14. Report 4.15 is focused on spin-wave propagation in strongly anisotropic iron monocrystalline waveguides which offers a promising solution to drastically reduce the required high bias fields necessary for spin waves carrying of spin currents. Finally, Report 4.16 discusses micromagnetic simulations of linear and nonlinear spin-wave propagation in nano-contact spin-valves.

D. Dynamik in Nanostrukturen und Domänenwänden

Die Magnetisierungsdynamik in magnetischen Nanostrukturen zeigt durch den Einfluss der Oberfläche und des Entmagnetisierungsfelds ein spezifisches Verhalten. Die Manipulation von Spinströmen in Nanostrukturen hat Anwendungspotenzial in effizienteren Computerchips und magnetischen Speichern, da in diesem Fall nicht nur die Ladung des Elektrons wie in der konventionellen Elektronik, sondern auch die Ausrichtung seines Spins zur Informationsverarbeitung verwendet werden kann. Um die Spininformation zu nutzen und sogenannte Spinelektronik- (oder Spintronik-) Bauteile konstruieren zu können, müssen verschiedene Probleme gelöst werden. Beispielhaft sei hier die kurze Ausbreitungsdistanz genannt, über die Elektronen ihren Spinzustand behalten (Spin-Diffusionslänge). Dieses Problem kann gelöst werden, indem man den klassischen Spintronikansatz mit Spinwellen kombiniert. Es ist bekannt, dass sich Spinwellen in ferromagentischen Materialien über Entfernungen ausbreiten können, die mehrere Größenordnungen über der Spin-Diffusionslänge liegen. Spinwellen können damit als Informationsträger für spintronische Bauteile dienen. Daher ist die detaillierte Untersuchung der Spinwellenausbreitung im Mikrometer-Maßstab in magnetischen Streifen nötig. Die phasenaufgelöste Brillouin-Lichtstreumikroskopie (BLS-Mikroskopie) die in unserer Arbeitsgruppe entwickelt wurde, eröffnet neue Möglichkeiten zur Untersuchung der linearen und nichtlinearen Spinwellendynamik in Nanostrukturen. Ein weiterer Schwerpunkt unseres Interesses ist die Untersuchung der Wechselwirkung von Spinwellen mit lokal verankerten Domänenwänden in Nanostrukturen. Die Möglichkeit, Domänenwände mit Spinwellen zu bewegen, kann zum Aufbau von Speicherbauteilen verwendet werden, bei denen die Information von Domänenwänden getragen wird (siehe auch Jahresbericht 2008, APL 945, 112502 (2009) und APL 94, 223510 (2009)).

In diesem Jahresbericht präsentieren wir Untersuchungen statischer und dynamischer Phänomene in Nanostrukturen. Bericht 4.12 zeigt die Ergebnisse der Charakterisierung des Einflusses von Vortex-Domänenwänden auf das Spinwellenspektrum in magnetischen Streifen mittels einer Kombination von MFM und BLS-Mikroskopie. In Bericht 4.13 werden Spinwelleninterferenzeffekte in magnetischen Mikrostreifen demonstriert, die mittels phasenaufgelöster BLS-Mikroskopie untersucht wurden. Die optische Detektion von Spintransport im Hochfrequenzbereich in nichtmagnetischen Metallen wird in Bericht 4.14 vorgestellt. Bericht 4.15 behandelt Spinwellenpropagation in stark anisotropen monokristallinen Eisenwellenleitern, die eine vielversprechende Reduktion der sonst für effektiven Spinstrom getragen durch Spinwellen notwendigen hohen Bias-Felder ermöglichen. Abschließend werden in Bericht 4.16 die Ergebnisse mikromagnetischer Simulationen linearer und nichtlinearer Spinnwellenpropagation in Nanokontakt-Spinventil-Strukturen diskutiert.

4.12 Influence of Vortex-domain walls on the spin-wave spectrum in magnetic stripes

P. Pirro, T. Brächer, B. Obry, K. Vogt, H. Schultheiss, P. Clausen, P.A. Beck, B. Leven, and B. Hillebrands[1]

Spin-wave excitation and propagation in small magnetic structures has been investigated experimentally [1–3] and by means of numerical studies [4, 5] during the last years. One aspect of the investigation of spin waves was their possible application in a new kind of logic devices [6] which would use the phase and amplitude of the waves as information carrier. On the other hand, also magnetic domain walls have been proposed as basic elements of data storage and logic applications [7]. This shows that it is really promising to work at the intersection of both fields, combining spin waves and domain walls. Consequently, several theoretical [8–10] as well as numerical studies [11–13] have treated this issue.

Here, we report on the experimental investigation of magnetic vortex domain walls (VDW) in micron-sized $Ni_{81}Fe_{19}$-stripes and their influence on the spin-wave spectrum. Two experimental techniques have been used to investigate both static and dynamic properties of this magnetic system: magnetic force microscopy (MFM) to ensure a reproducible nucleation and annihilation of the VDW as well as Brillouin light scattering microscopy (BLS) to characterize the magnetization dynamics.

The employed $Ni_{81}Fe_{19}$ thin film structures with a thickness of 40 nm and lateral dimensions in the micron range are produced with electron beam lithography, molecular beam epitaxy and lift-off technique on a thermally oxidized Si substrate and are capped with 2 nm of Al to prevent oxidation. They consist of stripes (width $w = 1.1 - 1.5\,\mu m$) with a 90° curve and a rectangular domain wall nucleation pad at one end. After saturation with a negative field of $B_{ext} = -40\,mT$ applied along

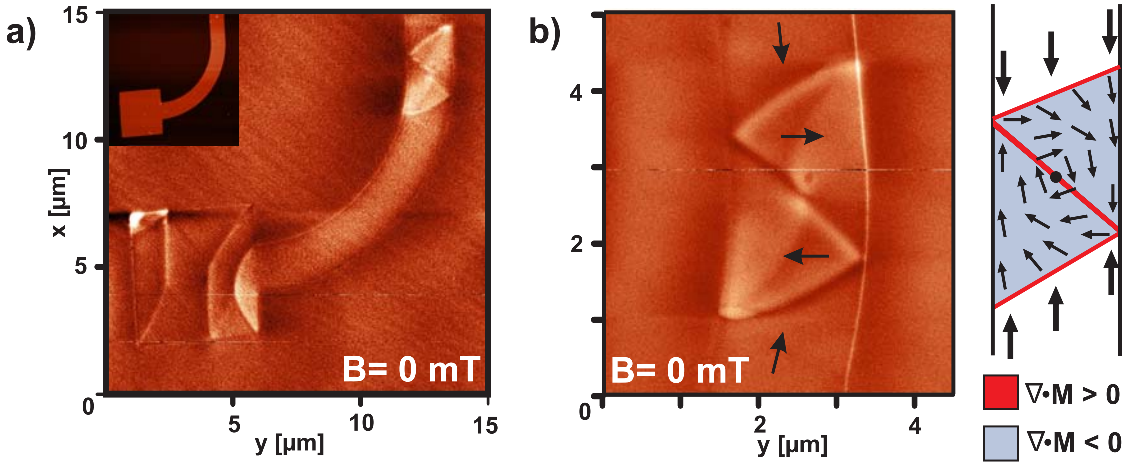

Fig. 1: a) MFM scan (at $B_{ext} = 0\,mT$) of the described $Ni_{81}Fe_{19}$-structure after the nucleation of a VDW which is composed of two characteristic triangular shaped regions. After the nucleation procedure described in the text also the nucleation pad is found to be in a complex multi-domain state. The inset shows the topography of the sample for comparison (AFM scan). b) MFM scan of the VDW together with a scheme of the magnetization and the polarity of the magnetic charges $\rho_M = -\nabla \cdot M$ which are detected by this method. The diagonally running 180° Néel wall can be readily identified.

---

[1] In collaboration with S. Wolff, B. Lägel, Nano+Bio Center, Technische Universität Kaiserslautern, Germany.

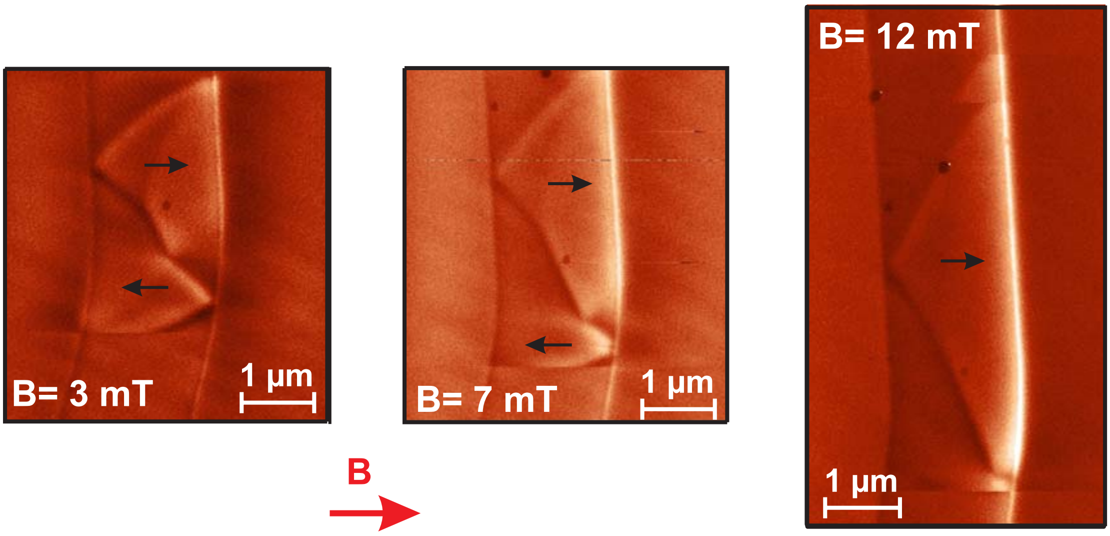

Fig. 2: MFM scan of a VDW at increasing external fields. The triangular shaped region which has its net magnetization along the external field (upper triangle) grows while the lower one is compressed. At $B_{\text{ext}} = 12\,\text{mT}$, this region is not longer stable and becomes influenced by the MFM-tip. A further increase of the field leads to the annihilation of the VDW.

the the y-axis, a VDW can be nucleated by applying a small positive field pulse along the same axis and annihilated with the inverse field. The reproducibility of this process as well as the detailed structure of the wall were checked with MFM (see Fig. 1). As these domain structures are very unstable in soft-magnetic $Ni_{81}Fe_{19}$, special low-coercivity tips must be used to obtain undistorted MFM scans. As described in [14], we see that this type of magnetic domain wall is composed of two triangular regions with opposite net magnetic moment separated by a Néel wall extending diagonally across the stripe and a vortex core at its center. If the domain wall is subjected to a small external field B_{ext}, it starts to deform and at $B_{\text{ext}} \approx 12\,\text{mT}$ it annihilates completely (see Fig. 2). This shows that the following experiments addressing the spin-wave spectrum cannot be performed as usual with an applied external field, but must be achieved at remanence.

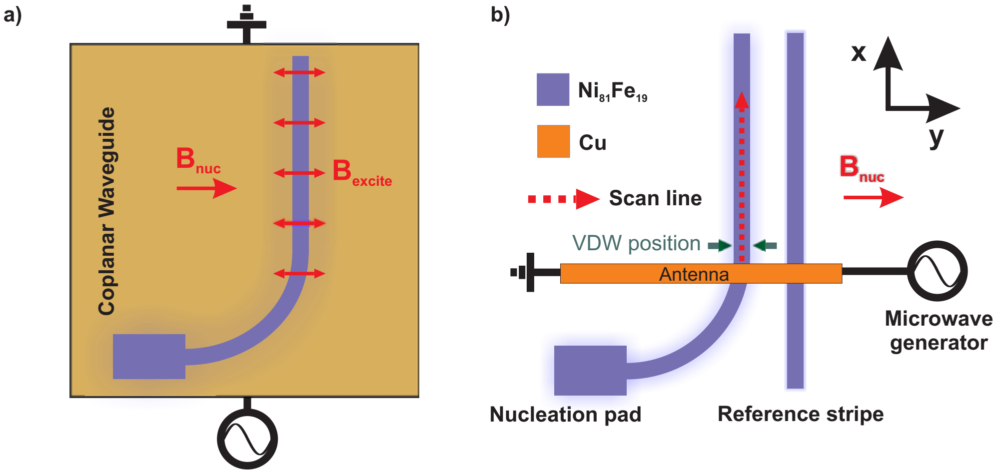

Fig. 3: a) Sample type A: the $Ni_{81}Fe_{19}$structure is patterned on top of a coplanar waveguide (CPW) (Au, width 50 µm, thickness 200 nm) which provides a homogeneous excitation field along the y-axis. b) Sample type B: the spin waves are excited locally by an antenna (width 2 µm, thickness 500 nm). As no VDW is nucleated in the straight stripe (in the considered field range) it can be used as a reference to assure that the changes in the spin-wave spectrum are really due to the nucleation of a VDW.

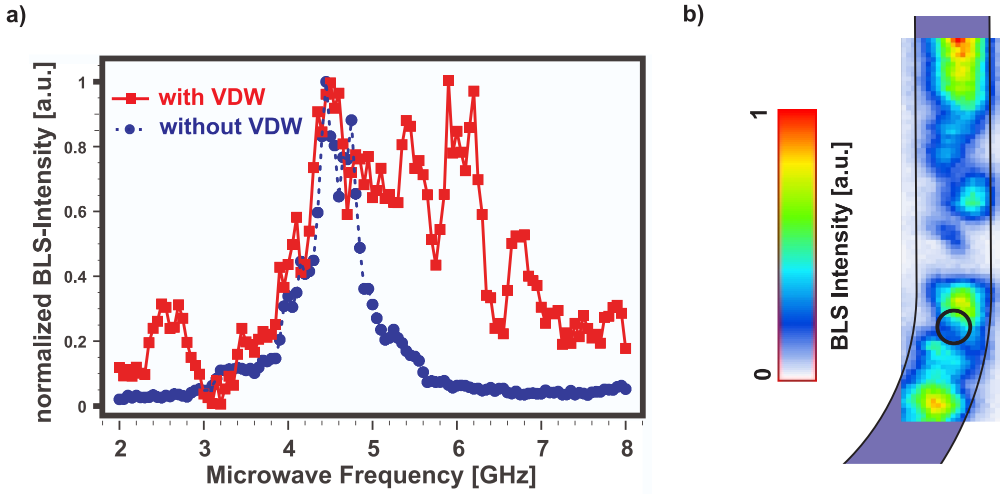

Fig. 4: a) Separately normalized BLS intensities with and without VDW as a function of the applied microwave frequency measured at the point indicated in b). The absolute values (not shown) of the intensity without the domain wall are seven times higher compared to the case when the domain wall is present ($B_{\mathrm{ext}} = 0\,\mathrm{mT}$ during scan). b) Space resolved BLS intensity at a frequency of 5.1 GHz measured on a $\mathrm{Ni}_{81}\mathrm{Fe}_{19}$-waveguide after nucleation of a VDW. The spin waves are excited continuously with a homogenous pumping field of the same frequency provided by the CPW below the magnetic structure ($B_{\mathrm{ext}} = 0\,\mathrm{mT}$, circle indicates the scanning position of a)).

After characterizing the static properties of the system, the influence on the spin-wave spectrum is investigated with two types of samples which differ only in the way the spin waves are excited. Type A (see Fig. 3a) consists of a coplanar waveguide (CPW) where the magnetic structures are placed on top of the central conductor, whereas in type B, the short-cut of a CPW is used as an antenna (see Fig. 3b). In both cases, the Oersted field of a microwave current driven by an external signal generator is used to excite the spin waves.

Figure 4a shows the influence of a VDW on the spin wave spectrum in a $\mathrm{Ni}_{81}\mathrm{Fe}_{19}$-waveguide for the sample type A: before the nucleation (blue dots), the spectrum exhibits one single peak which can be attributed to the first transversal spin-wave mode via the dispersion relation for thin magnetic films given in [15]. After the nucleation (red rectangles), this peak is broadened, additional peaks appear and the absolute intensity is drastically reduced (not shown owing to separate normalization) due to the inhomogeneous magnetization and effective fields. The spatial inhomogeneity of the spin-wave modes is also clearly visible in Fig. 4b, where the space resolved BLS intensity for one particular excitation frequency is shown.

The case of a local excitation of spin waves (sample type B) is shown in Fig. 5 where we first investigate the spin-wave spectrum in remanence without a domain wall. The frequency scan of the excitation field reveals two resonances in the considered region (see Fig. 5a) which can be attributed to the first and the third transversal mode via their mode profiles measured across the width of the stripe shown in Fig. 5b. Calculations of the dispersion relation [15] for the case of a stripe which is homogeneously magnetized along its long axis lead to the same results which further justifies our allocation to the first and third transversal mode.[2] The BLS intensity in the middle of the stripe along its long axis is measured before and after the nucleation of the VDW (Fig. 5c) and normalized to the maximum of both scans (thus in this case, the shown absolute intensity values can be compared). The spin-wave intensity at the edge of the antenna ($x = 0\,\mu\mathrm{m}$)

---

[2] With parameters: $M_s = 7.3 \cdot 10^5\,\mathrm{A/m}$, $w_{\mathrm{eff}} = 2\,\mu\mathrm{m}$, $A = 1.6 \cdot 10^{-11}\,\mathrm{J/m}$, a wavevector $k_x \approx 1.5\,\mu\mathrm{m}^{-1}$ has been calculated which can be efficiently excited with the used antenna.

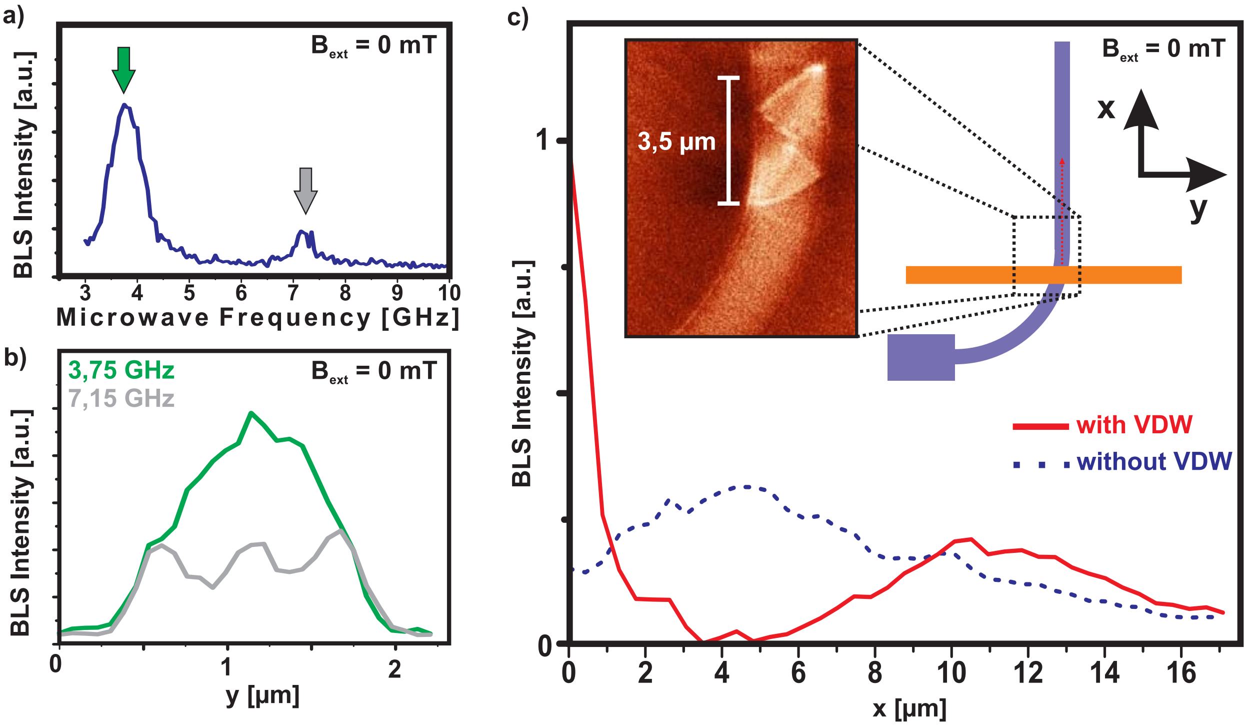

Fig. 5: a) Frequency scan of the magnetic excitation field revealing two resonances. b) Mode profiles (BLS intensity across the width of the stripe) of the two modes marked in a), proving the excitation of the first and third spin wave width mode. c) BLS intensity measured along the $Ni_{81}Fe_{19}$-waveguide before (dotted line) and after (solid line) the nucleation of a VDW.

is drastically increased when a domain wall is nucleated (in contrast to the general behavior in the case of the homogeneous excitation) but it drops below the level of the reference measurement over a short distance. This trend can be explained by two phenomena: first of all, the domain wall can reflect the spin waves leading to a standing wave with higher amplitude. Second, due to the inhomogeneous magnetization inside the wall, the torque which the field of the antenna can exert on the magnetic moments can be increased[3].

In summary, we have examined the reproducible nucleation and annihilation of magnetic VDWs in $Ni_{81}Fe_{19}$ microstripes using magnetic force microscopy and Brillouin light scattering. Before the nucleation of the wall, the spectrum can be explained by the common theory for spin waves in thin films. When a wall is present, the spectrum becomes broader and strongly position dependent due to the inhomogeneous magnetization in the vicinity of the wall. In the case of a homogeneous excitation field, the domain wall reduces the spin-wave intensity everywhere, whereas it can increase the intensity for particular positions in the case of a local confined excitation.

Financial support by EU (SPINSWITCH, MRTN-CT-2006-035327), Deutsche Forschungsgemeinschaft (DFG, GRK 792) and the Carl-Zeiss-Stiftung is gratefully acknowledged.

References

[1] K. Vogt, H. Schultheiss, S.J. Hermsdoerfer, P. Pirro, A.A. Serga B. Hillebrands, Appl. Phys. Lett. **95**, 182508 (2009).
[2] V.E. Demidov, S. Urazhdin, S.O. Demokritov, Appl. Phys. Lett. **95**, 262509 (2009).

---

[3] As can be seen in Fig. 2, parts of the magnetization point along the *y*-direction, thus also the field component pointing along the stripe length can contribute to the excitation.

[3] K. Perzlmaier, G. Woltersdorf, C.H. Back, Phys. Rev. B **77**, 054425 (2008).
[4] K-S. Lee, S.-K. Kim, J. Appl. Phys. **104**, 053909 (2008).
[5] S. Choi, K-S. Lee, S-K. Kim, Appl. Phys. Lett. **89**, 062501 (2006).
[6] A. Khitun, M. Bao, K.L. Wang, IEEE Trans. Magn. **44** (9), 2141-2152 (2008).
[7] D.A. Allwood, G. Xiong, R.P. Cowburn, Appl. Phys. Lett. **89**, 102504 (2006).
[8] C. Bayer, H. Schultheiss, B. Hillebrands, R.L. Stamps, IEEE Trans. Magn. **41** (10), 3094-3096 (2005).
[9] Y. Le Maho, J.V. Kim, G. Tatara, Phys. Rev. B **79** (17), 174404 (2009).
[10] S. Macke, D. Goll, J. Phys.: Conf. Ser. **200**, 042015 (2010).
[11] S.J. Hermsdoerfer, H. Schultheiss, C. Rausch, S. Schäfer, B. Leven, S.-K. Kim, B. Hillebrands, Appl. Phys. Lett. **94**, 223510 (2009).
[12] R. Hertel, W. Wulfhekel, J. Kirschner, Phys. Rev. Lett. **93**, 257202 (2004).
[13] D.-S. Han, S-K. Kim, J.-Y. Lee, S.J. Hermsdoerfer, H. Schultheiss, B. Leven, B. Hillebrands, Appl. Phys. Lett. **94**, 112502 (2009).
[14] R. McMichael, M.J. Donahue, IEEE Trans. Magn. **33** (5), 4167-4169 (1997).
[15] B.A. Kalinikos, A.N. Slavin, J. Phys. C: Solid State Phys. **19**, 7013 (1986).

4.13 Interference of spin waves in magnetic microstripes

T. Brächer, P. Pirro, B. Obry, H. Schultheiss, K. Vogt, P.A. Beck, B. Leven, and B. Hillebrands[1]

The investigation of propagating spin waves in micron-sized metallic ferromagnetic structures has been the subject of theoretical and experimental studies [1–3] due to their potential application in microwave signal processing and spin-wave logic devices [6, 10], but also due to the possibility to address basic physical phenomena related to the spin transfer torque [11, 12] and the interaction of spin waves with topological objects like domain walls [13–15, 19]. In all experimental studies the understanding of the excitation and propagation of spin waves is of vital importance, especially for the exploration of next-generation logic circuits which would use the phase and amplitude of the spin waves as an information carrier [6, 7, 10]. As the processing of data in these devices is performed by the interference of the different input waves, the ability of the spin waves to form stable and predictable interference patterns is of crucial importance. Consequently, several numerical studies [4, 8] were dedicated to the interference of spin waves in microstructures but the experimental proofs are still limited (see e.g. [21]).

In this report we present the experimental observation of interfering spin waves in micron-sized waveguides of $Ni_{81}Fe_{19}$ (see Fig. 1a) for detailed sample design). We find that the coherence length is at least as long as the achieved propagation distance of the locally excited spin waves. In addition, we show that the complex spin-wave intensity and phase patterns that are formed can be predicted quantitatively and that we can confirm the theoretical dispersion relation for the spin waves.

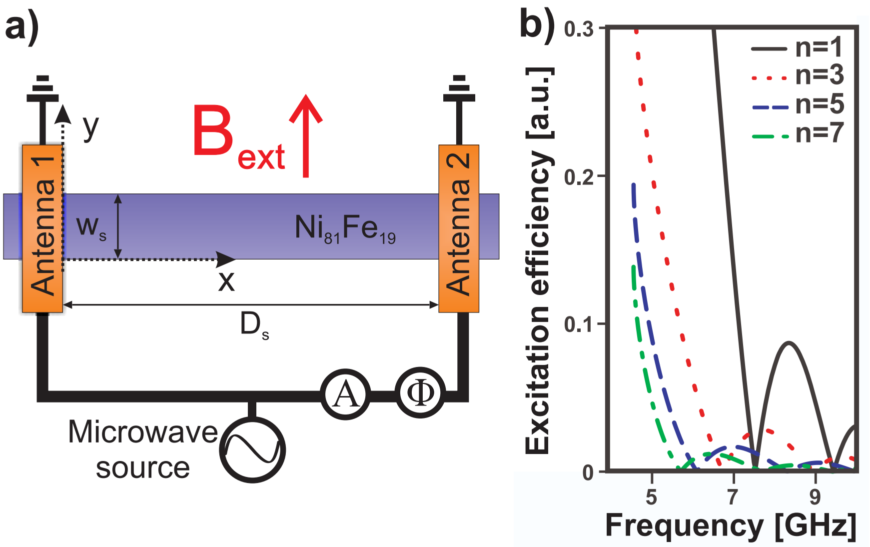

Fig. 1: a) Schematic sample design: a $Ni_{81}Fe_{19}$ microstripe (width $w_s = 4.1\,\mu m$, thickness $t_s = 40\,nm$) is placed between two microwave antennas (width $w_a = 2.2\,\mu m$) which are connected to the same microwave source (∼). A phase shifter (Φ) and an attenuator (A) are used to shift the relative phase and the amplitude between the two antennas respectively. b) Calculated excitation efficiencies for the width modes $n = 1, 3, 5, 7$ (parameter see Fig. 3) for the particular stripe and antennas shown in a) and an external magnetic field of 30 mT. Due to symmetry reasons, the excitation efficiency for the even modes vanishes.

---

[1] In collaboration with S. Wolff, B. Lägel, Nano+Bio Center, Technische Universität Kaiserslautern, Germany.

The investigated $\mathrm{Ni}_{81}\mathrm{Fe}_{19}$ structures have a thickness of 40 nm, a width w_s of 4.1 µm and lengths in the range of 15 to 20 µm and are patterned using electron beam lithography and lift-off technique. On top of the $\mathrm{Ni}_{81}\mathrm{Fe}_{19}$ stripe, two antennas (Cu) are processed which are connected to the same microwave source to excite phase locked coherent spin waves at $x = 0$ and $x = \mathrm{D}_s$. These waves propagate in opposite directions towards the center of the structure and interfere. The width of the antennas is $w_a = 2.2$ µm, resulting in efficient excitation of spin waves with wavelengths in the micron range. The distance D_s between the antennas is larger than the decay length of the propagating spin waves to allow their interference over a maximum distance.

To observe the spin-wave interference experimentally, we employ Brillouin light scattering (BLS) microscopy (for details see [17]). Spin waves are excited concurrently with both antennas at a monochromatic frequency and the space resolved BLS intensity (which is proportional to the spin-wave intensity) is recorded. During our measurements we apply a magnetic field B_{ext} in the range from 30 to 40 mT perpendicular to the length of the stripe (y-direction) to align the magnetic moments along the field axis.

A typical measurement taken in the middle of the stripe along the x-axis is shown in Fig. 2. Here, the intensity maxima and minima that are expected in the case of a standing wave (formed by the two phase locked waves propagating in opposite directions) are clearly visible. To compare our results with theoretical predictions, the dispersion relations for different transversal modes[2] labeled by n are shown in Fig. 3. They are calculated according to [23][3]. Modes with even n

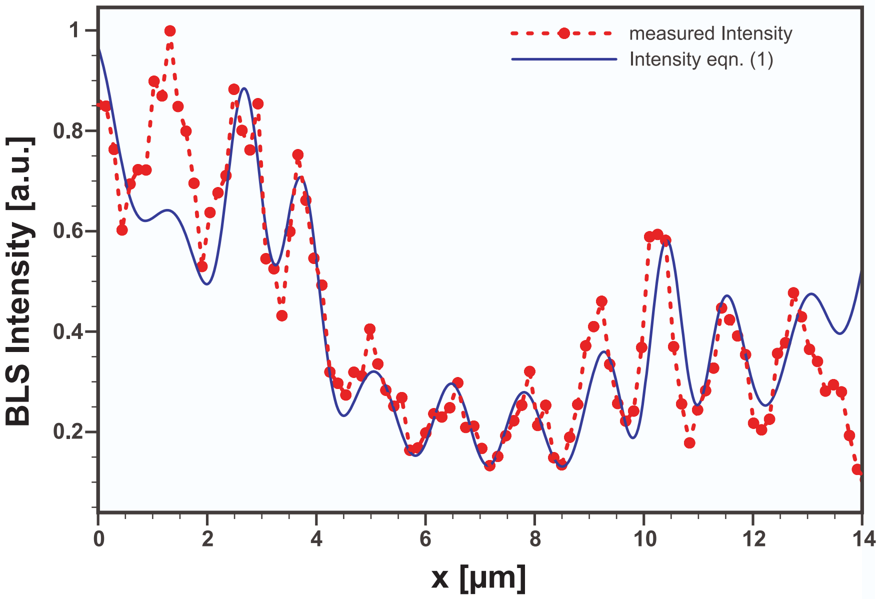

Fig. 2: Red dots : BLS intensity of interfering spin waves with a frequency $\nu = 7.13$ GHz at a field $B_{\mathrm{ext}} = 30$ mT and antenna spacing $D_s \approx 14.5$ µm. Blue dotted line: Spin-wave intensity calculated according to Eq. (1) taking into account transversal modes up to $n = 7$ (along x−axis, at $y = w_s/2$).

---

[2] Due to the confinement of the wave in y-direction, k_y is quantized: $k_y = \frac{n \cdot \pi}{w_{\mathrm{eff}}}, n \in \mathbb{N}^*$, w_{eff} is the effective quantization width of the spin wave (see [20] for details). In our case, w_{eff} was approximated by the measured width of the transverse intensity profile (≈ 3 µm for the applied magnetic fields).

[3] Material parameters used in the calculation of the spin-wave dispersion:
Saturation magnetization $M_s = 758 \cdot 10^3\,\mathrm{Am}^{-1}$
Gyromagnetic ratio $\gamma = 28\,\mathrm{GHzT}^{-1}$
Exchange constant $A = 1.6 \cdot 10^{-11}\,\mathrm{Jm}^{-1}$

cannot be excited with these antennas because the excitation field is homogenous along the y-direction and these modes have no net magnetic moment averaged across the sripe width [5]. The distances between the measured intensity maxima in Fig. 2 show a good agreement with half of the wavelength of the first spin wave mode $n = 1$ in Fig. 3. Nevertheless, to understand the spacial intensity distribution, especially effects like the increase of intensity for the maximum at $x = 10.5\,\mu\text{m}$, the interference of the spin waves must be described in more detail by taking into account higher transversal modes also.

We model the intensity of the spin waves assuming plain waves (in x-direction) with sinusoidal transverse mode profiles (in y-direction). The intensity of the formed stationary spin-wave interference pattern (averaged over one oscillation period) in between the antennas can be described by:

$$\begin{aligned} I(\nu) &= |A|^2 \\ &= \left| \sum_n \left[a_n \sin\left(\frac{n\pi}{w_{\mathrm{eff}}} y\right) e^{i(k_x^n(\nu)x+\Phi)} \right. \right. \\ &+ \left. \left. b \cdot a_n \sin\left(\frac{n\pi}{w_{\mathrm{eff}}} y\right) e^{-i(k_x^n(\nu)(D_s - x))} \right] \right|^2 \end{aligned} \tag{1}$$

where I denotes the spin-wave intensity, n the mode number with respect to the transversal quantization, a_n the amplitudes of the waves traveling in $+x$-direction, b the factor of imbalance of the antennas[4] (thus $a_n \cdot b$ are the amplitudes of the waves traveling in $-x$-direction) and D_s the distance between the antennas.

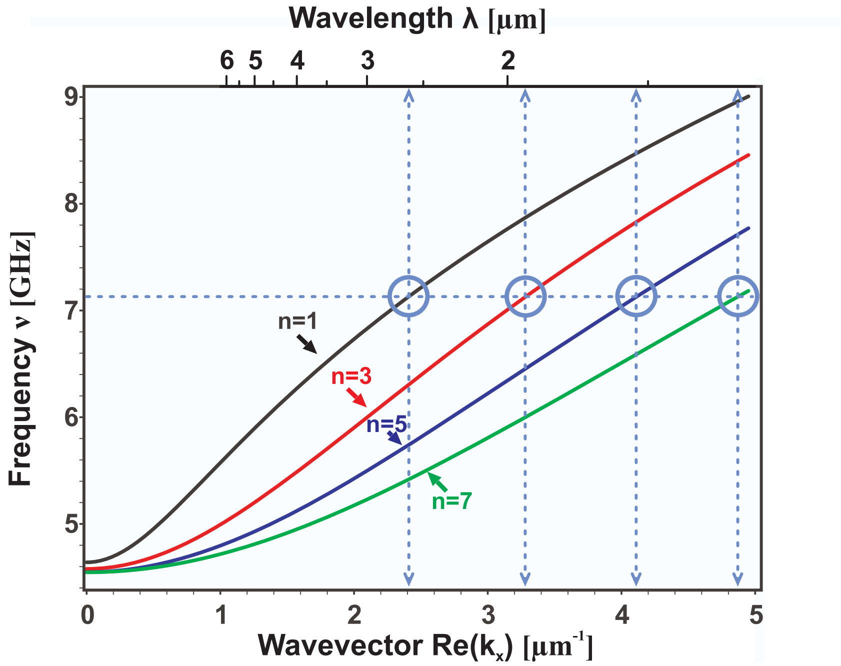

Fig. 3: Calculated dispersion relations for a $Ni_{81}Fe_{19}$ microstripe ($w_{\mathrm{eff}} = 3\,\mu\text{m}$, thickness $t_s = 40\,\text{nm}$, $B_{\mathrm{ext}} = 30\,\text{mT}$) for the transversal modes $n = 1, 3, 5, 7$. Circles and dotted lines indicate the resulting wavelengths and wavevectors at the used frequency of $\nu = 7.13\,\text{GHz}$.

---

[4] To obtain an almost symmetric intensity distribution we attenuate the microwave current in one antenna compared to the other because of the well know non-reciprocity of the spin-wave excitation in this configuration (see [5, 9]). The remaining imbalance is represented via the parameter b.

The complex wavevector k_x^n is related to the exponential amplitude decay length δ^n and the wavelength λ^n via:

$$\Im(k_x^n) = \frac{1}{\delta^n} \; ; \; \Re(k_x) = \frac{2\pi}{\lambda^n} \tag{2}$$

where the decay length δ^n was determined using the group velocity v_g^n and the lifetime τ of the spin waves:

$$\delta^n = v_g^n \tau = \frac{\partial \omega^n}{\partial k_x} \tau \tag{3}$$

We extracted v_g^n for the different modes from the dispersion relations shown in Fig. 3. τ was calculated according to [16], assuming the standard damping parameter α for $Ni_{81}Fe_{19}$ (α=0.01). Since we computed the frequency dependent relative excitation amplitudes a_1/a_n for the different width modes n (see Fig. 1a) by using the theory presented in [5, 9] the only fit parameters are the relative phase shift Φ between the two antennas and the factor of imbalance b, which both depend strongly on the experimental conditions (cable length, contacts).

As one can see in Fig. 2, there is a good agreement between the measured intensity and the theoretical calculation using Eq. (1), proving that we can predict all physical relevant parameters like wavelength, group velocity and relative excitation efficiency. In detail, only modes with uneven n can be excited by the antennas and only modes with $n \leq 7$ contribute significantly. The group velocity v_g^n and consequently the decay length δ^n decrease with increasing n and in the case of the chosen frequency $\nu = 7.13\,\text{GHz}$, this is also true for the relative amplitudes a_n (see Fig. 1a).

To visualize the influence of the different transversal modes it is convenient to look at the two-dimensional spin-wave intensity shown in Fig. 4 where the BLS measurement a) is compared to

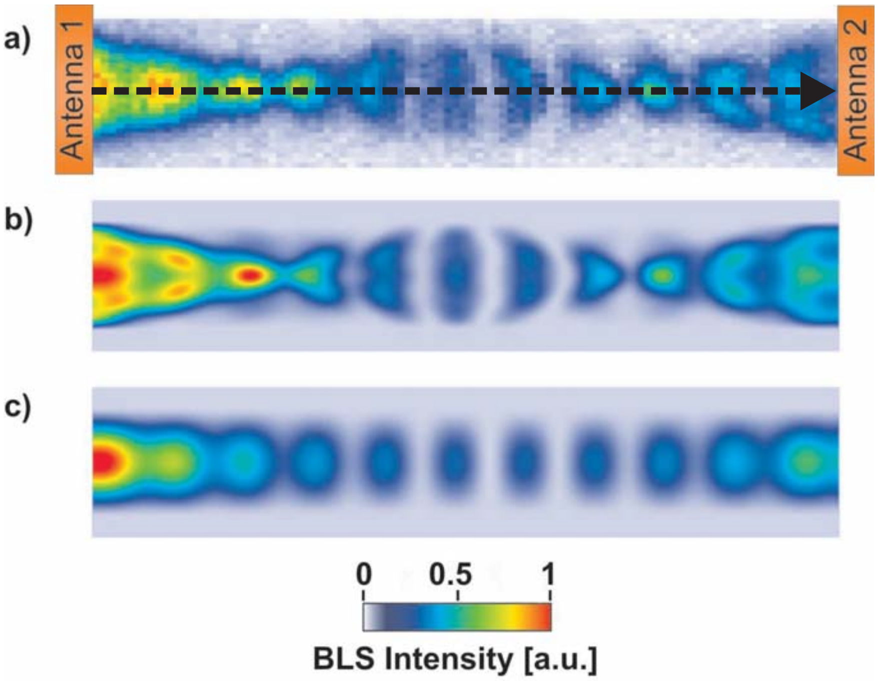

Fig. 4: a) Two-dimensional BLS-intensity map showing the interference of propagating spin waves in a $Ni_{81}Fe_{19}$-stripe (see Fig. 2 for parameters). The dashed line indicates the scan shown in Fig. 2. b) Calculations taking into account the modes $n = 1, 3, 5, 7$. c) Calculations taking into account only the first mode $n = 1$.

the complete calculation of Eq. (1) with $n = 1,3,5,7$ in b) and to the calculation taking into account only the first mode $n = 1$ in c). It is obvious that the interference of the different width modes leads to periodical convergence of the intensity (see [18]). This explains the local maximum shown in Fig. 2: it is situated at a point where the spin-wave intensity is concentrated in the middle of the stripe.

To verify our results further, we use phase-resolved Brillouin light scattering microscopy [1,2] to access directly the phase of the interfering spin waves. In Fig. 5, the measured phase φ is compared to the predicted values of the model in Eq. (1):

$$\varphi \quad = \quad \arctan\left(\frac{\Im(A)}{\Re(A)}\right) \tag{4}$$

where the complex amplitude A of the spin waves is calculated according to Eq. (1). Also for this measurement, the results show an excellent agreement with the theoretical predictions.

As can be seen in Fig. 5 one can nicely distinguish two regions: Near the antannas, the phase is dominated by one of the propagating waves, hence a linear increase in phase is visible. In the horizontal center of the stripes, both waves have comparable intensities and form a standing wave. The phase profile of standing spin waves consists of regions of constant phase which range over half the spin-wave wavelength and are separated by phase jumps of π (see [24] for more detail). Two of these phase jumps can be seen in Fig. 5. The plateau in the center has a width $\Delta x \approx 1,76\,\mu\text{m}$ which corresponds well with $\lambda/2 \approx 1,8\,\mu\text{m}$.

As it was already mentioned above, the spin waves are found to interfere coherently whenever a significant intensity from both antennas can be detected. Consequently, we can use the interference of the spin waves to measure their dispersion relation. To investigate a maximum frequency range,

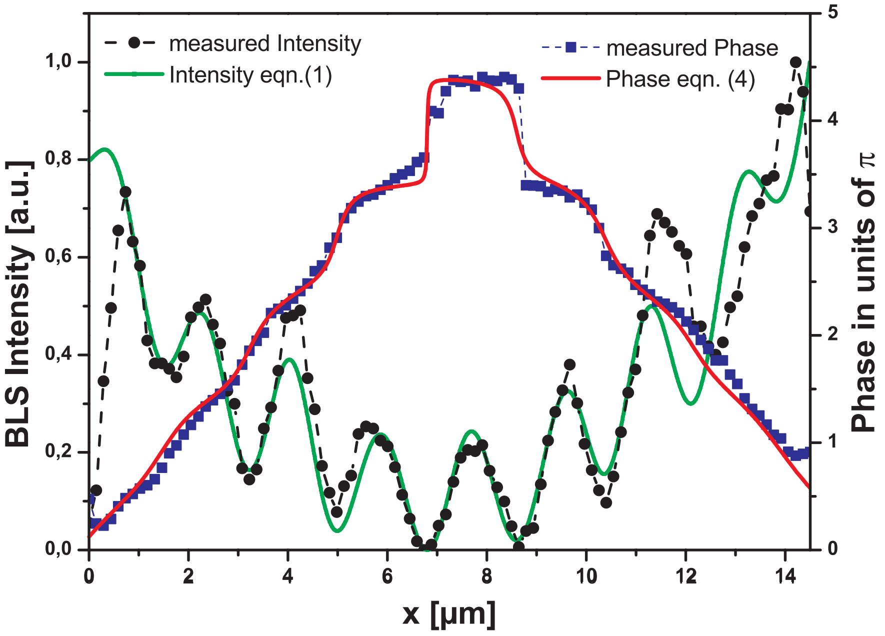

Fig. 5: Squares: Phase of interfering spin waves (at $B_{\text{ext}} = 40\,\text{mt}$, $\nu = 7.13\,\text{GHz}$) measured with phase resolved BLS microscopy and the comparison to the calculated phase according to Eq. (4) (red line). Dots: Corresponding BLS intensity and its calculation with Eq. (1) where the same parameter as for the phase calculation are used.

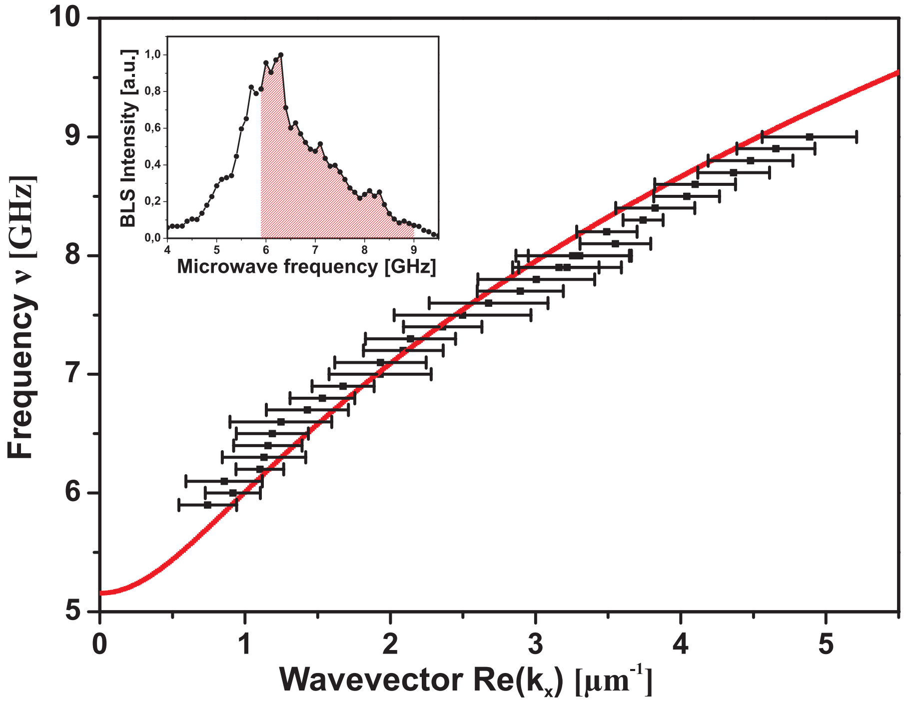

Fig. 6: Dispersion relation for the first width mode of the $Ni_{81}Fe_{19}$-stripe at $B_{\mathrm{ext}} = 35\,\mathrm{mT}$. The values for Re($k_x$) are measured via the average distance between two intensity maxima (see text). The inset shows the response of the sample to an applied microwave excitation. The dashed area indicates the frequency range in which the values for Re(k_x) were determined.

we utilize a sample with slightly changed dimension compared to the one shown in Fig. 1, but with an identical $Ni_{81}Fe_{19}$-stripe. First, we measure the BLS intensity at a fixed position as function of the microwave frequency (see inset of Fig. 6) to identify the frequency range in which propagating spin waves can be excited. Then, space resolved scans similar to the one in Fig. 2 are performed for different excitation frequencies in this range.

We take the average distance Δ between two intensity maxima to calculate the wavevector of the first transversal mode: $k_x^1 = \pi/\Delta$ (see Fig 6). Thus, the influence of higher transversal modes on the distance between two maxima is neglected, which is a useful approximation for the particular experimental parameters (note that in Fig. 4, the higher transversal modes do not change significantly the distance between the maxima in the middle of the stripe). The remaining influence of the higher transversal modes leads to small variations of Δ around the mean value represented by the error bars. The good agreement between the experimental results and theoretically calculated dispersion relation for the first transversal mode further justifies our approximation.

To conclude, we showed that propagating spin waves in microscopic waveguides interfere coherently, so the construction of micron-sized spin-wave logic devices should be principally possible. In addition, we demonstrated that wavelength, group velocity, decay length and excitation efficiency for the different transversal modes can be predicted by the theory for spin waves in thin magnetic films. Furthermore, the interference of the propagating spin waves was used to measure their dispersion relation in an extended frequency range.

Financial support by the Carl-Zeiss-Stiftung and Landungsforschungszentrum OPTIMAS is gratefully acknowledged.

References

[1] K. Vogt, H. Schultheiss, S.J. Hermsdoerfer, P. Pirro, A.A. Serga, B. Hillebrands, Appl. Phys. Lett. **95**, 182508 (2009).

[2] V.E. Demidov, S. Urazhdin, S.O. Demokritov, Appl. Phys. Lett. **95**, 262509 (2009).

[3] A.V. Chumak, P. Pirro, A.A. Serga, M.P. Kostylev, R.L. Stamps, H. Schultheiss, K. Vogt, S.J. Hermsdoerfer, B. Laegel, P.A. Beck, B. Hillebrands, Appl. Phys. Lett. **95**, 262508 (2009).

[4] K.-S. Lee, S.-K. Kim, J. Appl. Phys. **104**, 053909 (2008).

[5] V.E. Demidov, M.P. Kostylev, K. Rott, P. Krzysteczko, G .Reiss, S.O Demokritov, Appl. Phys. Lett. **95**, 112509 (2009).

[6] T. Schneider, A.A. Serga, B. Leven, B. Hillebrands, R.L. Stamps, M.P. Kostylev, Appl. Phys. Lett. **92**, 022505 (2008).

[7] M. Kostylev, T. Schneider, A.A. Serga, B. Hillebrands, Journal of Nanoelectronics and Optoelectronics, Volume 3, Number 1, March 2008.

[8] S. Choi, K.-S. Lee, S.-K. Kim, Appl. Phys. Lett. **89**, 062501 (2006).

[9] T. Schneider, A.A. Serga, T. Neumann, B. Hillebrands, Phys. Rev. B **77**, 214411 (2008).

[10] A. Khitun, M. Bao, K. L Wang, IEEE Trans. on magnetics, **44 (9)**, 2141-2152 (2008).

[11] V. Vlaminck, M. Bailleul, Science **322**, 410 (2008).

[12] S.-M. Seo, K.-J. Lee, H. Yang, T. Ono, Phys. Rev. Lett. **102 (14)**, 147202 (2008).

[13] Y. Le Maho, J.V. Kim, G. Tatara, Phys. Rev. B **79(17)**, 174404 (2009).

[14] D.-S. Han, S.-K. Kim, J.-Y. Lee, S.J. Hermsdoerfer, H. Schultheiss, B. Leven, B. Hillebrands, Appl. Phys. Lett. **94,** 112502 (2009).

[15] C. Bayer, H. Schultheiss, B. Hillebrands, R.L. Stamps, IEEE Trans. Magn., **41**, 3610 (2005).

[16] D.D. Stancil, A. Prabhakar, *Spin Waves Theory and Application* (Springer, New York, 2009).

[17] V.E. Demidov, S.O. Demokritov, B. Hillebrands, M. Laufenberg, P.P. Freitas, Appl. Phys. Lett. **85**, 2866 (2004).

[18] V.E. Demidov, S.O. Demokritov, K. Rott, P. Krzysteczko, G. Reiss, J. Phys. D: Appl. Phys. **41**, 164012 (2008).

[19] R. Hertel, W. Wulfhekel, J. Kirschner, Phys. Rev. Lett. **93**, 257202 (2004).

[20] C. Bayer, J.P. Park, H. Wang, M. Yan, C.E. Campbell, P.A. Crowell, Phys. Rev. B **69**, 134401 (2004).

[21] K. Perzlmaier, G. Woltersdorf, C.H. Back, Phys. Rev. B **77**, 054425 (2008).

[22] S.O. Demokritov, B. Hillebrands, A.N. Slavin, Phys. Reports **348**, 441 (2001).

[23] B.A. Kalinikos, A.N. Slavin, J. Phys. C: Solid State Phys. **19**, 7013 (1986).

[24] K. Vogt, *Zeit- und phasenaufgelöste Brillouin-Lichtstreumikroskopie an propagierenden Spinwellen*, Diploma Thesis, TU Kaiserslautern (2009).

4.14 Optical detection of spin transport in non-magnetic metals

F. Fohr, J. Hamrle, H. Schultheiss, A.A. Serga, and B. Hillebrands[1]

In spintronics, spin current injection from a magnetic to a non- magnetic material is an important and central issue [1, 2]. There are several ways to realize such an injection. Spin currents can be generated by charge current [3], spin Hall effect [4], or spin pumping [5, 6]. The spin polarization in the non- magnet can be detected indirectly by an increased damping in the injection layer [6, 7] or it can be probed by the conversion of spin current into voltage in a lateral spin valve [8] or via the inverse Spin Hall effect [9, 10]. In case of the spin pumping effect, the injected spin current is proportional to the cross product of the magnetization and its first time derivative and can be separated into a static (or longitudinal) component parallel and a dynamic (or transverse) component perpendicular to the external field. In this report we demonstrate that the dynamic component can be observed directly by means of Brillouin light scattering (BLS) microscopy in a non-magnetic material.

A direct imaging of the spin polarization in a non- magnetic metal is only possible using non- contact techniques. For instance, the spin polarization was mapped in a ferromagnet/semiconductor system by exploiting the connection of the spin polarization with the polarization of the probe laser light [11]. In metals, spin accumulation occurs only in the vicinity of the Fermi level (in order of tens of μeV), making the observation of the spin accumulation difficult using techniques such as XMCD microscopy [12].

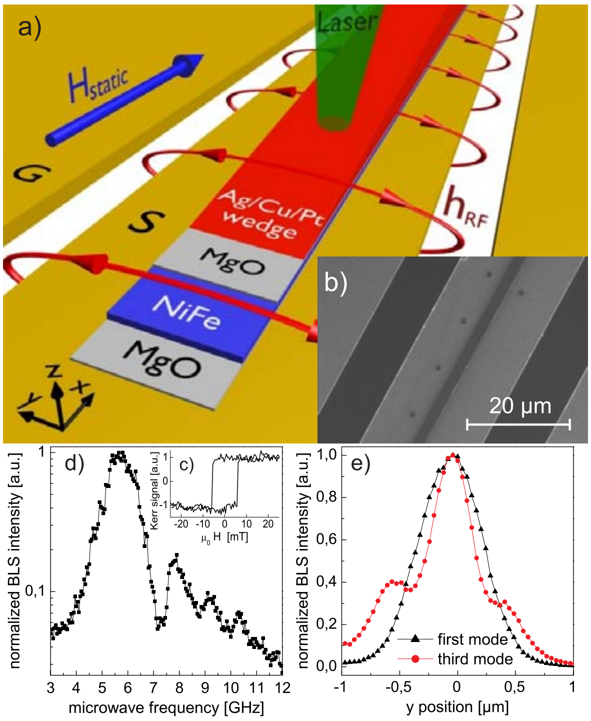

Fig. 1: a) Sample layout and b) SEM picture of the waveguide. A multilayer structure is prepared on top of a coplanar waveguide. A static magnetic field $\mu_0 H_{\mathrm{static}}$ of 20 mT is applied parallel to the signal line and perpendicular to the dynamic magnetic field $\mathbf{h}_{\mathrm{RF}}$, which is caused by an alternating microwave current flowing through the coplanar waveguide. The magnetization in the $Ni_{81}Fe_{19}$ is excited by $\mathbf{h}_{\mathrm{RF}}$ and spins are pumped into the metal wedge. c) MOKE hysteresis loop to determine the saturation field in x- direction, (d) BLS spectrum taken on pure $Ni_{81}Fe_{19}$ at a static magnetic field of 20 mT. e) BLS scans across the structure for the first two maxima of d) at microwave frequencies of 5.5 GHz and 7.8 GHz. The profiles correspond to the first and the third laterally standing spin wave mode.

---

[1] In collaboration with Y. Fukuma, L. Wang, Y. Otani, ASI, RIKEN, 2-1 Hirosawa, Wako 351- 0198, Japan; ISSP, University of Tokyo, 5-15-5 Kashiwanoha, Kashiwa 277- 8581, Japan; S. Kaltenborn, H.C. Schneider, Technische Universität Kaiserslautern, Germany.
J.H. is now at Institute of Physics, VSB - Technical University of Ostrava, CZ-70833 Ostrava-Poruba, Czech Republic.

Non- magnetic metals show a much higher spin orbit coupling compared to semiconductors which leads to a much shorter spin diffusion length. At room temperature the spin diffusion length in non-magnetic metals [13] approaches the optical resolution of a microscope and has not been imaged directly so far.

We detect the spin polarization in a metal wedge grown on top of a ferromagnetic layer (see Fig. 1). Light from a laser is focussed on the surface of the wedge and the inelastically scattered light is collected as a function of the local wedge thickness. This light originates from the non-magnetic layer due to inelastic scattering from the spin polarization as well as from the magnetic layer below the wedge as long as the accumulated optical path length is smaller, or at least comparable to the optical absorption length. The magnetic layer is excited externally by the RF field of a coplanar waveguide (CPW) near the ferromagnetic resonance frequency, and generates the spin polarization in the wedge layer via the spin pumping effect.

The design of our sample is shown in Fig. 1. The CPW is prepared by means of maskless laser photolithography on top of a oxidized silicon substrate. It consists of a 300 nm gold layer with a signal line (S) of 20 µm width separated from the ground planes (G) by a 10 µm wide gap. A microwave current is applied to the CPW and generates an oscillating magnetic field in y- direction using a coordinate system as defined in Fig. 1. To reach high microwave power in a wide frequency band and to prevent reflections, the microwave current is terminated by a load at the end of the CPW with impedance matching. On top of the CPW signal line a multilayer structure is deposited by means of electron beam evaporation.

The multilayer consists of: (*i*) a 7 nm thick MgO layer that prevents the microwave current from flowing into the metal wedge, because this would create a complicated current distribution and an unpredictable magnetic field disturbing the CPW magnetic field; (*ii*) a 30 nm thick $Ni_{81}Fe_{19}$ layer that is excited externally by the CPW magnetic field and serves as a pumping layer for the attached metal wedge; (*iii*) an optional second 7 nm thick MgO interlayer to block the spin pumping from the $Ni_{81}Fe_{19}$ layer into the metal wedge; (*iv*) a metal wedge composed of either silver, copper or platinum.

The optional MgO interlayer (*iii*) is used in a reference sample to separate the different contributions to the BLS intensity originating from the magnetic and the non- magnetic layer respectively. In the main sample without the MgO interlayer, the spin pumping into the metal is expected to occur, whereas in the reference sample the pumping mechanism is blocked by the MgO layer, which is insulating but optically transparent and therefore does not effect the detection with the probing laser light.

For absolut height calibration of the metal wedge, the scan position in x- direction is calculated into a total thickness. The topography was scanned in y- direction with a mechanical profilometer for different points along the wedge and for each of these profiles the thickness of the multilayer was extracted with the CPW level as reference level.

Figure 1d shows the BLS spectrum taken on pure $Ni_{81}Fe_{19}$ at an applied field of 20 mT in x-direction. The first and most pronounced maximum is visible at a frequency of 5.5 GHz but several other maxima develop at higher frequencies corresponding to higher laterally standing spin wave modes across the stripe [14, 15].

A spatially uniform precession cannot be excited in a 2 µm wide stripe due to pinning effects at the boundaries. Standing spin waves build up across the width of the stripe in y- direction and the spin pumping efficiency becomes dependent on this direction (Fig. 1e). The dynamic magnetization in the non- magnetic layer experiences additional dephasing due to the mixing of components pumped with opposite initial phases from neighbouring antinodes of higher order standing waves. To minimize this contribution to the dephasing, only the first standing spin wave mode, excited at a microwave frequency of 5.5 GHz and an external field of 20 mT was used in our BLS measurements. The maximum of the first mode is located in the middle of the stripe and the BLS detection efficiency decreases with increasing metal wedge thickness on top of the Ni$_{81}$Fe$_{19}$ layer.

In Fig. 2 the measured BLS intensities of the maximum of the first mode are shown for different scan positions in x- direction. With increasing wedge thickness the BLS signal decays exponentially over a range of almost four decades in intensity. In the silver (Fig. 2a) and the copper wedge sample (Fig. 2b) the slopes of the exponential decay are different for the main (dark dots) and the reference sample (bright dots) whereas in the platinum sample both slopes are the same within the error bars (Fig. 2c). The origin of the difference in silver and copper is the additional contribution to the BLS intensity from the spin polarization pumped from the underlying Ni$_{81}$Fe$_{19}$ layer. While the BLS signal of the main sample is determined by the optical decay from the signal originating

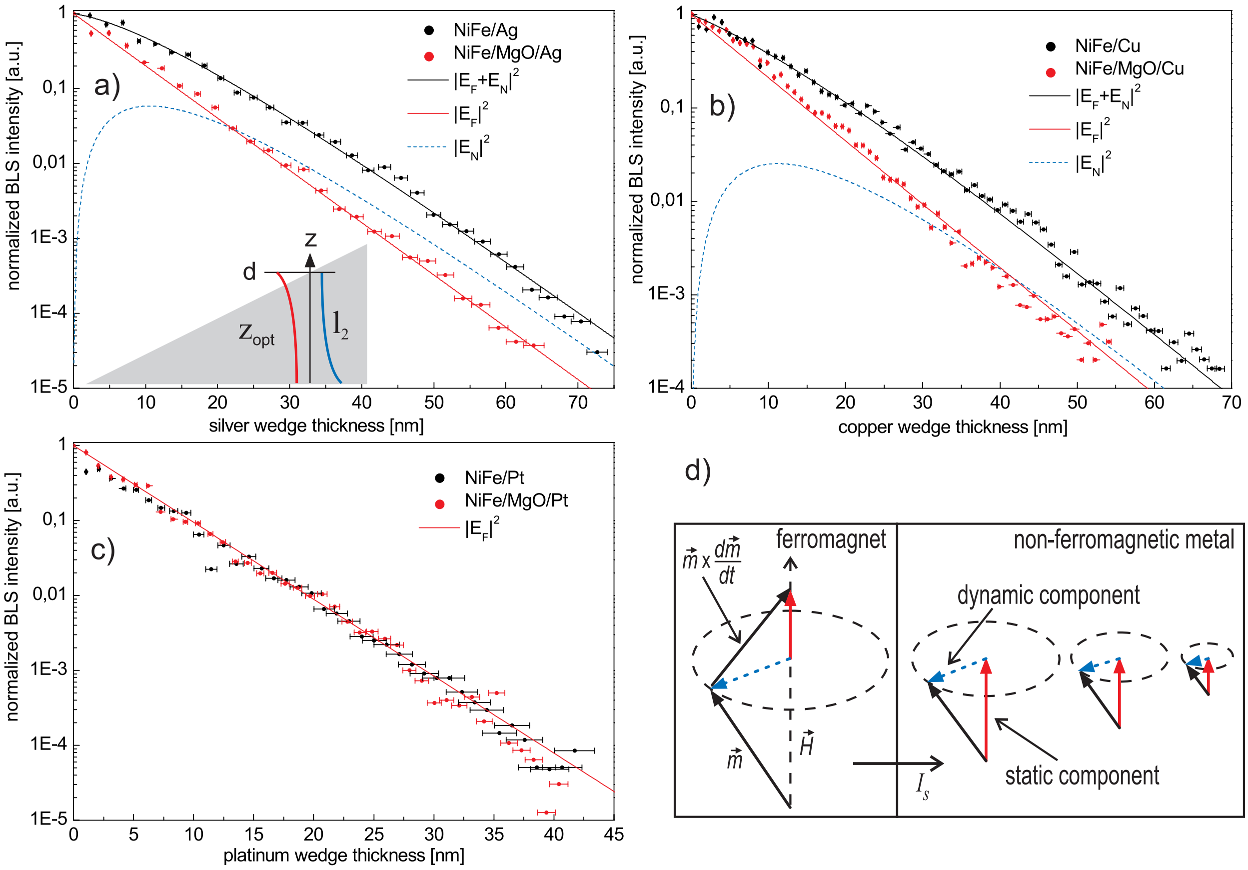

Fig. 2: BLS scan data of the silver a), the copper b) and the platinum c) wedged sample. Each graph shows the measurement of the main sample with active spin pumping (dark dots) and the respective reference sample with blocked spin pumping (bright dots). A difference between main and reference sample is only visible for silver and copper but not for platinum (see text). The error bars reflects the uncertainty in thickness determination by the mechanical profilometer. The dark and bright lines are fits of the scan data according to Eq. (1). The theoretical evolution of the pure spin part of the BLS signal (dotted line) can be derived from the fitting parameters. The inset in a) shows that the decaying optical part as well as the decaying spin part contribute to the total BLS intensity which is probed by the laser over the entire thickness. d) Scheme of the spin pumping effect. Magnetization is transferred from a ferromagnetic to an attached non- magnetic layer. The induced magnetization can be separated into a static (continuous arrow) and a dynamic (dotted arrow) component.

in $Ni_{81}Fe_{19}$ as well as by the decaying induced magnetization in copper, the signal from the sample with the MgO interlayer, which prevents spin pumping, contains only the signal originating from the $Ni_{81}Fe_{19}$ layer. In platinum this effect is not observable because the injected spin angular momentum is immediately transferred from the spin system to the lattice due to the high spin orbit interaction.

The total BLS intensity depends on the thickness of the metal wedge and consists of two contributions: One part of the signal is due to the precessing magnetization in the ferromagnet, the second part originates from the pumped spin polarization in the metal. The total BLS intensity is proportional to:

$$|E_F + E_N|^2 = |E_F|^2 + 2\,\mathrm{Re}\,(E_F E_N^*) + |E_N|^2 \tag{1}$$

where E_F and E_N are the electric fields of the probe laser light scattered inelastically in the magnetic and the non- magnetic layer, respectively. Inside the metal wedge of thickness d, i.e. for $0 < z < d$, the profile of the electric field originating from the incident light can be expressed as a damped wave (see inset of Fig. 2).

$$E_F = E_{F,0} \exp(2i\tilde{n}kd) \tag{2}$$

Here $\tilde{n} = n + i\kappa$ is the complex refractive index and $k = \omega/c$ is the vacuum wavevector of light. The factor 2 in the exponent takes into account that the BLS setup is prepared in backscattering geometry and the light has to pass through the structure twice.

The amplitude of the backscattered light from the non- magnetic layer is a sum of contributions originating from different depths of the wedge, weighted by the decaying probe laser amplitude as well as by the decaying contribution of the spin polarization to the scattered light.

$$E_N = \int_0^d E_{N,0} \exp[2i\tilde{n}k(d-z)] \exp\left(-\frac{z}{l_2}\right) dz \tag{3}$$

Here l_2 is the characteristic dephasing length of the dynamic spin polarization that gives rise to the BLS signal.

In Fig. 2 the fit curves (dark and bright lines) and the calculated BLS intensity for the pure spin part (dotted line), obtained by a numerical simulation using Eqs. (1)- (3), are shown in addition to the measurement data. The fitting parameters in the simulation are the ratio of the field strengths $E_{N,0}$ and $E_{F,0}$ at the $Ni_{81}Fe_{19}$/Cu interface, the complex refractive index $\tilde{n}$ in the metal and the dephasing length l_2. The results of this simulation as well as the parameters of the fits in Fig. 2 are summarized in Tab. 1. The contribution of the induced magnetization $|E_N|^2$ to the BLS signal is at maximum for wedge thicknesses below 20 nm, even if the BLS signal originated from the $Ni_{81}Fe_{19}$ layer, $|E_F|^2$ is dominant. Above wedge thicknesses of 20 nm in silver (45 nm in copper) $|E_N|^2$ becomes dominating over $|E_F|^2$.

With knowledge of l_2, a characteristic relaxation time T_2 can be calculated using a macroscopic spin wave- equation for the single- particle density matrix [16–18].

In this wave equation we describe the dynamics of conduction electrons in a magnetic field using dynamical macroscopic equations for the spin density $\rho_s(z,t) = \rho_\uparrow(z,t) - \rho_\downarrow(z,t)$ and the spin-current density $\mathbf{J}_s(z,t) = \mathbf{J}_\uparrow(z,t) - \mathbf{J}_\downarrow(z,t)$:

$$\frac{\partial \rho_s(z,t)}{\partial t} = -\gamma \rho_s(z,t) \times \mathbf{B} - \frac{\partial \mathbf{J}_s(z,t)}{\partial z} - \left.\frac{\partial \rho_s(z,t)}{\partial t}\right|_{\mathrm{int}} \tag{4}$$

Table 1: Fitting parameters of the BLS data in Fig. 2 and the resulting transverse relaxation time T_2 according to the macroscopic spin wave- equation.

Normal metal	$\tilde{n}$	$\tilde{n}_{lit}$ in [19]	l_2 (nm)	$E_{F,0}/E_{N,0}$	T_2 (fs)
Ag	0.13+i3.4	0.13+i3.2	9 ±1	16	3 ±1
Cu	1.07+i3.3	1.07+i2.6	10 ±1	26	5 ±1
Pt	2.08+i5.2	2.08+i3.6	0 ±2	>20	inst.

and

$$\mathbf{J}_s(z,t) = -D\frac{\partial \rho_s(z,t)}{\partial z} - \tau_e \gamma \mathbf{J}_s(z,t) \times \mathbf{B} - \tau_e \frac{\partial \mathbf{J}_s(z,t)}{\partial t} \tag{5}$$

where τ_e denotes the mean electron scattering time, γ is the absolute value of the electron $(g \approx 2)$ gyromagnetic ratio, $\mathbf{B}$ is the magnetic field and D is the diffusion constant.

As a generalization of Ref. [18], we include different longitudinal (or spin- lattice) relaxation times T_1 and transverse (or spin- spin) relaxation times T_2 in the form $\left(\partial \rho_s(x)/\partial t\right)|_{\text{int}} = \rho_s(x)/T_1$ and $\left(\partial \rho_s(y,z)/\partial t\right)|_{\text{int}} = \rho_s(y,z)/T_2$.

Therefore, the dynamical components of $\rho_s(z,t)$ in Eq. (4) decay with T_2 and the static component decays with T_1. It can be shown [18] that the relaxation times T_i depend on the corresponding decay lengths l_i as follows:

$$l_i = \frac{v_F}{\sqrt{3}}\sqrt{\tau_e T_i}\,; \quad i = 1,2 \tag{6}$$

where $T_1 = \tau_{\text{sf}}/2$ is determined by the spin- flip time and v_{F} is the Fermi velocity. According to Ref. [20] we use $\tau_e\,(\text{Cu}) = 25\,\text{fs}$ and $\tau_e\,(\text{Ag}) = 40\,\text{fs}$ in case of the mean electron scattering time and $v_{\text{F}}\,(\text{Cu}) = 1.57\,\text{nm/fs}$ and $v_{\text{F}}\,(\text{Ag}) = 1.39\,\text{nm/fs}$ in case of the Fermi velocity at room temperature. The small external magnetic field of 20 mT and the injection frequency of 5.5 GHz influence the decay lengths only on the fifth decimal place and are therefore neglected in Eq. (6). This result is also confirmed by our BLS measurements of the copper sample: The decay is unchanged within the error bars at an injection frequency of 9.3 GHz and an applied field of 70 mT.
To obtain the transverse relaxation time, we solve Eq. (4) and (5) numerically by using T_2 as a fit parameter to match the experimentally given value for l_2. The results of this calculation can be seen in Tab. 1. Note that the literature value of the longitudinal relaxation time T_1, being in the lower picosecond range [13,21], exceeds the value of T_2 determined by our BLS measurements by three orders of magnitude. This is remarkable because T_2 is usually considered equivalent to T_1, if the mean electron scattering time τ_e is much smaller than the reciprocal Larmor frequency [22].

To explain the small T_2, we propose an extrinsic effect acting differently on the transverse and the longitudinal component of the induced magnetization. We assume a non- homogeneous $\text{Ni}_{81}\text{Fe}_{19}$/ metal interface due to residual mass diffusion of nickel and iron atoms from the $\text{Ni}_{81}\text{Fe}_{19}$ layer into defects of the normal metal. The induced magnetization will give rise to a spin torque and a transfer of spin angular momentum from the conduction electrons to the magnetic impurities. The longitudinal component of the induced magnetization will not be affected by the impurities whereas the transverse component, which is perpendicular to the external field, will experience a torque trying to align the spin direction parallel to the field. The impurities will act as spin sinks which dissipate the transverse spin current ejected by the ferromagnetic layer. In [23] it is shown theoretically that this effect reduces the transverse component to nearly zero if the spin current is transmitted from a nonmagnet into a ferromagnet. In our case this ferromagnet is replaced by the paramagnetic impurities and the transverse spin current is limited to a few nanometers.

In conclusion we have proved for the first time the existence of magnetization in non- magnetic metals by optical means. We have also shown that the transverse magnetization component is directly accessible to Brillouin light scattering microscopy and decays faster in the non- magnetic material than usually assumed.

Financial support by the Deutsche Forschungsgemeinschaft and the Japan Science and Technology Agency within the project JST-DFG Hi380/21-1 is gratefully acknowledged.

References

[1] G.A. Prinz, Science **282**, 1660 (1998).
[2] S.A. Wolf et al., Science **294**, 1488 (2001).
[3] M. Johnson, Phys. Rev. Lett. **70**, 2142 (1993).
[4] J.E. Hirsch, Phys. Rev. Lett. **83**, 1834 (1999).
[5] R.H. Silsbee, A. Janossy, P. Monod, Phys. Rev. B **19**, 4382 (1979).
[6] Y. Tserkovnyak, A. Brataas, G.E. Bauer, Phys. Rev. Lett. **88**, 11 (2002).
[7] T. Gerrits, M.L. Schneider, T.J. Silva, J. Appl. Phys. **99**, 023901 (2006).
[8] T. Kimura, J. Hamrle, Y. Otani, K. Tsukagoshi, Y. Aoyagi , Appl. Phys. Lett. **85**, 3501 (2004).
[9] E. Saitoh, M. Ueda, H. Miyajima, Appl. Phys. Lett. **88**, 182509 (2006).
[10] T. Kimura, Y. Otani, T. Sato, S. Takahashi, S. Maekawa, Phys. Rev. Lett. **98**, 156601 (2007).
[11] S.A. Crooker, M. Furis, X. Lou, C. Adelmann, D.L. Smith, C.J. Palmstrøm, P.A. Crowell, Science **309**, 2191 (2005).
[12] O. Mosendz, G. Mihajlovic, J.E. Pearson, P. Fischer, M.Y. Im, S.D. Bader, A. Hoffmann, Phys. Rev. B **80**, 104439 (2009).
[13] J. Bass, W.P. Pratt Jr, J. Phys.: Condens. Matter **19**, 183201 (2007).
[14] S. O. Demokritov, B. Hillebrands, A. N. Slavin, Phys. Rep. **348**, 441 (2001).
[15] C. Bayer et al.Phys. Rev. B **72**, 064427 (2005).
[16] H. Smith, H.H. Jensen, Transport Phenomena, Clarendon, Oxford, (1989).
[17] Y. Qi, S. Zhang, Phys. Rev. B **67**, 052407 (2003).
[18] Y. Zhu, B. Hillebrands, H.C. Schneider, Phys. Rev. B **79**, 214412 (2009).
[19] E.D. Palik, Handbook of Optical Constants of Solids, Academic Press, Boston, (1985).
[20] N.W. Ashcroft, N.D. Mermin, Solid State Phyics, Holt, Rinehart and Winston, New York, (1976)
[21] F.J. Jedema, M.S. Nijboer, A.T. Filip, B.J. van Wees, Phys. Rev. B **67**, 085319 (2003).
[22] D. Pines, C.P. Slichter, Phys. Rev. **100**, 1014 (1955).
[23] M.D. Stiles, A. Zangwill, Phys. Rev. B **66**, 014407 (2002).

4.15 Spin-wave propagation in strongly anisotropic monocrystalline iron waveguides

F. Fohr, A.V. Chumak, A.A. Serga, K. Vogt, B. Leven, and B. Hillebrands[1]

The emerging field of spintronics, which operates not only with the electron's charge like conventional electronics, but also with its spin degree of freedom, is well recognized as a promising candidate for the development of future computing and information storage devices [1, 2]. One of the current challenges for spintronics are the short spin-diffusion lengths of spin currents which severely limit the distances over which information can be transferred. In nonmagnetic metals spin diffusion lengths can be of order of hundreds of nanometers at room temperature, while in ferromagnetic metals they are reduced to only several nanometers [3]. A possible solution has been recently proposed in [4], where the authors have shown that spin waves, which may propagate over macroscopic distances in ferromagnetic materials, can also be used as information carriers.

If they are to act as carriers of spin currents, spin waves typically require high values of bias magnetic field to compensate for the coercive fields and to shift the spin wave dispersion into the GHz range [4–6]. One of the most promising approaches reducing this field requirement is the use of ferromagnetic structures with high crystallographic anisotropy. The spin-wave frequencies in these ferromagnets are mostly determined by the values of the anisotropy fields and, in the limiting case, spin-wave propagation may be supported even in structures without a bias field. In addition, the possibility of controlling the anisotropy with an applied electric field offers new techniques for the excitation and manipulation of the spin waves in nano-structures. Recently, it has been shown in [7] that even relatively small electric fields can cause a significant change in the magnetic anisotropy of Au/Fe/MgO junctions.

In this report, we present the results of our experimental and theoretical studies of spin-wave propagation in thin Au/Fe/MgO waveguides with pronounced cubic and uniaxial surface-induced anisotropies. Measurements were performed using Brillouin light scattering (BLS) microscopy. The influence of uniaxial anisotropy on spin-wave frequencies was determined by studying waveguides of different thicknesses. The dependence of the spin-wave group velocity on the film thicknesses was probed in time resolved studies [8].

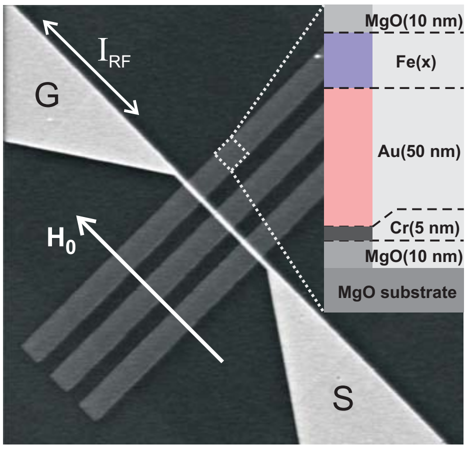

Fig. 1: SEM picture of the experimental structure. The inset shows the multilayer composition perpendicular to the sample plane. Spin waves in the iron waveguides are excited by a dynamic Oersted field, which originates from an alternating microwave current I_{RF} flowing through the antenna structure from the signal line (S) to the ground (G). A bias magnetic field H_0 is applied in the waveguides' plane and perpendicular to their long axes.

---

[1] In collaboration with Y. Shiota, T. Nozaki, Y. Suzuki, Osaka University, Tsukuba, 305-8568, Japan.

The structure we investigated is shown in Fig. 1. Three 5 µm-wide Fe/Au waveguides were prepared on top of a MgO substrate, separated from each other by a distance of 10 µm in order to avoid direct interaction and cross-talk. The thickness of the Fe film varies between 0.5 nm and 50 nm. The <100> axis of the mono-crystalline iron film, which is also the long axis of the waveguide, forms an angle of 45° with respect to the <100> axis of the gold layer. A bias magnetic field of $\mu_0 H_0 = 13\,\mathrm{mT}$ was applied in the film's plane perpendicular to the long axes of the waveguides, thus supporting the excitation and propagation of magnetostatic surface spin waves (MSSW). In order to excite spin waves, a 1 µm-thick gold antenna was placed on top of the multilayer waveguides. A microwave current was applied between the ground (G) and the signal line (S) of the antenna so as to generate an alternating magnetic field perpendicular to the bias field. Spin-wave propagation in these Fe waveguides was studied by means of time and space resolved BLS microscopy with a spatial resolution of 250 nm and a time resolution of 0.5 ns [6, 8].

The normalized spectra of the spin waves excited by the antenna measured close to the antenna (solid line) and at a distance of 10 µm away from it (dashed line) are shown in the inset of Fig. 2. One can see that in comparison with the spectrum measured 10 µm from the antenna, that one measured close to the antenna is much wider and shifted to lower frequencies. One can understand this by the following fact: in a distance of 10 µm from the antenna, only propagating spin waves are detected by BLS, while at a position close to the antenna one can detect both propagating waves and the uniform precession of the magnetization i.e. the ferromagnetic resonance (FMR). Due to the positive slope of their dispersion relation, propagating MSSW waves have frequencies above the FMR frequency which agrees well with the results shown in Fig. 2. The FMR frequency lies to the left-hand side of the spectrum measured close to the antenna (see vertical dashed line in the inset of Fig. 2). In our experiments, the FMR frequency is shifted from the intensity maximum of the propagating waves by approximately 2 GHz. Assuming that this shift is constant for all iron film thicknesses t, we are able to determine the FMR frequencies.

In order to explain the thickness dependence of the frequency shown in Fig. 2, the dispersion relations for the experimental structures, were calculated. Our calculations are based on the relation obtained in [9], allowing for effective fields of the cubic and uniaxial anisotropies. Taking into consideration that in our case the uniaxial anisotropy is induced by surface effects [10] we can obtain the following dispersion relation:

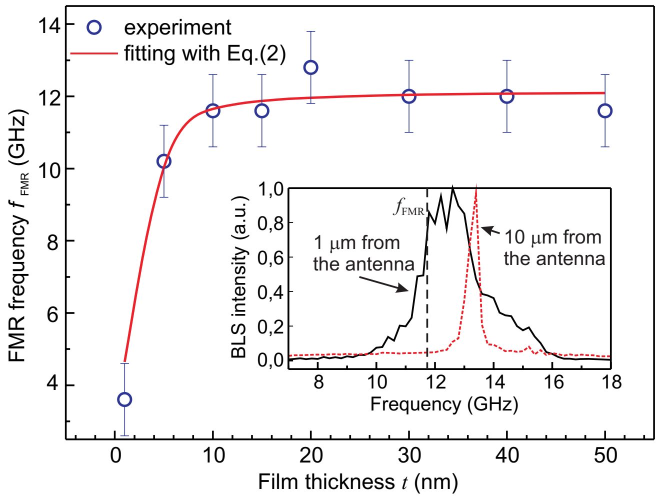

Fig. 2: Dependence of the FMR frequency on the Fe film thickness in experiment (open circles) and according to the fit (line). The inset shows the spectra of spin waves measured close to the antenna (solid line), and at a distance of 10 µm for a Fe waveguide thickness of $t = 10\,\mathrm{nm}$. A bias magnetic field of $\mu_0 H_0 = 13\,\mathrm{mT}$ was applied in the direction shown in Fig. 1.

$$\omega^2 = \omega_{\mathrm{H}}^{\mathrm{eff}}\left[\omega_{\mathrm{H}}^{\mathrm{eff}} + \omega_{\mathrm{M}} - 2\gamma\frac{H_{\mathrm{u}}}{t}\right] + \frac{1}{4}\left[\omega_{\mathrm{M}}^2 - 2\omega_{\mathrm{M}}\gamma\frac{H_{\mathrm{u}}}{t}\right]\left[1-\exp\left(-2t\sqrt{k^2+\left(\frac{n\pi}{w}\right)^2}\right)\right], \qquad (1)$$

where $\omega_{\mathrm{H}}^{\mathrm{eff}} = \gamma H_0 + 2\gamma H_{\mathrm{a}}$, $\omega_{\mathrm{M}} = 4\pi\gamma D M_0$. γ is the gyromagnetic ratio, H_0 the bias magnetic field, M_0 the saturation magnetization, D is the demagnetizing factor ($D = 1$ for an infinitely wide waveguide), H_{a} the effective field of cubic anisotropy, H_{u} the effective field of a surface-induced uniaxial anisotropy written in units of field times distance, w and t are the width and the thickness of the waveguide, k is the longitudinal wavenumber and n is the order of the width mode.

When considering absent anisotropies and an infinitely wide waveguide ($w \to \infty$), Eq. (1) resembles the dispersion relation (4.110b) in [11]. It should also be mentioned, that the effective fields of the anisotropies H_{a} and H_{u} can vary for different methods of the sample fabrication and, in general, are determined experimentally.

The equation for the FMR frequency can be obtained from Eq. (1) in the limit of $k \to 0$. For a wide waveguide $w \to \infty$, we obtain a solution similar to Eq. (3.13) in [10]:

$$f_{\mathrm{FMR}} = \omega_{\mathrm{FMR}}/2\pi = \sqrt{\omega_{\mathrm{H}}^{\mathrm{eff}}\left[\omega_{\mathrm{H}}^{\mathrm{eff}} + \omega_{\mathrm{M}} - 2\gamma\frac{H_{\mathrm{u}}}{t}\right] + \frac{1}{4}\left[\omega_{\mathrm{M}}^2 - 2\omega_{\mathrm{M}}\gamma\frac{H_{\mathrm{u}}}{t}\right]}. \qquad (2)$$

Examining this formula, we can qualitatively determine the influence of the crystallographic anisotropies on the FMR frequency and spin-wave frequencies in general. We see that the cubic anisotropy field is added to the applied external magnetic field and therefore creates an effective biasing field $H_{\mathrm{eff}} = H_0 + H_{\mathrm{a}}$. As a result, the frequency of the spin waves is not equal to zero even for an absent applied magnetic field H_0. On the other hand, the effective field of the uniaxial anisotropy has a negative sign, so that it acts to decrease the FMR frequency. Due to the fact that this anisotropy is induced by the Au layer, on which the Fe waveguides are grown, its influence decreases as the Fe film thickness increases. As a result, the frequency for a thicker layer is higher than for a thinner one (see Fig. 2). The fit of the experimental data in Fig. 2 with Eq. (2) allows us to determine the values of the relevant fields to: $\mu_0 H_{\mathrm{a}} = 50\,\mathrm{mT}$ and $\mu_0 H_{\mathrm{u}} = 0.7\,\mathrm{mT}\cdot\mu\mathrm{m}$.

In the context of spin wave spintronics the group velocity of spin waves is an important parameter since it determines (i) the speed of information transfer and (ii) the distance over which information

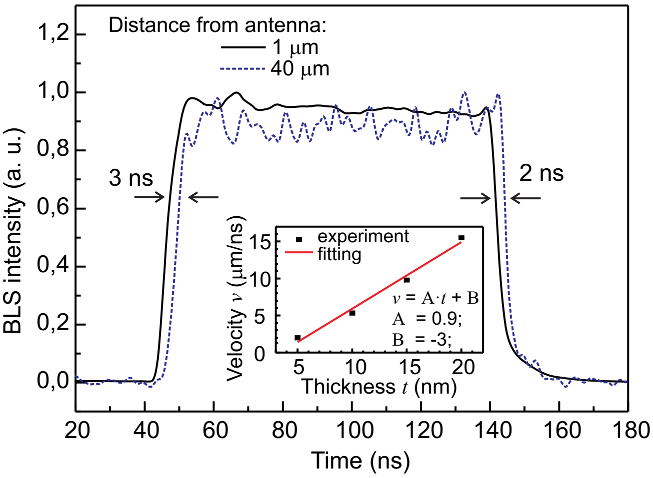

Fig. 3: Spin-wave pulses with 100 ns duration detected by time-resolved BLS microscopy at a distance of 1 µm (solid line) and 40 µm (dotted line) from the antenna for an Fe waveguide of thickness $t = 20\,\mathrm{nm}$. A time shift is observed between both pulses indicating a propagating spin wave. The resulting group velocities of the spin wave pulses can be seen in the inset for different waveguide thicknesses. An almost linear increase of the group velocity as the waveguide thickness increases is observable.

can be transferred. In order to determine the group velocity of the spin waves in our experiment, we used time resolved BLS microscopy. Propagating microwave pulses of 100 ns duration were applied to the antenna so as to excite spin-wave packets in the Fe waveguide that propagate away from the antenna. These packets were then detected by BLS microscopy at different distances from the antenna and their group velocities were determined as a ratio of the distance to the measured time delay.

In Fig. 3, the time profiles of the spin wave pulses are shown. One can clearly see the time shift between the front and the back of the delayed pulses. The dependence of the velocity as a function of the film thickness is shown in the inset. These values are based on an average of the decays between the front and back edge of the pulses. The corresponding fit shows that the spin-wave group velocity decreases almost linearly with decreasing film thickness.

We make several observations about the features of the results presented in Fig. 3. First of all, we were able to detect spin-wave propagation in a 20 nm-thick Fe waveguide at a distance of 40 µm from the exciting antenna. This implies, that the free path of the waves in Fe is several times longer than it is in permalloy ($\mathrm{Ni_{81}Fe_{19}}$) based structures [6]. This result could be explained by a lower spin-wave damping parameter or higher spin-wave group velocity in the iron. Secondly, the theoretical group velocity $v = \partial\omega/\partial k$ obtained from Eq. (1) gives a much smaller value than we observed experimentally. Understanding this discrepancy will require further theoretical and experimental studies of spin wave propagation in these structures. The third important observation we make is that the linear fit in the inset in Fig. 3 does not go to zero for zero thickness t. This result is in agreement with our theory which suggests that the group velocity should decrease due to the influence of uniaxial anisotropy, and that, in general case, the dependence $v(t)$ should cross the line $v = 0$ at a critical film thickness $t_{\mathrm{cr}} = 2\gamma H_{\mathrm{u}}/\omega_{\mathrm{M}}$ when the spins will be pointing perpendicularly to the film plane due to surface anisotropy [10].

In conclusion, we have studied spin-wave propagation in anisotropic epitaxial MgO/Fe/Au structures of different Fe thicknesses t both experimentally and theoretically. We have found that the spin-wave frequencies can be very high in such structures with cubic anisotropy ($>$10 GHz) even for small applied bias fields ($\approx$13 mT). In contrast, uniaxial surface-induced anisotropy decreases the spin-wave frequency and is more pronounced for thin Fe layers.

Financial support by the Deutsche Forschungsgemeinschaft (DFG, HI 380/21-1) is gratefully acknowledged.

References

[1] J.F. Gregg, Nature Materials **6**, 798 (2007).
[2] S.D. Bader, S.S.P. Parkin, Annual Review of Condensed Matter Physics **1** (2010).
[3] J. Bass, W.P. Pratt Jr, J. Phys.: Condens. Matter **19**, 183201 (2007).
[4] Y. Kajiwara, K. Harii, S. Takahashi, J. Ohe, K. Uchida, M. Mizuguchi, H. Umezawa, H. Kawai, K. Ando, K. Takanashi, S. Maekawa, E. Saitoh, Nature **464**, 262 (2010).
[5] A.A. Serga, A.V. Chumak, B. Hillebrands, J. Phys. D **43**, 264002 (2010).
[6] K. Vogt, H. Schultheiss, S.J. Hermsdoerfer, P. Pirro, A.A. Serga, B. Hillebrands, Appl. Phys. Lett. **95**, 182508 (2009).
[7] T. Maruyama, Y. Shiota, T. Nozaki, K. Ohta, N. Toda, M. Mizuguchi, A.A. Tulapurkar, T. Shinjo, M. Shiraishi, S. Mizukami, Y. Ando, Y Suzuki, Nature Nanotechnology **4**, 158 (2009).
[8] S.O. Demokritov, B. Hillebrands, A. N. Slavin, Phys. Rep. **348**, 441 (2001).
[9] B.A. Kalinikos, M.P. Kostyley, N.V. Kozkus, A.N. Slavin, J. Phys.: Condens. Matter **2**, 9861 (1990).
[10] J.A.C. Bland, B. Heinrich, *Ultrathin Magnetic Structures II*, Springer-Verlag Berlin Heidelberg (1994).
[11] D.D. Stancil, *Theory of Magnetostatic Waves*, Springer (1993).

4.16 Micromagnetic simulation of linear and nonlinear spin-wave propagation in nano-contact spin-valves

F. Ciubotaru, A.A. Serga, B. Leven, and B. Hillebrands[1]

The spin-wave emission from a point contact spin-valve structure is a topic of intensive research due to the large potential for on-chip data transfer. Here we report on micromagnetic simulations of the spin-wave distribution and on the analysis of the nonlinear effects detected experimentally [1] in such devices.

The structure investigated experimentally consists of an extended spin-valve multilayer sequnece IrMn(6 nm) / $Co_{90}Fe_{10}$(5 nm) / Cu(3.5 nm) / $Ni_{81}Fe_{19}$(7 nm) (Fig. 1a) with lateral dimensions of $15 \times 45\,\mu m^2$. The electric current is injected through a nanoscaled metallic point contact with a diameter of ~ 100 nm on top of the spin valve. The permalloy layer acts as magnetic free layer and the $Co_{90}Fe_{10}$ layer, which is exchange biased by the IrMn antiferromagnet, serves as a reference layer for the giant magnetoresistance measurements. The free layer is saturated by an external magnetic field **H** applied in the plane of the magnetic layer, along to the long axis of the spin-valve stack.

Spin waves were excited in the structure by applying a microwave current through the stack with various frequencies (2 GHz to 12 GHz). The dynamic response of the device was measured using Brillouin light scattering microscopy (BLS). This technique allows us to probe the spin waves with a spatial resolution of 250 nm and a frequency resolution of up to 50 MHz [2, 3]. The BLS intensity spectra were recorded near the point contact. The obtained map of BLS frequency versus microwave excitation frequency for an applied field of 248 Oe is displayed in Fig. 1b with intensity color coded. The diagonal in the figure represents the efficiency of the excitation of spin waves with a frequency that is equal to the applied microwave frequency f. Simultaneously with the directly excited spin waves, strong nonlinear effects appear, namely, the generation of modes with integer multiple frequencies ($2f$) and modes with noninteger factors ($0.5f$) with respect to

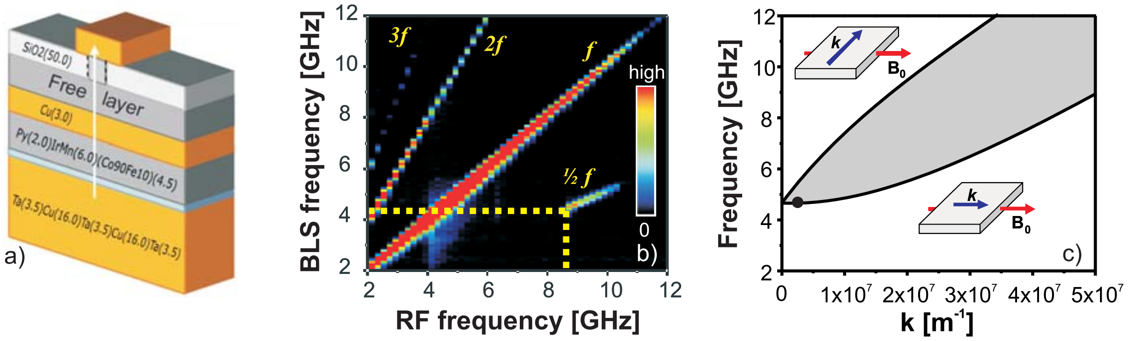

Fig. 1: a) Schematic configuration of the spin-valve stack. b) Spin-wave amplitudes measured with Brillouin light-scattering microscopy as a function of the RF excitation frequency (x-axis) and the position in the Brillouin light-scattering spectrum (y-axis) for an in-plane magnetic field of 248 Oe; c) Spin-wave dispersion band calculated for the free layer. The black circle denotes the frequency at the bottom of the spin waves band.

---

[1] In collaboration with X. Janssens, M. van Kampen, Dr. L. Lagae, IMEC, Leuven, Belgium; L. Lopez Diaz, Department of Physics, University of Salamanca, Spain; M. Kostylev, University of Western Australia, Perth, Australia; Prof. A.N. Slavin, Department of Physics, Oakland University, Rochester, MI, USA.

the excitation frequency. The excitation of these nonlinear modes can be understood within the framework of three-magnon scattering processes (confluence and splitting) [4] in which the total energy and momentum are conserved. In the case of confluence, two magnons with frequency f combine into a single magnon with doubled frequency $2f$. In the other case, one magnon with frequency f splits in two magnons, each one having halve the frequency $f/2$. One can see from Fig. 1b that the splitting process does not occur below a frequency limit marked with a dashed line. This limit can be derived from the analytical dispersion relations [5] of spin-wave eigenmodes calculated for the free layer (displayed in Fig. 1c). The upper (lower) curve corresponds to spin waves propagating perpendicular (parallel) to the magnetization vector, respectively. These two extremal dispersion curves define the upper and lower boundaries of the frequency band in which spin-wave eigenmodes are allowed. Therefore, taking energy conservation into account, it is expected that a splitting process can occur only if the excitation frequency is at least twice the frequency at the bottom of the spin-wave band (noted f_0). The observed threshold frequencies for the $f/2$ modes match the frequency at the bottom of the spin-wave band (black circle in Fig. 1c).

Altough if the Brillouin light scattering microscopy is a very powerful technique, it cannot provide all information related to the intimate behavior of the magnetization in the case of splitting of magnons. Information related to the spatial distribution of the oscillation amplitudes for nonlinear modes (with good accuracy), directions of propagation and wave numbers for linear and nonlinear modes could not be extracted from performed experiment. Moreover, up to now there is no theory for magnon splitting processes in ultrathin magnetic films which we could use for a quantitative comparison with our experimental results. On the other hand, knowing the propagation direction of spin waves emitted by each contact is of crucial importance for both the transfer of information between nanocontacts and the spin-wave synchronization of nano-oscillators.

Thus micromagnetic simulations are an important tool since they provide insight into the phenomena not achievable in the experiment. We performed systematic simulations [6] and the results (in agreement with experimental findings) allowed us a better characterization and understanding of the process that takes place in nanocontact structures.

As a starting point we considered a thin permalloy layer of 7 nm thickness with lateral dimensions of $1.5 \times 1.5\,\mu\text{m}^2$ (Fig. 2a). The material parameters of permalloy used to simulate the magnetization dynamics are: saturation magnetization $\mu_0 M_S = 1\,\text{T}$, exchange stiffness constant $A = 1.3 \times 10^{-11}$ J/m and no magnetocrystalline anisotropy. The simulated area was discretized into $N_x \times N_y \times N_z = 300 \times 300 \times 2$ cells, each cell having a size of $5 \times 5 \times 3.5\ \text{nm}^3$. Magnetic side charges were added artificially in order to prevent the creation of domains at the edges. A spatial distribution of the Gilbert damping (α) given by:

$$\alpha = \alpha_0 + \lambda \left[1 + \arctan\left(\frac{\rho - R}{\sigma} \right) \right] \quad . \tag{1}$$

with $\lambda = 1$, $R = 800\,\text{nm}$ and $\sigma = 100\,\text{nm}$ ensure a constant value $\alpha_0 = 0.01$ in the center of the sample for a radius of $\sim 500\,\text{nm}$. $\rho = \sqrt{x^2 + y^2}$ in which x and y denote the spatial coordinates. With the above parameters, the damping is increased more than fifty times at the edges and avoids the reflection of the spin waves at the boundaries. As in the experiment, a magnetic field of 250 Oe was applied in-plane of the sample along the x-axis. The precession of magnetization is excited by the dynamical Oersted field created by a microwave current injected through a contact placed in the center of the sample. The contact has a diameter of 100 nm. We calculate [7] the current distribution and the corresponding Oersted field in the permalloy layer with and without the contribution of the asymmetric top electrode. It was found that the lead induces an asymmetry

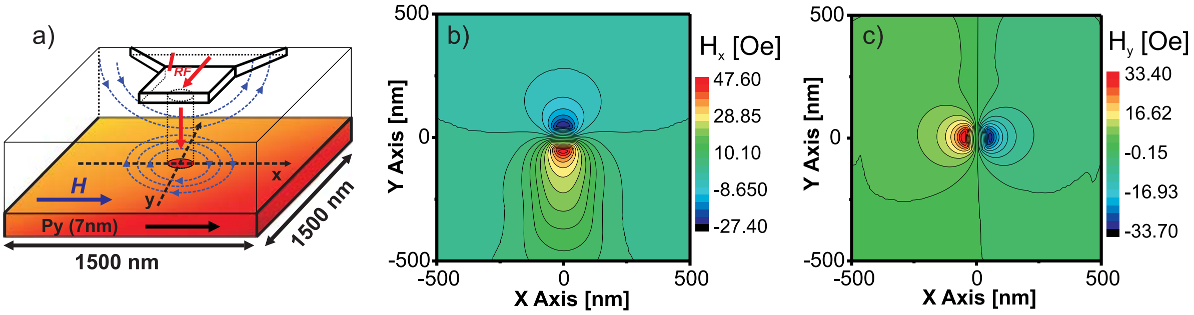

Fig. 2: a) Schematic representation of the sample with the contact in the center and a nonmagnetic metallic asymmetric lead situated at 60 nm above the sample (as in the experiment). Spatial distribution of the Oersted field components parallel b) and perpendicular c) to the applied field calculated for a direct current of 1 mA.

for the Oersted field component parallel to the external field while the perpendicular component remains virtually unchanged, as can be seen in Fig. 2b and Fig. 2c. For the simulations of the magnetization dynamics we use the distribution of the Oersted field with the contribution of the lead included.

Reproducing the entire experimental map from Fig. 1b by micromagnetic simulations is not suitable due to extremely long computational times. However, the properties of the emitted spin waves can be obtained by splitting the range of the applied microwave frequencies in three *intervals*, and assuming that the magnetization behaves similar for each frequency within one section.

The frequency range for the *first interval* starts with zero and the upper limit is given by the bottom of the spin-waves dispersion band f_0 ($\sim$4.65 GHz in our case). We have chosen a representative applied microwave frequency $f = 4$ GHz. Analyzing the magnetization fluctuation in time for each computational cell and performing the Fast Fourier Transform (FFT), we obtained the oscillation frequency for each component of the magnetization. Taking a cell at the edge of the contact one may see a response of the magnetization with the same frequency as the excitation one (f), but also generation of up to three higher harmonics: $2f$, $3f$ and $4f$ (Fig. 3a). The appearance of the higher modes is related to the strong nonuniformity of the internal field and to the elipticity of the magnetization precession. It has to be noted that we used a quite large applied microwave power in order to have a good contrast for the observation of the higher harmonics. Since the pumping frequency is smaller than f_0, no *eigenmodes* can be excited with the same frequency f (see Fig. 1c). In consequence, the oscillations of magnetization at the frequency $f = 4$ GHz are coming from forced excitations due to the dynamical Oersted field created by the microwave

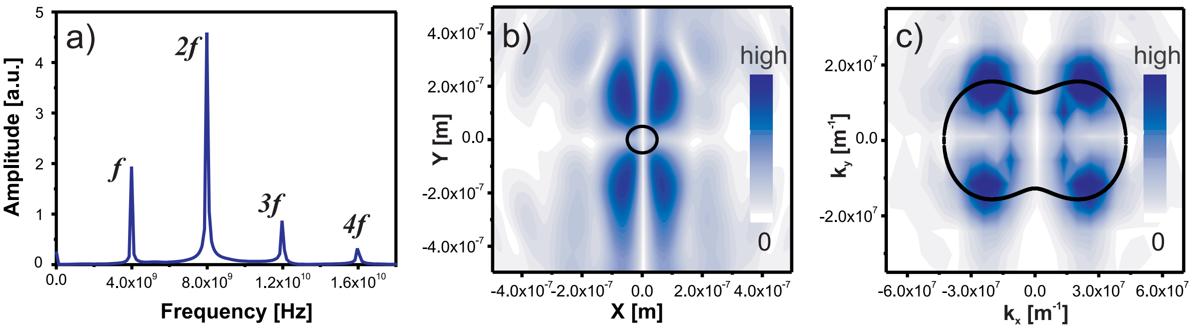

Fig. 3: a) Magnetization oscillation spectrum for a cell at the edge of the contact for a pumping frequency $f = 4$ GHz. b) Spatial distribution of the amplitude of the magnetization oscillation at $2f = 8$ GHz. c) Distribution of the $2f$ mode in the wavevector space with the intensity color coded. The black line represents the constant-frequency curve calculated analytically for a frequency of 8 GHz.

current. Of interest is the second harmonic since this one is an eigenmode of the system. Figure 3b shows the spatial distribution of this mode. The black circle in the center marks the position of the nanocontact. The spatial distribution is obtained by taking the amplitude value at $2f = 8\,\mathrm{GHz}$ from the frequency spectra of each cell and displaying them as a function of the position. An important observation is that this mode is localized in relatively tiny regions outside the contact area. The amplitude is decreasing very fast with the distance, thus making the experimental observation of the $2f$ mode difficult. The wavevectors of the emitted spin waves are determined by applying the two-dimensional Fourier transform in space to the already calculated components (real and imaginary parts) of the temporal FFT. Figure 3c shows the distribution of the $2f$ mode in the wavevector space. The k_x and k_y axes are the wave numbers that indicate the in-plane directions of propagation parallel and, respectively, perpendicular to the external applied magnetic field. The black curve in the figure represent the analytical constant-frequency curve calculated from the dispersion relations [5] for a frequency of 8 GHz. The good agreement between the theory and the simulation confirms that the $2f$ mode is a true eigenmode of the system. As one may see from the figure, for this mode there are four maxima which correspond to spin-wave emission from the contact with a wavevector under an angle of $33^\circ \pm 5^\circ$ with respect to the applied field.

The limits for the *second interval* of applied frequencies are chosen as follows: the lower one is given by f_0 and the upper limit is that frequency for which its half is just a little bit below f_0. Within this frequency range all eigenmodes of the system can be exited except the ones with half-integer factor $0.5f$ relative to the driving microwave frequency f. In other words, the splitting of magnons with the frequency f is forbidden. For simulation we fix the pumping frequency $f = 8\,\mathrm{GHz}$. Figure 4a shows the frequency spectra extracted for the same cell as in the previous case. Simultaneously with the directly excited spin waves with frequency f, two additional harmonics ($2f$, $3f$) can be observed. Of interest is the magnetization response at the pumping frequency f. In contrast to the previous case, a variety of spin wave modes can be excited with the same frequency f, since this one is included in the spin wave dispersion band (Fig. 1c). The spatial distribution of the magnetization oscillation amplitude for the mode with $f = 8\,\mathrm{GHz}$ is displayed in Fig. 4b. The black circle in the center is representing the position of the nanocontact. One can observe a

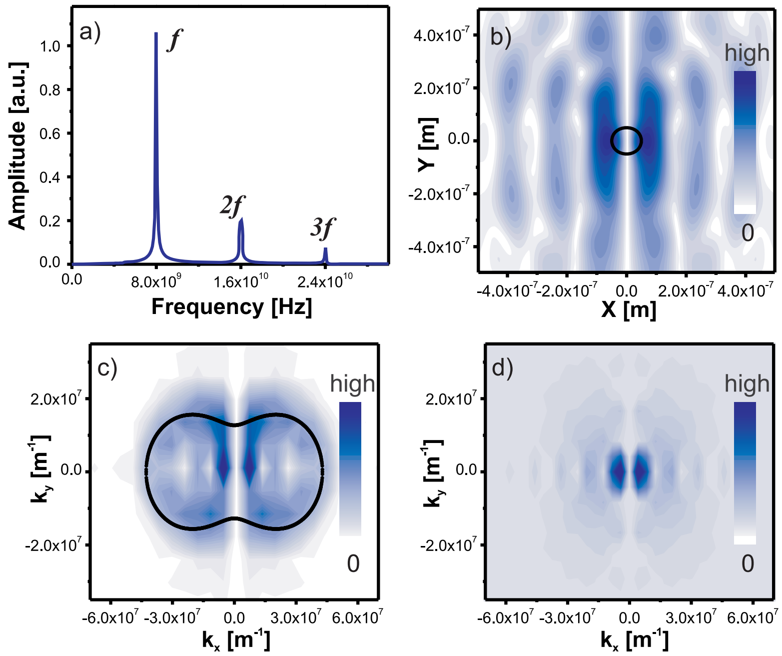

Fig. 4: a) Magnetization oscillation spectrum for a cell at the edge of the contact at the pumping frequency $f = 8\,\mathrm{GHz}$. b) Spatial distribution of the amplitude of the magnetization oscillation at $f = 8\,\mathrm{GHz}$ and the position of the nanocontact in the center (black circle). c) Distribution of the f mode in the wavevector space. The black line represents the constant-frequency curve calculated analytical for a frequency of 8 GHz. d) Distribution of the perpendicular component of the Oersted field computed in the wavevector space.

very different localization of this mode in comparison to the one from the previous case (4 GHz excitation frequency) extracted at the same frequency of 8 GHz. The maxima are located on the left and on the right side of the contact. This fact can be understood tacking into account the excitation mechanism for the f mode. The main driving field at the pumping frequency is the Oersted field component perpendicular to the bias field with a very similar amplitude distribution in space (see Fig. 2c). The analysis in the phase space (Fig. 4c) shows that the most efficient excited spin waves are the ones that are propagating with wavevectors nearly perpendicular with respect to the bias field. The excitation efficiency is decreasing once with the spin wave propagation angle, becoming close to zero for a spin wave travelling parallel to the bias field. The contour in the wavevector space obtained from our simulation matches very well the analytical constant-frequency curve calculated at 8 GHz (black line in the figure). Nevertheless, the extracted data from the simulation shows two more maxima located at small wave numbers. The origin of those maxima is traced back to the spatial configuration of the driving excitation field. Figure 4d presents the distribution of the perpendicular component of the Oersted field computed in the wavevector space. Comparing this two distributions (magnetization and excitation field) one can observe that the maxima are located at the same wave numbers.

For the *third interval*, the lower limit is given by the minimal pumping frequency that allows the splitting of magnons with the driving frequency ($2 f_0 = 9.3$ GHz). For the upper limit there is no constriction. We set the excitation frequency to $f = 11$ GHz. From the frequency spectrum shown in Fig. 5a, one sees that modes with noninteger factors ($0.5f$ and $1.5f$) are appearing in addition

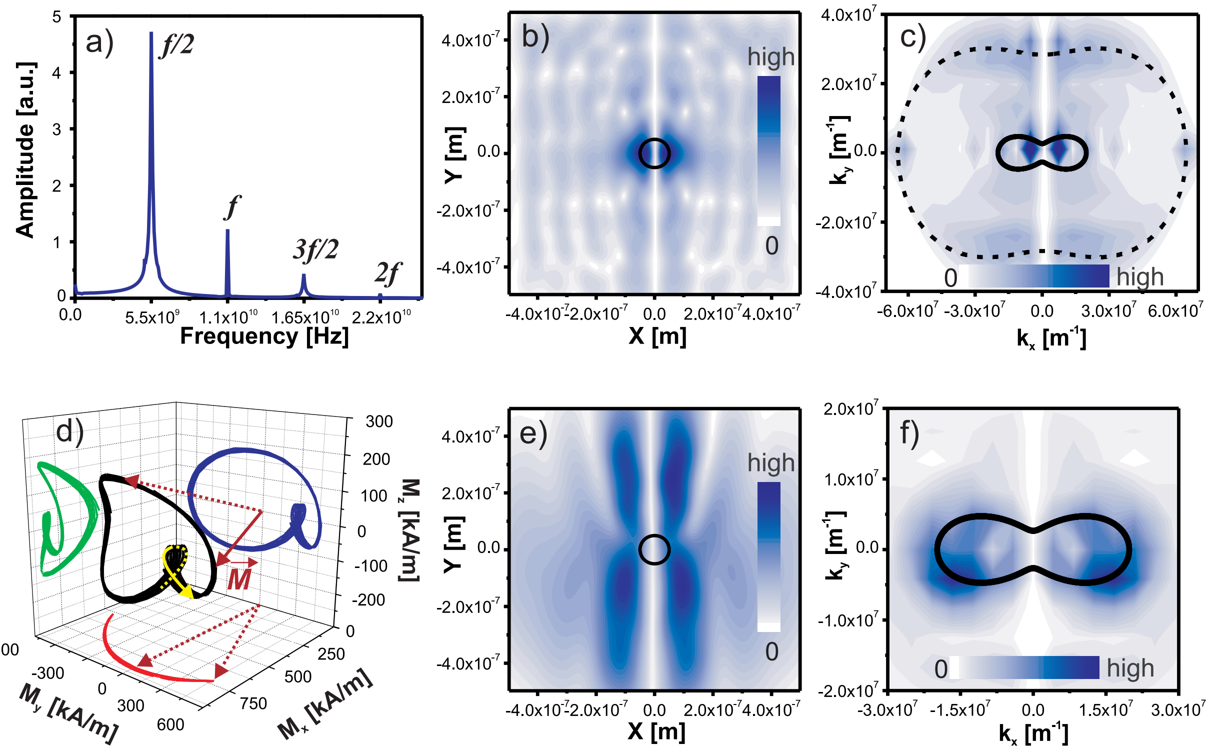

Fig. 5: a) Magnetization oscillation spectrum for the same cell as in the previous cases at the pumping frequency $f = 11$ GHz. b) Spatial distribution of the amplitude of the magnetization oscillation at $f = 11$ GHz and the position of the nanocontact in the center (black line). c) Distribution of the f mode in the wavevector space. The dash and continue curves represent the constant-frequency curve calculated analytical for 11 GHz and 5.5 GHz, respectively. d) Trajectory of the local magnetization vector tip for the cell at the edge of the contact. e) Spatial distribution of the $f/2$ mode. f) Distribution of the $f/2$ mode in phase space. The black line represents the constant-frequency curve calculated analytical for a frequency of 5.5 GHz

to the integer harmonics (f and $2f$). The data is proving that the law of energy conservation for three-magnon scattering processes is fulfilled, since any mode could be obtained as a combination (confluence or splitting) of the other modes. The linearly excited mode f behave very similar as in the previous case. The spatial distribution shows a localization of the mode at the edges of the contact (Fig. 5b). The distribution in the phase space demonstrates travelling spin waves with wavevectors perpendicular to the bias field (Fig. 5c). A very good agreement with the analytical constant-frequency curve (black curve in the figure) calculated at 11 GHz was obtained. The local magnetization shows that the precession of its vector tip has a steady but complicated trajectory when the process of three-magnon scattering takes place, different from a typical clamshell orbit found in thin films. This fact is illustrated in Fig. 5d. The spatial distribution extracted for the $f/2$ mode is presented in Fig. 5e. The black circle indicates the position of the nanocontact. One can observe that this mode is localized outside the contact area in the region where the directly excited mode is propagating. The analysis in the phase space (displayed in Fig. 5f) of the $f/2$ mode shows two maxima of the intensity distribution. These maxima correspond to a propagation of spin waves with wavevectors under an angle of $13^\circ \pm 2^\circ$ with respect to the bias field. The asymmetry with respect to the k_x-axis (wavevectors parallel to the bias field) could be related to additional contributions of the lead to the internal field.

It has to be marked that the wave numbers obtained from the intensity distributions in the phase space for both f and $f/2$ modes do not fulfill the momentum conservation law. Moreover, from the slowness surfaces calculated for 5.5 GHz and 11 GHz (Fig. 5c) one sees that the conservation of momentum during the splitting process, is not satisfied in fact for any combination of wavevectors. In other words, there is no pair of wavevectors at the frequency of 5.5 GHz that can combine into one corresponding to 11 GHz, or vice versa. This observations shows that in the given configuration, the three-magnon scattering processes does not take place in the free space. The splitting processes can occur only in the near field region of the point contact. To reveal the mechanism underlaying the splitting (confluence) process is a task of a future research.

In conclusion we performed a micromagnetic analysis of the linear and nonlinear spin waves modes excited by microwave currents in a nanocontact structure. Spectral positions of those modes are determined both in the space, frequency and phase domains. The obtained spatial patterns of the oscillation amplitude of the magnetization shows that the linear excited mode with a frequency matching the microwave one is mostly concentrated at the edge of the contact, while the nonlinear modes are located outside the contact. The analysis in the phase space demonstrate that the directly excited mode is propagating with a wavevector perpendicular to the external bias field. The nonlinear modes are emitted from the contact under certain angles with respect to the static field.

Financial support by the EU (SPINSWITCH, MRTN-CT-2006-035327) is gratefully acknowledged.

References

[1] H. Schultheiss, X. Janssens, M. van Kampen, F. Ciubotaru, S.J. Hermsdoerfer, B. Obry, A. Laraoui, A.A. Serga, L. Lagae, A.N. Slavin, B. Leven, B. Hillebrands, Phys. Rev. Lett. **103**, 157202 (2009).
[2] V.E. Demidov, S.O. Demokritov, G. Reiss, K. Rott, Appl. Phys. Lett. **90**, 172508 (2007).
[3] V.E. Demidov, S.O. Demokritov, B. Hillebrands, M. Laufenberg, P.P. Freitas, Appl. Phys. Lett. **85**, 2866 (2004).
[4] A.G. Gurevich, G.A. Melkov, *Magnetization Oscillations and Waves*. Boca Raton, FL: CRC (1996).
[5] B.A. Kalinikos, A.N. Slavin, J. Phys. C **19**, 7013 (1986).
[6] The simulations were performed using the OOMMF open code: M.J. Donahue, D.G. Porter, Report NISTIR 6376, NIST, Gaithersburg, MD, USA (1999)
[7] LLG Micromagnetics software developed by M. R. Scheinfein.

E. Heusler Compounds and other Magnetic Films

Heusler compounds are promising as a new class of materials due to their possible use in the novel field of spin-dependent devices, such as non-volatile memory with low energy consumption and new types of magnetic sensors. The interest in Heusler compounds comes from the half-metallic character of their spin-split band structure, as predicted by ab-initio calculations for many compounds of this material class. Half-metallic character means that the material provides metallic behavior for electrons with one spin component (e.g. for electrons with spins oriented ‘up’), and insulating behavior for the other spin orientation (e.g. for electrons with spins oriented ‘down’). As such, these materials may exhibit a 100 % spin polarization at the Fermi level, which would make them ideal candidates for e.g. spin polarizers or spin detectors. Heusler compounds are materials with the very general composition X_2YZ (with X, Y being a transition metal and Z an element from the III-V groups), where each element X,Y,Z can be chosen from about 10 different elements. Hence, the desired properties of the Heusler compounds can be tuned by adjusting their composition. The most well-known example is the group of Co_2YZ compounds showing a large Curie temperature, a large magnetic moment, and are predicted to provide half-metallic behavior. Furthermore, for a fine tuning, quaternary Heusler compounds can be used, such as $X_2YZ1_{1-x}Z2_x$, where Z1 and Z2 are different chemical elements.

Our group was part of a larger initiative, the Research Unit 559 funded by the Deutsche Forschungsgemeinschaft, allying several research groups at the Universities of Kaiserslautern, Mainz and Sendai. This initiative ended in summer 2010. Within this initiative, our goal was to investigate magnetic properties of Heusler compounds, namely the exchange stiffness, the magnetic anisotropy and the magneto-optical properties. The follow-up project is established as Japanese-German Research program “*Advanced Spintronic Materials and Transport Phenomena*” ASPIMATT.

In Report 4.17 we provide a study on the quadratic magneto-optical Kerr effect on epitaxial Co_2MnSi thin films for different annealing temperatures. In parallel to the increasing $L2_1$ ordering with higher annealing temperatures we observe an increase of the QMOKE while it is not present for the low annealing temperatures. Consequently, we conclude that we can link the higher degree of $L2_1$ ordering with the presence of QMOKE.

Report 4.18 discusses the magnetic behavior of embedded antiferromagnetic elements at remanence. We find that it is dominated by rectangular domains appearing on two opposed edges. While the inner region of the squares is still coupled antiferromagnetically, behaving like the environment, the coupling in the edge domain region is ferromagnetic. For elements smaller than 4 µm, the domains meet in the center and the coupling becomes completely ferromagnetic, i.e. they lose their antiferromagnetic coupling completely and cannot be treated as individual elements anymore.

E. Heusler-Legierungen und andere magnetische Schichten

Heusler-Verbindungen sind eine vielversprechende Materialklasse aufgrund ihrer möglichen Verwendung für neuartige, den magnetischen Spin nutzende Bauteile, z.B. für nichtflüchtige Computerspeicher mit geringem Energiebedarf oder für neue magnetischen Sensoren. Aufgrund ihres spin-aufgespaltenen Valenzbands zeigen diese synthetischen anorganischen Verbindungen ein halbmetallisches Verhalten: Für eine der beiden Spinorientierungen (z.B. Spin “up”) verhält sich das Material wie ein Metall, für die entgegen gesetzte Orientierung (z.B. Spin “down”) wie ein Isolator. Diese Verbindungen können daher eine vollständige Spinpolarisation an der Fermi-Kante aufweisen. Damit sind Heusler-Verbindungen ideale Kandidaten für Spinpolarisatoren oder Spindetektoren. Heusler-Verbindungen haben die chemische Struktur X_2YZ, wobei X, Y, Z aus etwa zehn verschiedenen Elementen des Periodensystems gewählt werden können. Die gewünschten Eigenschaften der Heusler-Verbindungen können daher durch die geeignete chemische Zusammensetzung eingestellt werden. Außerdem sind viele Heusler-Verbindungen mit den Anforderungen der modernen Halbleitertechnik kompatibel (z.B. können sie epitaktisch auf Gallium-Arsenid (GaAs) aufgewachsen werden). Weitere Vorteile sind, das sie stabil und relativ einfach zu wachsen sind und oft aus preisgünstigen Materialien bestehen. Die am besten untersuchten Beispiele sind Kobalt-basierende Verbindungen (Co_2YZ). Diese zeigen eine hohe Curie-Temperatur, ein großes magnetisches Moment und, wie von ab-initio Rechnungen vorhergesagt, ein halbmetallisches Verhalten.

Als Teil einer Kooperation mit Arbeitsgruppen an den Universitäten Kaiserslautern, Mainz und Sendai haben wir die magnetischen Eigenschaften von Heusler-Verbindungen hinsichtlich der Stärke der Austauschwechselwirkung (Austausch-Steifigkeitskonstante), der magnetischen Anisotropien und der magneto-optischen Eigenschaften untersucht.

In Bericht 4.17 stellen wir eine Studie der Abhängigkeit des quadratischen magneto-optischen Kerr-Effekts (QMOKE) dünner Co_2MnSi Schichten von der Anlasstemperatur vor. Wir beobachten, dass sich parallel zur Erhöhung der $L2_1$ Ordnung mit steigender Anlasstemperatur der QMOKE Effekt einstellt und wächst. Daraus folgern wir eine direkte Verknüpfung des QMOKE-Effektes mit dem $L2_1$ Ordnungsgrad.

Bericht 4.18 beschreibt die Untersuchung des magnetischen Verhaltens eingebetteter antiferromagnetischer Strukturen in Remanenz. Dieses wird dominiert von rechteckigen Domänen, die an den gegenüberliegenden Rändern der Elemente nukleieren. Während das Innere der Elemente antiferromagnetisch gekoppelt bleibt, sind die Randgebiete ferromagnetisch gekoppelt. Bei Elementen, die kleiner als 4 µm sind, treffen die Domänen in der Mitte aufeinander und die gesamte Kopplung wird ferromagnetisch. Das heißt, sie verlieren ihre antiferromagnetische Kopplung und können nicht mehr als individuelle Elemente betrachtet werden.

4.17 Quadratic magneto-optical Kerr effect on epitaxial Co_2MnSi thin films

G. Wolf, J. Hamrle, and B. Hillebrands[1]

Cobald-based Heusler compounds have been extensively investigated because they were predicted to be half metallic ferromagnets. This property made them promising candidates for applications in spintronic devices. Their structural and electronic properties strongly depend on the crystal structure. The ordering in the crystal structure can be improved with post deposition annealing, which has been demonstrated for several systems [1–4]. During this intense characterization process of the magnetic, electronic and structural properties of these materials, it has been observed that some of the Co-based Heusler compounds show the second order magneto-optic Kerr effect. This has been reported for Co_2FeSi [5], $Co_2FeSi_{0.5}Al_{0.5}$ [6], Co_2MnGe [7, 8] and Co_2MnSi [9]. In the case of Co_2MnSi, the authors mentioned the presence of a quadratic magneto-optical Kerr effect, but did not further investigate the dependance on the annealing temperature. This work here follows the question, if there is a correlation between the second order magneto-optic Kerr effect and the crystallographic structure of the compound. We investigated a series of samples of Co_2MnSi with different post deposition annealing temperatures, similar to the previous work. It was reported that Co_2MnSi changes its crystallographic ordering from the B2 structure to the $L2_1$ structure with higher annealing temperature.

The Co_2MnSi films were epitaxial grown on MgO substrates with a 40 nm thick Cr buffer layer by inductively coupled plasma-assisted magnetron sputtering. The Co_2MnSi film thickness is 30 nm in combination with a 1.3 nm thick Al layer, to prevent oxidation. After deposition the samples were annealed at different temperatures, in order to achieve different degrees of ordering. The annealing temperatures range from 300 °C up to 500 °C.

In order to verify the increasing $L2_1$ ordering with the annealing temperature, X-ray diffraction was measured. In Figure 1a the pole scans (scan the in-plane angle ϕ) of the (111) reflection are shown. For the lower annealing temperature (300 °C and 350 °C) no (111) reflection can be seen, whereas

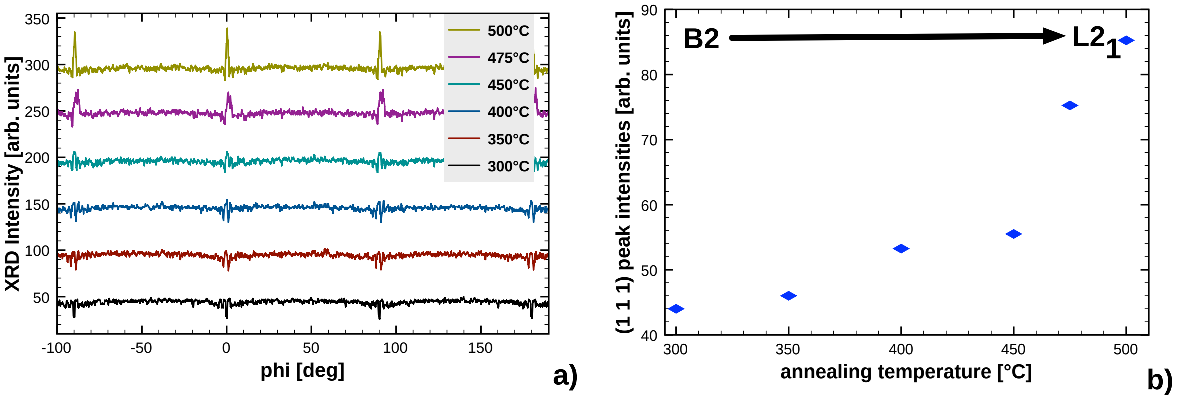

Fig. 1: a) X-ray diffraction pole scans of the (111) peak for different post deposition annealing temperatures. b) Extracted (111) peak intensities as function of the annealing temperature.

---

[1] In collaboration with T. Kubota, Y. Ando, Department of Applied Physics, Graduate School of Engineering, Tohoku University, Sendai, Japan.
J.H. is now at Institute of Physics, VSB - Technical University of Ostrava, CZ-70833 Ostrava-Poruba, Czech Republic.

it increases up to the maximum intensity for an annealing temperature of 500 °C. Since the (111) reflection is characteristic for the $L2_1$ structure, we conclude that the ordering changes from the B2 to the $L2_1$ crystal structure with the annealing temperature, as it was previously reported [9].

The Co_2MnSi thin films were investigated by means of magneto-optic Kerr effect (MOKE). The applied method, to determine the quadratic MOKE (QMOKE), has been successfully used in several other works [6, 7, 10, 11]. In this section only a brief description of the underlying theory and the experimental method is given.

Starting from the most general case, the longitudinal MOKE configuration, the Kerr signal is determined by several contributions

$$\Theta_{\mathrm{Kerr}} = \theta_{\mathrm{L}} M_{\mathrm{L}} + \theta_{\mathrm{P}} M_{\mathrm{P}} + \sum \theta_{\mathrm{ij}} M_{\mathrm{i}} M_{\mathrm{j}} \quad , \tag{1}$$

where θ_{L}, θ_{P} and θ_{ij} are proportionality factors, containing the angle of incidence, the index of refraction and the magneto-optic constants. M_{L} is the magnetization component in the film plane, parallel to the plane of the incident light (longitudinal component), M_{T} is the magnetization component in the film plane, perpendicular to the plane of the incident light (transversal component), and M_{P} is the magnetization component out of the film plane (polar component). Since soft magnetic thin films are subject of this investigation, the strong demagnetizing fields force the magnetization into the film plane, which allows us to neglect the out of plane component M_{P}. The measured Kerr signal is now determined by the linear longitudinal term and the second order terms. The exact Kerr angle can be calculated by expanding the dielectric tensor as a function of the magnetization up to the second order and using a wave equation formalism (for a detailed description see [10, 12, 13]). For the investigated system with a cubic symmetry and a (100) interface plane the Kerr angle is given by

$$\begin{aligned}\Theta_{\mathrm{Kerr}} &= BKM_{\mathrm{L}} \\ &\quad +A\left(-\frac{K^2}{\varepsilon}+2G_{44}+\frac{\Delta G}{2}\right)M_{\mathrm{L}}M_{\mathrm{T}} \qquad\qquad (2) \\ &\quad -A\frac{\Delta G}{2}\cos(4\alpha)M_{\mathrm{L}}M_{\mathrm{T}} \\ &\quad -A\frac{\Delta G}{4}\sin(4\alpha)(M_{\mathrm{L}}^2-M_{\mathrm{T}}^2)\end{aligned}$$

$$\tag{3}$$

where ε is the dielectric constant, K the linear magneto-optic constant and $\Delta G = G_{11} - G_{12} - 2G_{44}$, with G_{11}, G_{12} and $2G_{44}$ being the elements of the quadratic magneto-optic tensor. The factors A and B are optical weighting factors that are even and odd functions of the angle of incidence. The angle α is the orientation of the crystallographic axes with respect to the plane of incidence (see Fig. 3a). In Eq. (2) three different contributions to the total Kerr signal appear: (I) the linear contribution proportional to M_{L}, (II) the contribution proportional to the product of $M_{\mathrm{L}}M_{\mathrm{T}}$ and (III) the contribution proportional to the difference of the squares of the magnetization components $M_{\mathrm{L}}^2 - M_{\mathrm{T}}^2$. It is obvious that both second order contributions depend on the sample orientation and on the value of ΔG. The $M_{\mathrm{L}}M_{\mathrm{T}}$ contribution also has a constant offset, that depends on all magneto-optic constants.

To separate the different contributions, the Kerr-effect magnetometer described in [14] was used. The setup uses probing light of a wavelength of 638 nm. All measurements are limited to the Kerr rotation. Saturation fields are applied in the 8 directions indicated in Fig. 3a (This method is

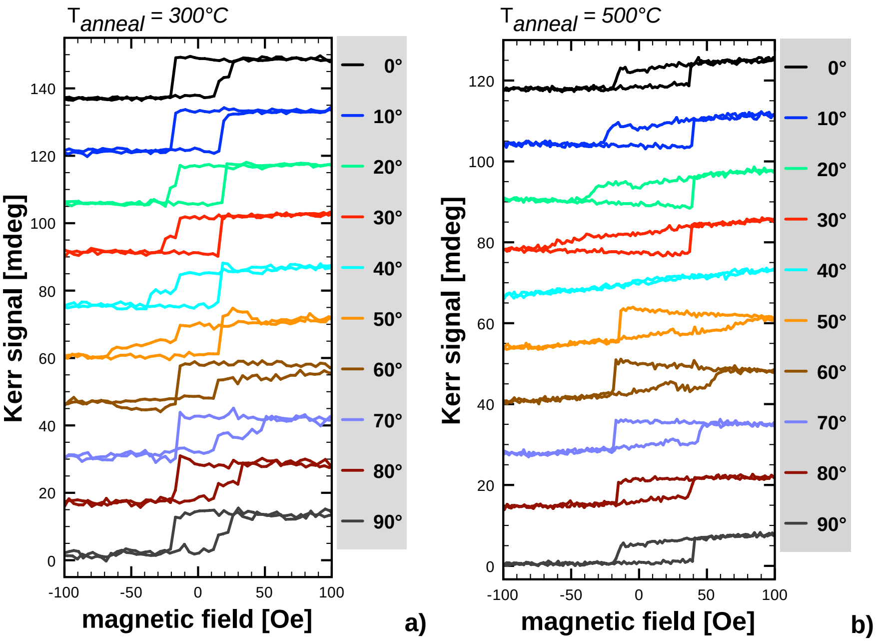

Fig. 2: Magnetization reversal curves for a) a sample annealed at 300 °C and b) annealed at 500 °C for different sample orientations with respect to the magnetic field, ranging from 0° to 90°.

often referred as 8 field method). In these directions either the $M_L M_T$ contribution or the $M_L^2 - M_T^2$ contribution is zero and the remaining contribution can be extracted. Rotating the sample in plane, we can obtain the QMOKE contributions as a function of the sample orientation. This procedure was applied to a sample series of Co_2MnSi thin films.

Before using the 8 field method, magnetization reversal loops were obtained as a function of the sample orientation with respect to the applied magnetic field. Figure 2 shows the magnetization reversal curves for different orientations for a sample annealed at 300 °C (a) and a sample annealed at 500 °C (b). The Kerr signal is rather small compared to the noise level for all the samples. The shape of the magnetization reversal loops changes with the sample orientation due to the magnetic anisotropy. The magnetic easy axis can be found at 0° and 90° orientation (corresponding to the [110] directions of the Co_2MnSifilm), whereas the hard axis is found at 45° orientation (corresponding to the [100] directions). This behavior is expected for a system with cubic symmetry. The shape of the reversal loops is not only determined by the magnetic anisotropy, but also by the nucleation and movement of magnetic domains. In the case of the sample annealed at 500°C one can observe an asymmetry in the reversal loops, which is due to the quadratic MOKE. But since the signal to noise ratio is quite small, it is not possible to clearly distinguish between quadratic MOKE and noise here.

The 8 field method was employed to separate the quadratic components from each other and from the linear MOKE. Since this method uses saturation fields it is not sensitive to any effects like the formation and movement of domains as visible in the reversal loops. Figure 3b presents a typical result of the 8 field method for a sample annealed at 475 °C. The signal was recorded at perpendicular incidence, where the longitudinal contribution vanishes. It is obvious that both quadratic contributions follow the sin (cos) function as expected from Eq. (2). Fitting the experimental data, amplitudes of the sin (cos) and the constant offset were extracted. These values are directly correlated to the second order magneto-optic constants, especially the ΔG value and thus the strength of the QMOKE. Figure 4 shows these amplitudes and offset as a function of the annealing temperature. The values for the amplitude of the $M_L M_T$ and the $M_L^2 - M_T^2$ contributions are the same within the experimental error for each annealing temperature. This is expected from the model

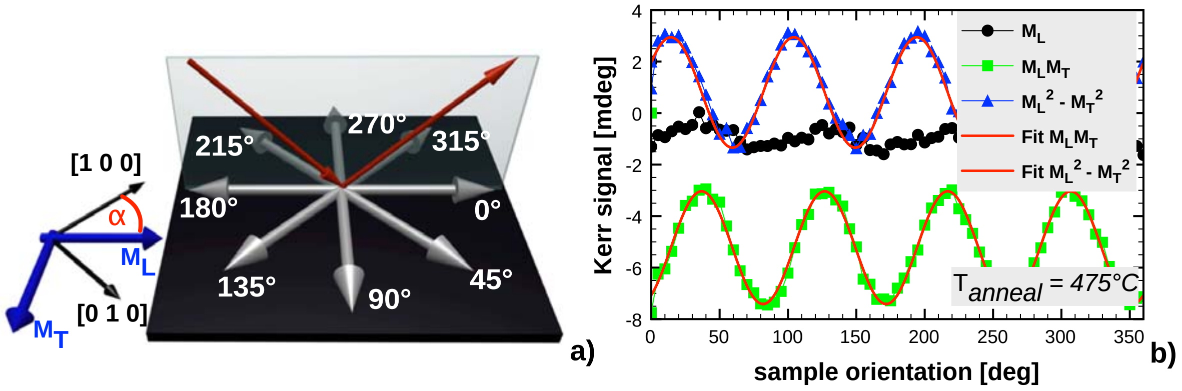

Fig. 3: a) Schematic drawing of the 8 field method. b) The separated QMOKE contributions as a function of the sample orientation α for a sample annealed at 475 °C recorded at perpendicular incidence. M_L contribution (dots), $M_\mathrm{L}M_\mathrm{T}$ contribution (squares), $M_\mathrm{L}^2 - M_\mathrm{T}^2$ contribution (triangles), fit function according to Eq. (2) (lines).

(see also [5]) and thus a good indication that the cubic model we applied is correct. For the low annealing temperatures (300 °C and 350 °C) the values are rather small, so that they can be assumed to be zero within the error bar. This leads to the conclusion that no or only very small QMOKE is present for these annealing temperatures. For the higher annealing temperatures the values of the amplitudes increase up to the maximum value of 2.1 mdeg for an annealing temperature of 475 °C. Since the $\mathrm{L2_1}$ ordering is strongly correlated to the annealing temperature, we can summarize that the ΔG value increases with higher ordering and is zero for structure without $\mathrm{L2_1}$ ordering.

The offset of the $M_\mathrm{L}M_\mathrm{T}$ contribution is larger than the amplitudes, but generally it follows the same trend as the amplitudes. According to Eq. (2) the linear magneto-optic constants K and G_{44} contribute to the offset. Since K is, in general, a small number ($K \ll 1$) and in the order of the quadratic magneto-optic constants (see below), it can be neglected in a first approximation. The difference between amplitudes and offset is now only given by the G_{44} factor. The difference between offset and amplitude is not changing drastically, so it can be assumed that G_{44} is not changing drastically with the annealing temperature. This underlines the conclusion that the ΔG factor is increasing with annealing temperature.

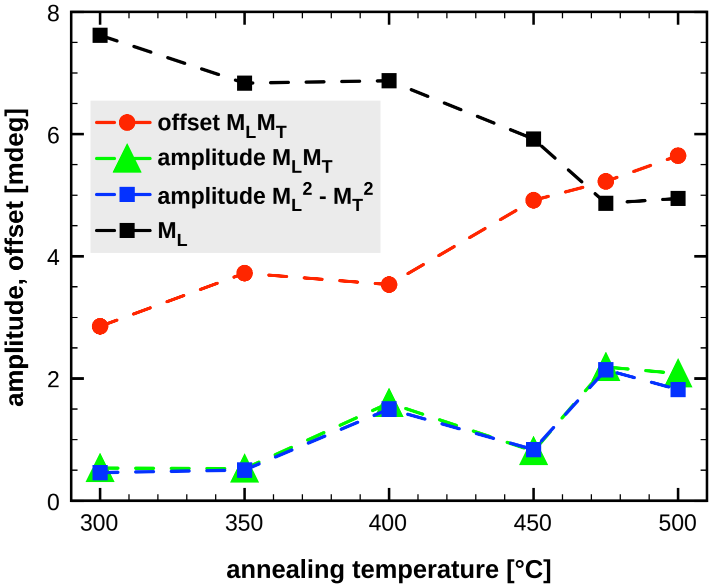

Fig. 4: The M_L contribution (at angle of incidence of 45 °), the amplitudes and offset of the $M_\mathrm{L}M_\mathrm{T}$ contribution and the amplitude of the $(M_\mathrm{L}^2 - M_\mathrm{T}^2)$ (at perpendicular incidence) as a function of the post deposition annealing temperature.

At this point it is worth noting that the linear magneto-optical component, obtained at an angle of incidence of 45°, is decreasing with annealing temperature (black squares in Fig. 4).

In summary, we investigated the dependance of the quadratic magneto-optical Kerr effect on the post deposition annealing temperature of Co_2MnSi films. The X-ray diffraction reveals that the $L2_1$ ordered structure is present in the samples with higher annealing temperatures. We observe that the QMOKE is not present for the low annealing temperatures, while it is increasing for higher annealing temperatures. We also find that for samples, which exhibit QMOKE, the measured 8 field curves fit very well to the theoretical prediction for a cubic system. Although the linear magneto-optic constant is in general quite small in this system, it also decreases with the higher annealing temperature. Comparing the QMOKE strength with the LMOKE strength, we showed that the QMOKE is of a similar magnitude in highly ordered Co_2MnSi. Based on these results we can link the higher degree of $L2_1$ ordering with the presence of QMOKE, even though the linear MOKE is quite small. Namely the cubic magneto-optical term ΔG increases with $L2_1$ order. A similar increase of QMOKE with higher ordering was observed on $Co_2FeSi_{0.5}Al_{0.5}$ [6].

Financial support by Deutsche Forschungsgemeinschaft (DFG, FOR 559 and FOR 1464) is gratefully acknowledged.

References

[1] Y. Sakuraba, M. Hattori, M. Oogane, H. Kubota, Y. Ando, A. Sakuma, T. Miyazaki, J. Phys. D **40**, 1221 (2007).
[2] Y. Takamura, R. Nakane, S. Sugahara, J. Appl. Phys. **107**, 09B111 (2010).
[3] W. Wang, H. Sukegawa, R. Shan, T. Furubayashi, K. Inomata, Appl. Phys. Lett. **92**, 221912 (2008).
[4] T. Ishikawa, T. Marukame, K. Matsuda, T. Uemura, M. Arita, M. Yamamoto, J. Appl. Phys. **99**, 08J110, (2006).
[5] J. Hamrle, S. Blomeier, O. Gaier, B. Hillebrands, H. Schneider, G. Jakob, K. Postava, C. Felser, J. Phys. D **40**, 1563 (2007).
[6] S. Trudel, G. Wolf, J. Hamrle, B. Hillebrands, P. Klaer, M. Kallmayer, H.J. Elmers, H. Sukegawa, W. Wang, K. Inomata, submitted to Phys. Rev. B .
[7] S. Trudel, J. Hamrle, B. Hillebrands, T. Taira, M. Yamamoto, J. Appl. Phys. **107**, 43912 (2010).
[8] P. K. Muduli, W.C. Rice, L. He, B.A. Collins, Y.S. Chu, F. Tsui, J. Phys.: Condens. Matter **21**, 296005 (2009).
[9] O. Gaier, J. Hamrle, S.J. Hermsdoerfer, H. SchultheißB. Hillebrands, Y. Sakuraba, M. Oogane, Y. Ando, J. Appl. Phys. **103**, 103910 (2008).
[10] K. Postava, D. Hrabovsky, J. Pistora, and A. R. Fert, S. Visnovsky, T. Yamaguchi, J. Appl. Phys. **91**, 7293 (2002).
[11] M. Buchmeier, R. Schreiber, D. E. Bürgler, C. M. Schneider, Phys. Rev. B **79**, 064402 (2009).
[12] S. Visnovsky, Czech. J. Phys. B **36**, 625 (1986).
[13] S. Visnovsky, R. Lopusnik, M. Bauer, J. Bok, J. Fassbender, B. Hillebrands, Opt. Express **9**, 121 (2001).
[14] S. Trudel, G. Wolf, H. Schultheiß, J. Hamrle, T. Kubota, Y. Ando, B. Hillebrands, Rev. Sci. Inst. **81**, 026105 (2010).

4.18 Magnetic behavior of embedded antiferromagnetic elements at remanence

R. Neb, P.A. Beck, T. Sebastian, P. Pirro and B. Hillebrands[1]

The magnetic behavior of tiny magnetic elements is subject to intensive research because of the importance in magnetic recording devices. In our approach, small magnetic elements are created by gentle focused ion beam irradiation of an antiferromagnetically coupled magnetic double layer. By adjusting the parameters of the irradiation it is possible to create elements which do not protrude from the surface significantly, in comparison to the tens or even hundreds of nanometers when using other techniques. Such elements are called "embedded elements". Previous works investigated bilayer elements with ferromagnetic interlayer coupling in an antiferromagnetically environment. Blomeier et al. [1, 2] could show that the magnetic behavior of these elements strongly depends on their size. Based on that work we study the opposite situation of antiferromagnetically coupled squares of different size, embedded in a ferromagnetically coupled environment in remanence.

As in Ref. [1, 2] we used an Fe/Cr/Fe trilayer, grown by Molecular Beam Epitaxy (MBE) in an UHV chamber with a base pressure better than $2 \cdot 10^{-11}$ mbar on MgO(100) substrates. The substrate was heated to 600 K for about half an hour to remove water and adsorbates from the sample surface. Then it was irradiated by an O^+/Ar^+ plasma for fifteen minutes in order to eliminate carbon residua. Afterwards an Fe(10 nm)/Cr(0.7 nm)/Fe(10 nm) trilayer was grown at a temperature of 120°C. In order to prevent the sample from corrosion a 2 nm Cr cap layer was grown on top at room temperature. The quality of the epitaxial growth was controlled *in-situ* by Low Energy Electron Diffraction (LEED).

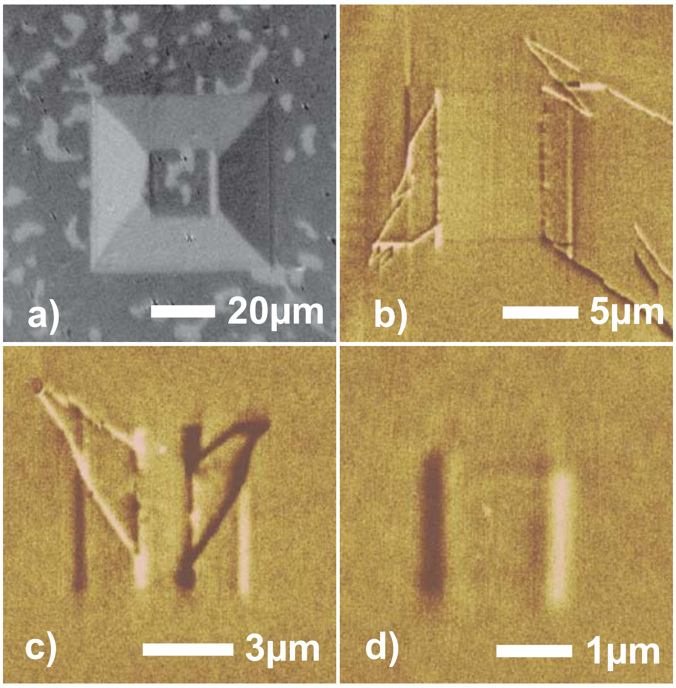

Fig. 1: a) Kerr image of a $20 \times 20\,\mu m^2$ antiferromagnetically coupled square inside a $50 \times 50\,\mu m^2$ ferromagnetically coupled host square. A typical pattern can be seen inside the inner square [3]. b)-d) MFM images of $10 \times 10\,\mu m^2$, $5 \times 5\,\mu m^2$ and $2 \times 2\,\mu m^2$ antiferromagnetically coupled squares in a $50 \times 50\,\mu m^2$ ferromagnetically coupled host square at remanence. Along the vertical edges rectangular domains can be seen, except for the smallest square. The small stripes in d) indicate a magnetic charge contrast between the inner square, magnetized from left to right, and the outer region.

---

[1] In collaboration with S. Pofahl, R. Schäfer IFW Dresden, Dresden, Germany; B. Reuscher, M. Kopnarski IFOS, Kaiserslautern, Germany.

The chosen Cr interlayer thickness ensures that the two Fe layers couple antiferromagnetically. The coupling can be changed to ferromagnetic by irradiating the system with high-energy ions to modify the Cr interlayer. As it has been shown in Ref. [1, 2] this allows for the creation of customized ferromagnetically coupled areas. By choosing an appropriate ion dose, the topography is left mainly unaltered and the irradiated elements are embedded into the surrounding.

We used this technology to pattern $50 \times 50\,\mu\mathrm{m}^2$ irradiated elements which form the ferromagnetically coupled host. In the center, squares of different size between $20\,\mu$m and $2\,\mu$m were left non-irradiated and thus still couple antiferromagnetically. Irradiation was done using a FEI ALTURA 865 dual-beam focused 30 keV Ga^+-ion beam source with a spot diameter of about 40 nm. An ion fluency of $2.7 \cdot 10^{16}\,\mathrm{ions/cm}^2$ was used for all samples.

The magnetic properties of these antiferromagnetically coupled squares were examined by Kerr imaging and Magnetic Force Microscopy (MFM). Figure 1a shows a Kerr image of a $20 \times 20\,\mu\mathrm{m}^2$ non-irradiated element inside a $50 \times 50\,\mu\mathrm{m}^2$ irradiated host element in remanence. It is clearly visible that the inner region behaves like the antiferromagnetically coupled environment, both showing typical patch domains with domain sizes of about 5-10 μm in diameter [3]. Two rectangle domains can be seen on opposite sides of the element. As shown in prior studies [2], the coupling between (small) ferromagnetic elements embedded into an antiferromagnetically coupled area is limited to a distance of roughly 1 μm. If the antiferromagnetic area is sufficiently large, most of it is insensitive to the influence of the surrounding ferromagnetic region and will behave like a homogeneous antiferromagnetically coupled layer system. It is likely to assume that any inverse pattern, widely independent of shape, will show the same behavior if its size is of the same order.

Smaller samples were studied by MFM. Figures 1b-d show squares of different sizes in remanence. The magnetic images are dominated by two rectangular edge domains. They have a width of about 2 μm for any size of the antiferromagnetic squares, and they are only apparent on two of the four sides of the squares, although the Fe/Cr/Fe trilayer has a fourfold symmetry. The direction of the edge domains is the same for all squares on a sample, which suggests that the symmetry of the sample is broken. From Fig. 1d it is evident that the edge domains inside the element are not apparent for squares as small as $2 \times 2\,\mu\mathrm{m}^2$. This indicates a merging of the two edge domains, leading to a homogeneous magnetization from left to right in the center, which leads to a magnetic charge contrast at the border between inner and outer square.

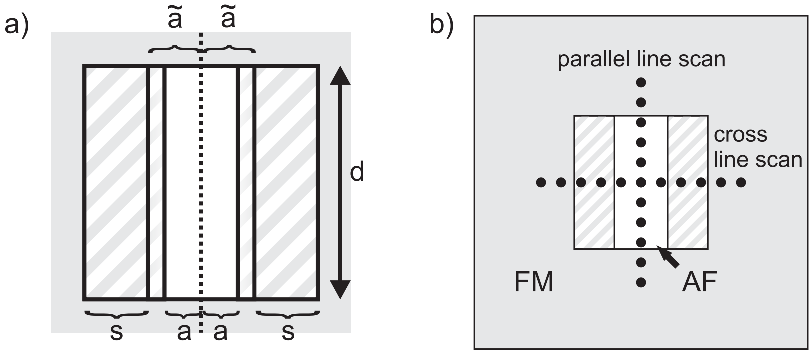

Fig. 2: a) Definition of the parameters used. d is the edge length of the inner square, s the width of the edge domains, a the distance between center and inner domain edge. If a linear transition from ferromagnetic to antiferromagnetic coupling is assumed, then $\tilde{a}$ is the difference between the center and the starting point of the transition, hence $(\tilde{a} - a)$ is the transition regime width. b) Illustration of the scan directions. The scanning can be used to determine the coupling nature of the different areas.

In order to examine the nature of the coupling in the edge domains, we use Magneto-Optical Kerr-Effect magnetometry (Micro-MOKE) to investigate the hysteresis loops. Ferromagnetic coupling leads to a strong jump of magnetization near zero field, while antiferromagnetic coupling does not show such a behavior (examples are not depicted here). However, since the laser spot has a Gaussian distribution with a measured standard deviation of 0.51 µm, contributions of the ferromagnetic as well as the antiferromagnetic regime are visible even if the spot is perfectly centered inside the antiferromagnetic square, which leads to ambiguous hysteresis loops. To cope with this, we assume a simple model for the magnetization as drawn in Fig. 2. The edge domains in this model are assumed to be perfectly ferromagnetic, while the interior is perfectly antiferromagnetic. In this simple model we assume no transition region, so that $a = \tilde{a}$. Thus the jump height $J(x)$, which corresponds to twice the remanence for a perfect ferromagnetic rectangular hysteresis curve (see Fig. 3), can be calculated by

$$J(x) = J_{\max}\left(1 - \frac{1}{\sigma\sqrt{2\pi}}\int_{-a-x}^{a-x} \mathrm{e}^{\frac{x'^2}{2\sigma^2}}\,\mathrm{d}x'\right)$$

where a is half the width of the area between the edge domains (see Fig. 2a), σ the standard deviation of the beam, and $J_{\max}$ the jump height for a completely ferromagnetic area. Calculation of the integral yields:

$$J(x) = J_{\max}\left\{1 - \frac{1}{2}\left[\operatorname{erf}\left(\frac{a+(x+b)}{\sqrt{2}\sigma}\right) + \operatorname{erf}\left(\frac{a-(x+b)}{\sqrt{2}\sigma}\right)\right]\right\}$$

where we introduced an offset b to x which accounts for the deviation of the Gaussian distribution from the chosen origin, and erf represents the error function (see [4]). Figure 4 presents an overview of the measured values, while the inset shows the results of a typical scan and the fitted curve. We can conclude that the domain width is 1.8 ± 0.1 µm and is independent of the size of the square. To assist these estimations, we also performed a parallel line scan (see Fig. 2b) and extracted the minimum $J_{\max}$ values. In terms of the model the minimum $J_{\max}$ can be calculated as

$$J_{\max}(d) = 1 - \operatorname{erf}\left(\frac{d-2s}{\sqrt{8}\sigma}\right)\operatorname{erf}\left(\frac{d}{\sqrt{8}\sigma}\right) \tag{1}$$

where d denotes the edge length and s the domain width. By using that the minimum $J_{\max}$ value can be measured directly in the center of the square, Eq. (1) can be obtained simply by setting x

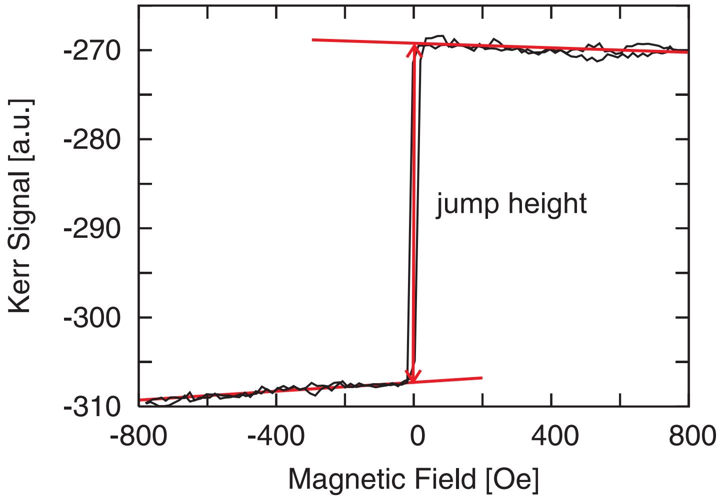

Fig. 3: Explanation of the jump height. The high-field and low-field shoulder of the hysteresis loop are fitted by a linear function. The difference is taken at zero field, yielding the jump height. For a rectangular ferromagnetic loop, this corresponds to twice the remanence.

and b in Eq. (1) to zero and using the relation $d-2s=2a$. The second erf-function stems from the two-dimensional extension of the sample; in the second dimension there are no edge domains, which results in $s=0$ in this dimension. The equation is normalized to 1, which corresponds to a completely ferromagnetic area. The fitted curve (Fig. 5) shows that this behavior is well matched, which corroborates our simple model. Values for s and σ coincide with the expected values. Since antiferromagnetic coupling is lost for squares of 3.5 µm edge length or smaller, we can conclude that the reason for this disappearance is the meeting of the edge domains in the center. This also indicates that creating smaller elements will not lead to different results, as these elements are always coupled ferromagnetically.

We can estimate the influence of a finite border size between the ferromagnetic and antiferromagnetic regions. The simplest model is also shown in Fig. 2a. The abrupt transition from ferromagnetic to antiferromagnetic regime (and back) is replaced by a linear transition with a width of $a-\tilde{a}$. The calculation is too long to be presented here in detail. Using the abbreviations

$$g_{y,z}(x) := \frac{1}{2}\left(\mathrm{erf}\left(\frac{z+x}{\sqrt{2}\sigma}\right)+\mathrm{erf}\left(-\frac{y+x}{\sqrt{2}\sigma}\right)\right)$$

$$h_{y,z}(x) := \frac{\sigma}{\sqrt{2\pi}}\left(\mathrm{e}^{\left(-\frac{(z+x)^2}{2\sigma^2}\right)}-\mathrm{e}^{\left(-\frac{(y+x)^2}{2\sigma^2}\right)}\right)$$

we obtain the relation

$$\begin{aligned} J(x) &= J_{\max}\left(g_{-\tilde{a},\tilde{a}}-\frac{h_{-a,-\tilde{a}}+h_{\tilde{a},a}}{a-\tilde{a}}\right. \\ &\qquad \left.+\frac{(a-x)g_{-a,-\tilde{a}}-(a+x)g_{\tilde{a},a}}{a-\tilde{a}}\right) \quad . \end{aligned} \tag{2}$$

However, the fit is ambiguous. Using different values for a and $\tilde{a}$ leads to nearly the same curve under the condition that $a_{\mathrm{eff}} := a+\tilde{a}$ is kept constant and $\tilde{a}$ is of the order of 100 nm or smaller. a_{eff} can be interpreted as half of the effective length of the antiferromagnetic regime. This shows that finite boundaries only lead to an increase of a in the fit by half the boundary size. Since these boundaries are about one order of magnitude smaller as the edge domain width, this error is negligible.

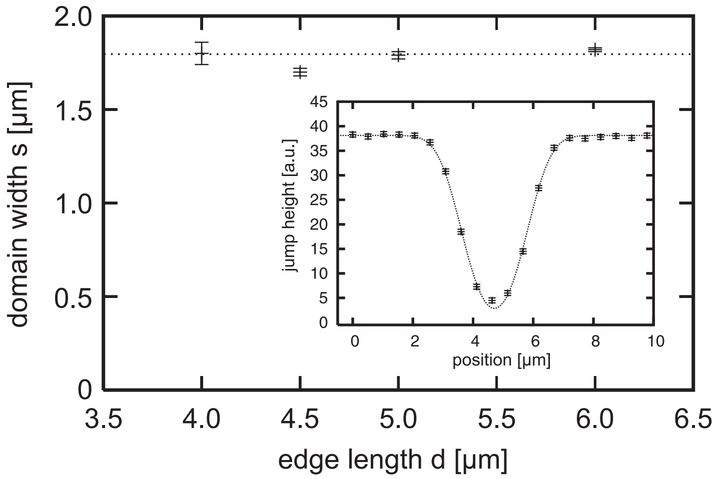

Fig. 4: Results of the determination of the edge domain width for different edge lengths via cross line scans. The width is about 1.8 µm, independently of the square size. The dotted line marks a width of 1.8 µm. Inset: Example for a cross line scan. The height of the jump is plotted versus the spot position. For the fit Eq. (1) is used, which yields the domain width.

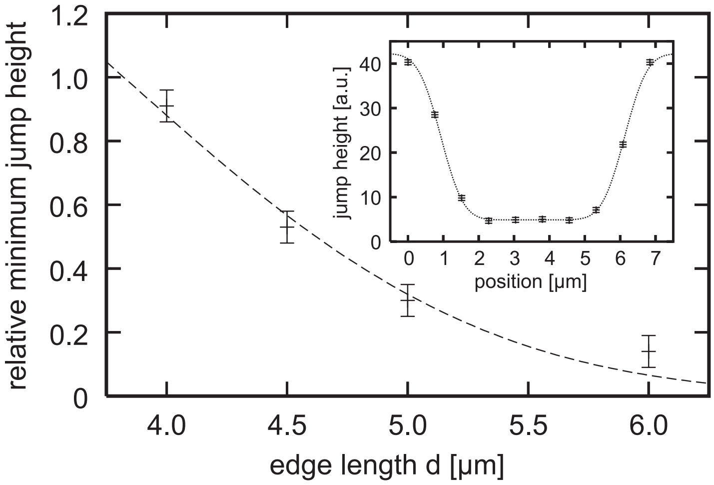

Fig. 5: Results of the parallel line scans. The minimum value of $J_{\max}$ is plotted versus the edge length of the square. The fit follows from Eq. (1) and yields a domain width of $1.91 \pm 0.05\,\mu\text{m}$. Inset: Example for a long line scan. $J_{\max}$ is plotted versus the spot position x. The distinctive plateau in the center allows for the determination of the minimum value of $J_{\max}$. The depicted fit is a modification of Eq. (1), where the erf-term was corrected by an additional factor which accounts for the finite size in perpendicular direction.

We have shown that the behavior of antiferromagnetically coupled squares in remanence is dominated by rectangular domains appearing on two opposed edges. While the inner region of the squares is still coupled antiferromagnetically, behaving like the environment, the coupling in the edge domain region is ferromagnetic. These domains break the fourfold symmetry of the sample. Micro-MOKE cross line scans of the hysteresis loops have shown that the edge domains have always the same width of 1.8 µm. When the sample size decreases below 4 µm, the domains meet in the center and the coupling becomes completely ferromagnetic. Thus we conclude that elements smaller than 4 µm lose their antiferromagnetic coupling completely and can't be treated as an individual element. This stands in contrast to the previous investigations of ferromagnetic square arrays, where a distance of more than 1 µm between two squares was sufficient to inhibit the interaction between them.

Financial support by the Deutsche Forschungsgemeinschaft (DFG, HI 380/18-3 and GRK 792) is gratefully acknowledged. We would like to thank U. Wolff (IFW, Dresden) for providing access to the MFM.

References

[1] S. Blomeier, P. Candeloro, B. Hillebrands, B. Reuscher, A. Brodyanski, M. Kopnarski, Phys. Rev. B **74**, 184405 (2006).

[2] S. Blomeier, B. Hillebrands, B. Reuscher, A. Brodyanski, M. Kopnarski, R.L. Stamps, Phys. Rev. B **77**, 094405 (2008).

[3] M. Rührig, R. Schäfer, A. Hubert, R. Mosler, J.A. Wolf, S. Demokritov, P. Grünberg, Phys. Stat. Sol. A **125/2**, 635-656 (1991).

[4] *Handbook of Mathematical Functions*, edited by N. Abramovitz and I. Stegun (Dover Publications, New York, 1965).

F. Applied Research and Technology

A general aim of our group is to span our research efforts between basic science and applied topics. Part of this is the development of new instrumentation and the advancement of the experimental techniques.

In Report 4.19 we present a new all-optical method to investigate the shape anisotropy of individual micron sized elements made of $Ni_{81}Fe_{19}$. We use a combination of Kerr microscopy with high angular resolution in the determination of the hysteresis loops and a quantitative analysis of the measured data. In Report 4.20 the development of TMR-based memory cells for low-cost, low-density memory is reported.

F. Angewandte Forschung und Technologie

Ein generelles Ziel der Arbeitsgruppe ist es, Forschung in der Breite zwischen erkenntnisorientierter Grundlagenforschung und angewandter Forschung zu betreiben. Ein Teil der Arbeit ist dabei der apparativen Entwicklung und der Fortentwicklung der Experimentiertechniken gewidmet.

Im Bericht 4.19 stellen wir eine neue rein optische Methode zur Bestimmung der Formanisotropie von individuellen mikrometergroßen magnetischen Elementen vor. Hierzu setzen wir eine Kombination aus Kerr-Mikroskopie und der Bestimmung von Hysteresekurven mit hoher Winkelauflösung, vereint mit einer quantitativen Analyse der Messdaten ein. In Bericht 4.20 berichten wir über die Entwicklung von TMR-basierenden Speicherzellen für Anwendungen im Niedrigkostenbereich und kleiner Speicherdichte.

4.19 All optical investigation of the shape anisotropy of individual micron sized $Ni_{80}Fe_{20}$ elements

T. Sebastian, A. Conca, G. Wolf, B. Leven, and B. Hillebrands[1]

Magnetic microstructures with dimensions of a few micrometers play a crucial role in the design of magnetic field sensors for positioning in robotics, for the automotive industry and in data storage applications such as MRAM cells. Magnetic properties of industrial devices are largely controlled via the shape anisotropy of the constituent elements.

The magneto-optical Kerr effect (MOKE) is a well established technique to characterize crystalline or induced anisotropies in magnetic thin films [1]. Recently, MOKE has been also used to investigate the anisotropy of micron sized elements embedded in arrays [2–4]. The resulting signal is an average over many elements and the details of the switching process of the single elements are lost. Some phenomena, like the effect of border roughness, pinning centers or the presence of crystallites in polycrystalline materials cannot be studied using this approach. Additionally, the large packing density in the arrays, needed to obtain a good signal-to-noise ratio, may lead to the presence of dipolar interactions between neighboring elements. In contrast to this, the results discussed in the present report are determined on individual micron sized elements with elliptical shape using a new micro-focused MOKE setup (µMOKE). This approach is highly relevant regarding spintronic applications like MRAM devices or magnetic sensors. In these cases, the ability to control the anisotropic switching properties of single elements becomes crucial. In MRAM devices, for instance, this is the key to narrow the distribution of magnetic properties.

The new µMOKE setup is equipped with a micro-focused HeNe-laser beam with a spotsize of 1 µm. An off-center incidence of the laser beam on the focusing objective ensures a wave-vector component of the probing light parallel to the external magnetic field and thus longitudinal MOKE geometry. The sample is mounted on a horizontal positioning stage with an accuracy in the range of $\sim$10 nm. In order to allow for the analysis of magnetic anisotropies, a rotating unit is employed to change the sample orientation with respect to the external field and the plane of incidence of the laser. In addition, the sample is illuminated by a LED and a CCD camera provides an image which is used to stabilize the sample position during the measurement process. For this purpose, a specially designed software routine with an automated picture recognition algorithm is used to correct the sample position during the measurement.

The elements under investigation have elliptical shape with different sizes and aspect ratios (ARs), given by the ratio between the long and short axis of the element. The sizes of the long axes vary from 2 µm to 8 µm while the ARs range from 2 to 10. These ellipses have been fabricated from a 5 nm thick $Ni_{80}Fe_{20}$ film produced by dc-sputtering. During the growth process the film easy axis was induced by applying an external magnetic field. Afterwards, the resulting polycrystalline material was structured using electron beam lithography and ion beam etching. To prevent dipolar interaction between neighboring elements their distance was set to 50 µm.

Before structuring the elements, the magnetic properties of the film were measured using a conventional MOKE setup with spatial resolution not better than 100 µm. According to the obtained results, the long axis of the ellipses was aligned parallel to the easy axis of the film.

---

[1] In collaboration with Sensitec GmbH, Mainz, Germany; B. Lägel, Nano+Bio Center, Technische Universität Kaiserslautern, Germany.

In order to analyze the results, we apply an extended Stoner-Wohlfarth-model [5,6]. This macrospin model uses the free enthalpy of the system containing a Zeeman-term caused by the external field and a term taking the anisotropy of the system into account:

$$g(\alpha_\mathrm{M}) = -H_\mathrm{ext} M_\mathrm{S} \cos(\alpha_\mathrm{M} - \alpha_\mathrm{H}) + g_\mathrm{ani}(\alpha_\mathrm{M}, \alpha_\mathrm{Ku}, \ldots) \tag{1}$$

Here α_M and α_H describe the directions of the magnetization vector and the external field, respectively. The second term of Eq. (1) consists of a magnetocrystalline contribution, which is the same for all elements under investigation, and a contribution caused by the shape anisotropy. Thus, it contains the easy axis directions corresponding to the different anisotropies - explicitely shown is the easy axis direction of a uniaxial anisotropy α_Ku. The shape anisotropy takes the influence of the element geometry on the magnetic properties into account and has to be calculated for each individual ellipse according to:

$$\begin{aligned} g_\mathrm{ani}(\alpha_\mathrm{M}) &= \frac{1}{2} M_\mathrm{S}^2 \left(N_1 \alpha_1^2 + N_2 \alpha_2^2 + N_3 \alpha_3^2\right) + \ldots && (2) \\ N_1 &= \frac{c}{a} \left(1 - e^2\right)^{1/2} \frac{K - E}{e^2} && (3) \\ N_2 &= \frac{c}{a} \frac{E - \left(1 - e^2\right) K}{\left(e^2 \left(1 - e^2\right)\right)^{1/2}} && (4) \\ N_3 &= 1 - N_1 - N_2 && (5) \end{aligned}$$

Here, N_i are the demagnetizing factors as calculated by Osborn [7] for the case of a very flat ellipsoid, K and E are the complete elliptic integrals. Magnetic reversal is simulated within this model by minimizing Eq. (1) in terms of the magnetization direction α_M, which is described by the direction cosines α_i in Eq. (2). For a thickness of only 5 nm an in-plane magnetization is expected, and thereby a description of the problem using only the in-plane angle of the magnetization is sufficient. Hysteresis can be incorporated in the model by using the perfect delay convention [8], which leaves the magnetization in the corresponding local minimum of the free enthalpy instead of switching it immediately to the global minimum. Additionally, the model includes a thermal energy density which allows the magnetization to overcome the energy barrier between the local and the global energy minimum. With this inclusion non-coherent phenomenon like the formation of domains or thermal excitation are phenomenologically treated in the model. However, the simplicity of the model permits only a partial treatment, since this phenomena can be only fully included by performing micromagnetic simulations. However, the calculation of the hysteresis loops for all the orientations of the sample is not possible due to the extremely large required computing time. As a result of the incomplete inclusion of non-coherent processes, the model predicts coercive fields that are higher than those obtained from measurements. This point is dicussed later when addressing the measurement results. The material parameters used for the simulations are $M_\mathrm{S} = 800 \cdot 10^3\,\mathrm{A/m}$, $K_\mathrm{u} = 0.1 \cdot 10^3\,\mathrm{J/m^3}$ and $K_\mathrm{b} = 0.3 \cdot 10^3\,\mathrm{J/m^3}$. These values are in accordance with material constants of NiFe available in literature [9,10].

In the following, the experimental results obtained with the new µMOKE setup are presented. In Fig. 1 the angular dependence of the coercive field for ellipses with a long axis of 6 µm is shown. The sample was rotated in steps of $\Delta\varphi = 3^\circ$ and, for each orientation of the individual elements with respect to the external magnetic field, a hysteresis loop was measured and the coercive field extracted. An angle of $\varphi = 0^\circ$ corresponds to an external magnetic field parallel to the long axis of

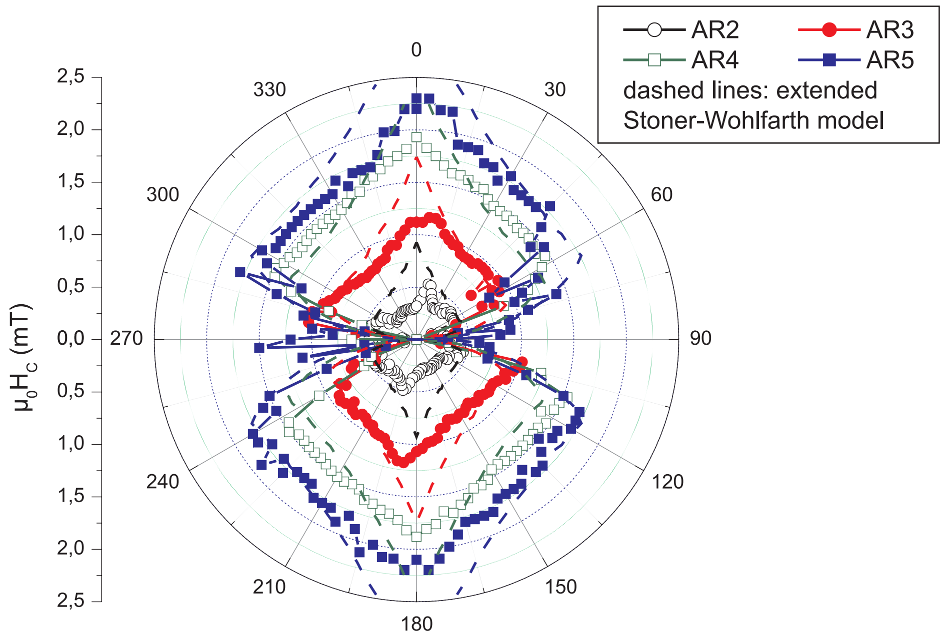

Fig. 1: Angular dependence of the coercive field for different elliptical elements with a long axis of 6 μm and variable aspect ratio AR. The short axes of the elements are 3 μm (hollow circles AR2), 2 μm (filled circles AR3), 1.5 μm (hollow squares AR4) and 1.2 μm (filled squares, AR5). An orientation with $\varphi = 0°$ or $\varphi = 180°$ corresponds to a hysteresis loop measured along the long axis of the element. The dashed lines represent calculations according to the extended Stoner-Wohlfarth model explained in the text.

the ellipse. In Fig. 1, it is possible to observe that the overall trend of the angular dependence of the coercive field reflects an effective total uniaxial anisotropy. Furthermore, there is a large increase of the maximal coercive field compared to the unstructured NiFe-film. The elements exhibit an easy axis with highest coercive fields ranging from $\mu_0 H_C \approx 0.5\,\text{mT}$ to $2.5\,\text{mT}$ for an angle close to $\varphi = 0°$ (or equivalently $\varphi = 180°$). Deviations from this behavior can be observed for the ellipses with AR 2 and AR 3, where the highest coercive field does not coincide with the long axis direction. There are two main reasons to explain this deviation. First of all, during the structuring process, a small error of ±5° cannot be discarded. A misalignment between the long axis and the easy axis of the sample would be expected to have a larger effect on elements with smaller AR. For increasing AR the shape anisotropy becomes dominant and overcomes the effect of the misalignment. The second reason lays in the polycrystalline nature of the NiFe film. The orientation of the thin film easy axis was measured with a conventional MOKE setup, which proportionates a signal averaged over a large area. However, it is reasonable to expect local fluctuations of the easy axis orientation due to small film inhomogeneities.

Figure 2 shows the angular dependence of the coercive field measured on ellipses with a long axis of 3 μm and ARs ranging from 2 to 5. As in the previous case, the overall trend of the coercivity as a function of the sample orientation φ follows the behavior expected from an uniaxial anisotropy caused by the elliptical shape of the elements under investigation. Maximal coercive fields lie in the range of $\mu_0 H_C \approx 1\,\text{mT}$ to $4\,\text{mT}$. The measurements shown in Fig. 2 indicate also an increasing effect of the shape anisotropy for increasing AR. Furthermore, an increasing shape anisotropy for ellipses with smaller size can be recognized when comparing the data with corresponding results for ellipses with the same AR but long axis of 6 μm.

The dashed lines in Figs. 1 and 2 represent a calculation with the extended Stoner-Wohlfarth model. The model is able to reproduce the qualitative trends visible in the experimental data. Quantita-

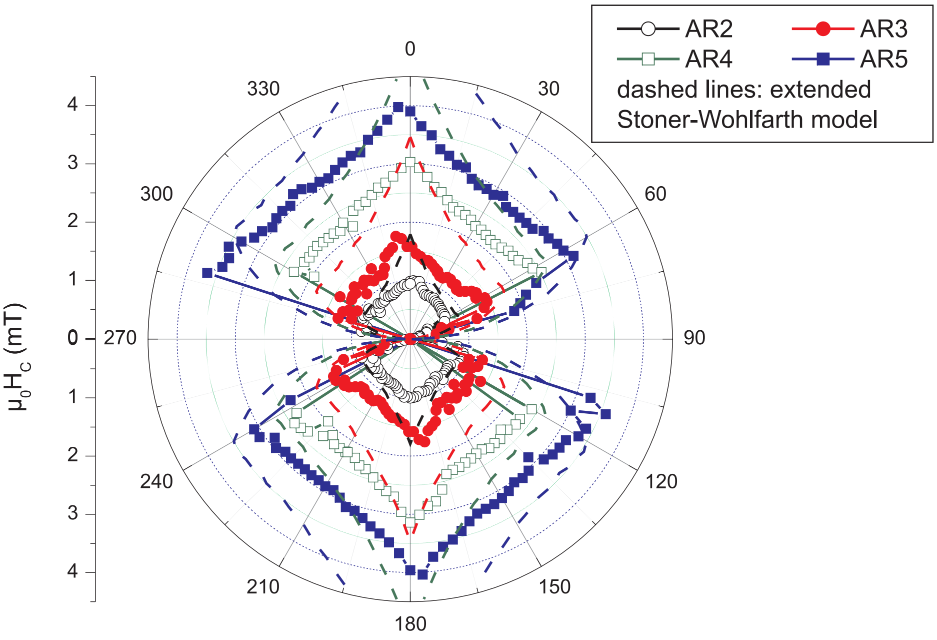

Fig. 2: Angular dependence of the coercive field for different elliptical elements with a long axis of 3 µm and variable aspect ratio AR. The short axes of the elements are 1.5 µm (hollow circles AR2), 1 µm (filled circles AR3), 0.75 µm (hollow squares AR4) and 0.6 µm (filled squares, AR5). An orientation with $\varphi = 0°$ or $\varphi = 180°$ corresponds to a hysteresis loop measured along the long axis of the element. The dashed lines represent calculations according to the extended Stoner-Wohlfarth model explained in the text.

tively however, the model prediction deviates in the range around $\varphi = 0°$ resulting in an overestimation of the coercive field. It must be noted that, since we are using a macrospin model, we asume a single domain particle behavior. This is not to be expected for structures with the elements dimensions used for this study. Additionally, the model assumes a perfect alignment of the long axis with the easy axis of the film and, for $\varphi = 0°$, also with the field. Such a perfect alignment is not achievable. The nucleation of domains in the structures will always lead to a reduction of H_C with respect to the expected values from a single domain particle. Border roughness or small defects in the elliptical form will also lead to a non homogenous demagnetizing field even in an ideally saturated case, this effect will also facilitate the formation of domains and hence, the reduction of H_C. Despite these facts the qualitative results and tendencies predicted by the model can be used to predict the behavior of elements as well as to classify experimental results.

Additional information on the role of the size and AR in the magnetic properties of microstructures can be obtained by measuring H_C for a fixed angle φ for a large number of elements with different dimensions. In Fig. 3 the results of these measurements for $\varphi = 0°$ (left panel) and $\varphi = 30°$ (right panel) are shown. Together with the experimental data, the predicted values using the Stoner-Wohlfarth model (lines) are also shown. For clarity reasons, for the $\varphi = 0°$ case, only the simulations for AR = 2 are plotted. It was already commented that for $\varphi = 0°$ the extended Stoner-Wohlfarth model overestimates the values of H_C . This is clearly visible in the left panel of Fig. 3. Nevertheless, the general trend is quite well reproduced. This is more evident in the right panel for $\varphi = 30°$ where the simulation predictions are compared with the experimental results for all ARs. In general the model predicts H_C better for smaller AR and for larger sizes. This is quite surprising, since we are employing a macrospin model and it is clearly to be expected that such a model fits better with smaller structures since these are closer to a single domain behavior. There is another point that becomes increasingly important for large ARs. This is the deviation from the ideal expected elliptical shape and the actual structure obtained after lithography. A certain

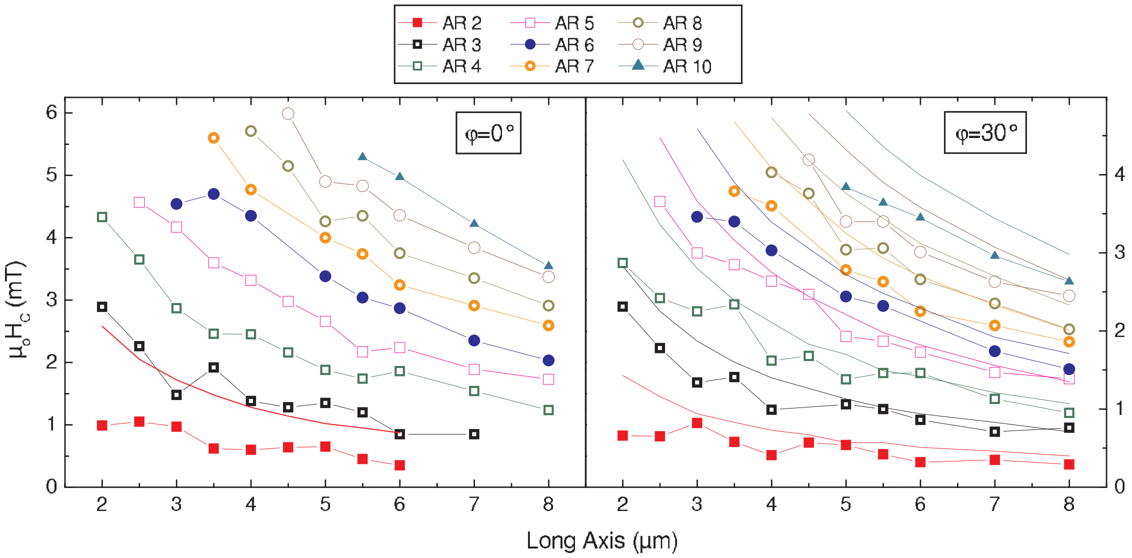

Fig. 3: Coercive field as a function of the long axis of $Ni_{80}Fe_{20}$ elliptical elements for different ARs and fixed orientation angle φ. The left panel shows the case for measurements along the long axis ($\varphi = 0°$) while for the right panel the applied field has an angle $\varphi = 30°$ respect to the long axis. The lines show the results obtained using the extended Stoner-Wohlfarth model. For clarity reasons, for the $\varphi = 0°$ case, only the simulations results for AR = 2 are plotted.

deviation of several tenths of nanometer can be expected. For a long axis of 5 µm for instance, the difference in the short axis between AR 9 And 10 is only 55 nm.

These results show that the new µMOKE setup allows for a quantitative and systematic study of the influence of the shape anisotropy on the magnetic behavior of single elements. The influence of different geometries on the magnetic reversal could be illustrated for a large number of elliptically shaped elements. Calculations according to an extended Stoner-Wohlfarth model served to confirm the trends visible in the experimental data. In addition, this new approach gives the opportunity to investigate dipolar interactions of neighboring magnetic elements, which is not accessible with conventional MOKE techniques. This issue will be addressed in future works.

Financial support by the Bundesminsterium für Bildung und Forschung (BMBF, VDI- TZ 13N9913) and the Deutsche Forschungsgemeinschaft (DFG, Graduate School of Excellence *Materials Science in Mainz*) is gratefully acknowledged.

References

[1] J. Hamrle, S. Blomeier, O. Gaier, B. Hillebrands, R. Schäfer, M. Jourdan, Journal of Applied Physics **100**, 103904 (2006).
[2] L. Thevenard, H.T. Zeng, D. Petit, R.P. Cowburn, Journal of Applied Physics **106**, 63902 (2009).
[3] S.M. Weekes, F.Y. Ogrin, and P.S. Keatley, Journal of Applied Physics **99**, 08B102 (2006).
[4] P. Vavassori, D. Bisero, F. Carace, a. di Bona, G. Gazzadi, M. Liberati, S. Valeri, Physical Review B **72**, 1 (2005).
[5] T. Mewes, H. Nembach, J. Fassbender, B. Hillebrands, J.- V. Kim, R. Stamps, Physical Review B 67, 1 (2003).
[6] E.C. Stoner and E.P. Wohlfarth, Philosophical Transactions of the Royal Society A: Mathematical, Physical and Engineering Sciences **240**, 599 (1948).
[7] J. Osborn, Physical Review **67**, 351 (1945).
[8] S. Nieber and H. Kronmueller, Phys. Status Solidi B **165**, 503 (1991).
[9] F.B. Humphrey, M. Redjdal, Physica Status Solidi (a) **201**, 1771 (2004).
[10] W. Hiebert, a. Stankiewicz, M. Freeman, Physical Review Letters **79**, 1134 (1997).

4.20 Development and characterization of a TMR-based memory system

A. Ruiz Calaforra, A. Conca Parra, B. Leven, and B. Hillebrands[1]

In this report, we present the development and characterization of a memory chip system based on magnetic tunneling junctions (MTJs). It consists of a 4×4 bit memory cell device, designed and produced in the industrial environment of the Sensitec GmbH, Mainz, in the framework of the MultiMag project. This project aims at the direct interlinking between research competencies and industrial production lines and thus defines challenges for both sides. Since the resistive state of a MTJ is determined by the magnetic configuration of the two electrodes that form the junction, these types of memory devices have the advantage of being non-volatile. This research is not directed to compete in speed or storage capacity with well established magnetic random access memory (MRAM) techniques and it is not oriented to computer applications. However, it shares the same architecture and functional principle. Instead the objective is to proportionate stable, durable and non-volatile memories for industrial equipment that requires only a small storage capacity for calibration parameters or production details.

The production process includes the design of the lithography masks compatible with a mass wafer processing in an industrial environment, the testing of the lithography steps and parameters needed for the fabrication of the microstructures and the characterization of the memory chips. The chip concept is based on a switching mode realized with two field pulses independent from each other. Previous work [1,2] show how crossed coplanar waveguides can be used for switching the magnetization with nanosecond pulses in single micron-sized elliptical elements. The basic unit consists of two copper current lines (top and bottom) defined in typical MRAM-architecture and an elliptical MTJ element lying on the intersection. To allow for a broader study of the switching properties

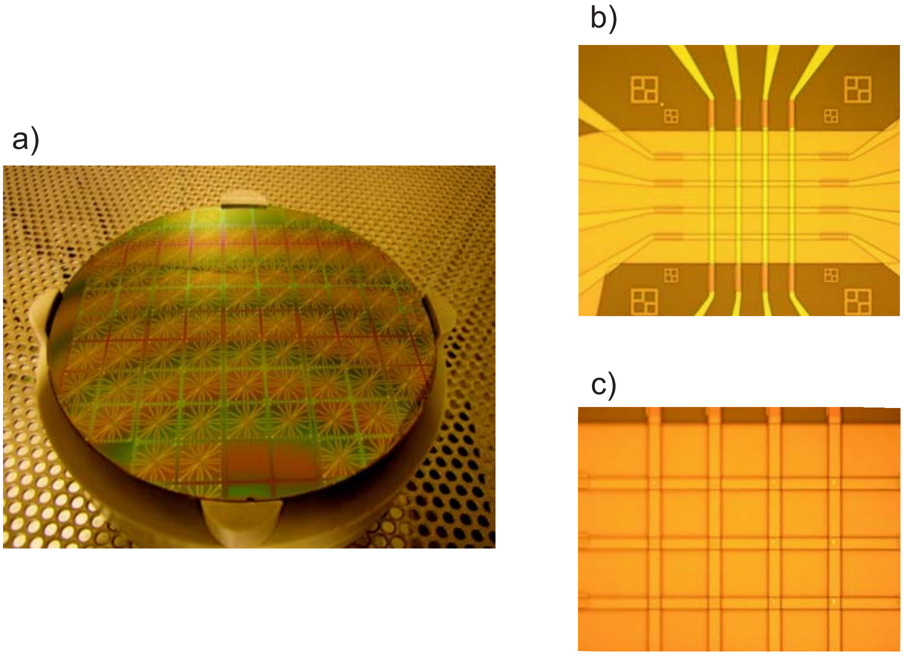

Fig. 1: a) Photograph of a memory array wafer at Sensitec. b) Micrograph of the chip structure before processing the elliptic MTJs. c) Micrograph of one of the chips for the case of elliptical elements in the 0° orientation configuration. Here, an enlarged area of the current line intersections is shown before processing the electrical contact pads to allow for a clear insight into the structure.

---

[1] In collaboration with Sensitec GmbH, Mainz, Germany; B. Lägel, S. Wolff, Nano+Bio Center, Technische Universität Kaiserslautern, Germany.

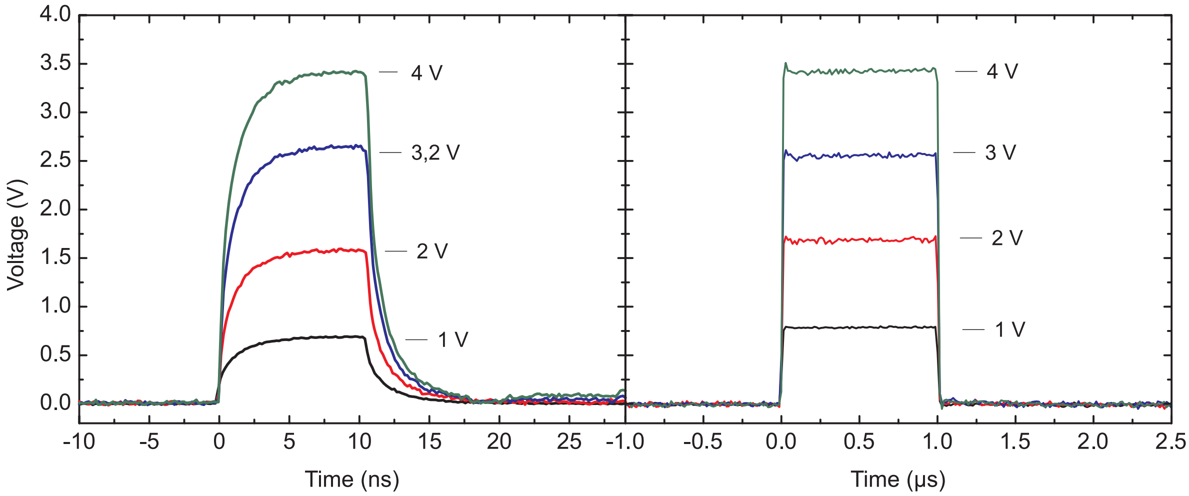

Fig. 2: Recorded pulses measured with a 40 GSa/s oscilloscope. The pulses were sent through one of the top current lines. Similar results were obtained for the bottom lines. Left: 10 ns pulse, right: 1 µs pulse.

of the MTJ two orientations (45°and 0°) of the long axis with respect to the current lines have been chosen. An additional current line is added to reset the magnetization which in needed for the stroboscopic MOKE measurements used for the characterization of the dynamic properties of the elements. Furthermore it allows for the magnetic initialization of the whole array system. Between all metallization layers an isolating amorphous 800 nm AlO_x layer is deposited. Finally contact pads are adjusted allowing for the electrical characterization of the MTJ.

The current lines are prepared employing a combination of UV-lithography and etching techniques. The copper film thickness is 300 nm. The MTJs have been defined in a standard electron beam lithography process. A photograph of a structured wafer can be seen in Fig. 1a. The wafer contains 16 flashfields each comprising 4 chips with 4×4 elements. Each chip contains 4 elements with varying dimensions for one of the two possible orientations (45°and 0°). Figure 1b shows a topview microscope image of the chip area while in Fig. 1c the intersection area, where the larger ellipses are processed for the 0°configuration, is shown at an enlarged scale. A 250 µm wide reset line can be seen, as well as 8 orthogonal oriented current lines with a width of 10 µm.

The transmission characteristics of the current lines was analyzed using an oscilloscope (40 GSa/s) and a network analyzer. Figure 2 exemplarily shows the recorded pulse profiles for different pulse amplitudes and two fixed pulse durations (1 µs, right and 10 ns, left) after transmission through one of the top current lines. As can be seen in Fig. 2 the transmission loss for the 1 µs pulses is of about 15% of the input voltage, whilst the transmission losses increase to about 20% for the 10 ns pulses. In the left panel of Fig. 2 it can also be seen that the rectangular pulse profile is modified during the transmission showing a pulse increase and decrease time of about 3 ns. This is due to the limited transmission characteristic of the current lines for high frequencies (above 2 GHz) as measured with the network analyzer. This effect also occurs for the 100 times longer pulses, but is not this evident due to the longer pulse duration. However, knowing these transmission characteristics the current lines can also be used for fast switching experiments.

An important part of this project includes the investigation of the static and dynamic magnetic properties of the MTJ elements as well as their optimization towards fast and reliable switching. To do so, the choice of the material of the free layer of the MTJ as well as the dimension and shape of the element is of major importance.

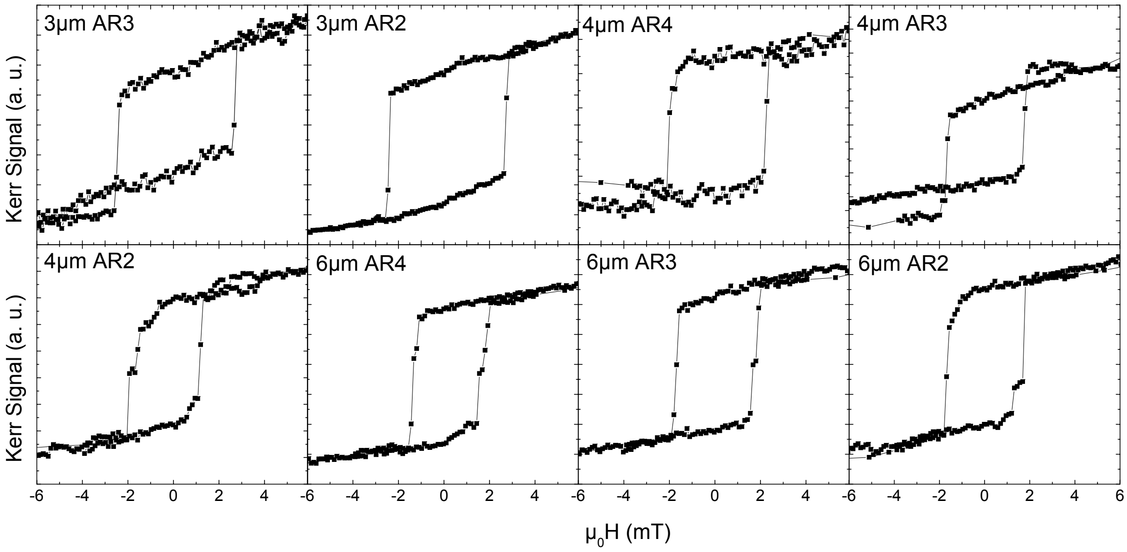

Fig. 3: Hysteresis loops measured along the long axis for CoFeB elliptical elements with different dimensions from a 0°oriented chip.

As good candidates for the free layer of the MTJ the ferromagnetic materials CoFe, CoFeB and NiFe are known because of their high spin polarization [3–6]. To determine the anisotropy and coercive field values of these materials, angular-resolved magneto-optical Kerr effect (MOKE) magnetometry was employed on continuous 5 nm thick films [7]. The results of the 360° scans of the CoFeB and NiFe films reveal each a uniaxial anisotropy with small coercive fields ($\mu_0 H_C = 0.1 - 0.5\,\mathrm{mT}$) while CoFe shows a strong biaxial anisotropy and larger coercivity values (4 mT).

To optimize the switching behavior of the MTJs towards reliability and moderate speed we analyze the domain formation during the process. This can be tailored by adjusting the geometrical parameters of the junction such as dimension and shape, which define the shape anisotropy of the elements. To do so, micromagnetic simulations using the OOMMF-code [8] were performed for elliptical elements with long axes of 6 µm and 3 µm respectively. First, the stability against domain formation was studied. For this, a saturation field was simulated pointing in a direction 5°apart the short axis direction thus defining a homogeneously aligned initial magnetization state of the element. We studied the relaxation behavior of the three different materials with two different thicknesses (5 and 10 nm), respectively. Furthermore, the long axis dimensions and aspect ratios (long axis to easy axis ratio) were varied. A second set of simulations were carried out for elements magnetized along the long axis excited by a 2 ns square field pulse along the short axis direction to determine the final magnetization state and its evolution during the pulse excitation. Different field amplitudes were studied. The first set of simulations reveal that larger thicknesses or bigger sizes induce intermediate domain states. The second set of simulations show that elements with higher aspect ratio or smaller size relax faster and that the final magnetization state depends strongly on the phase of the precession at the end of the pulse. Additionally it was found that elements with higher aspect ratio or smaller size relax preferentially in homogeneously magnetized states. CoFe elements display a very different behavior from CoFeB and NiFe due to the strong biaxial anisotropy and higher damping, which makes this material difficult to control. Consequently, we concluded from the simulations that CoFeB and NiFe elements with long axis dimensions from 4 to 3 µm and aspect ratios of 3 and 4 guarantee for a good reliability against domain formation as well controllable reproducible switching.

Following these theoretical results the MTJ elements have been designed and very recently the first completed wafers produced in the industrial environment of the Sentitec GmbH, Mainz, were delivered. They consist of one sample comprising a CoFeB/MgO/CoFeB MTJ stack and one sample with a single CoFeB reference layer adjusted to the free layer electrode of the MTJ stack. The static magnetic properties of the CoFeB elements were characterized employing a micro-focused MOKE setup as described in article 4.19 of this Annual Report. The corresponding hysteresis loops are summarized exemplarily in Fig. 3. As important working criteria two points have been identified: First, reliable and reproducible switching can be expected if all elements defined on the wafer with the same dimensions exhibit comparable coercive field values H_C. This was proven, showing that at least in each chip of the wafer, the properties of the elements are well controlled. Second, the influence of the size and the aspect ratio on the coercivity H_C and thus on the power consumption of the application is of major importance. Higher coercive field values have been detected for smaller elements (3 and 4 μm) and for higher aspect ratios (3 and 4). This leads to a higher applied voltage needed for switching and, in consequence, larger power consumption. Furthermore, it can be deduced from Fig. 3 that the elements with an aspect ratio of 3 and 4 show sharper switching and a more squared hysteresis loop as compared to those obtained from elements with an aspect ratio 2.

In conclusion, the static switching experiments confirmed well the simulation results. CoFeB and NiFe elements with long axis dimensions from 4 to 3 μm and aspect ratios of 3 and 4 have been identified to be good candidates for applications as the exhibit good reliability against domain formation as well as controllable reproducible switching with moderate power consumption.
Time-resolved measurements will be performed to establish the adequate strategy to identify optimized candidates for a reliable, reproducible and less power consuming switching.

Financial support by the State of Rhineland-Palatinate (*Technologieplattform Spintronik in Rheinland-Pfalz*) and the Bundesminsterium für Bildung und Forschung (BMBF, VDI- TZ 13N9913) is gratefully acknowledged.

References

[1] P. Martín Pimentel, H. Grimm, B. Leven, B. Hillebrands, J. Appl. Physics **102**, 063913 (2007).

[2] P. Martín Pimentel,S. Trellenkamp, S. Wolff, S.J. Hermsdoerfer, H.T. Nembach, B. Leven, B. Hillebrands, Appl. Phys. Lett. **88 (12)**, 122510 (2006).

[3] D.J. Monsmaad S.S. Parkin, Appl. Phys. Lett. **77**, 5, 720 (2010).

[4] T. Kubota et al., Jpn. J. Appl. Phys. **46**, L250-L252 (2007).

[5] J.S. Moodera, J. Magn. Mater. **200**, 248 (1999).

[6] D. Wang et al., IEEE Trans. on Mag. **40**, 2269 (2004).

[7] T. Sebastian, G. Wolf, A. Conca Parra, B. Hillebrands, *Anisotropy of single magnetic elements*, AG Magnetismus Annual Report (2009).

[8] M.J. Donahue et al., Report NISTIR 6376, Gaithersburg, MD (1999).

Chapter 5: Publications

Most publications can be downloaded from http://www.physik.uni-kl.de/hillebrands.

5.1 published

1. *Non-resonant wave front reversal of spin waves used for microwave signal*
   V.I. Vasyuchka, G.A. Melkov, A.N. Slavin, A.V. Chumak, V.A. Moiseienko, B. Hillebrands
   J. Phys. D: Appl. Phys. **43**, 325001 (2010).

2. *Analytical expression of the magneto-optical Kerr effect and Brillouin light scattering intensity arising from dynamic magnetization*
   J. Hamrle, J. PiŽtora, B. Hillebrands, B. Lenk, M. Münzenberg
   J. Phys. D: Appl. Phys. **43**, 325004 (2010).

3. *Wide-range wavevector selectivity of magnon gases in Brillouin light scattering spectroscopy*
   C.W. Sandweg, M.B. Jungfleisch, V.I. Vasyuchka, A.A. Serga, P. Clausen, H. Schultheiss, B. Hillebrands, A. Kreisel, P. Kopietz
   Rev. Sci. Instrum. **81**, 073902 (2010).

4. *YIG magnonics*
   A.A. Serga, A.V. Chumak, B. Hillebrands
   J. Phys. D: Appl. Phys. **43**, 264002 (2010).

5. *Nondiffractive subwavelength wave beams in a medium with externally controlled anisotropy*
   T. Schneider, A.A. Serga, A.V. Chumak, C.W. Sandweg, S. Trudel, S. Wolff, M.P. Kostylev, V.S. Tiberkevich, A.N. Slavin, B. Hillebrands
   Phys. Rev. Lett. **104**, 197203 (2010).

6. *Spin-wave tunneling through a mechanical gap*
   T. Schneider, A.A. Serga, A.V. Chumak, B. Hillebrands, R.L. Stamps, M.P. Kostylev
   EPL **90**, 27003 (2010).

7. *Magnetic anisotropy, exchange and damping in cobalt-based full-Heusler compounds: an experimental review*
   S. Trudel, O. Gaier, J. Hamrle, B. Hillebrands
   J. Phys. D: Appl. Phys. **43**, 193001 (2010).

8. *Reverse Doppler effect of magnons with negative group velocity scattered from a moving Bragg grating*
   A.V. Chumak, P. Dhagat, A. Jander, A.A. Serga, B. Hillebrands
   Phys. Rev. B **81**, 140404 (R) (2010).

9. *Magneto-optical investigation of epitaxial Co-rich Co_2MnGe thin films*
   S. Trudel, J. Hamrle, B. Hillebrands, T. Taira, M. Yamamoto
   J. Appl. Phys. **107**, 043912 (2010).

10. *Tandem magneto-optical Kerr effect magnetometer for the study of quadratic effects*
   S. Trudel, G. Wolf, H. Schultheiss, J. Hamrle, B. Hillebrands
   Journal of Physics: Conference Series **200**, 112010 (2010).

11. *Magnonic crystal based forced dominant wavenumber selection in a spin-wave active ring*
    A.D. Karenowska, A.V. Chumak, A.A. Serga, J.F. Gregg, B. Hillebrands
    Appl. Phys. Lett. **96**, 082505 (2010).
12. *Probing quadratic magneto-optical Kerr effects with a tandem dual-beam system*
    S. Trudel, G. Wolf, H. Schultheiss, J. Hamrle, B. Hillebrands
    Rev. Sci. Instrum. **81**, 026105 (2010).
13. *Structure, exchange stiffness and magnetic anisotropy of* $Co_2MnAl_xSi_{1-x}$ *Heusler compounds*
    T. Kubota, J. Hamrle, Y. Sakuraba, O. Gaier, M. Oogane, A. Sakuma, B. Hillebrands, K. Takanashi, Y. Ando
    J. Appl. Phys. **106**, 113907 (2009).
14. *Spin wave propagation in a microstructured magnonic crystal*
    A.V. Chumak, P. Pirro, A.A. Serga, M. Kostylev, R.L. Stamps, H. Schultheiss, K. Vogt, S.J. Hermsdörfer, B. Lägel, P.A. Beck, B. Hillebrands
    Appl. Phys. Lett. **95**, 262508 (2009).
15. *All-optical detection of phase fronts of propagating spin waves in a* $Ni_{81}Fe_{19}$ *microstripe*
    K. Vogt, H. Schultheiss , S.J. Hermsdoerfer , P. Pirro , A.A. Serga , B. Hillebrands
    Appl. Phys. Lett. **95**, 182508 (2009).
16. *Exchange stiffness in the* Co_2FeSi*-based Heusler compound*
    O. Gaier, J. Hamrle, S. Trudel, B. Hillebrands, H. Schneider, G. Jakob
    J. Phys. D: Appl. Phys. **42**, 232001 (2009).

5.2 in press

1. *All-linear time reversal by a dynamic artificial crystal*
   A.V. Chumak, V.S. Tiberkevich, A.D. Karenowska, A.A. Serga, J.F. Gregg, A.N. Slavin, B. Hillebrands
   Nat. Commun., in press.

5.3 submitted

1. *Near- and far-field excitation of lateral standing spin waves in a magnetic microstripe*
   K. Vogt, H. Schultheiss, S. Schäfer, B. Leven, B. Hillebrands
   submitted to Appl. Phys. Lett..
2. *Temporal behavior of the inverse spin Hall voltage in a magnetic insulator-nonmagnetic metal structure*
   M.B. Jungfleisch, A.V. Chumak, V.I. Vasyuchka, A.A. Serga, B. Obry, H. Schultheiss, P.A. Beck, A.D. Karenowska, E. Saitoh, B. Hillebrands
   submitted to Phys. Rev. Lett..
3. *Magnetic behavior of embedded antiferromagnetic elements at remanence*
   R. Neb, P.A. Beck, T. Sebastian, P. Pirro, S. Pofahl, R. Schäfer, B. Reuscher, M. Kopnarski, B. Hillebrands
   submitted to Appl. Phys. Lett..

4. *Magneto-optical observation of four-wave scattering in a 15 nm $Ni_{81}Fe_{19}$ film during large angle magnetization precession*
   H.T. Nembach, K.L. Livesey, M.P. Kostylev, P. Martin-Pimentel, S. Hermsdörfer, B. Leven, J. Fassbender, R.L. Stamps, B. Hillebrands
   submitted to Phys. Rev. B.

5. *Variable damping and coherence in a high-density magnon gas*
   S. Schäfer, V. Kegel, A.A. Serga, B. Hillebrands
   submitted to Phys. Rev. Lett..

5.4 Ph.D. theses

1. *Parametrisch angeregte kohärente Wechselwirkungen in räumlich eingeschränkten Magnonengasen*
   Sebastian Schäfer, TU Kaiserslautern, October 2010.

2. *Kohärenz und Dämpfungsverhalten von Spinwellen in magnetischen Mikrostrukturen*
   Helmut Schultheiss, TU Kaiserslautern, June 2010.

3. *Untersuchungen zur Wechselwirkung von Spinwellen und Domänenwänden in dünnen magnetischen Strukturen*
   Sebastian Hermsdörfer, TU Kaiserslautern, December 2009.

4. *Dynamische Kontrolle von Spinwellen durch lokalisierte, magnetische Inhomogenitäten*
   Timo Neuman, TU Kaiserslautern, December 2009.

Chapter 6: Conferences, Workshops, Schools, Seminars

(shown in chronological order; if not indicated otherwise the contributions were presented by the first author)

6.1 Conferences

6.1.1 Invited talks

A.A. Serga:
Magnon gases and condensates
APS March Meeting 2010, Portland, U.S.A., March 2010

A.A. Serga:
Spin wave logic
International Conference on Superconductivity and Magnetism (ICSM 2010), Antalya, Turkey, April 2010

A.V. Chumak:
Progress in magnonic crystals
KITPC Conference “Progress in Spintronics and Graphene Research”, Beijing, China, June 2010

A.A. Serga:
Formation and collapse of guided spin-wave bullets in a medium with induced magnetic anisotropy
International Conference “Nonlinear Waves - Theory and Applications”, Beijing, China, June 2010

B. Hillebrands:
Magnonic crystals (opening plenary talk)
Joint European Magnetic Symposia (JEMS) 2010, Kraków, Poland, August 2010

A.V. Chumak:
Frequency conversion and time reversal via a dynamic magnonic crystal
Joint European Magnetic Symposia (JEMS) 2010, Kraków, Poland, August 2010

A.V. Chumak:
Progress in magnonic crystals
IEEE 7th International Symposium on Metallic Multilayers (MML2010), Berkeley, U.S.A., September 2010

B. Hillebrands:
Magnonic Crystals
International Conference on Nanoscale Magnetism (ICNM), Istanbul, Türkey, September 2010

6.1.2 Contributed talks and posters

A.V. Chumak, T. Neumann, A.A. Serga, M.P. Kostylev, B. Hillebrands:
Current-controlled dynamic magnonic crystal
11th Joint MMM-INTERMAG Conference, Washington DC, U.S.A., January 2010

S. Schäfer, V. Kegel, A.A. Serga, B. Hillebrands:
Fast parabolic-like pump-free decay of parametrically excited magnons
11th Joint MMM-INTERMAG Conference, Washington DC, U.S.A., January 2010

A.A. Serga, A.V. Chumak, V.V. Vasyuchka, M.P. Kostylev, B. Hillebrands:
Parametrical recovery of a spin-wave signal stored in a magnonic crystal
11th Joint MMM-INTERMAG Conference, Washington DC, U.S.A., January 2010

A.V. Chumak, P. Pirro, A.A. Serga, M.P. Kostylev, H. Schultheiss, K. Vogt, S.J. Hermsdörfer, B. Lägel, P.A. Beck, B. Hillebrands:
Spin-wave propagation in a microstructured magnonic crystal
2nd International Conference on Metamaterials, Photonic Crystals and Plasmonics (META'10), Cairo, Egypt, February 2010

A.A. Serga, T. Schneider, A.V. Chumak, C.W. Sandweg, S. Trudel, S. Wolff, M.P. Kostylev, V.S. Tiberkevich, A.N. Slavin, B. Hillebrands:
Non-diffractive wave beams of sub-wavelength width in a medium with externally controlled anisotropy
2nd International Conference on Metamaterials, Photonic Crystals and Plasmonics (META'10), Cairo, Egypt, February 2010

S. Schäfer, V. Kegel, A.A. Serga, B. Hillebrands:
Fast parabolic-like pump-free decay of parametrically excited magnons
International Symposium "Novel states in correlated condensed matter - from model systems to real materials", Berlin, March 2010

V.I. Vasyuchka, A.A. Serga, C.W. Sandweg, A.V. Chumak, T. Neumann, B. Obry, H. Schultheiss, G.A. Melkov, V.S. Tiberkevich, A.N. Slavin, B. Hillebrands:
Interaction of two magnon condensates
International Symposium "Novel states in correlated condensed matter - from model systems to real materials", Berlin, March 2010

C.W. Sandweg, A.A. Serga, V.I. Vasyuchka, G.A. Melkov, D.V. Slobodyanyuk, B. Hillebrands:
Dynamics of a magnon gas directly driven by parametric pumping
International Symposium "Novel states in correlated condensed matter - from model systems to real materials", Berlin, Germany, March 2010

B. Leven, P. Pirro, K. Vogt, S.J. Hermsdörfer, H. Schultheiss, B. Hillebrands:
Brillouin light scattering study of domain walls in $Ni_{81}Fe_{19}$ *microstructures*
4th Seeheim Conference on Magnetism 2010, Frankfurt, Germany, April 2010

F. Ciubotaru, A.A. Serga, B. Leven, L. Lopez Diaz, B. Hillebrands:
Micromagnetic simulations of nonlinear spin-wave excitation in spin-valve nanocontacts
International Symposium on Advanced Magnetic Materials and Applications, Sendai, Japan, July 2010

K. Vogt, H. Schultheiss, P. Pirro, A.A. Serga, B. Hillebrands:
All-optical detection of phase fronts of propagating spin waves in magnetic micro-structures
Spin Age 2010 - A SpinAps Retreat, Pajaro Dunes (CA), U.S.A., August 2010

T. Sebastian, A. Conca Para, G. Wolf, B. Leven, B. Hillebrands:
Anisotropy studies of individual microstructured elements using the magnto-optical Kerr effect (MOKE)
SpinAge 2010 - A SpinAps Retreat, Pajaro Dunes (CA), U.S.A., August 2010

F. Ciubotaru, A.A. Serga, B. Leven, L. Lopez Diaz, B. Hillebrands:
Non-local three magnon scattering processes in nanosized spin-valve contacts
Joint European Magnetic Symposia (JEMS) 2010, Kraków, Poland, August 2010

A.D. Karenowska, J.F. Gregg, A.V. Chumak, A.A. Serga, B. Hillebrands:
Spin information transfer and transport in hybrid spinmechatronic structures
Joint European Magnetic Symposia (JEMS) 2010, Kraków, Poland, August 2010

A.D. Karenowska, A.V. Chumak, A.A. Serga, J.F. Gregg, B. Hillebrands:
Magnonic crystal based wavenumber selection in spin-wave active rings
Joint European Magnetic Symposia, Kraków, Poland, August 2010

R. Neb, P.A. Beck, T. Sebastian, P. Pirro, B. Reuscher, S. Pofahl, R. Schäfer, B. Hillebrands:
Inversely patterned structures in exchange coupled Fe/Cr/Fe-trilayers
AOFA, Kaiserslautern, Germany, September 2010

G. Wolf, S. Trudel, H. Schultheiss, J. Hamrle, W. Wang, H. Sukegawa, K. Inomata, B. Hillebrands:
Quadratic magneto-optical Kerr effect on epitaxial $Co_2FeSi_{0.5}Al_{0.5}$ *thin films*
IEEE 7th International Symposium on Metallic Multilayers (MML 2010), Berkeley, California, September 2010

A. Conca Para, T. Sebastian, G. Wolf, B Leven, B. Hillebrands:
Study of the transition between multi- and single domain switching in mesoscopic magnetic structures
IEEE 7th International Symposium on Metallic Multilayers (MML 2010), Berkeley, California, September 2010

6.1.3 Contributions to the DPG Frühjahrstagung

17 contributions: DPG Frühjahrstagung, Regensburg, March 2010

6.2 Workshops and Schools

6.2.1 Invited talks

B. Hillebrands:
Magnonic Crystals
4th International Workshop of Spin Current & 2nd International Workshop on Spincaloritronics, Sendai, Japan, February 2010

A.A. Serga:
Bose-Einstein condensate of magnons and supercooling of magnon gas
NordicSpin'10 - 2nd Nordic Workshop on Spintronics and Nanomagnetism, Gimo, Sweden, May 2010

B. Hillebrands:
Magnonic Crystals
Workshop "Mesomag", LEA Meeting Institut Néel, Grenoble, France, May 2010

B. Hillebrands:
Fundamentals on Spin Waves
IEEE Magnetics Society Summer School, Dresden, Germany, August 2010

6.2.2 Contributed talks and posters

M. Oogane, Y. Ando, J. Hamrle, B. Hillebrands:
Large magneto-resistance effect and magnetic properties in Co_2*-based Heusler compounds*
JST-DFG Workshop on Nanoelectronics, Bad Honnef, Germany, January 2010

F. Fohr, J. Hamrle, H. Schultheiss, A.A. Serga, B. Hillebrands, Y. Fukuma, Y. Otani:
Detection of spin accumulation in spin momentum transfer devices using Brillouin light scattering microscopy
JST-DFG Workshop on Nanoelectronics, Bad Honnef, Germany, January 2010

M.B. Jungfleisch:
Brillouin Light Scattering Spectroscopy
SFB/TRR49 Student Seminar, Höchst-Hassenroth, Germany, July 2010

A. Ruiz Calaforra, A. Conca Parra, B. Leven, B. Hillebrands:
Study of the influence of size and aspect ratio on the switching properties of magnetic elliptical elements
IEEE Magnetics Society Summer School, Dresden, Germany, August 2010

P. Pirro, T. Brächer, S.J. Hermsdörfer, B. Obry, H. Schultheiss, K. Vogt, P.A. Beck, P. Clausen, B. Leven, B. Hillebrands:
Distortion of the magnetization dynamics by domain walls
IEEE Magnetics Society Summer School, Dresden, Germany, August 2010

A.V. Chumak, V.S. Tiberkevich, A.D. Karenowska, A.A. Serga, J.F. Gregg, A.N. Slavin, B. Hillebrands:
Frequency conversion and time reversal via a dynamic magnonic crystal
Joint JST/DFG- Workshop: Spin Wave Aspects in Spintronics, Diemerstein, Germany, October 2010

F. Ciubotaru, A.A. Serga, L. Lopez Diaz, B. Leven, B. Hillebrands:
Micromagnetic analysis of nonlinear spin-wave excitation in spin-valve nanocontacts
Joint JST/DFG- Workshop: Spin Wave Aspects in Spintronics, Diemerstein, Germany, October 2010

F. Fohr, Y. Fukuma, S. Kaltenborn, J. Hamrle, H. Schultheiss, L. Wang, A.A. Serga, H.C. Schneider, Y. Otani, B. Hillebrands:
Optical detection of spin transport in non-magnetic metals
Joint JST/DFG- Workshop: Spin Wave Aspects in Spintronics, Diemerstein, Germany, October 2010

M.B. Jungfleisch, A.V. Chumak, V.I. Vasyuchka, A.A. Serga, P.A. Beck, E. Saitoh, B. Hillebrands:
Temporal behavior of the inverse spin Hall effect induced voltage in magnetic insulator - metal structure
Joint JST/DFG- Workshop: Spin Wave Aspects in Spintronics, Diemerstein, Germany, October 2010

R. Neb, P.A. Beck, T. Sebastian, P. Pirro, B. Reuscher, S. Pofahl, R. Schäfer, B. Hillebrands:
Inversely patterned structures in exchange coupled Fe/Cr/Fe-trilayers
Joint JST/DFG- Workshop: Spin Wave Aspects in Spintronics, Diemerstein, Germany, October 2010

B. Obry, K. Vogt, H. Schultheiss, P. Pirro, B. Hillebrands:
Spin-wave eigenmodes in small magnetic disks in the vortex state
Joint JST/DFG- Workshop: Spin Wave Aspects in Spintronics, Diemerstein, Germany, October 2010

A.A. Serga, V.S. Tiberkevich, C.W. Sandweg, V.I. Vasyuchka, A.V. Chumak, T. Neumann, B. Obry, G.A. Melkov, A.N. Slavin, B. Hillebrands:
Temporal dynamics of a pump-free Bose-Einstein condensate of magnons
Joint JST/DFG- Workshop: Spin Wave Aspects in Spintronics, Diemerstein, Germany, October 2010

A.A. Serga, V.S. Tiberkevich, C.W. Sandweg, V.I. Vasyuchka, A.V. Chumak, T. Neumann, B. Obry, G.A. Melkov, A.N. Slavin, B. Hillebrands:
Bose-Einstein condensate of magnons and supercooling of magnon gas
Joint JST/DFG- Workshop: Spin Wave Aspects in Spintronics, Diemerstein, Germany, October 2010

V.I. Vasyuchka, C.W. Sandweg, A.A. Serga, G.A. Melkov, D.V. Slobodyanyuk, B. Hillebrands:
Evolution of parametrically driven magnon gas
Joint JST/DFG- Workshop: Spin Wave Aspects in Spintronics, Diemerstein, Germany, October 2010

K. Vogt, H. Schultheiss, S.J. Hermsdoerfer, P. Pirro, A.A. Serga, B. Hillebrands:
All-optical detection of phase fronts of propagating and standing spin waves in a $Ni_{81}Fe_{19}$ *microstripe*
Joint JST/DFG- Workshop: Spin Wave Aspects in Spintronics, Diemerstein, Germany, October 2010

6.3 Meetings and Trade Fairs

A. Conca Parra, A. Ruiz Calaforra, B. Leven, B. Hillebrands:
Report on MULTIMAG project
Bi-annual project meeting, Mainz, Germany, November 2009

G. Wolf, B. Leven, B. Hillebrands:
Report on HEUSPIN project
Bi-annual project meeting, Bielefeld, Germany, March 2010

A. Conca Parra, A. Ruiz Calaforra, B. Leven, B. Hillebrands:
Report on MULTIMAG project
Bi-annual project meeting, Mainz, Germany, March 2010

F. Ciubotaru, B. Leven, B. Hillebrands:
Report on SPINSWITCH project
Bi-annual project meeting, Grenoble, France, April 2009

A. Conca Parra, A. Ruiz Calaforra, B. Leven, B. Hillebrands:
Presentation of MULTIMAG project
Hannover Messe 2010, Hannover, Germany, April 2010

A. Ruiz Calaforra, J. Paul, A. Conca Parra, B. Leven, B. Hillebrands:
Report on MultiMag project: TeMoRy
Sensitec GmbH meeting, Mainz, Germany, May 2010

G. Wolf, B. Leven, B. Hillebrands:
Report on HEUSPIN project
final project meeting, Mainz, Germany, June 2010

F. Ciubotaru, B. Leven, B. Hillebrands:
Report on SPINSWITCH project
Project final meeting, Palaiseau, France, September 2009

F. Fohr, S. Kaltenborn, Y. Fukuma, A.A. Serga, H.C. Schneider, Y. Otani, B. Hillebrands:
Project meeting, Kaiserslautern, Germany, October 2010

T. Sebastian, B. Jungfleisch, A.A. Serga, B. Hillebrands:
Introduction to Brillouin Light Scattering and progress of the collaboration
2nd ASPIMATT meeting, Sendai, Japan, October 2010

A.A. Serga, B. Hillebrands:
Nonlinear spin-wave dynamics and radiation properties of small Heusler devices
2nd ASPIMATT meeting, Sendai, Japan, October 2010

6.4 Invited colloquia

B. Hillebrands:
Magnonengase und -Kondensate
Berliner Physikalisches Kolloquium im Magnus-Haus, Berlin, Germany, December 2009

B. Hillebrands:
Magnon gases and condensates
Seminar of SFB 491, Duisburg, Germany, January 2010

6.5 Seminars

B. Obry, B. Hillebrands:
Nanoskopische Brillouin-Lichtstreuspektroskopie - Der Weg zur Dynamik des Nanomagnetismus
Workshop of GRK 792, Münchweiler a.d. Alsenz, Germany, April 2010

T. Sebastian, B. Hillebrands:
Introduction to Brillouin Light Scattering
1st MAINZ Ph.D. Student Seminar, Geseke, Germany, July 2010

C.W. Sandweg, V.I. Vasyuchka, A.A. Serga, G.A. Melkov, D.V. Slobodyanyuk, B. Hillebrands:
Evolution of parametrically driven magnon gas
Annual Retreat of SFB/TRR49, Kaiserslautern, Germany, October 2010

6.6 Awards and Fellowships

B. Hillebrands:
"IEEE Fellow" for his internationally regarded contributions to the understanding of magnetic excitations, including linear and nonlinear spin waves,
January 2010

B. Hillebrands:
Election as member of the Academy of Sciences and Literature in Mainz,
June 2010

T. Neumann:
"Promotionspreis 2009 der Alumni-Vereinigung Physik" of TU Kaiserslautern for his Ph.D. thesis "Dynamische Kontrolle von Spinwellen durch lokalisierte, magnetische Inhomogenitäten",
June 2010

K. Vogt:
Personal fellowship by Carl-Zeiss-Foundation for preparing her Ph.D. thesis "Zeit- und phasenaufgelöste Brillouin-Lichtstreumikroskopie an propagierenden Spinwellen",
June 2010

Appendix: Impressions from 2010

Ph.D. defense Dr. Timo Neumann

Ph.D. defense Dr. Sebastian Hermsdörfer

Ph.D. defense Dr. Sebastian Schäfer

Ph.D. defense Dr. Helmut Schultheiss